

ADF 301061

AD-A190 235

AD

CONTRACT REPORT BRL-CR-585

**COMPUTATIONAL MODEL FOR
ARMOR PENETRATION
2ND ANNUAL REPORT**

**SRI INTERNATIONAL
333 RAVENSWOOD AVENUE
MENLO PARK, CA 94025**

OCTOBER 1987

APPROVED FOR PUBLIC RELEASE; DISTRIBUTION UNLIMITED.

**US ARMY BALLISTIC RESEARCH LABORATORY
ABERDEEN PROVING GROUND, MARYLAND**

**REPRODUCED BY
U.S. DEPARTMENT OF COMMERCE
NATIONAL TECHNICAL INFORMATION SERVICE
SPRINGFIELD, VA. 22161**

88 3 22 104

DESTRUCTION NOTICE

Destroy this report when it is no longer needed. DO NOT return it to the originator.

Additional copies of this report may be obtained from the National Technical Information Service, U.S. Department of Commerce, Springfield, VA 22161.

The findings of this report are not to be construed as an official Department of the Army position, unless so designated by other authorized documents.

The use of trade names or manufacturers' names in this report does not constitute indorsement of any commercial product.

UNCLASSIFIED
SECURITY CLASSIFICATION OF THIS PAGE

0190 235

REPORT DOCUMENTATION PAGE				Form Approved OMB No 0704-0188 Exp Date Jun 30, 1986	
1a. REPORT SECURITY CLASSIFICATION Unclassified			1b. RESTRICTIVE MARKINGS		
2a. SECURITY CLASSIFICATION AUTHORITY			3. DISTRIBUTION / AVAILABILITY OF REPORT		
2b. DECLASSIFICATION / DOWNGRADING SCHEDULE					
4. PERFORMING ORGANIZATION REPORT NUMBER(S) PYU-7893			5. MONITORING ORGANIZATION REPORT NUMBER(S) BRL-CR-585		
6a. NAME OF PERFORMING ORGANIZATION SRI International		6b. OFFICE SYMBOL (If applicable)	7a. NAME OF MONITORING ORGANIZATION Ballistic Research Laboratory ATTN: SLCBR-TB		
6c. ADDRESS (City, State, and ZIP Code) 333 Ravenswood Avenue Menlo Park, CA 94025			7b. ADDRESS (City, State, and ZIP Code) Aberdeen Proving Ground, MD 21005-5066		
8a. NAME OF FUNDING / SPONSORING ORGANIZATION		8b. OFFICE SYMBOL (If applicable)	9. PROCUREMENT INSTRUMENT IDENTIFICATION NUMBER DAAK11-78-C-0115		
8c. ADDRESS (City, State, and ZIP Code)			10. SOURCE OF FUNDING NUMBERS		
			PROGRAM ELEMENT NO.	PROJECT NO.	TASK NO.
			WORK UNIT ACCESSION NO.		
11. TITLE (Include Security Classification) COMPUTATIONAL MODEL FOR ARMOR PENETRATION, 2nd Annual Report					
12. PERSONAL AUTHOR(S) D.C. Erlich, L. Seaman, D.R. Curran (Project Supervisor), D.A. Shockey, R.D. Caligiuri, R. Burbach					
13a. TYPE OF REPORT Contract Report		13b. TIME COVERED FROM Oct 79 TO Oct 80		14. DATE OF REPORT (Year, Month, Day)	
15. PAGE COUNT					
16. SUPPLEMENTARY NOTATION					
17. COSATI CODES			18. SUBJECT TERMS (Continue on reverse if necessary and identify by block number)		
FIELD	GROUP	SUB-GROUP			
11	06		Computational model, Armor penetration, Shear banding,		
19	04		Fragmentation, Depleted uranium, RHA, Two-dimensional wave propagation		
19. ABSTRACT (Continue on reverse if necessary and identify by block number)					
<p>Results are reported from the second year of a three-year BRL/AMMRC/SRI program to develop a computational capability for predicting the behind-the-armor fragment environment for spaced armor attacked by long-rod penetrators. The baseline materials chosen were rolled homogeneous steel armor (RHA) and depleted uranium (DU) for the penetrator.</p> <p>Phenomenological studies involving both quarter and full-scale ballistics tests at velocities up to 1.5 km/s and obliquities from 0° to 70° clearly revealed shear banding to be the principal phenomenon controlling both penetrator erosion and armor failure. A detailed, phenomenological scenario for oblique armor penetration is given.</p> <p>Contained fragmenting cylinder (CFC) experiments were performed to characterize the resistance of RHA to shear banding; a significant anisotropy was observed. The SHEAR3 computational model for shear banding was refined and calibrated with respect to previously obtained data from CFC experiments using 4340 steel (R_c40).</p> <p>A quarter-scale ballistics experiment was performed at BRL to provide a downrange fragmentation data base using materials (4340 steel and RHA) for which data on resistance</p>					
20. DISTRIBUTION / AVAILABILITY OF ABSTRACT <input checked="" type="checkbox"/> UNCLASSIFIED/UNLIMITED <input type="checkbox"/> SAME AS RPT. <input type="checkbox"/> DTIC USERS			21. ABSTRACT SECURITY CLASSIFICATION Unclassified		
22a. NAME OF RESPONSIBLE INDIVIDUAL Michael Scheidler			22b. TELEPHONE (Include Area Code) 301/278-6836		22c. OFFICE SYMBOL SLCBR-TB-W

19. ABSTRACT (Cont'd)

to shear banding existed. Preliminary armor penetration calculations using the SHEAR3 model were performed to simulate this BRL experiment, and preliminary results indicate that a phenomenologically based model, describing fragmentation as the nucleation, growth, and coalescence of shear bands, can be used to predict a fragmentation environment.

The phenomenological experiments indicated the need for a set of specific computational features for armor penetration simulations, such as finite-element numbering, and intersecting and wandering slide lines. Because these features were not all contained in one existing program, a program called Composite HEMP was written and assembled, incorporating many of those features. Testing of this code continues.

Accession For	
NTIS CRA&I	<input checked="" type="checkbox"/>
DTIC TAB	<input type="checkbox"/>
Unannounced	<input type="checkbox"/>
Justification	
By	
Distribution /	
Availability Codes	
Dist	Avail and/or Special
A-1	



SUMMARY

Goal and Approach.

The goal of this three-year program is to develop, in cooperation with the U.S. Army Ballistic Research Laboratory (BRL) and the U.S. Army Materials and Mechanics Research Center (AMMRC), a computational method for predicting armor penetration by projectile impact, and in particular, the back-of-the-armor fragment size and velocity distributions. An example of the extensive fragmentation produced at high impact velocities is illustrated in Figure S1, which shows three consecutive flash x-ray exposures of a steel rod penetrating a steel armor plate.

The research has focused on long rod steel and depleted uranium (DU) penetrators attacking rolled homogeneous steel armor (RHA) plates. The ultimate goal of the program is to be able to computationally simulate normal and oblique rod impacts of both single and multiple target plates; however, the work to date has concentrated on single target plate configurations.

The computations must be based on those material properties that govern the fracture and fragmentation; only by basing the computational material models on the actual microstructural failure modes and associated material properties can the experimental results be extrapolated to arbitrary geometries and designs. Therefore, the approach comprises the following steps:

- (1) Perform penetration phenomenology experiments to establish the key operative microstructural failure modes.
- (2) Perform additional experiments and analyses to measure the kinetics of the pertinent failure modes.
- (3) Develop computational models of those kinetics.
- (4) Calibrate the models with laboratory experimental data.
- (5) Modify and adapt a computer code to handle the failure kinetics models.



94-7883-108

FIGURE S1 RADIOGRAPHS TAKEN 30, 145, AND 285 μ s AFTER 1.55 km/s IMPACT OF A 4340 STEEL (R_C 40) ROD ONTO AN RHA TARGET PLATE

Both backscatter and downrange fragments are seen. The penetrator travels from right to left.

- (6) Perform computational simulations of key penetration experiments to test the resultant capability.

At the end of the second year some progress has been made on each of these steps and two key results have been obtained. First, the dominant fragmentation mechanism in both target and penetrator has been found to be the nucleation, growth, and coalescence of adiabatic shear bands. Therefore, our efforts have focused on gaining a quantitative understanding of the shear banding behavior and on constructing a computational model of that behavior.

Second, the resultant computational model gives strong promise of successfully predicting the back-of-the-armor fragmentation, as shown in Figure S2. In this figure we compare the observed cumulative back-of-the-armor fragment size distribution from the experiment of Figure S1 with the calculated fragment size distributions for both penetrator and target just before break-out of the penetrator. Not only is the predicted distribution of the same order as that observed, but the predicted total fragment masses from both penetrator and target are in fair to good agreement with observation.

As discussed below in the section on computational simulations, the comparison can only be semiquantitative at this state for several reasons. However, this preliminary comparison is extremely encouraging because it indicates that the program approach is working and that it is possible to predict back-of-the-armor fragmentation based on basic, measurable properties of the target and penetrator materials.

The program status is summarized in more detail below.

Phenomenology Experiments

A penetration phenomenology data base has been generated by BRL and SRI for 4340 steel and DU long rod penetrators striking single RHA target plates at normal and oblique impact angles. The data include back-of-the-armor fragment size and velocity distributions for comparison with computational simulations. The key microstructural failure mode identified for long rods striking relatively thick plates is adiabatic shear banding.

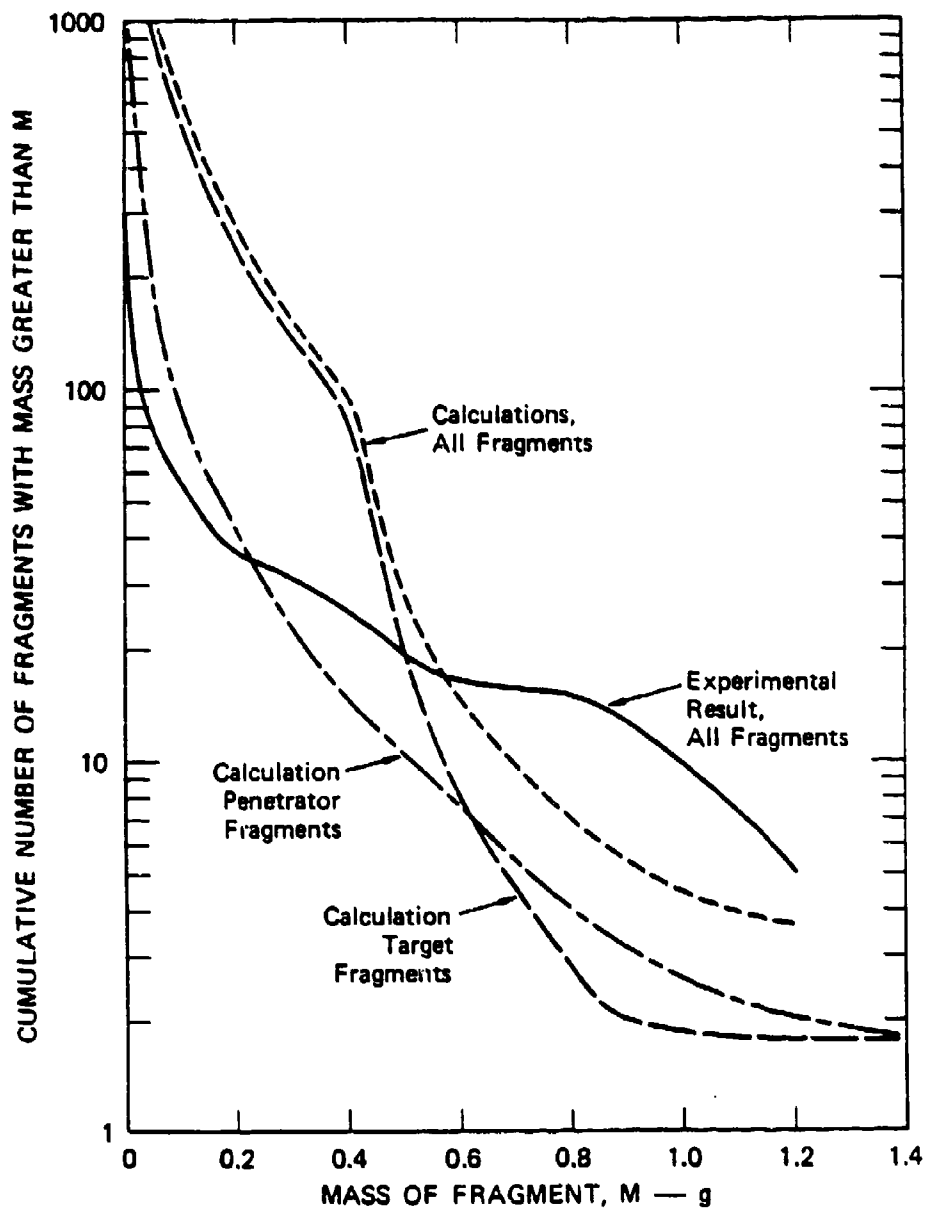


FIGURE S2 COMPARISON OF MEASURED DOWNRANGE FRAGMENT SIZE DISTRIBUTION FROM EXPERIMENT SHOWN IN FIGURE S1 WITH DISTRIBUTIONS CALCULATED FROM COMPUTER SIMULATION

The role played by the adiabatic shear bands changes significantly as the impact velocity increases. At velocities below the ballistic limit, little shear banding occurs in the RHA target. Instead, the target deforms plastically to form a cavity as the penetrator material flows around and back out the cavity. However, shear banding does dominate in the penetrator deformation and backflow. This is shown in Figure S3, which is a section through a thick steel target struck by a long steel rod. Shear banding caused the penetrator nose to divide into fragments, which then flowed back out of the cavity to form back-scatter fragmentation. Figure S4 shows similar pictures for thinner targets at normal impact velocities just below the ballistic limit. No shear banding in the targets is seen, and the beginning of the shear-band-induced penetrator fragmentation and backflow is evident.

For oblique impacts just below the ballistic limit, the situation is similar to that for normal impact, as shown in Figure S5. Backflow of shear-banded fragments from the penetrator causes a scalloped cavity boundary, similar to those seen in the normal impact case.

At impact velocities just above the ballistic limit, the picture changes dramatically, as shown in Figure S6. The plastic flow in the target has now become localized by adiabatic shear banding to form a target plug. The shear banding in the target is confined to the narrow region that defines the plug; the plug diameter is close to that of the expanded nose of the penetrator.

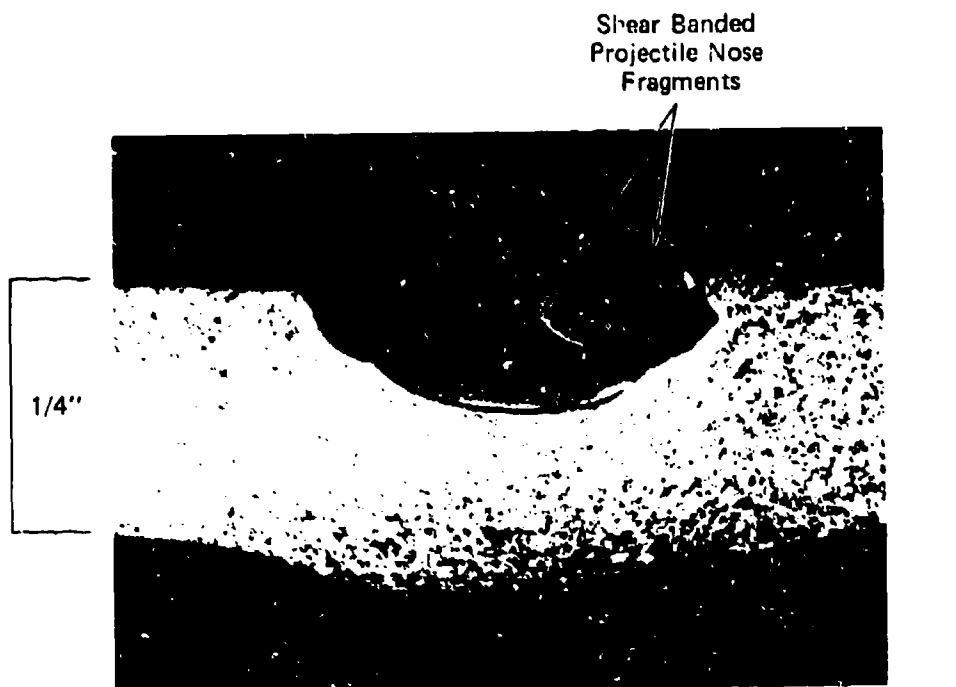
As the impact velocities increase further to values well above the ballistic limit for both oblique and normal impacts, the picture changes again. Now the penetration velocity is comparable to, or greater than, the plastic wave velocities in the target, and high plastic strains and associated shear banding are concentrated in a bow wave around the penetrator nose. Thus, extensive shear banding occurs throughout the plug and adjacent to the plug region, as shown in Figure S7 for the experiment depicted in Figure S1. The plug and collateral material are shattered by shear banding, and a spray of target and penetrator fragments emerges behind the armor.



MP-7893-91

FIGURE S3 CROSS SECTION THROUGH A TARGET IMPACTED PERPENDICULARLY
BY A LONG-ROD PENETRATOR, SHOWING BACKWARD FLOW OF SHEAR
BAND-ERODED PENETRATOR MATERIAL (Photograph courtesy of BRL)

Note: Horizontal hole near bottom was pre-drilled for instrumentation access.



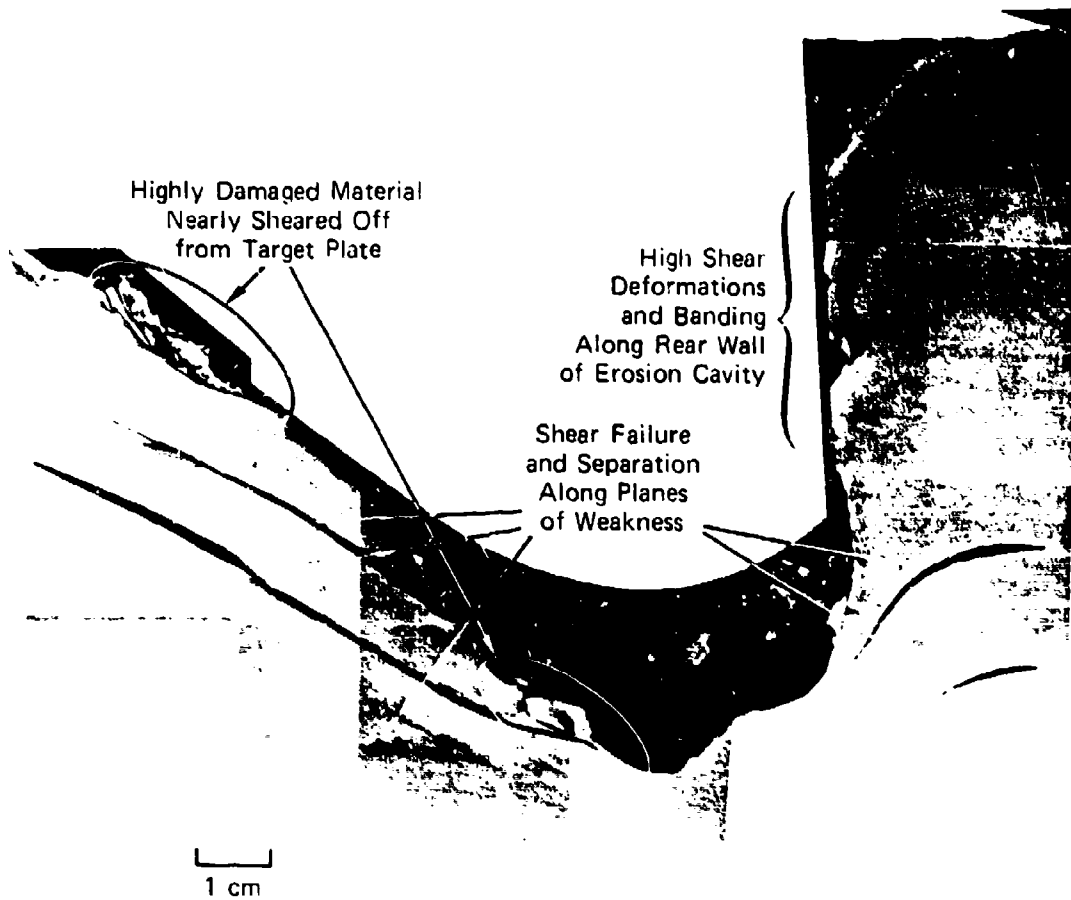
(a)



(b)

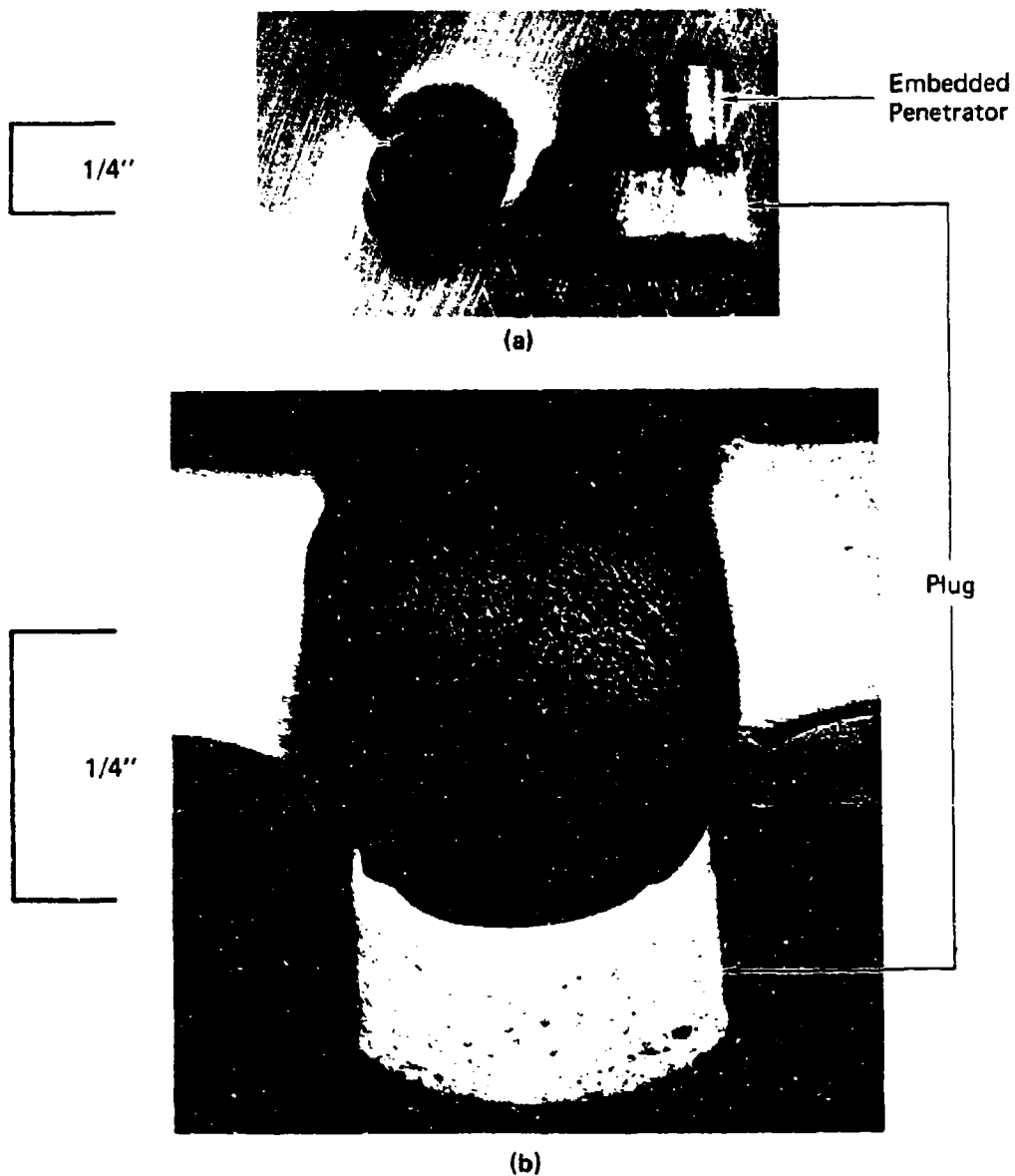
MP-7893-121

FIGURE S4 CROSS SECTIONS THROUGH CENTERS OF RHA TARGETS IMPACTED BY BLUNT-NOSED 4340 STEEL PROJECTILES



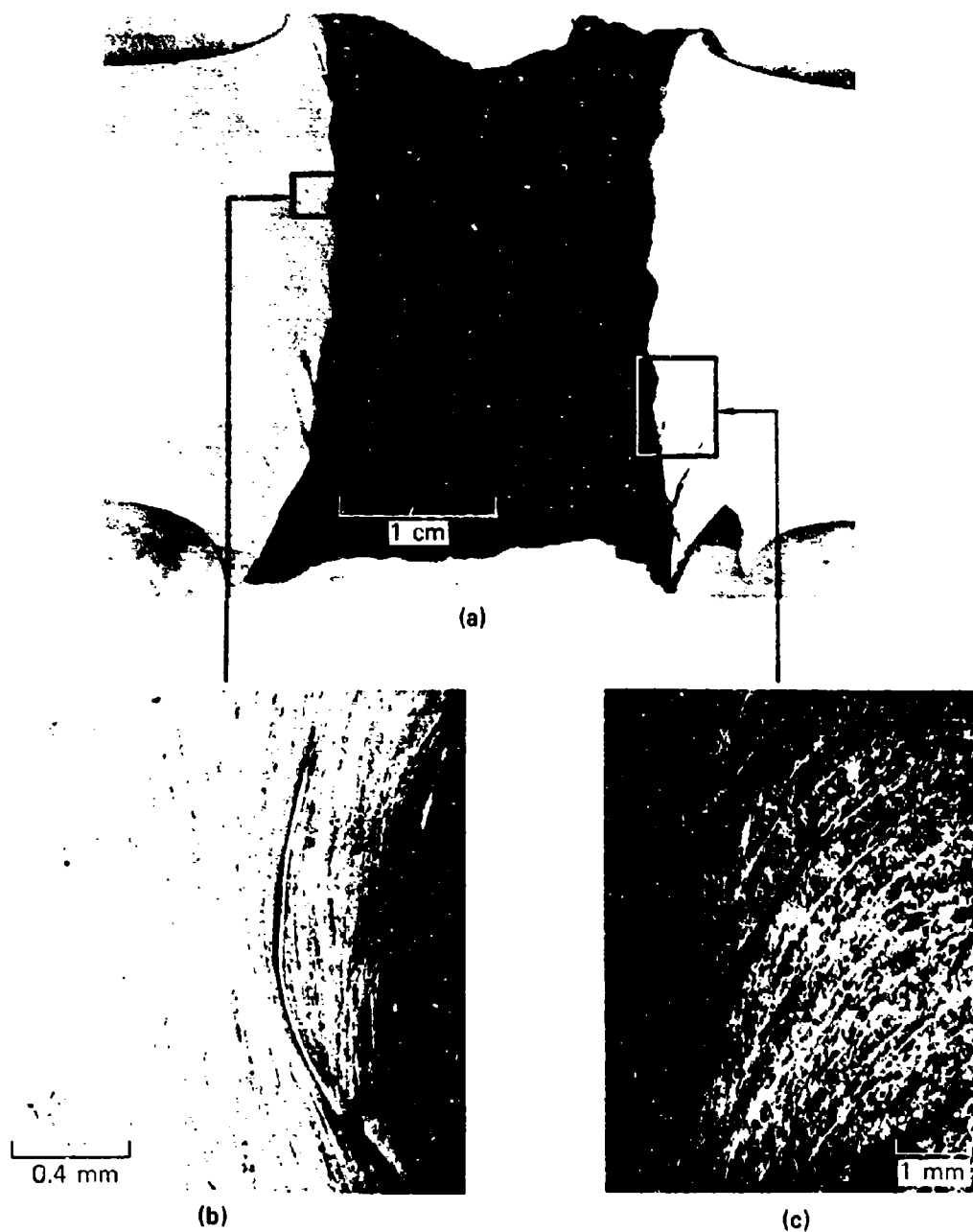
MA-7893-89

FIGURE S5 CROSS SECTION OF CRATER FORMED BY IMPACT OF FULL-SCALE STEEL LONG-ROD PENETRATOR INTO 4-INCH-THICK RHA TARGET AT VELOCITY OF ≈ 1.5 km/s AND OBLIQUITY OF $\approx 70^\circ$



MP-7893-42A

FIGURE S6 BLUNT-NOSED 4340 STEEL PROJECTILE EMBEDDED IN RHA TARGET PLUG (a) AND CROSS SECTION THROUGH IMPACT AXIS (b) FOLLOWING IMPACT AT 792 m/s



MP-7893-114

FIGURE S7 CROSS SECTION THROUGH CENTER OF RHA TARGET (a) IMPACTED BY BLUNT-NOSED 4340 STEEL PROJECTILE AT 1.55 km/sec AND TWO DETAILED VIEWS (b) AND (c) SHOWING DENSE SHEAR BANDING IN REGION ADJACENT TO PENETRATION HOLE

Target is from experiment depicted in Figure S1.

Experiments to Measure Shear Band Kinetics

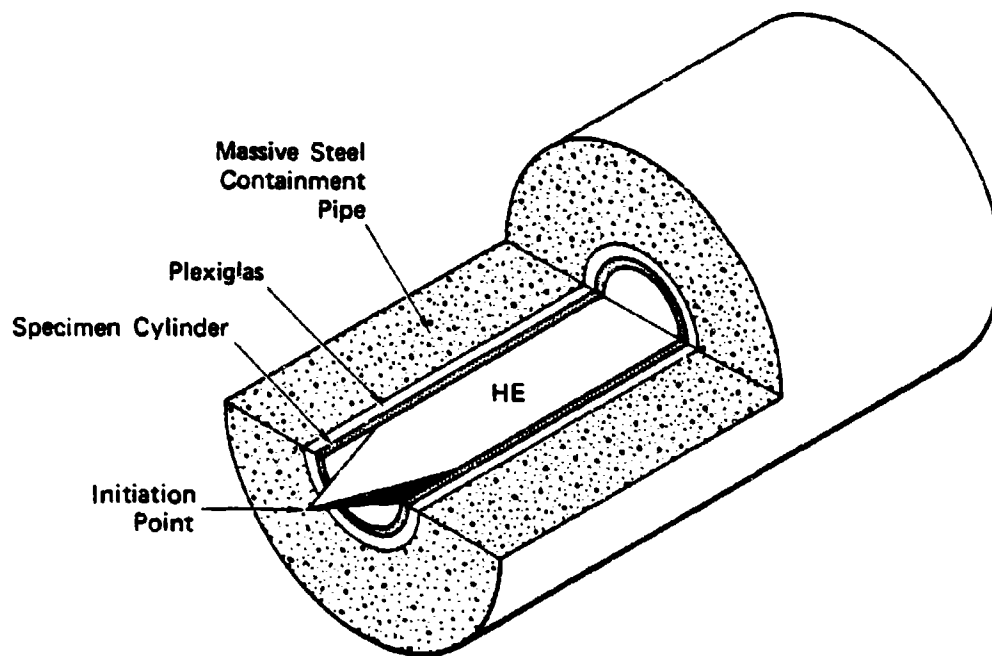
After adiabatic shear banding was identified as the dominant failure mode, the next step in the program was to perform a series of experiments to measure the shear band kinetics. In addition to the usual mechanical tests, these experiments consisted of applying internal explosive loads to thick-walled cylinders of the test material so that they expanded to final dimensions controlled by massive containment cylinders. The setup for this contained fragmenting cylinder (CFC) experiment is shown in Figure S8. Shear bands originating at the inner surface of the cylinder were counted, measured, and correlated with computed stress and strain histories, as shown in Figure S9, to deduce the shear band kinetics formulae.

This procedure has now been completed for a previously available data base for 4340 steel and is under way for a data base generated during the past year for RHA material. Similar data for DU will be taken during the upcoming year.

Computational Model Development

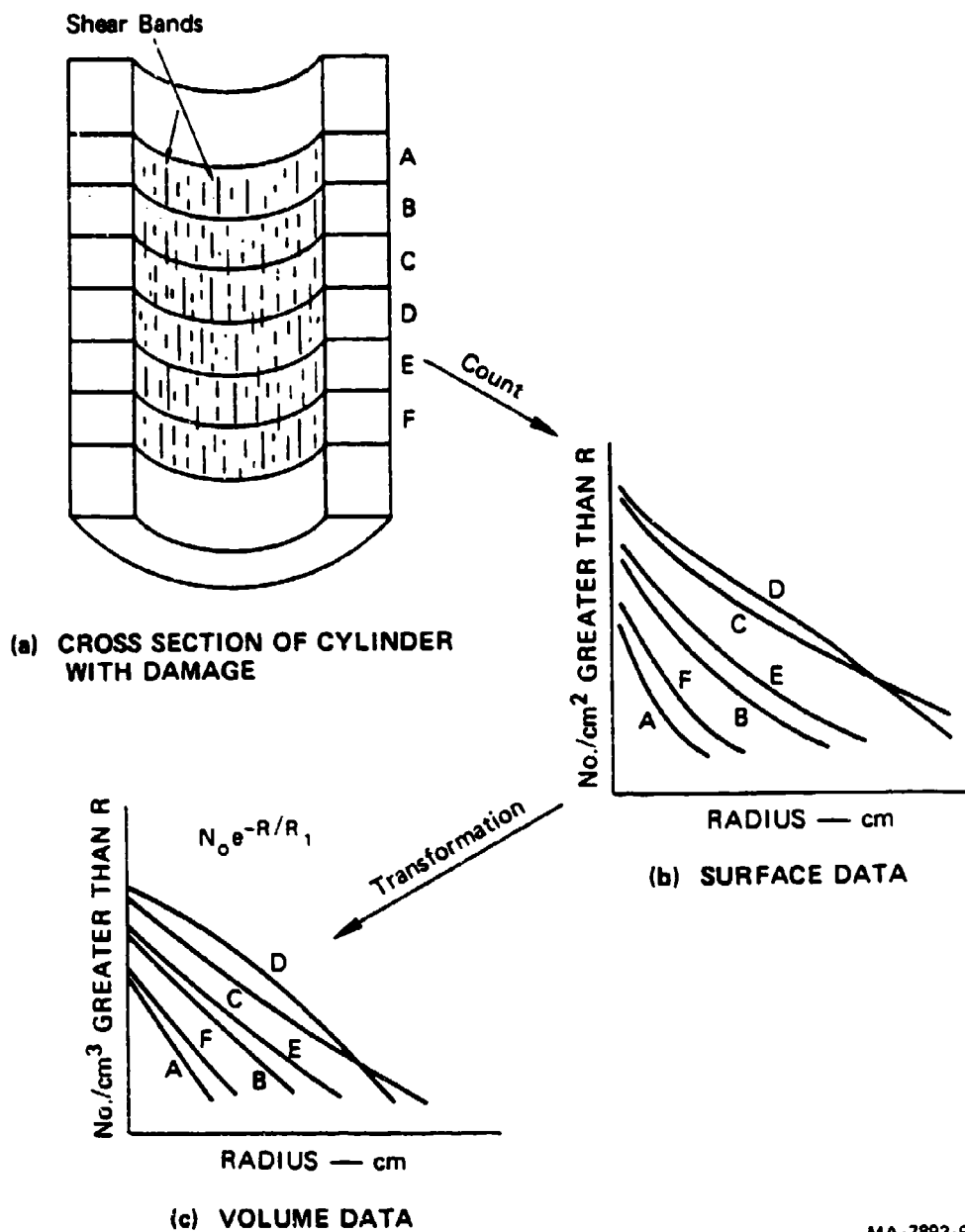
A computational model of the observed shear band kinetics has also been completed. The model, called SHEAR3, describes the nucleation, growth, and coalescence of the shear bands to form fragments. SHEAR3 produces good to fair agreement with a variety of CFC data for 4340 steel and will soon be calibrated against RHA steel CFC data.

To fulfill the program goals, SHEAR3 must be based on the fundamental material properties that govern the shear band kinetics. The status of relating measured SHEAR3 parameters to more fundamental properties is as follows. First, the shear band nucleation process appears at least partially understood. Localization into shear bands occurs in 4340 steel at the value of equivalent plastic strain predicted by plastic instability theory, namely, the strain at which the rate of strength reduction from thermal softening exceeds the rate of strength increase from the work hardening. Thus, the nucleation threshold strain depends on basic material properties, as desired. However, other observed features of the nucleation behavior have not yet been related to more fundamental material properties. For example, the shear band propagation



MA-7893-130

FIGURE S8 SCHEMATIC OF CONTAINED FRAGMENTING CYLINDER (CFC)
EXPERIMENTS FOR STUDYING SHEAR BAND KINETICS



MA-7893-98

FIGURE S9 STEPS IN OBTAINING CUMULATIVE SHEAR BAND DISTRIBUTIONS FROM CONTAINED FRAGMENTING CYLINDER DATA

threshold is governed by the resolved shear strain in the plane of the band rather than by the equivalent plastic strain, and the nucleation sites have not yet been related to microstructural heterogeneities or to instability wavelengths. Work is continuing to better relate these aspects of nucleation to basic properties.

Second, the observed shear band propagation is consistent with a viscous growth relation similar to that measured previously for tensile voids and cracks. However, the dependence of this propagation relation on more fundamental material properties has not yet been established, and work is under way to gain a better understanding of this process.

Finally, as the shear bands propagate and coalesce to form fragments, the material softens and the amount of shear stress that can be supported decreases. SHEAR3 contains a description of this work softening process, which is assumed to depend on the frictional forces in the sliding bands and on the material anisotropy. SHEAR3 currently describes the frictional effect, but not the anisotropy. Work is therefore continuing to improve the model to handle material anisotropy.

Calibration of the Model

As mentioned above, the SHEAR3 model has been calibrated with laboratory mechanical and CFC data for 4340 steel, and calibration with mechanical and CFC data for RHA is in progress. During the upcoming year, we plan to perform similar calibration experiments for DU.

Computer Code Development

A wave propagation computer code has been developed during the past year to be used in conjunction with SHEAR3 for computationally simulating penetration events. The code is a modification of the HEMP code and is called Composite HEMP. This code, which is now in the debugging stage, has the following features. First, the input/output is similar to that for the versions of HEMP now in use at BRL and AMMRC. Second, the cell numbering algorithm has been changed to a finite element scheme used,

for example, by the EPIC code. This scheme has several advantages, including easier inclusion of double slide lines near the penetrator/target interface. Third, an automatic rezoning algorithm has been included. Fourth, a self-locating and self-orienting internal slide line subroutine has been planned, but has not yet been written. Finally, the NAG/FRAG family of failure models, including SHEAR3, has been inserted into the code.

During the upcoming year, Composite HEMP will be used in computational simulations of selected penetration experiments.

Computational Simulations

Preliminary computational simulations of several normal impacts of 4340 steel rods on RHA targets have been performed during the past year with the TROTT code, an in-house SRI code that is similar to HEMP. TROTT contains the SHEAR3 failure model, but does not contain the finite element numbering scheme or a double slide line algorithm. The purpose of these calculations was, first, to test the potential of SHEAR3, using material parameters based on CFC experiments, for simulating long rod impact events, and, second, to help design the experiment shown in Figures S1 and S7. The results of the calculations are shown in Figures S10 through S12. The conditions of the calculations were similar to those of the experiment shown in Figures S1 and S7, where a 1.02-cm-diameter by 17.16-cm-long 4340 steel ($R_c 40$) rod normally impacted a 2.54-cm-thick by 19.24-cm-diameter RHA target plate at 1550 m/s.

Figure S10 shows a plot of computed equivalent plastic strain contours in the penetrator and target 17 μ s after impact. The contours with equivalent plastic strains of 0.2 represent approximately the onset of shear banding, and values of 0.6 correspond roughly to complete fragmentation. (SHEAR3 computes different levels of damage in four separate orientations, but detailed plots of the damage contours in these orientations would be difficult to present in a single illustration.)

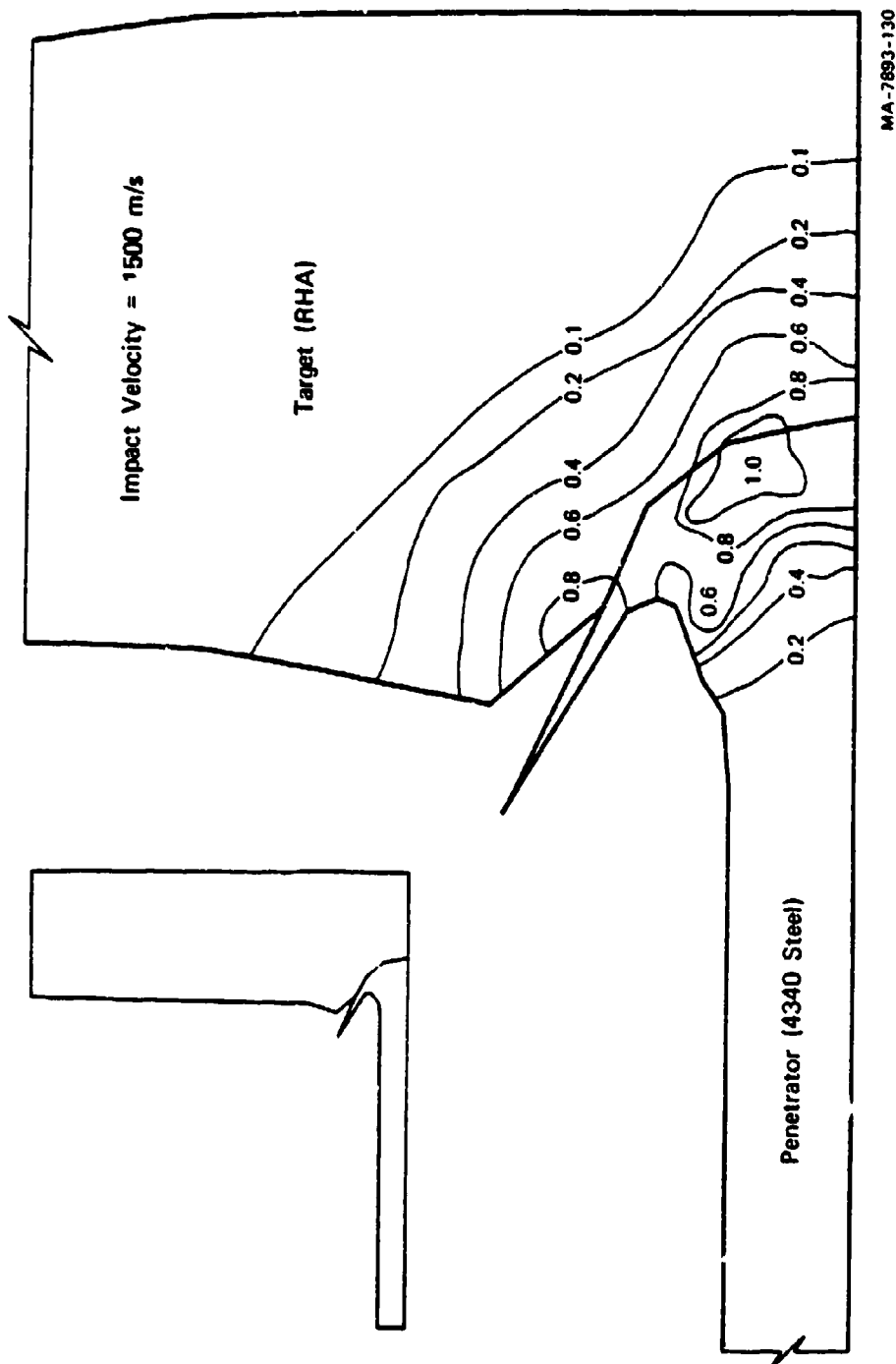


FIGURE S10 CONFIGURATION OF TARGET AND PENETRATOR AT 17 μ s IN TROT SIMULATION WITH NO SLIDE LINE.
INCLUDING CONTOURS OF EQUIVALENT PLASTIC STRAIN

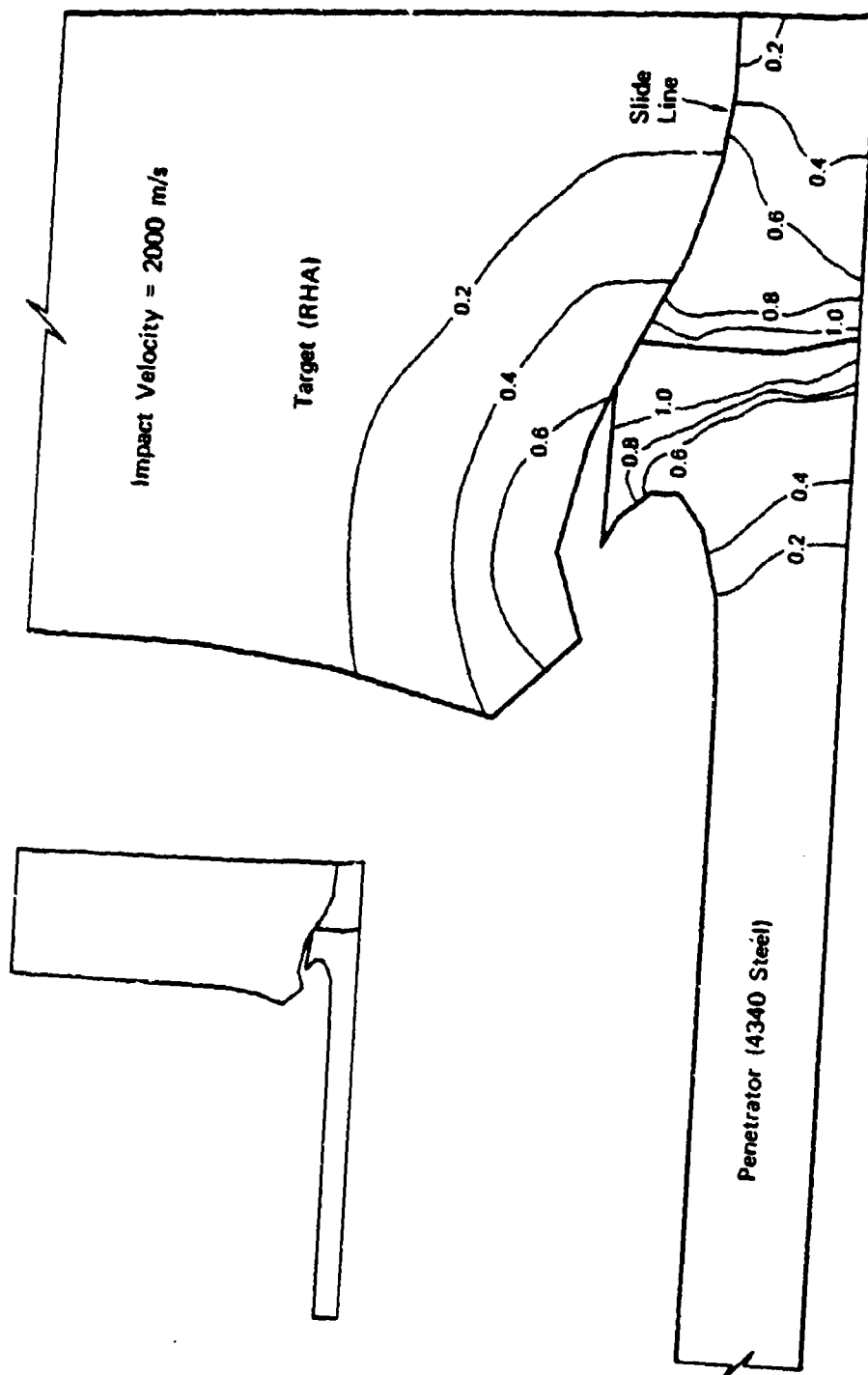


FIGURE S11 CONFIGURATION OF TARGET AND PENETRATOR AT 17 μ s IN TROTT SIMULATION WITH UNZIPPING SLIDE LINE, INCLUDING CONTOURS OF EQUIVALENT PLASTIC STRAIN

MA-7893-131

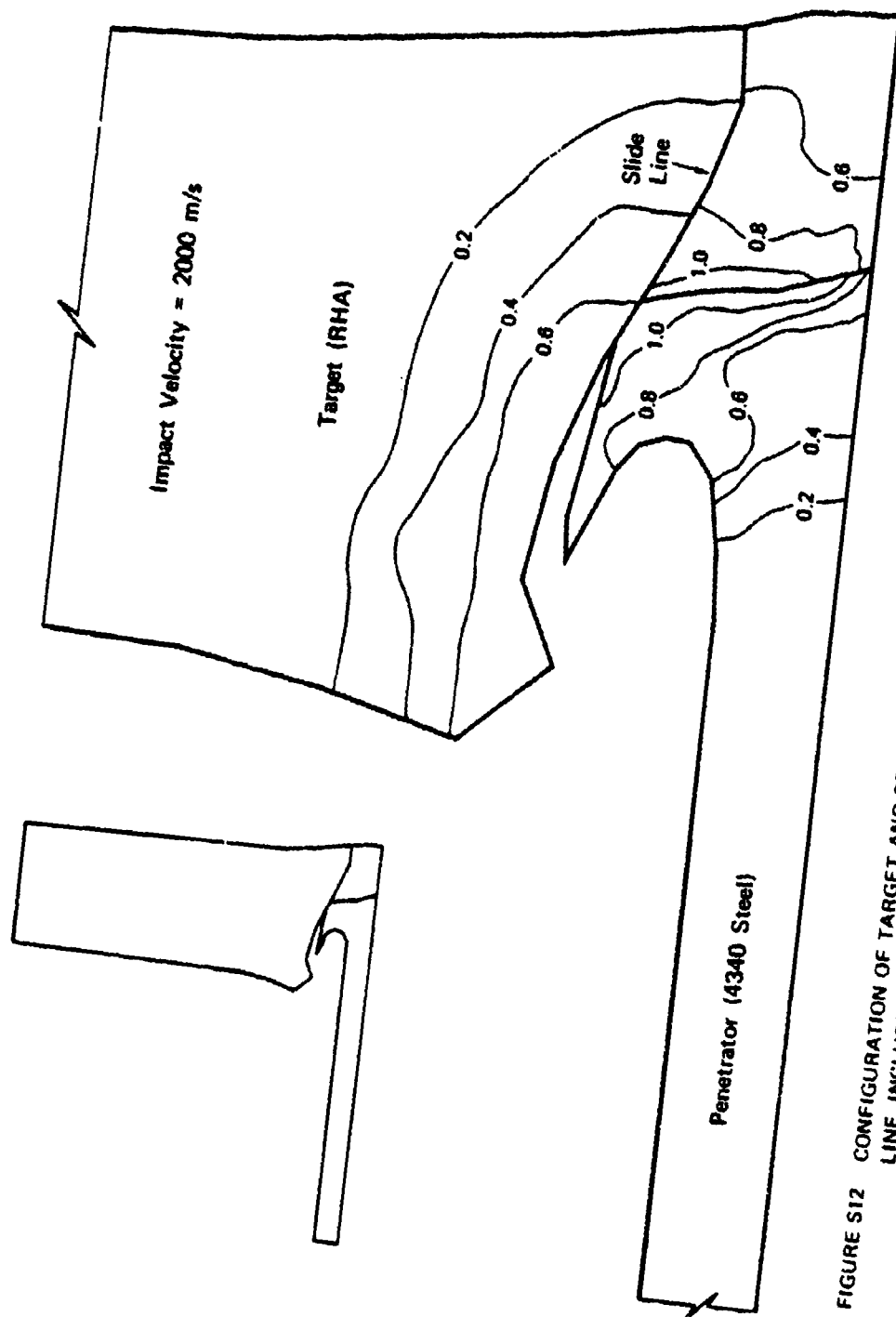


FIGURE S12 CONFIGURATION OF TARGET AND PENETRATION AT 23 μ s IN TROTT SIMULATION WITH UNZIPPING SLIDE

MA-7803-132

It can be seen that a large strain gradient develops at the boundary of what can be considered a developing plug, but the plug is being fragmented completely by a fragmentation front that looks like a "bow wave" ahead of the mushrooming penetrator nose. In addition, the penetrator nose itself is heavily fragmented, as is a collateral region outside the plug, although the fragmentation wave in this region lags behind that inside the plug.

Figures S11 and S12 show similar plots at 17 and 23 μ s after impact, respectively, for a case when the impact velocity is 2000 m/s. The results are similar to those of Figure S10. In particular, in Figure S12 it is seen that at 23 μ s after impact, the fragmentation front has nearly reached the rear surface. We would expect that when the front reached the rear surface, a spray of fragments would be released from the target and penetrator. The total number of fragments and their mass distribution for both the penetrator and the target at the time shown in Figure S12 were shown previously in Figure S2, along with the observed mass distribution from the experiment of Figure S1.

The computed mass fraction of the penetrator that was completely fragmented at the time shown in Figure S12 is 31%, in fair agreement with the value of 40% obtained by measuring the mass of the recovered unfragmented distal portion. Furthermore, the computed mass lost from the target in the form of the plug and collaterally fragmented material is 35 grams, in good agreement with the 34 grams obtained by weighing the armor plate before and after the experiment.

Comparison of computations with observations in Figure S2 shows that we compute too many small fragments and too few large ones. This discrepancy can have several causes. First, an unknown number of small fragments were not recovered in the experiment. Second, since the SHEAR3 parameters for RHA have not yet been derived from the CFC data, we used in the computations the measured nucleation threshold strain for RHA but the nucleation rate function appropriate for the 4340 penetrator steel. On the basis of our experience with another ductile steel (Armco iron), we expect the nucleation rate to be less for the RHA than for the 4340 steel. Accounting for both of these factors would reduce the

difference between observation and computation. Another cause for computational error is the as-yet unmodeled effect of the significant anisotropy of the RHA. Furthermore, the calculations of Figures S11 and S12 used a somewhat higher impact velocity than was achieved in the experiment.

These computations were terminated because of excessive cell distortion--a problem that illustrates the need for the rezoning and slide line features contained in the Composite HEMP code.

The above uncertainties mean that these comparisons of computed and observed fragment size distributions can only be semiquantitative. Nevertheless, the computations provided the information desired. The overall approach is shown to be promising; SHEAR3 parameters obtained from laboratory CFC experiments appear to produce encouraging results in the penetration computations. At an impact velocity well above the ballistic limit, SHEAR3 will produce a spray of target and penetrator fragments with a reasonable mass or size distribution. Work is continuing to perform a similar computational simulation of the case in which a plug formed at a velocity just above the ballistic limit (Figure S6). Further calculations must then await the determination of the SHEAR3 parameters for RHA material.

Future Work

During the third year of the program, the following work is planned:

- Conclude analyses of the RHA CFC experiments to obtain the SHEAR3 parameters for that material.
- Generate CFC and tensile test data for DU, and analyze the data to obtain the SHEAR3 parameters.
- Continue the effort to relate the measured SHEAR3 parameters to more fundamental material properties.
- Continue development of the Composite HEMP code.
- Perform Composite HEMP simulations of normal and oblique penetration experiments.

ILLUSTRATIONS

S1	Radiographs Taken 30, 145, and 285 μ sec After 1.55 km/sec Impact of a 4340 Steel (R _c 40) Rod onto an RHA Target Plate	iv
S2	Comparison of Measured Downrange Fragment Size Distribution from Experiment Shown in Figure S1 with Distributions Calculated from Computer Simulation	vi
S3	Cross Section Through a Target Impacted Perpendicularly by a Long-Rod Penetrator, Showing Backward Flow of Shear Band-Eroded Penetrator Material	viii
S4	Cross Sections Through Centers of RHA Targets Impacted by Blunt-Nosed 4340 Steel Projectiles	ix
S5	Cross Section of Crater Formed by Impact of Full-Scale Steel Long-Rod Penetrator into 4-inch-Thick RHA Target at Velocity of \approx 1.5 km/s and Oblliquity of \approx 70°	x
S6	Blunt-Nosed 4340 Steel Projectile Embedded in RHA Target Plug (a) and Cross Section Through Impact Axis (b) Following Impact at 792 m/s	xi
S7	Cross Section Through Center of RHA Target (a) Impacted by Blunt-Nosed 4340 Steel Projectile at 1.55 km/s and Two Detailed Views (b) and (c) Showing Dense Shear Banding in Region Adjacent to Penetration Hole	xii
S8	Schematic of Contained Fragmenting Cylinder (CFC) Experiments for Studying Shear Band Kinetics	xiv
S9	Steps in Obtaining Cumulative Shear Band Distributions from Contained Fragmenting Cylinder Data	xv
S10	Configuration of Target and Penetrator at 17 μ s in TROTT Simulation with No Slide Line, Including Contours of Equivalent Plastic Strain	xviii
S11	Configuration of Target and Penetrator at 17 μ s in TROTT Simulation with Unzipping Slide Line, Including Contours of Equivalent Plastic Strain	xix
S12	Configuration of Target and Penetration at 23 μ s in TROTT Simulation with Unzipping Slide Line, Including Contours of Equivalent Plastic Strain	xx

VII	SIMULATIONS OF PROJECTILE PENETRATIONS	103
VIII	PLANS FOR THE THIRD YEAR	113
	REFERENCES	115
APPENDICES		
A	REPRESENTATION OF THE SHEAR BAND DISTRIBUTION BY MULTIPLE SIZE GROUPS	117
B	COMBINATION PROCESS TO MAINTAIN THE DISTRIBUTION AS A SINGLE EXPONENTIAL.	127
C	VOLUME-TO-SURFACE TRANSFORMATION FOR SHEAR BANDS.	135
D	WORK-HARDENING MODEL.	145
E	AN ANALYTICAL TRANSFORMATION OF SURFACE COUNTS TO A VOLUME SIZE DISTRIBUTION	151
F	FEATURES OF COMPOSITE HEMP.	157
	DISTRIBUTION LIST.	201

1.	Recovered Segment of Steel Penetrator (a) and Axial Cross Section (b) of Proximal End	8
2.	Detailed View of Proximal Region Showing Shear Bands and Associated Cracks	11
3.	Two Views (a) and (b) of the Piece of the Recovered RHA Target Plate, and Three Slabs (c) of the Plate Made by Slices at Locations Shown in (b).	13
4.	Detailed View of Part of the Polished, but Unetched, Axial Plane, Showing the Important Failure Phenomena.	15
5.	Two Conceptual Scenarios for Relative Motion Across Sheared Planes of Weakness In a Target Impacted by a Long-Rod Penetrator at a High Angle of Obliquity.	17
6.	Cross Section Through a Target Impacted Perpendicularly by a Long-Rod Penetrator, Showing Backward Flow of Eroded Penetrator Material	18
7.	Transverse Plane 2, Showing Vertical Crack Development in Final Stages Before Complete Penetration.	19
8.	Detail of Transverse Plane 2, Showing Transformed Region Adjacent to Lowest Vertical Crack	21
9.	Section of Transverse Plane 2 Extending Along an Entire Length of a Shear Plane of Weakness	22
10.	RHA Target Plate Impacted Obliquely by a Uranium-3/4 wt% Titanium Alloy Penetrator	24
11.	Detailed Views Along the Flat Surface Oriented Perpendicularly to Penetrator Axis	26
12.	Adiabatic Shear Bands in Uranium-3/4 wt% Titanium Alloy Penetrator Fragment Embedded in Steel Target Plate.	27
13.	Recovered Uranium-3/4 wt% Titanium Penetrator After Perforation of Scaled Triple Armor.	29
14.	Detailed Views of the Fractured Impact End of the Recovered Penetrator Seen in Figure 13(a)	30

15.	Entrance (a) and Exit (b) Holes of Recovered RHA Target Plate, and Residual 4340 Steel Penetrator Fragment (c).	32
16.	Polished and Etched Cross Section (a) of the Proximal End of the Residual 4340 Steel Penetrator Fragment, with Detail (b) of Shear Banded Region.	33
17.	Polished and Etched Cross Section (a) Through RHA Target and Detailed Views (b) and (c) Showing Dense Shear Banding in Region Adjacent to Penetration Hole	34
18.	Blunt-Nosed 4340 Steel Projectile Embedded in RHA Target Plug (a) and Cross Section Through Impact Axis (b) Following Impact at 792 m/s	36
19.	Sections Through Recovered Downrange 4340 Steel Penetrator Fragments, Showing Extensive Internal and External Shear Banding	37
20.	Sections Through Recovered Downrange RHA Target Fragments, Showing Extensive Shear Deformation and Resultant Banding	38
21.	Cross Section of RHA Contained Fragmenting Cylinder Experiments.	42
22.	Geometry and Nomenclature for Shear Bands in Fragmenting Cylinder Experiments	43
23.	CFC Specimens Machined from RHA Slab, Showing Mode 1 Shear Bands in Planes Perpendicular to Rolling Plane	45
24.	Two Views of Half of the RHA Specimen Tube L-4 Recovered from CFC Experiments.	46
25.	Polished and Etched Section Through RHA Specimen Tube L-4, Showing Preponderance of Shear Banding Damage in Rolling Direction.	47
26.	Two Views of Half of the RHA Specimen Tube T-7 Recovered From CFC Experiment.	48
27.	Half of RHA Specimen (a) T-9, and (b) T-10 Recovered from CFC Experiments	49
28.	Final Wall Thickness as a Function of Axial Position for All of the RHA Specimen Tubes Recovered from CFC Experiments	51
29.	Photographs of Inside Surface of One Piece of Specimen T-7	52
30.	Sample Shear Band Size Distribution from 4340 Steel CFC Experiments	53

31.	Section Perpendicular to Axis of RHA Specimen T-7, Showing High Density of Shear Bands and Difficulty in Determining Band Depth.	55
32.	Fragment (a) and (b) Used in Shear Band Profile Study for 4340 Steel and Measured Profile (c) of Shear Band No. 6	56
33.	Schematic of BRL Ballistics Experiment.	58
34.	Vertical (V_1 and V_2) and Horizontal (H_1 and H_2) Radiographs Showing Penetrator Travel (from right to left) Before Impact. .	59
35.	Horizontal Radiographs Revealing Backscatter Fragmentation (H_3 at ≈ 30 μ s after impact) and Downrange Fragmentation (H_4 and H_5 at ≈ 145 and 285 μ s, respectively, after impact) . .	61
36.	Vertical Radiograph V_5 Revealing Downrange Fragmentation at ≈ 285 μ s After Impact	64
37.	Computer Plots of Fragments Observed on (a) Vertical Radiograph V_5 and (b) Horizontal Radiograph H_5 , as Received from BRL . . .	65
38.	Overall View (a) of Witness Plates with Detail (b) of Heavily Impacted Region with Fragment Holes (Circles) Numbered	66
39.	Measured Mass-Versus-Length Data for the Recovered Fragments and a Least-Squares Fifth Order Polynomial Fit to the Data. . .	67
40.	Preliminary Mass (a) and Velocity (b) Distributions Calculated from Quarter-Scale Test, as Received from BRL.	68
41.	Variation of the Distribution Parameter r_1 with Axial Position for Six Contained-Fragmenting-Cylinder Experiments in 4340 Steel at $R_c = 40$	74
42.	Variation of the Number of Shear Bands n_0 with Axial Position for Six Contained-Fragmenting-Cylinder Experiments in 4340 Steel at $R_c = 40$	75
43.	Comparison of the Variation of the Number of Shear Bands n_0 with Axial Position for Contained-Fragmenting-Cylinder Experiments in 4340 Steel	76
44.	Comparison of the Variation of the Size Parameter r_1 with Axial Position for Contained-Fragmenting-Cylinder Experiments in 4340 Steel.	77
45.	Shear (S) and Normal (σ) Stresses on a Block Containing a Shear Band	83
46.	Steps in Obtaining Cumulative Shear Band Distributions from Contained Fragmenting Cylinder Data	85

47.	Computed Plastic Shear Strain in the Mode 1 Direction at Three Axial Positions in 4340 Steel Cylinder 2	87
48.	Measured Number of Shear Bands Versus Computed Plastic Strain for Determining an Initial Estimate of the Nucleation Rate Parameter	88
49.	Measured Size Parameter for Shear Bands Versus Computed Plastic Strain for Determining an Initial Estimate of the Growth Rate Parameter	89
50.	Configuration and Detail of Results for Test Problem 2 Using Composite Hemp	99
51.	Configuration for Test Problem 3 and Computed Results at 37 μ s (300 cycles), Using Composite Hemp	100
52.	Configuration of Target and Penetrator at 17 μ s in TROTT Simulation with No Slide Line Including Contours of Equivalent Plastic Strain	104
53.	Configuration of Target and Penetrator at 17 μ s in TROTT Simulation with Unzipping Slide Line, Including Contours of Equivalent Plastic Strain	106
54.	Configuration of Target and Penetration at 23 μ s in TROTT Simulation with Unzipping Slide Line, Including Contours of Equivalent Plastic Strain	109
55.	Comparison of Measured Downrange Fragment Size Distributions from Experiment Shown in Figure S1 with Distributions Calculated from Computer Simulation	110
A1	Shear Band Size Distribution Represented by a Series of Points and Exponential Line Segments	A-2
A2	Nucleation and Growth Processes for a Shear Band Distribution Given by a Series of Points	A-4
B1	Shear Band Size Distributions Computed by SHEAR3 at 43% Plastic Strain Using Different Procedures for Representing the Band Size Distribution	B-5
B2	Results of Three Pure Shear Tests with SHEAR3 Using Different Procedures for Representing the Band Size Distribution	B-6
C1	Slice of Thickness dh Through a Circle of Radius R	C-3
D1	Definition of Quantities for Multisegmented Work-Hardening Curve.	D-2

E1	Volume Counts N, R Computed from the Area Count $n - n_0 e^{-r/r_1}$	E-3
F1	Configuration of Four Cells Surrounding Node j and Its Mass M	F-4
F2	Grid for Leapfrog Calculations Showing Increments in Space and Time	F-4
F3	Data Input and Geometry for a Steel Projectile Impacting a Rigid Circular Trough	F-14
F4	Data Input for a Running Detonation in a Contained Fragmenting Cylinder	F-17
F5	Data Input and Geometry for a One-Dimensional Impact of Two Steel Plates	F-19
F6	Data Input and Geometry for a Two-Dimensional Plane-Strain Impact of Two Steel Plates	F-20
F7	A Portion of a Grid Showing Independent Numbering of Nodes and Cells	F-22
F8	Cell Size Variation Patterns That May Be Used with a Finite-Element Numbering Technique	F-24
F9	Geometry of Human Head for Study of Impact and Concussion Showing Finite-Element Layout for Circular Object	F-25
F10	Possible Configuration of Cells and Nodes Along a Wandering Slide Line Representing a Growing Crack or Shear Band	F-27
F11	Minimum Wave Paths for a Quadrilateral Cell	F-34

Tables

1.	Parameters and Qualitative Results for RHA Contained Fragmenting Cylinder Experiments.	44
2.	Input Data for Shear Banding in 4340 Steel, R_c 40.	72
3.	Status of Composite HEMP	98
F1	Input Parameters and Definitions	F-8

CONTENTS

SUMMARY	iii
ACKNOWLEDGMENTS	xxiii
LIST OF ILLUSTRATIONS	xxvi
LIST OF TABLES	xxxii
I INTRODUCTION	1
A. Approach	2
B. Summary of First Year's Progress	3
C. Report Organization	5
II PHENOMENOLOGICAL STUDIES	7
A. Full-Scale Impact of Steel into RHA	7
1. Analysis of the Penetrator	7
2. Analysis of the Target	9
3. Summary	23
B. Quarter-Scale Impact of DU into RHA Triple Armor	23
C. Quarter-Scale Impact of Steel into RHA at Zero Obliquity	31
D. Phenomenological Conclusions and their Significance for the Computational Model	39
III MATERIALS CHARACTERIZATION EXPERIMENTS	41
IV DOWNRANGE FRAGMENTATION DATA BASE ACQUISITION	57
V SHEAR BAND MODEL DEVELOPMENT	71
A. Shear Band Parameters for 4340 Steel, $R_c 40$	71
B. Modification of the Shear Band Model SHEAR3.	78
1. Nucleation	78
2. Growth	79
3. Representation of the Distribution	79
4. Work Hardening	80
5. Damage Assignment	81
C. Procedure for Fitting Shear Band Model to Data	84
D. Plans for the Shear Band Model Refinement.	90
1. Anisotropy	90
2. Coalescence and Fragmentation	91
VI SYNTHESIS OF A COMPOSITE CODE FOR PENETRATOR SIMULATIONS	93
A. Requirements	93
B. Review of Available Codes	95
C. Synthesis and Testing of a Code	97

ACKNOWLEDGMENTS

The SRI portion of this BRL/AMMRC/SRI program has benefited greatly from the technical support received from Drs. Gerald Moss and John Mescall, the BRL and AMMRC project monitors, respectively, as well as from the interest and encouragement shown by Dr. Richard Vitali of BRL and Dr. Edward Wright of AMMRC. Acknowledgments are also owed to Ralph Papirno, Michael Staker, Greg Olson, and Morris Azrin of AMMRC and to Bryan Scott and Paul Netherwood of BRL for useful technical discussions.

We deeply appreciate the assistance and technical expertise provided by various BRL employees in the design, performance, and analysis of the quarter-scale ballistics experiment. In particular, we would like to acknowledge Jim Barb for reading the radiographs and performing the computational analysis, Tony Ricchiazzi and Graham Silsby for technical assistance throughout the experiment, and the quarter-scale facility crew led by Bernie McKay.

Excellent computational and experimental support at SRI was provided by Bonita Lew, James Kempf, Adolph Urweider, Dante Petro and Margaret Menting.

I INTRODUCTION

The traditional empirical approach for designing armor and weapons has often been effective in gaining successive incremental improvements over the established state of the art. However, as more complex weapon and armor systems are introduced, the usually very lengthy and expensive empirical approach becomes less and less tractable. In recent years numerical finite difference and finite element methods have been developed to the point where they are capable of handling complex shapes, deformations, and material behavior and therefore promise to be useful in armor and penetrator design.

The computational approach to ordnance design is an iterative procedure in which approximate computational simulations of an ordnance event are first performed using estimated values of material properties. Test firings are then carried out to evaluate the performance of the design, to provide data for comparison with calculated results, and to indicate the adequacy of the material property values. The test results then suggest changes in the initial ordnance design and guide the selection of material descriptions and dynamic material property tests for the next series of computational simulations. Test firings of a second generation design are then performed, and the results are compared with computational results, as before. The iterative process is repeated until the ordnance refinements produce the desired performance. This approach, currently being developed by the DoD, reduces the overall design effort because the interaction of experiments and calculations leads more rapidly to an acceptable design.

Material response that must be modeled in computational simulations of ordnance events include a thermodynamic equation of state, plastic flow, and material disintegration. Existing descriptions of thermodynamic equations of state are adequate for most calculations in ordnance design, and concepts of perfect plasticity are adequate for many ordnance

applications. The most serious limitation in efficient ordnance design is in the modeling of material disintegration. Disintegration can occur by several mechanisms, depending on the material and the conditions of stress, temperature, and strain rate. Detailed examinations of material recovered from many and varied ordnance events have identified three main material failure modes: brittle fracture, ductile fracture, and localized shear failure. Of these three microscopic failure modes, the last two are more common in metallic armor.

Although simple failure criteria may suffice to obtain reliable computational simulations of certain ordnance events, other situations require a detailed model and hence a detailed physical understanding of nucleation, growth, and coalescence of cracks, voids, and shear bands. Whereas a significant amount of relevant research has already been done in this area, much more is required to allow adequate computations to be performed.

A. Approach

The objective of this three-year program is to develop for the U.S. Army Materials and Mechanics Research Center (AMMRC) and Ballistic Research Laboratory (BRL) a computational material-disintegration model for simulating the long-rod penetration of spaced armor. This model will provide the capability for predicting the behind-the-armor fragment environment for given penetrator attacks and will aid in armor and penetrator design.

Our approach to meet this objective has the following six main parts:

- (1) Materials are selected for study, and penetration phenomenology experiments are performed in which rods are fired at various velocities and angles of incidence against target plates. The rod and target specimens are recovered, sectioned, and metallographically examined to reveal the key microstructural damage mechanisms that govern failure and disintegration of both penetrator and target. The baseline materials chosen for study are depleted uranium (DU)-3/4 wt% titanium alloy rods fired against rolled homogeneous armor (RHA) targets. Additional materials that may be studied in the future are tungsten alloy rods and electroslog-remelt (ESR) steel armor.

- (2) Laboratory material property characterization experiments are performed, where necessary, to measure the properties that govern the damage mechanisms. Experiments are chosen to exercise a particular failure mechanism in a geometry that is relatively simple to model. The contained fragmenting cylinder (CFC) test, for example, is used to study shear band nucleation and growth.
- (3) Previously developed computational models of the various damage processes are modified and adapted to describe the observed failure mechanisms. The models are all based on the nucleation and growth (NAG) approach, which attempts to simulate qualitatively and quantitatively the actual micro-mechanical failure processes involved.
- (4) These models are calibrated against the experimental data by computationally simulating the material characterization experiments. Parameters are obtained that quantitatively describe each material's behavior, for use in subsequent armor penetration computations.
- (5) A computer code is assembled, containing the features that have been seen to be necessary to simulate the long-rod penetration of armor. Although this code includes many of the same features found in the various HEMP codes, it must also contain some new logic to handle the complex phenomenology of armor penetration, and it must incorporate the material models developed above.
- (6) Finally, the ability of the models to correctly predict the main features of long-rod penetration of spaced armor is assessed, and if the results are promising, the models are used to predict behind-the-armor fragment environments and to aid in armor and penetrator design.

It should be emphasized that these six parts to our approach are not performed sequentially, but are developed simultaneously, with a large amount of interaction necessary between them.

B. Summary of First Year's Progress

The experimental progress made during the first year of the program, as detailed in the first annual report,¹ is shown graphically in the Program Technical Milestones chart. RHA material was obtained from BRL early in the program, and a metallurgical characterization was performed. Quasi-static tensile tests were performed with samples cut from three orthogonal directions, and stress-strain curves were obtained that showed the RHA to be very similar to that described by Benck² and Hauver³ and to exhibit a large degree of anisotropy in its ductility.

Phenomenology experiments were performed, involving normal-incident rod impacts onto 1/4-inch-thick RHA plates at velocities near the ballistic limit (655 to 792 m/s). At these moderate velocities, the target failed by catastrophic shear band-induced plugging following substantial homogeneous deformation, but without any significant internal damage or fragmentation of the plug or the adjacent target regions (see Figures S4-and S6 of the Summary).

A series of CFC experiments was begun using RHA specimens of different orientations. The series was completed during the second year, and the results are reported in Section III.

Finally, an experimental technique was developed to enable us to determine the constitutive relations, or flow curve, of a material in compression at the same high strain rates existing in a long-rod armor penetration. This technique, called the symmetric rod impact test (or symmetric Taylor test), involves photographing (at $\approx 10^6$ frames/s) the silhouettes of the cylindrical specimens during the actual deformation phase following a high-speed impact. The event is then simulated by a two-dimensional computer code (such as HEMP), varying the flow parameters until the computed and experimental deformations agree. The feasibility of this approach was tested successfully using aluminum specimens.¹

Progress made in the computational part of the program during the first year included development of fracture models, acquisition of a HEMP program, and derivation of a criterion for shear band nucleation.

A greatly expanded version of the shear band model was developed and preliminary efforts were made to correlate the model with the 4340 data from contained fragmenting cylinders. Major changes were in the nucleation and growth processes, and in the algorithm for stress relaxation caused by the developing damage.

A ductile fracture model for intermediate strain rates (durations of 10 to 100 μ sec) was derived by combining features from fracture models applicable to either shock or quasi-static loading. The model was not implemented in a computer subroutine.

Several computer simulations were made with the TROTT code of blunt-nosed penetrators impacting steel targets. These simulations showed many general features of penetration calculations, including the needs for rezoning and slide-line capabilities. In attempt to satisfy those needs, we acquired a version of the two-dimensional wave propagation code HEMP and made arrangements to obtain a more recent version of the code with intersecting (or double) slide lines.

A single criterion for the initiation of shear bands was derived from stability considerations: when the rate of stress reduction caused by thermal softening equals or exceeds the rate of work-hardening, the material becomes constitutively unstable. This criterion was able to correctly rank materials according to their propensity to form shear bands.

C. Report Organization

This report describes our progress during the second year of the program and our plans for the third year. Section II describes the phenomenological experiments, and Section III describes the materials characterization experiments (parts 1 and 2 of our approach as outlined above). Section IV describes an additional experiment performed to provide a downrange fragmentation data base for early comparison with our developing computer predictions capability. This allows us to determine at an early state if our phenomenologically based computational models can indeed predict fragmentation and velocity distributions.

Development of the shear band model (part 3 of the program) and calibration of this model against the experimental data (part 4) are described in Section V. Synthesis of a composite code for penetrator simulations (part 5) is discussed in Section VI, and preliminary simulations of projectile penetrations (part 6) is described in Section VII. Section VIII gives our plans for completing this work during the third year of the program.

II PHENOMENOLOGICAL STUDIES

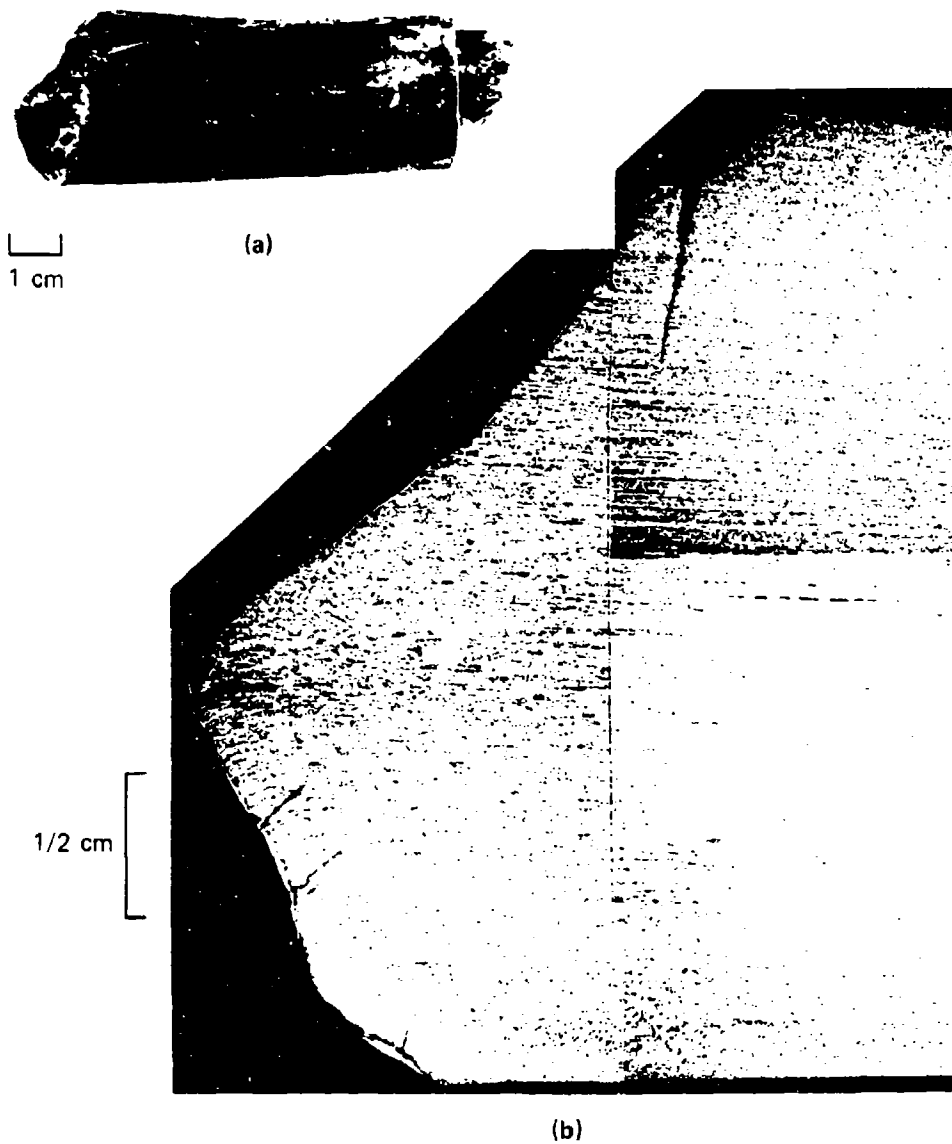
During this past year, we studied the phenomenology of armor penetration by examining recovered specimens from three different types of ballistics experiments: (1) a full-scale, high-velocity, high-obliquity impact of hardened steel into RHA, stopping just short of full penetration, (2) a series of quarter-scale impacts of DU into RHA triple armor at various velocities, and (3) a quarter-scale, zero-obliquity impact of 4340 steel into RHA, well above the ballistic limit. In all cases studied, shear banding was seen to be the dominant failure mechanism of both the target and penetrator.

A. Full-Scale Impact of Steel into RHA at High Obliquity

We performed a metallographic examination of sections of the target and penetrator recovered from the ballistics test witnessed by attendees of the February 1980 project meeting at BRL. In this full-scale test, a 1-inch-diameter long-rod steel penetrator, impacting at a high velocity (≈ 1500 m/s) and a high angle of obliquity ($\approx 70^\circ$), stopped just short of penetrating a 4-inch-thick slab of RHA. This incomplete penetration allowed us to observe some important phenomenology that would have been difficult or impossible to see if complete penetration had occurred. The sections we examined included a distal 2-inch section of the penetrator (the only large penetrator piece recovered) and a slab of the target that included half of the damaged region. The following is a detailed report on the results of this examination and the phenomena we observed.

1. Analysis of the Penetrator

The recovered penetrator piece is shown in Figure 1 along with a polished and etched cross section through the center of the proximal end. A hardness traverse across the specimen yielded values of $R_C 51 \pm 1$ for the undamaged end. Our past experience with steels of this hardness led us to expect shear banding at relatively low shear strains ($< 20\%$),



MP-7893-86

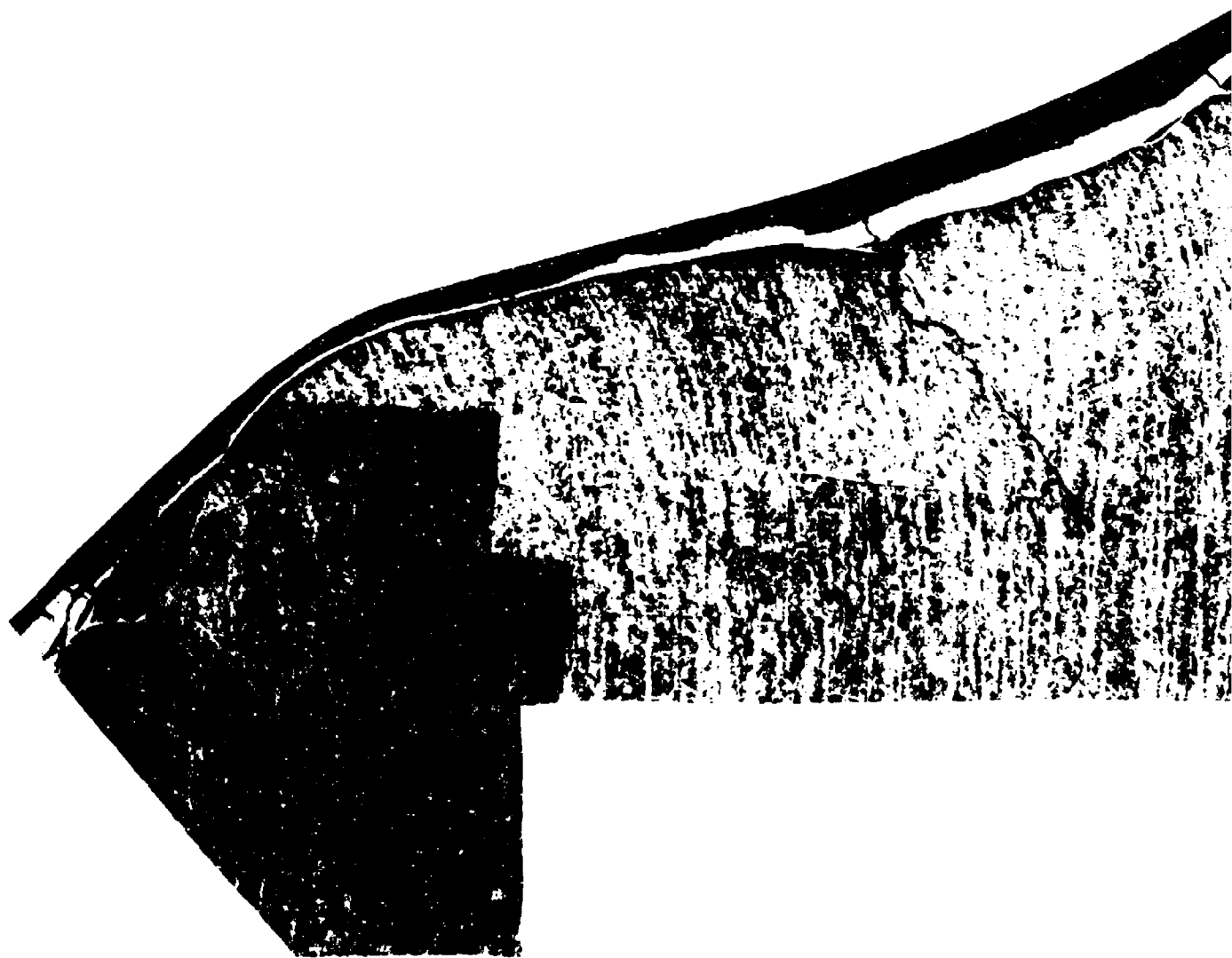
FIGURE 1 RECOVERED SEGMENT OF STEEL PENETRATOR (a) AND AXIAL CROSS SECTION (b) OF PROXIMAL END

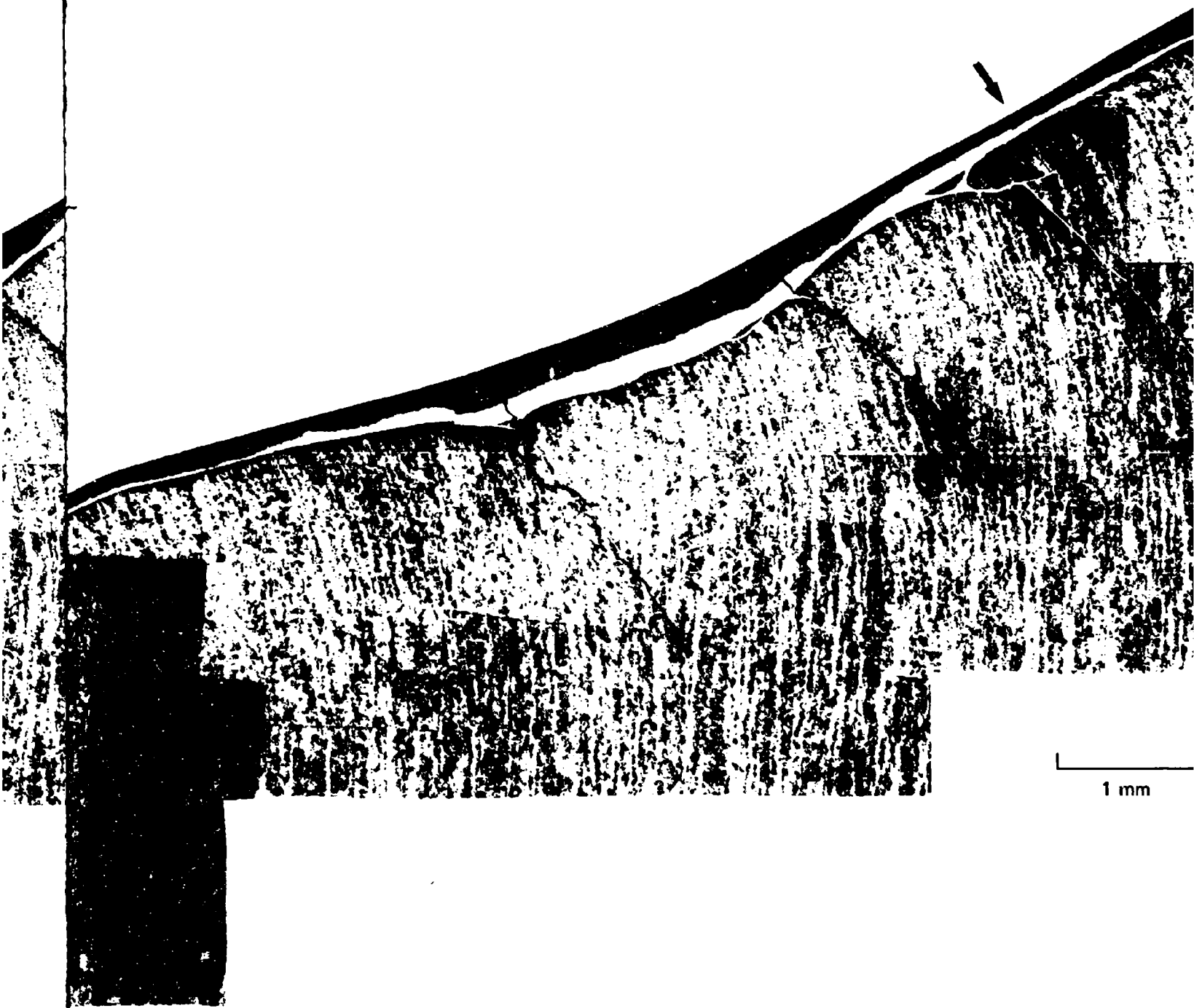
and this is precisely what we see when we look at the proximal region under higher magnification (see Figure 2). A consistent pattern of shear bands extending into the penetrator at angles of $45^\circ \pm 10^\circ$ from the axis is seen, with the bands cutting through material having undergone relatively small shear strain (as shown by distortion of the extrusion-induced texture). The maximum shear displacement along a band appears to be about 50 μm . Cracking has occurred along or very near a few of the bands, and it is by separation along these cracks that the penetrator retains its pointed nose while eroding during a penetration. Arrows in Figure 2 point to material surrounded by shear bands; we believe this material would have been eroded next if the penetration process had continued.

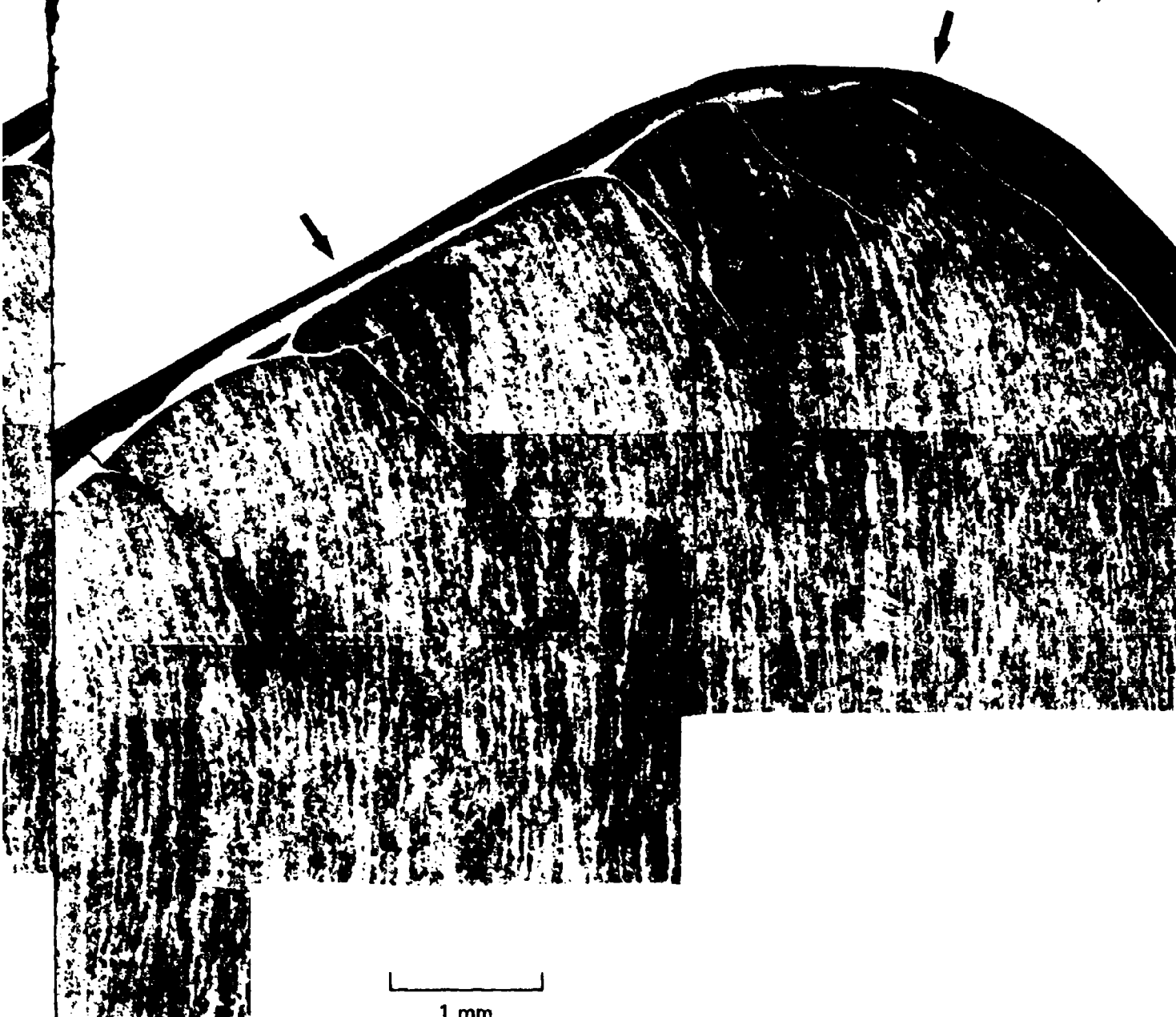
The photographed cross section (Figure 1b) shows two cracks that are apparently not connected with a shear band. The largest of these, a crack perpendicular to the axis, transverses material that has undergone negligible shear deformation. The role of these tensile cracks in the penetrator erosion is not clearly understood. They may not even have occurred during the erosion regime. In any case, the proximal surface of the penetrator consists of material transformed during shear banding and/or subsequent sliding of the penetrator across the target; the surface contains no tensile cracks. Therefore, although we cannot entirely eliminate tensile cracking in the penetrator from the scenario, we believe that shear banding and subsequent separation along the banded surface are the important mechanisms in penetrator erosion.

2. Analysis of the Target

The piece of the recovered 4-inch-thick RHA target plate sent to us by BRL is seen in Figure 3(a) and (b). The penetrator entered at the upper left at an angle of approximately 70° , deforming and removing significant amounts of the RHA as it travelled into the target, until it finally stopped fairly close to full perforation with its axis rotated to a more perpendicular angle with respect to the target face. Since the piece we received was cut on a plane going through the axis of impact (referred to here as the axial plane), it contained



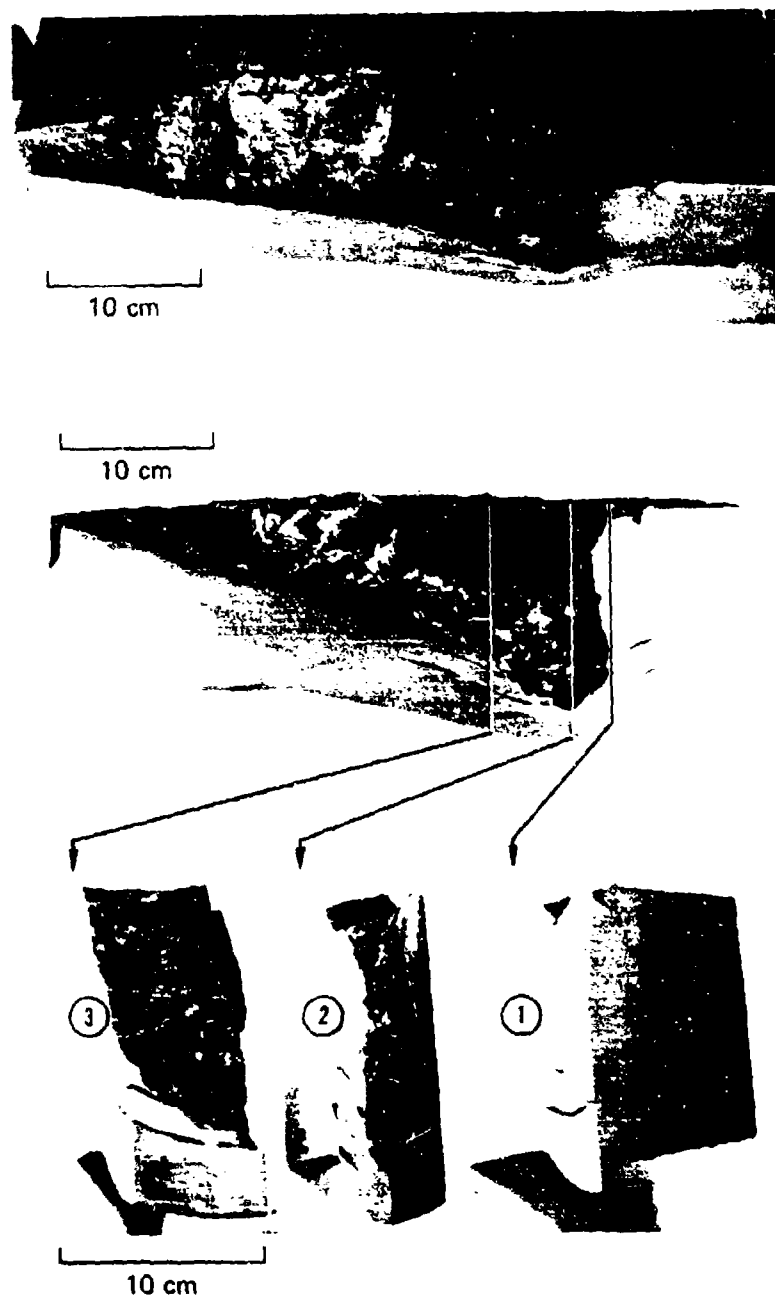




MB-7893-87

**FIGURE 2 DETAILED VIEW OF PROXIMAL
REGION SHOWING SHEAR BANDS
AND ASSOCIATED CRACKS**

Arrows point to material completely
surrounded by shear bands.



MP-7893-88

FIGURE 3 TWO VIEWS (a) AND (b) OF THE PIECE OF THE RECOVERED RHA TARGET PLATE, AND THREE SLABS (c) OF THE PLATE MADE BY SLICES AT LOCATIONS SHOWN IN (b)

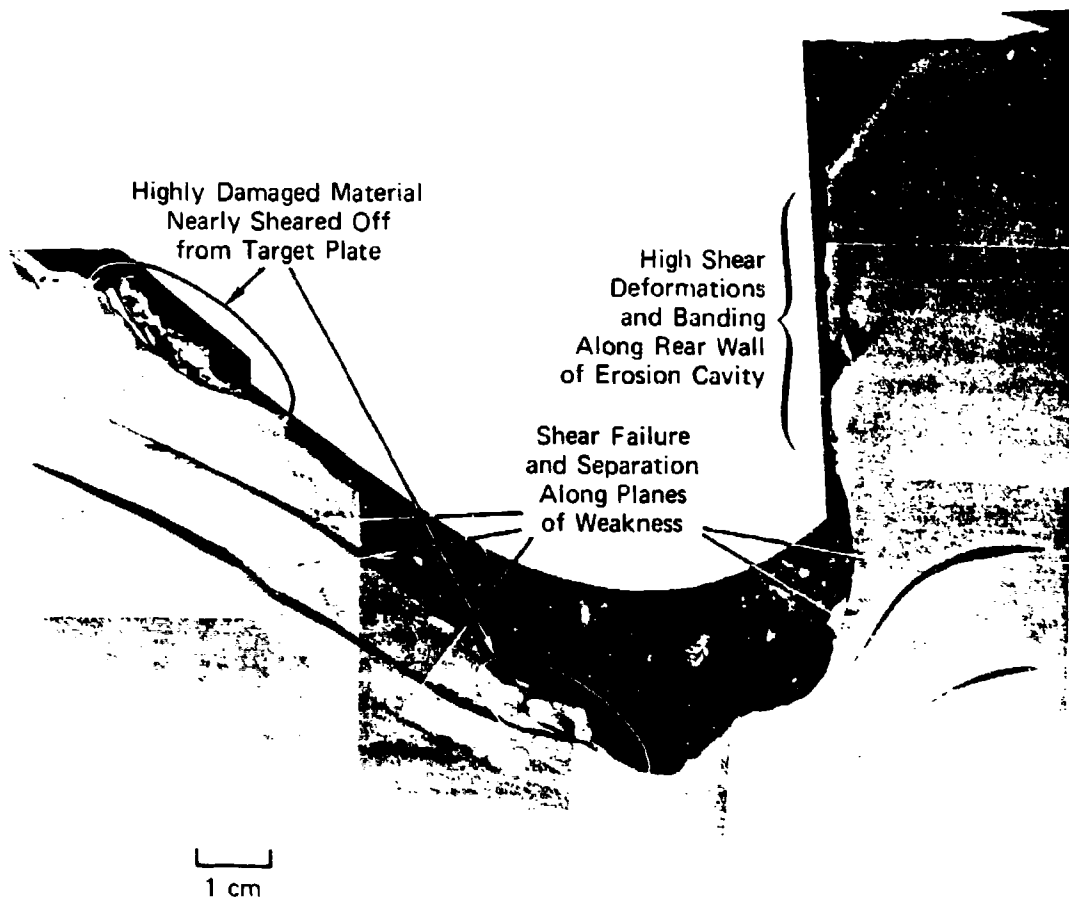
roughly half of the damaged target. Assuming that the remaining half of the damaged target is similar, roughly 5 kg of RHA was eroded from the impact side by the 21 kg penetrator, leaving an irregular scalloped and scoured surface.

Three slices perpendicular to the axial plane were made in the RHA target piece so as to view damage farther away from the impact axis. Three of the slabs created are shown in Figure 3(c). The planes made by the slices are referred to here as the transverse planes 1, 2, and 3.

A detailed view of part of the axial plane is shown in Figure 4, which reveals most of the important aspects of the damage phenomenology. Because of the extreme difficulty in polishing, etching, and metallographing a 32-kg piece of steel, the surface shown in Figure 4 is polished but unetched. Hence shear bands do not show up white in this figure. However, subsequent photographs of etched surfaces of the easier-to-handle sliced slabs (shown in Figure 3c) confirmed the presence of the shear banding failures reported below.

The two principal features of target damage, as seen in Figure 4, are shear failure and separation along planes of weakness and the shearing off and removal of the more damaged material. It had been determined (see Section III) that a 4-inch-thick RHA plate has a significant anisotropy in its resistance to shear banding. Planes parallel to the rolling plane undergo shear banding at strains well below those required in any other planes. Thus we see, inside the target, material that has sheared and separated along the planes of weakness. These shear failures often extend 10 cm or more, and by studying Figure 3(c), one can see the three-dimensional nature of the distorted sheared planes.

The damage process is somewhat analogous to a deck of cards that is held firmly at the left end and bent downward at the right. Individual cards will slide with respect to their nearest neighbors and severe bending may cause a gap to grow between the cards. The upper cards will slide to the left with respect to the lower cards, just as the upper layers of the RHA slide toward the left with respect



MA-7893-89

FIGURE 4 DETAILED VIEW OF PART OF THE POLISHED, BUT UNETCHED, AXIAL PLANE, SHOWING THE IMPORTANT FAILURE PHENOMENA

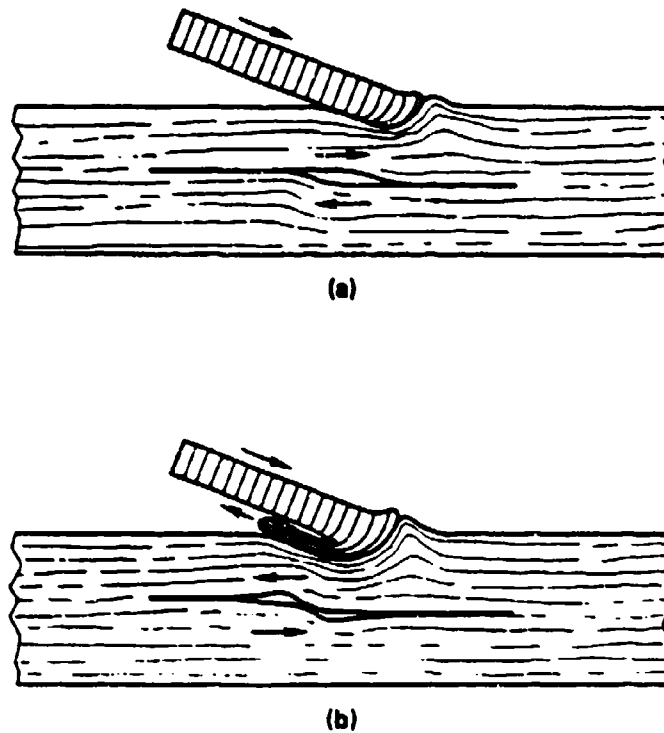
to the lower layers (as is shown by the arrow next to the longest sheared planes in Figure 4).

This relative motion is opposite to what one might first expect. A long rod projectile at a high angle of obliquity impacting a target with planes of weakness parallel to the target face might be expected to cause the motion shown schematically in Figure 5(a), with the projectile dragging the upper layer of the target to the right. Actually, the upper layers are pushed in the direction opposite to that of the projectile. We believe this to be caused (as shown in Figure 5(b) by eroded material from the front of the projectile traveling backward along the body of the projectile, in a manner similar to that shown for a right-angle impact in Figure 6. The heavily distorted material from the front of penetrator is forced to flow backward along the still advancing penetrator body, damaging and then shearing off adjacent target material. The areas circled in Figure 4 are highly damaged target regions almost sheared off in the direction opposite to the motion of the projectile.

As the projectile penetrates farther into the target and as the remaining, unpenetrated layer of the target becomes thinner, there is less resistance to deformation in the direction perpendicular to the target face than in the original direction of the impact. Hence, the uneroded portion of the projectile turns in the direction of least resistance, and further penetration begins to look like a more normal impact.

The phenomenology that occurs in the final stages leading to full penetration can be best seen by examining transverse plane 2, which is shown in detail in Figure 7.* This transverse plane, which was cut perpendicular to the point of deepest penetration by the projectile into the target, exhibits several sheared and separated planes of weakness extending as much as 5 cm away from the axis of penetration. Vertical cracks, perpendicular to the planes of weakness, have opened very near the farthest extremity of these failed planes. The lowermost of these cracks has reached the back surface and forms the lateral boundary of a

*The image is reversed with respect to that in Figure 3(c).



MA-7893-90

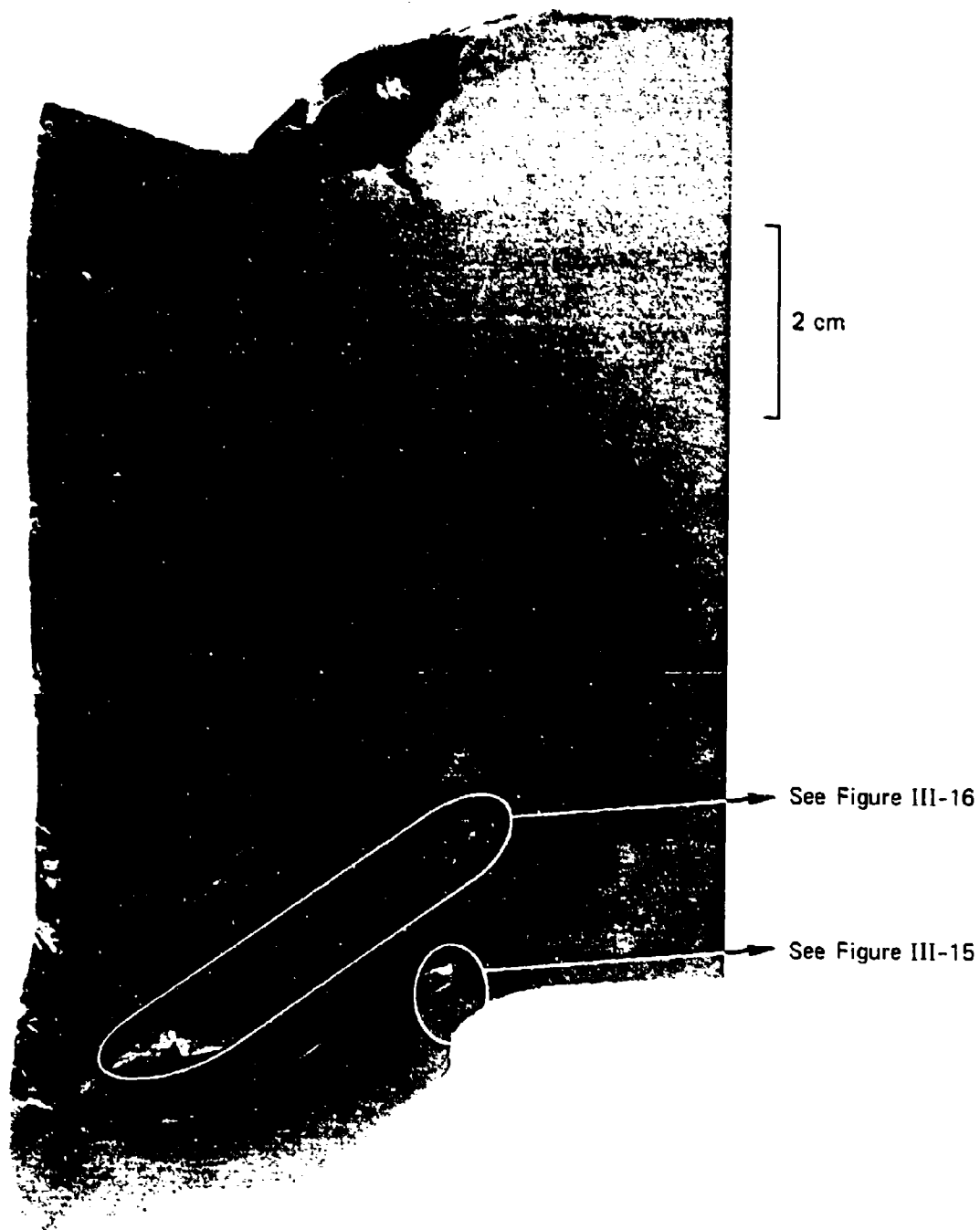
**FIGURE 5 TWO CONCEPTUAL SCENARIOS FOR RELATIVE
MOTION ACROSS SHEARED PLANES OF WEAKNESS
IN A TARGET IMPACTED BY A LONG-ROD
PENETRATOR AT A HIGH ANGLE OF OBLIQUITY**



MP-7893-91

FIGURE 6 CROSS SECTION THROUGH A TARGET IMPACTED PERPENDICULARLY BY A LONG-ROD PENETRATOR, SHOWING BACKWARD FLOW OF ERODED PENETRATOR MATERIAL (Photograph courtesy of BRL)

Note: Horizontal hole near bottom was predrilled for instrumentation access.



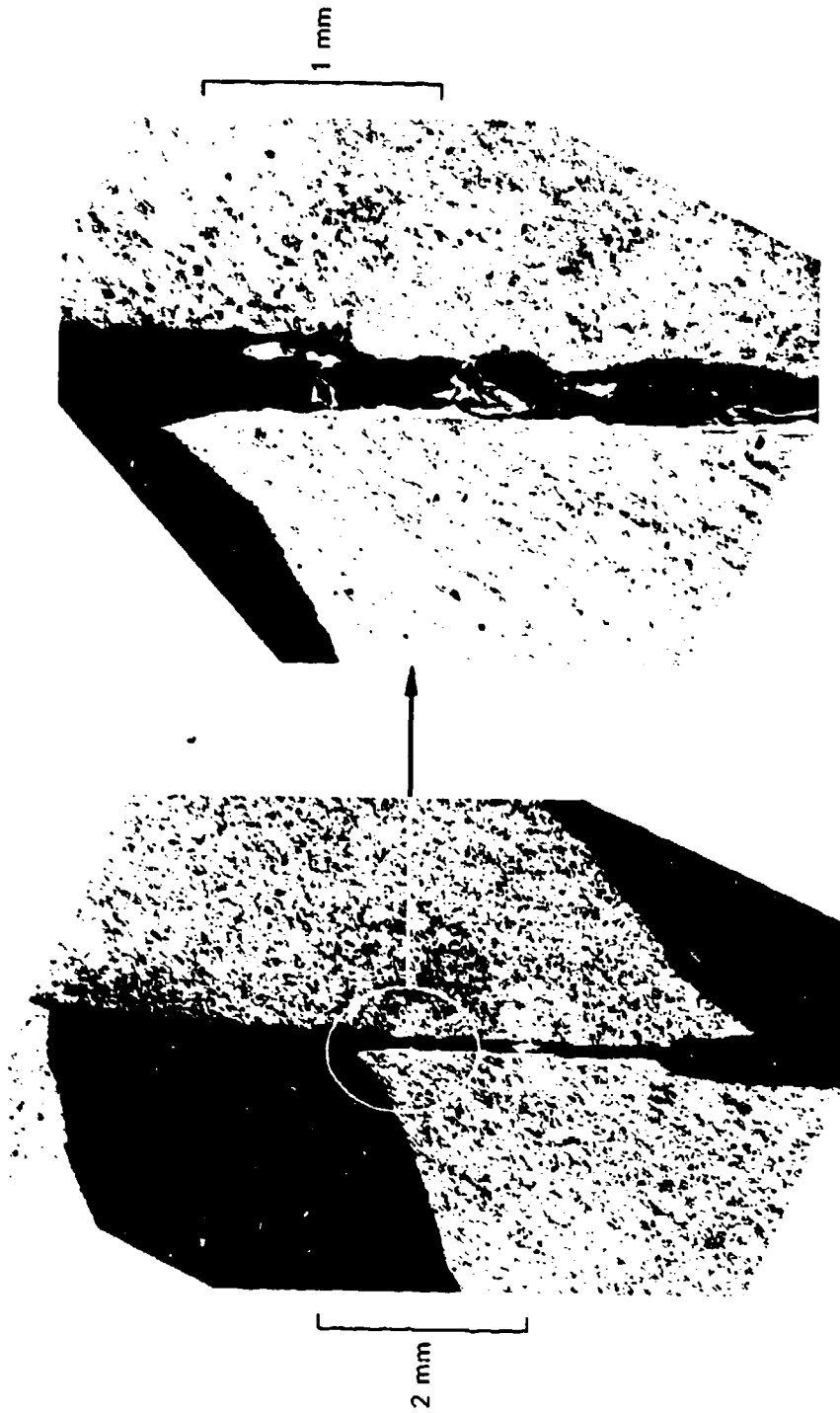
MP-7893-92A

FIGURE 7 TRANSVERSE PLANE 2, SHOWING VERTICAL CRACK DEVELOPMENT
IN FINAL STAGES PRIOR TO COMPLETE PENETRATION

large piece that was very close to being ejected from the back of the target. This would have been the large piece, often called the "plug," that has been seen for oblique impacts just above the ballistic limit (as reported by Ricchiazzi of BRL at the February 1980 project meeting). Another of these vertical cracks, which already extends halfway across the material between two failed planes of weakness, would have formed the next section of target material to be ejected. Thus it appears that the final stages of penetration, at least in cases close to the ballistic limit (but possibly also in cases well above the ballistic limit), are controlled by the growth of vertical cracks across already failed planes of weakness and their intersection with the back surface of the target.

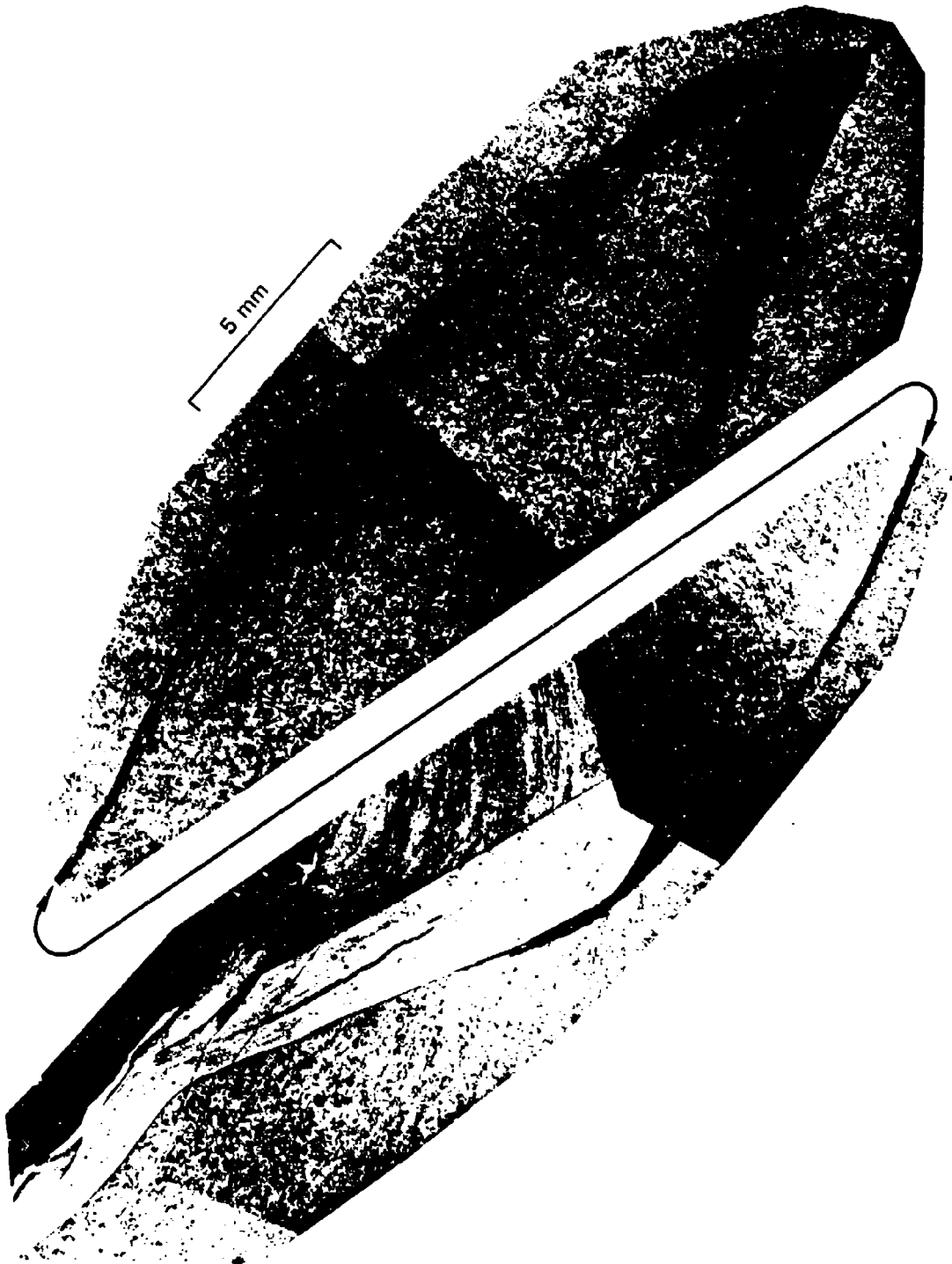
Figures 8 and 9 contain higher magnification photographs of the two vertical cracks discussed above. The relative smoothness of the crack edge and the presence of a white transformed region in Figure 8 seem to indicate that this lowermost vertical crack is a shear band. However, the roughness of the crack edge and the absence of any transformed region in Figure 9 indicate the possibility of tensile fracture in the second vertical crack.

Both of these mechanisms are distinct possibilities: shear banding has clearly occurred in the plane of weakness, and continued shear distortions will eventually trigger banding across the planes of weakness. Tensile failure is also a possibility. After the material is separated into parallel slabs by shear failure along planes of weakness, further bending of the slabs may induce local tensile stresses parallel to the slab surface at the upper, or convex, edge of the slab (just as local compressive stresses will be induced at the lower, or concave, edge of the slab). If the region is far enough away from the axis of penetration, the local tensile stress may exceed the more global compressive stresses by enough to cause a Mode I tensile crack to open and propagate downward. Which mechanism occurs at any particular vertical crack site depends on which failure criteria--shear banding or tensile--are satisfied first.



MP-7893-93

FIGURE 8 DETAIL OF TRANSVERSE PLANE 2. SHOWING TRANSFORMED REGION ADJACENT TO LOWEST VERTICAL CRACK



MP-7893-94

FIGURE 9 SECTION OF TRANSVERSE PLANE 2 EXTENDING ALONG AN ENTIRE LENGTH OF A SHEAR PLANE OF WEAKNESS

3. Summary

The information obtained about the damage phenomenology for oblique penetration near the ballistic limit of a hardened steel projectile into an RHA target can be summarized as follows. The projectile bores into the target, deforming the RHA downward, activating shear failure along planes of weakness in the target and in the front of the projectile. Further penetration causes shear failure across the planes of weakness, and the backflowing material from the front of the projectile shears out the damaged target material.

Further penetration causes the projectile to turn more normal to the target face, which increases the distortion of the remaining uneroded layers of the target. Finally, vertical tensile or shear cracks at positions away from the penetration axis propagate across the planes of weakness and intersect the back surface, removing a large "plug" of material and completing the penetration process.

B. Quarter-Scale Impact of DU into RHA Triple Armor

In October 1979, we received from BRL a shipment of recovered fragments from quarter-scale experiments involving the impact of DU-3/4 wt% Ti penetrators into RHA triple armor. Although complete information was not available on the test conditions of the experiments, we examined two of the penetrators metallographically to study the failure phenomenology.

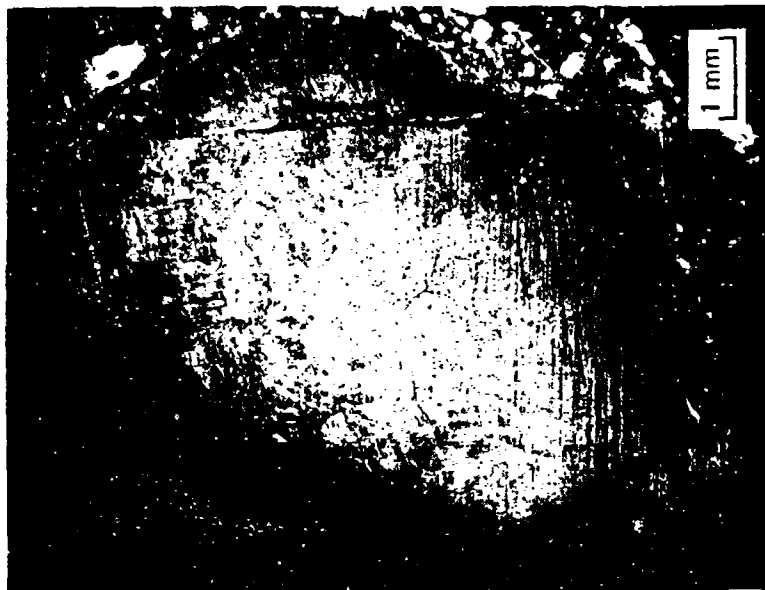
The first DU penetrator fragment we examined was embedded in what we believe is the last of the three RHA target plates, as seen in Figure 10(a). An electrolytic polishing technique was used that did not affect the RHA plate. The crater shape suggests a highly oblique impact.

Figure 10(b) is a more highly magnified view of the embedded penetrator fragment. The wavy lines running through the fragment are prior γ grain boundaries resulting from the 850°C solutionizing treatment. At this temperature, the equilibrium phase for a U-3/4 wt% Ti alloy is a solid solution of Ti in γ (body centered cubic) uranium.⁴



(a) Overall View of Penetrator Fragment Embedded in Target

The target plate was cut in half, ground on 600 grit paper, and electropolished in a solution of 118 g CrO_3 dissolved in 100 cc distilled water and four parts glacial acetic acid. The voltage was 20 VDC, 0.8 A, held for 5-6 minutes.



(b) More Detailed View of Penetrator Fragment

The wavy lines in the fragment are prior γ grain boundaries. Note also the flat surface oriented perpendicular to the penetrator axis.

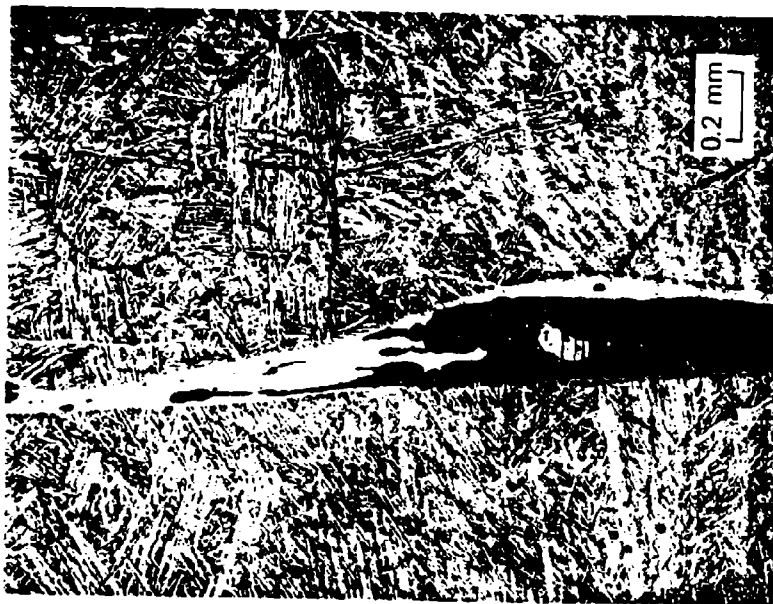
MP-7893-67

FIGURE 10 RHA TARGET PLATE IMPACTED OBLIQUELY BY A URANIUM 3/4 wt% TITANIUM ALLOY PENETRATOR

Grain growth in the solid solution at this temperature is fairly rapid, permitting the formation of γ grains. Quenching from the solutionizing treatment transforms the γ (b.c.c.) uranium to α (orthorhombic) uranium by a diffusionless (martensitic) transformation.⁵ The location of the prior γ grain boundaries can still be detected, however, because the resultant lens-shaped α grains initiate and propagate from the γ grain boundaries.

The flat surface oriented perpendicular to the penetrator axis is most probably the tail end of the penetrator. The fragment to the right of this surface was probably one of the many eroded from the penetrator during the perforation of the first two plates. This particular piece, traveling in the cloud of particles trailing the main body of the penetrator, struck and welded itself to the tail end of the penetrator already embedded in the third target plate. The structure of the interface between the residual penetrator and this fragment is detailed in Figure 11. Figure 11(a) shows that the area of contact between the two fragments consists of a wide, featureless zone, which suggests that excessive localized heating occurred when the fragment impacted the tail end of the penetrator, possibly enough heat to induce melting to resolidification. Figure 11(b) shows how the α -uranium grains adjacent to the featureless zones are severely sheared, suggesting the the localized heating was caused by frictional drag between the fragment and the tail end of the penetrator.

Examination of the residual penetrator itself revealed little information on the mechanisms by which it broke up. However, examination of the fragment attached to the tail end of the penetrator revealed a number of what appear to be adiabatic shear bands. These bands are detailed in Figure 12. The sheared nature of the α -uranium grains in the vicinity of the bands. Figure 12(b) suggests that a large amount of localized plastic deformation has occurred. The featureless interior of the bands suggests that rapid heating and cooling occurred during this shearing process. As Figure 12(a) indicates, the bands extend for large distances through the fragment. Since this fragment was separated from the main penetrator early in the penetration process,



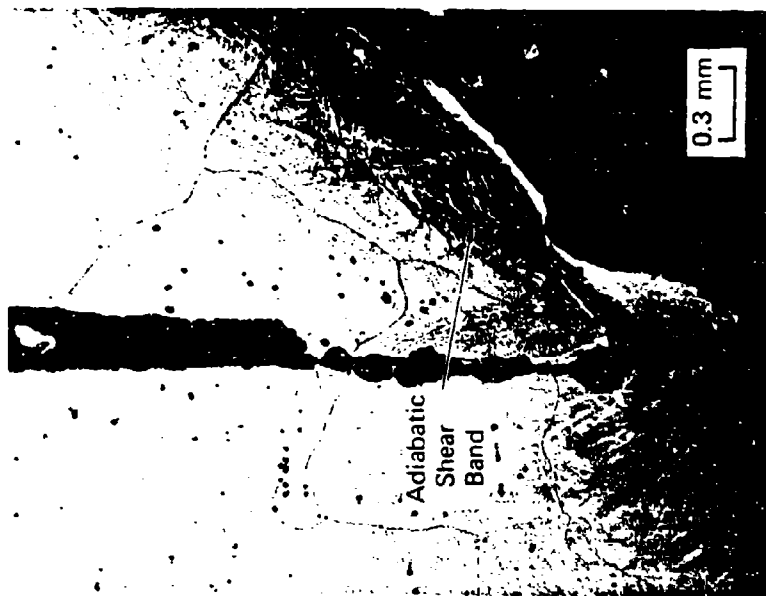
(a) Micrograph illustrating that portions of the flat surface are composed of wide, featureless zones, indicative of friction-induced melting and resolidification.



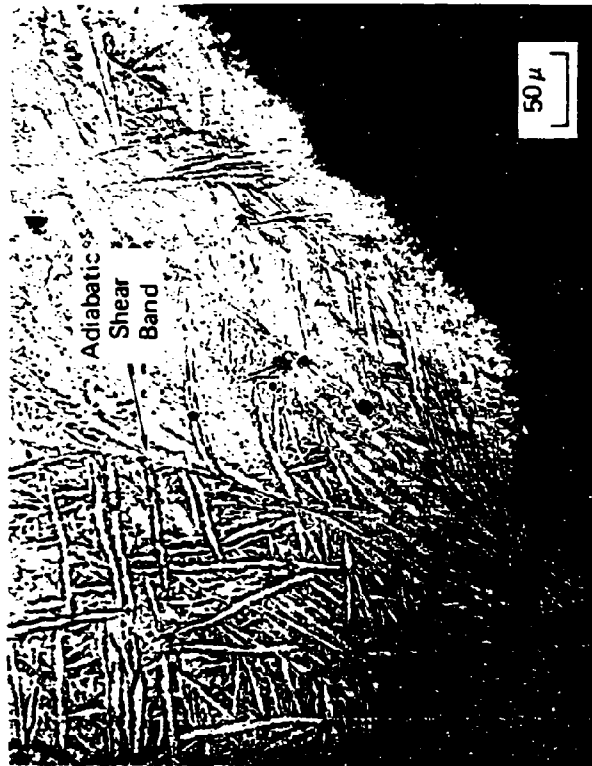
(b) More detailed view showing that the α -uranium platelets in the matrix have been severely distorted near the edges of the zones, suggestive of a large amount of friction-induced shear.

MP-7893-68

FIGURE 11 DETAILED VIEWS ALONG THE FLAT SURFACE ORIENTED PERPENDICULARLY TO PENETRATOR AXIS
[As seen in Figure 10(b)]



(a) Overall view of the shear bands in the penetrator fragment. The bands are not as easily identified as they are in steel.



(b) More detailed view of the bands showing that they can be identified by the localized shearing of the α -uranium platelets.

MP-7893-69

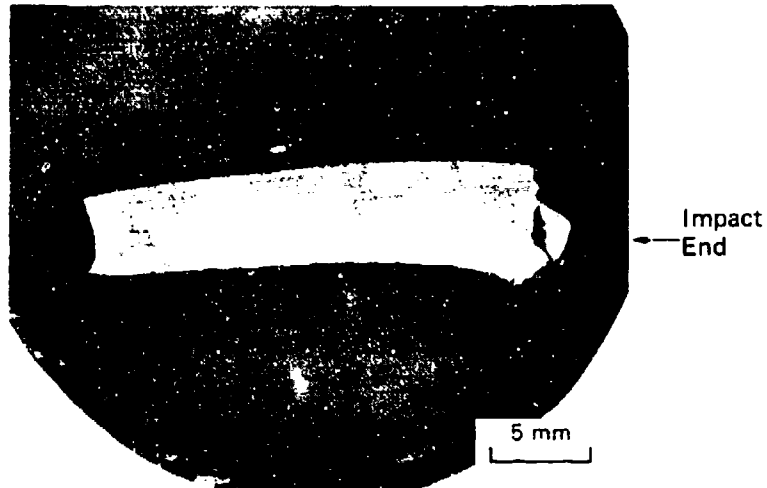
FIGURE 12 ADIABATIC SHEAR BANDS IN URANIUM-3/4 wt% TITANIUM ALLOY PENETRATOR FRAGMENT EMBEDDED IN STEEL TARGET PLATE

it appears that, at least in the early stages of penetration, the penetrator was fractured by the nucleation, growth, and coalescence of adiabatic shear bands. The failure mechanisms that were operative later could not be surmised from the residual penetrator fragment.

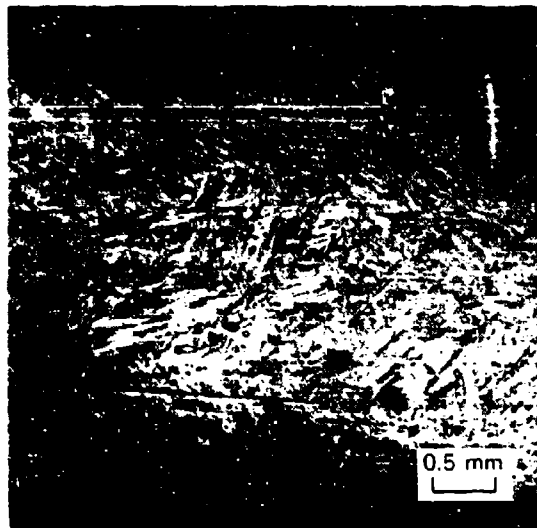
The second DU fragment examined was recovered after complete perforation through the triple armor. Its impact velocity was 985 m/s, its residual velocity was 562 m/s, and its residual mass was 12.8 g. The original angle of obliquity is unknown. A cross-sectional view of the penetrator is shown in Figure 13(a). Detailed examination of the penetrator shaft away from the impact end (Figure 13b) revealed no evidence of any activated microfailure mechanisms. The visible porosity was caused by the pullout of uranium oxide inclusions during grinding and electropolishing, and not by plastic flow. The globular inclusions are trapped inside the ingot during casting and are then strung out in lines parallel to the rod axis during extrusion.

The situation is different near the impact end of this penetrator. It is evident from Figure 13(a) that extensive localized failure occurred during impact. Figure 14 shows that this failure was caused by adiabatic shear band formation. The lens-shaped α -uranium grains are noticeably sheared in the vicinity of these bands (Figure 14b). From Figure 14(a), it is also apparent that separation along the shear band is not simply due to brittle crack propagation. The surfaces of the separated shear band are quite irregular, suggesting that void coalescence contributed to the separation process. Irrespective of the actual separation mechanism, it is clear that adiabatic shear band nucleation, growth, and coalescence played a dominant role in the breakup of this penetrator during the perforation of spaced triple armor.

It is evident from the observations made on the two uranium-3/4 wt% titanium penetrator fragments that adiabatic shear banding does occur in this alloy and, furthermore, is the dominant failure mechanism for erosion of the penetrator nose during a high velocity impact.



(a) Overall view of the recovered penetrator showing how the impact end was fractured and the shaft bent during perforation.



(b) View of the microstructure of the penetrator shaft back from the impact end. The holes most likely resulted from oxide inclusions strung out along the extrusion axis and then pulled out during grinding and electropolishing.

MP-7893-70

FIGURE 13 RECOVERED URANIUM-3/4 wt% TITANIUM PENETRATOR
AFTER PERFORATION OF SCALED TRIPLE ARMOR



(a) Overall view of one of the shear bands found near the fractured end. Separation has occurred along most of the shear band length.



(b) Higher magnification view of the tip of the shear band in (a). Shearing of the α -uranium platelets near the unseparated part of the shear band is quite visible. Note the offset prior γ grain boundary in the upper left-hand corner of the micrograph.

MP-7893-71

FIGURE 14 DETAILED VIEWS OF THE FRACTURED IMPACT END OF THE RECOVERED PENETRATOR SEEN IN FIGURE 13(a)

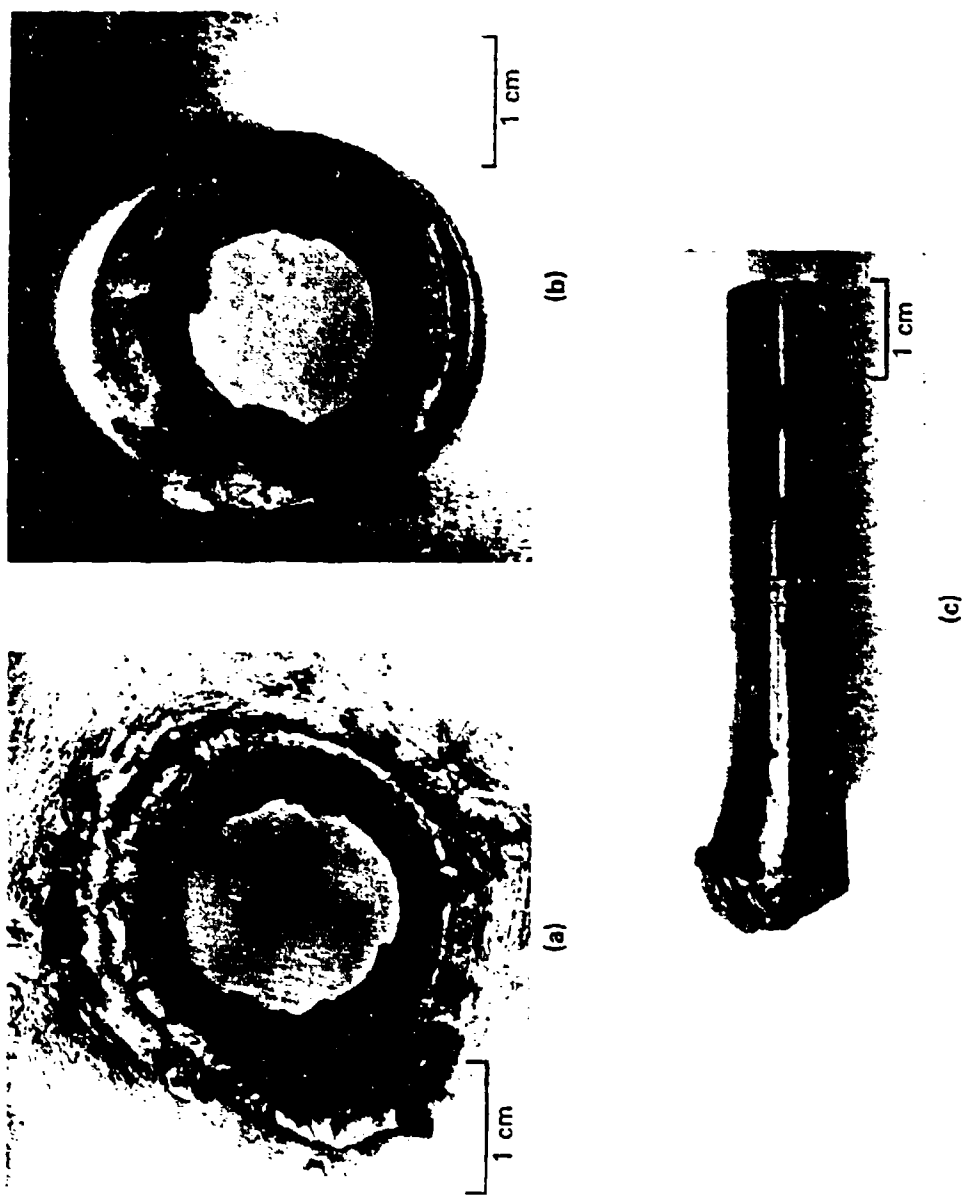
C. Quarter-Scale Impact of Steel into RHA at Zero Obliquity

To obtain downrange fragmentation data, we fired a 1.02-cm-diameter, blunt-nosed 4340 steel ($R_c 40$) long-rod projectile at a normal angle and a velocity of 1.55 km/s through a 2.54-cm-thick plate of RHA (cut from a 10-cm-thick slab). This experiment is discussed in detail in Section IV. In addition, we examined the recovered target, residual penetrator, and some downrange fragments to add to our phenomenology data base, and in particular to compare the failure mechanisms evident in RHA subjected to a high velocity normal-angle penetration with those of the high velocity high-obliquity penetration discussed above and with those of the lower velocity, normal-angle tests performed last year.

Photographs of these recovered samples are shown in Figure 15, and polished and etched cross sections of the residual projectile and target plate are shown in Figures 16 and 17, respectively. The proximal end of the residual 4340 steel projectile exhibits shear banding failure in planes approximately 45° to the impact axis, very similar to that shown in Figure 1 and 2 for the full-scale oblique-impact case. This implies that the phenomenology of penetrator erosion at high impact velocities is not strongly dependent on the angle of impact.

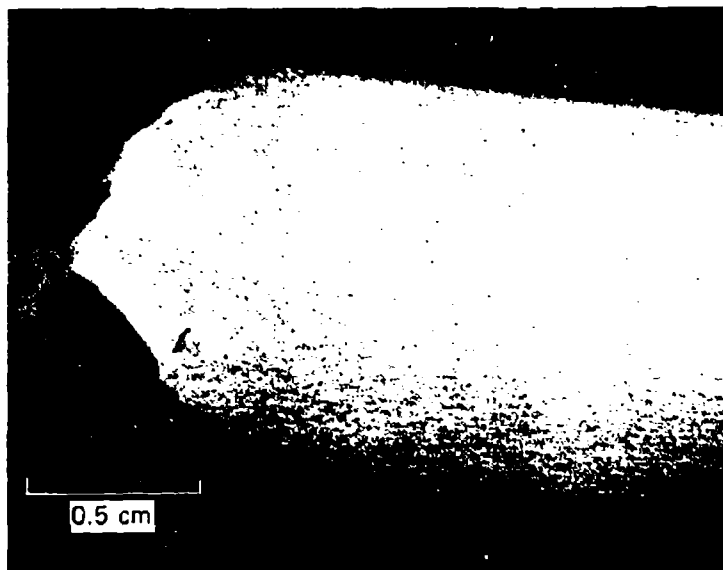
Figure 17 shows a highly gouged and scalloped inside edge of the RHA target hole and a very high density of shear bands on planes of weakness in this highly anisotropic material. Figure 17(c) shows clearly that the material fails along these bands. This failure is followed by increased distortion as the material slides along the failed planes until finally the highly damage material is sheared out by bands cutting across the planes of weakness (as shown in Figure 17b). That is what gives the surface its scalloped appearance and is the same process shown in Figure 4 for an oblique impact.* Furthermore, as can be seen in the bottom right-hand corner of Figure 17(a), a

*Note that for the oblique impact case, the final shearing across the planes of weakness occurs in the direction opposite to that of the projectile motion because of the backflowing erosion. In the normal impact case, the final shearing is in the direction of projectile motion except in approximately the upper quarter of the target plate, where projectile backflow is again dominant.

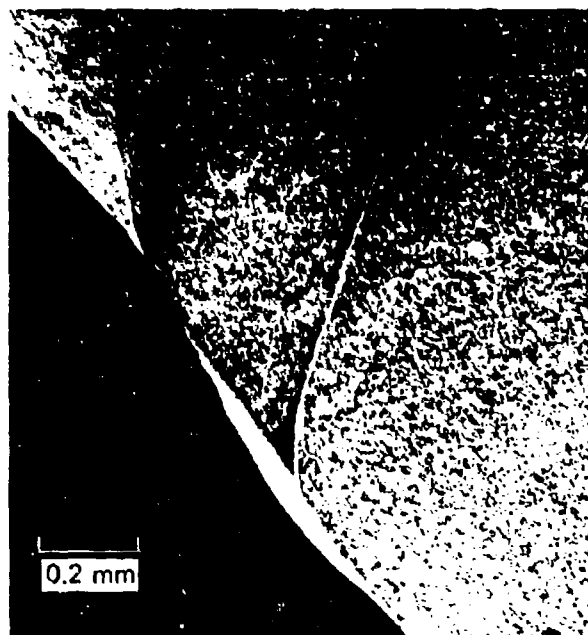


MP-789J-111

FIGURE 15 ENTRANCE (a) AND EXIT (b) HOLES OF RECOVERED RHA TARGET PLATE,
 AND RESIDUAL 4340 STEEL PENETRATOR FRAGMENT (c)
 Asymmetry in (a) is caused by pusher plate impact.



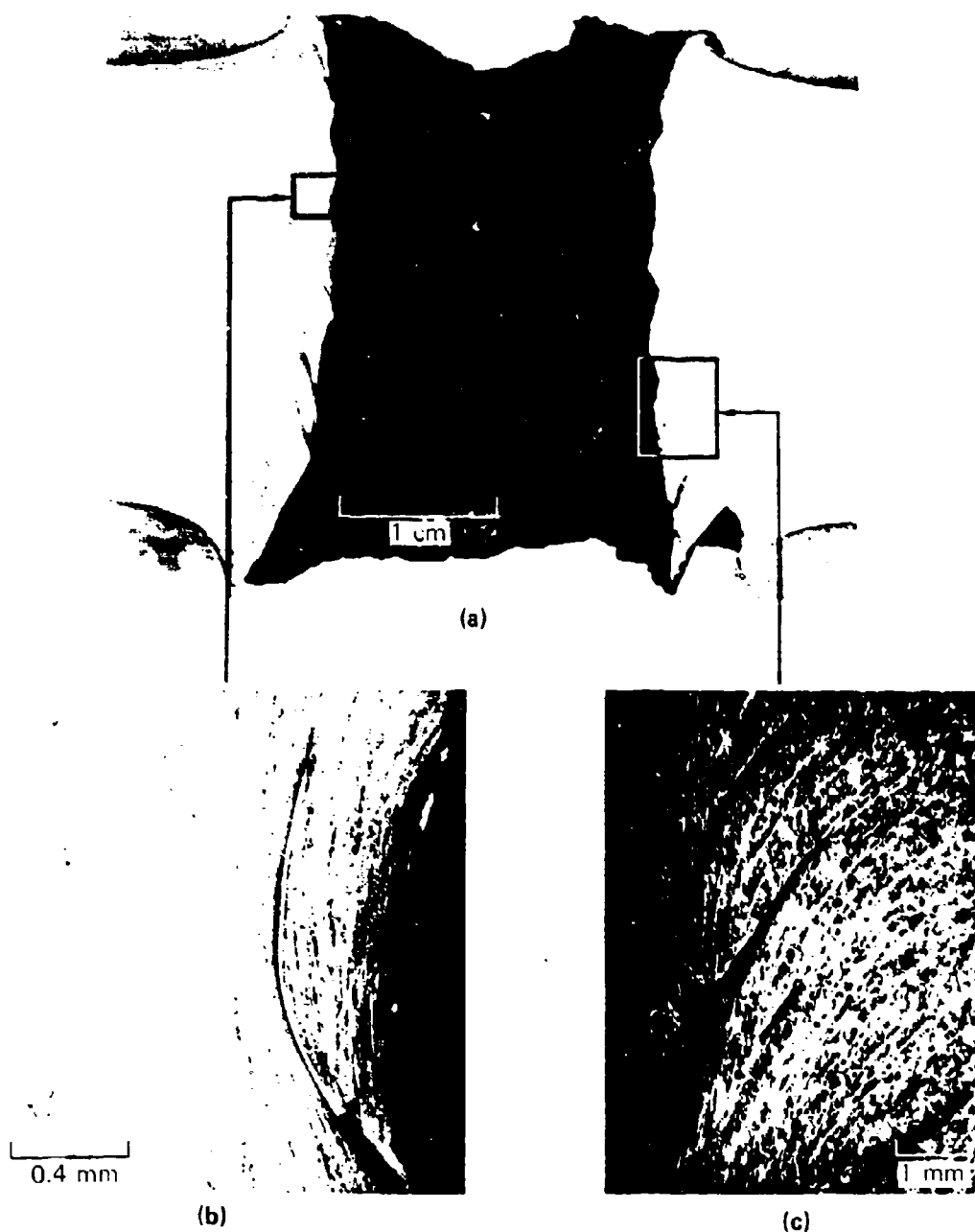
(a)



(b)

MP-7893-112

FIGURE 16 POLISHED AND ETCHED CROSS SECTION (a) OF THE PROXIMAL END OF THE RESIDUAL 4340 STEEL PENETRATOR FRAGMENT, WITH DETAIL (b) OF SHEAR BANDED REGION



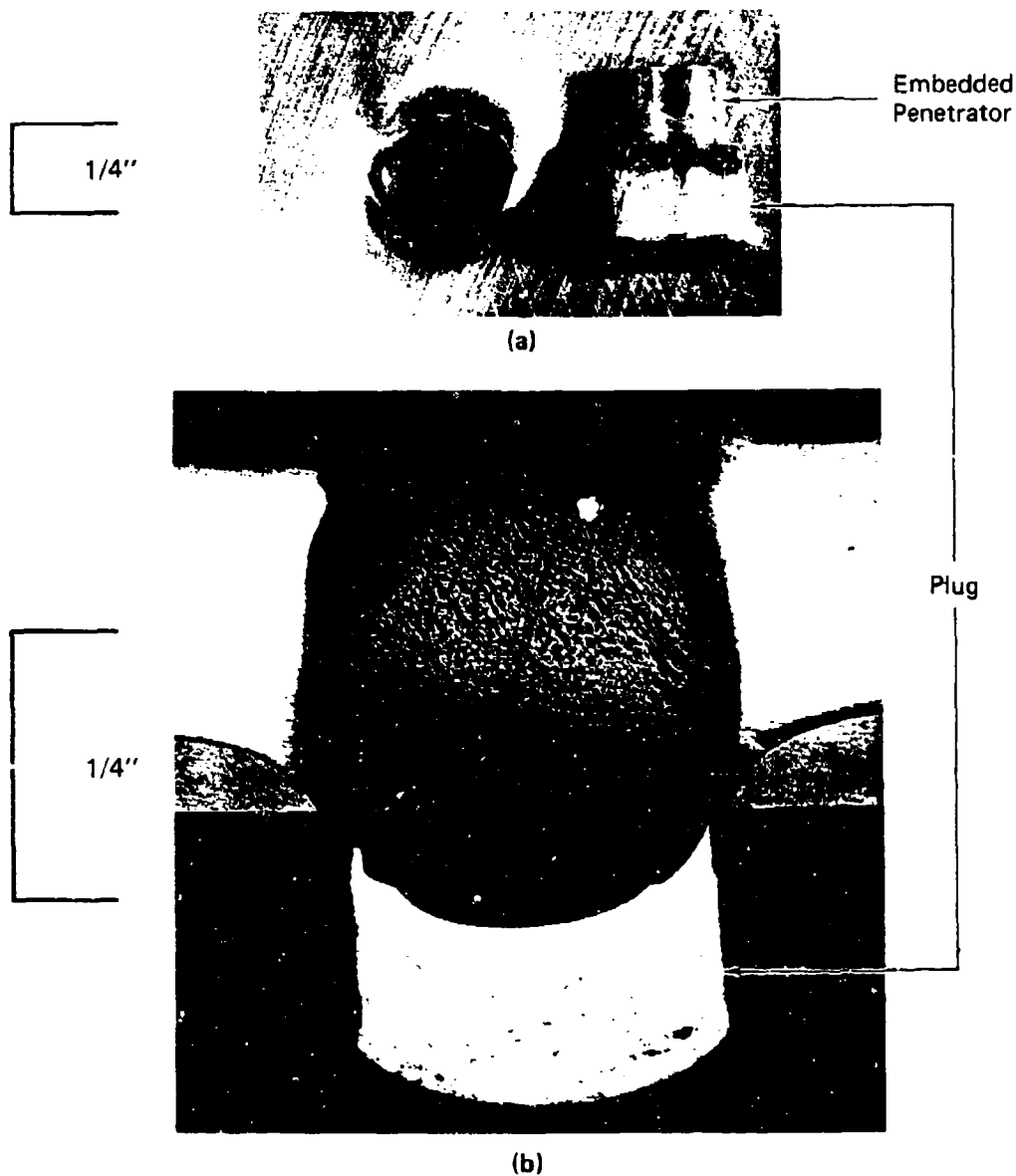
MP-7893-114

FIGURE 17 POLISHED AND ETCHED CROSS SECTION (a) THROUGH RHA TARGET AND DETAILED VIEWS (b) AND (c) SHOWING DENSE SHEAR BANDING IN REGION ADJACENT TO PENETRATION HOLE

large fragment (extending $\approx 120^\circ$ of circumferential arc and weighing ≈ 7 g) was removed by the propagation of a vertical tensile crack from a failed plane of weakness to the back target surface in a location far removed from the penetration axis. Again this is similar to what is observed for an oblique impact (see Figure 7).

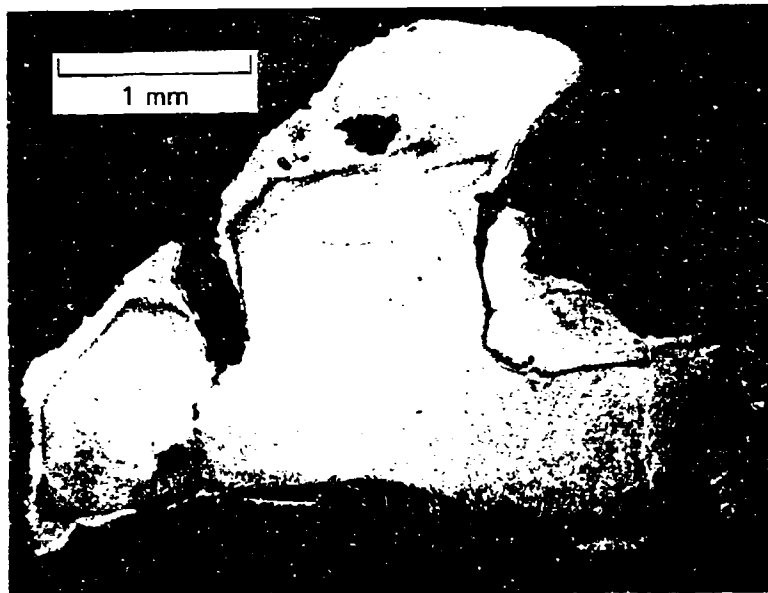
Thus it appears that much of the same phenomenology occurring in a high velocity oblique-angle impact is evident in a high velocity normal-angle impact. As a contrast, Figure 18 shows the results of a blunt-nosed normal-angle impact performed last year at about half the velocity of the test described above (0.792 km/s, or just above the ballistic limit), using the same RHA target material and a somewhat harder 4340 steel penetrator ($R_c 50$). In the lower velocity case, no shear banding along planes of weakness is observed, and the smooth appearance of the plug walls is indicative of a vertical shear band traversing the entire thickness of the target. These two types of penetration behavior, as seen in Figures 17 and 18, are significantly different, and our computer code must be able to predict the differences, using the same failure models and material properties, and varying only the impact velocity.

Finally, we examined metallographically some of the downrange fragments that were recovered. The samples were chosen to span the size range of the recovered fragments and were sliced in random directions. The polished and etched surfaces from the 4340 steel penetrator fragments are shown in Figure 19 and those from the RHA target fragments are shown in Figure 20. The white-etching bands that show up readily on the etched 4340 surfaces occur on the internal or not-yet-separated surfaces, as well as on the external, already-separated surfaces. Shear banding is less apparent on the RHA surfaces because the lower carbon content decreases the tendency to form martensite. Nevertheless, one can easily see the large shear deformations in the grain structure and the long cracks running through these regions. One can also see in some of the RHA fragments (as at the left side of Figure 20a) what appears to be a string of ductile voids. It is difficult to tell by metallographic inspection whether this is subsequent tensile failure along an

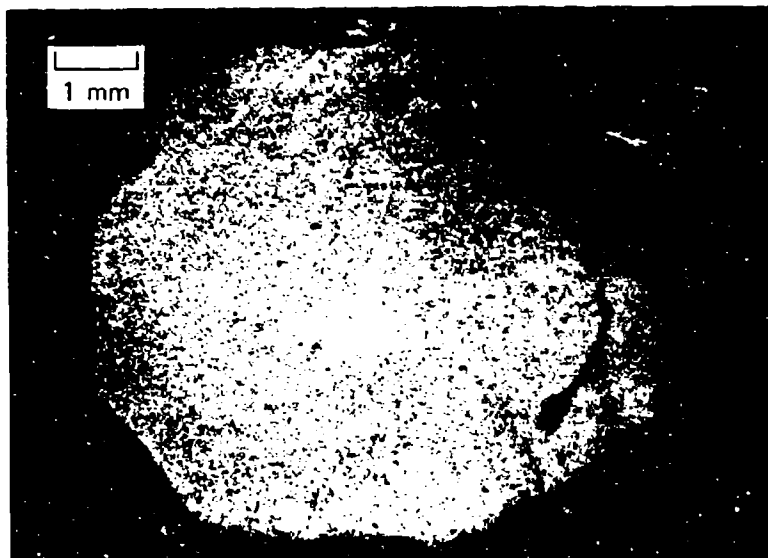


MP-7893-42A

FIGURE 18 BLUNT-NOSED 4340 STEEL PROJECTILE EMBEDDED IN RHA TARGET
PLUG (a) AND CROSS SECTION THROUGH IMPACT AXIS (b)
FOLLOWING IMPACT AT 792 m/s



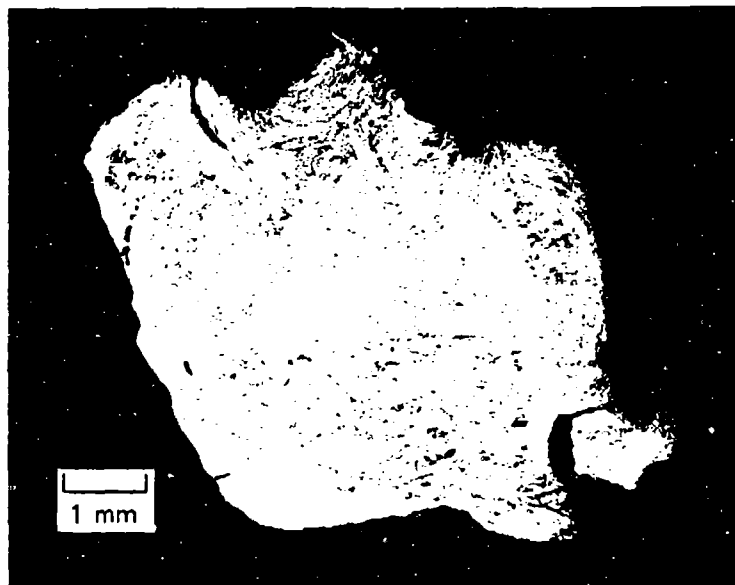
(a)



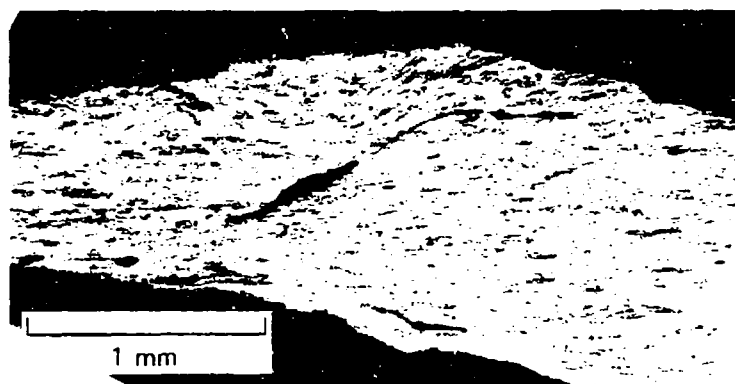
(b)

MP-7893-119

FIGURE 19 SECTIONS THROUGH RECOVERED DOWNRANGE 4340 STEEL PENETRATOR FRAGMENTS, SHOWING EXTENSIVE INTERNAL AND EXTERNAL SHEAR BANDING



(a)



(b)

MP-7893-120

FIGURE 20 SECTIONS THROUGH RECOVERED DOWNRANGE
RHA TARGET FRAGMENTS, SHOWING EXTENSIVE
SHEAR DEFORMATION AND RESULTANT BANDING

existing shear band or a subsequent shear band along existing tensile voids. However, since our computations show that large shear deformations precede any large tensile stresses in the target (except perhaps in a narrow region adjacent to the downrange surface), we conclude that shear band failure is the prime mechanism of importance in target fragmentation.

D. Phenomenological Conclusions and their Significance for the Computational Model

The following five conclusions can be drawn concerning the phenomenology of high velocity penetration of moderate-to-thick armor by long-rod penetrators on the basis of the experiments described above:

- (1) Shear banding is the principal failure mechanism in both the penetrator and the target, and it is the coalescence of shear bands that forms the bulk of the downrange (and uprange) fragments.
- (2) Shear-band-induced penetrator backflow and shear failure along planes of weakness are significant mechanisms of target erosion.
- (3) Projectiles change direction within the target (oblique impacts only), seeking the path of least resistance.
- (4) Tensile failure may be a factor, but only in specific instances such as at the rear of the target plate in the final stages of penetration for a projectile just above the ballistic limit.
- (5) Most of the failure mechanisms occurring in a highly oblique impact will also be found in a normal impact of the same velocity using the same materials.

Although we have examined only a few target and penetrator materials (RHA, DU, 4340 steel in this program and a tungsten alloy in a previous program)⁶ in a velocity range up to 1.5 km/s, we believe that these phenomenological results are applicable to a more general range of materials and conditions. For example, we expect to see the same phenomena at velocities up to the start of the hypervelocity regime, where strength effects are no longer important. Also, because of the high compressive stresses and shear strains found in the critical regions of long-rod penetration, we expect the shear failure scenarios to be relevant to most any material, particularly metals, that may be considered for armor or penetrator use.

The purpose of the phenomenology experiments, in addition to providing a deeper understanding of the physical processes involved in an armor penetration, is to guide us in selecting the types of failure models and other features to be put in our predictive computer code and the types of materials characterization experiments to be performed on the materials of interest. From each of the five conclusions listed above, we can elicit a guideline to aid us in our future work on the computational modeling of armor penetration. They are as follows:

- (1) Shear banding parameters are important for each material of interest, including both penetrator and target materials.
- (2) An anisotropic shear banding model is needed, and the computer code needs to be able to handle the extreme deformation and material ejection that accompany penetrator backflow.
- (3) A self-directing or wandering slide line is needed to handle the rotation of a projectile in an oblique impact.
- (4) Tensile failure parameters may be relatively unimportant, particularly in the projectile.
- (5) Simulations of normal impacts (which of course are much easier to perform than oblique impacts because of the two-dimensionality of the problem) are valid tests of the computer model's ability to calculate fragmentation distributions because they involve most of the phenomenology (except for projectile rotation) occurring in an oblique impact.

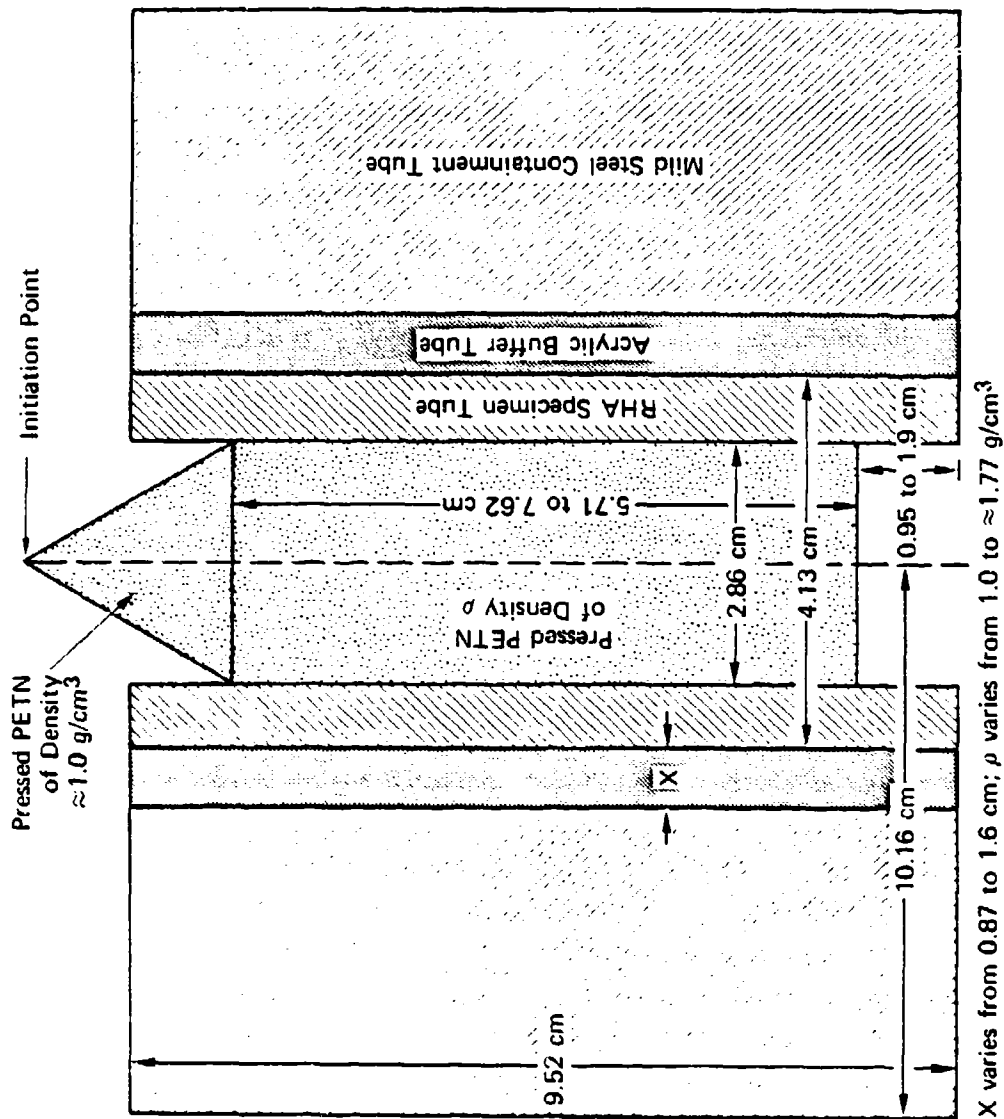
III MATERIALS CHARACTERIZATION EXPERIMENTS

During the second year of this program, we completed a series of nine contained fragmenting cylinder (CFC) experiments using RHA specimen tubes. A schematic diagram of the CFC experiments is shown in Figure 21. Figure 22 shows the shear band orientation modes possible. A detailed description of the CFC method has been given earlier by Erlich et al.⁶ Table 1 shows the experimental parameters and the qualitative damage results for these experiments.

Since quasi-static tensile tests had revealed a significant anisotropy in tensile failure in RHA,¹ we expected a similar anisotropy to exist with respect to resistance to shear banding. Early experiments with RHA specimen tubes whose axes were in the long transverse direction of the RHA slab (the L-specimen, as shown in Figure 23) confirmed our expectations. The preponderance of shear bands in planes nearly parallel to the rolling plane in specimens L-2 and L-4 (as seen in Figures 24 and 25, for example) clearly showed that shear banding will occur at lower strains in the rolling plane than in planes perpendicular to the rolling plane.

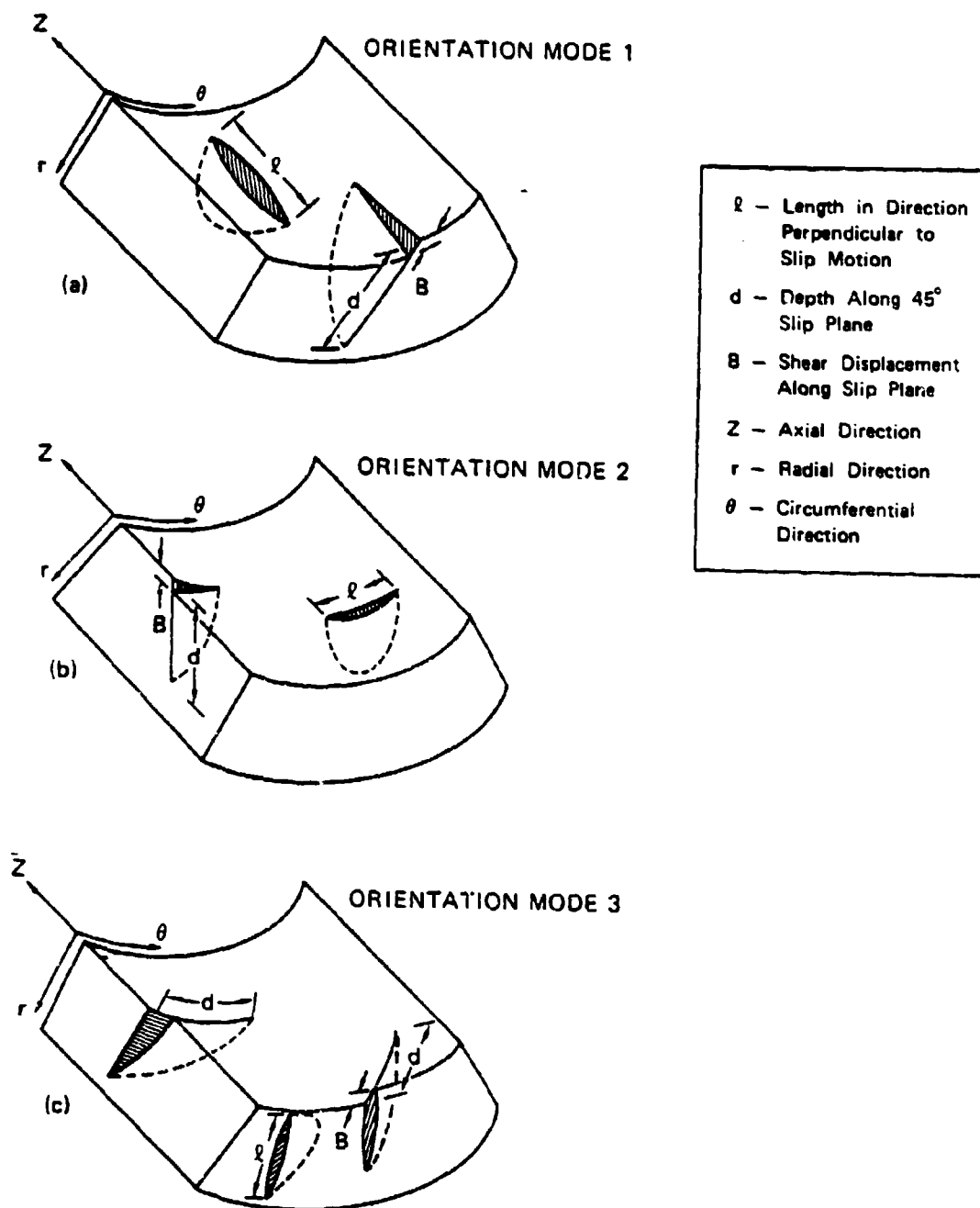
Once it was clear that by using L-specimens we could not obtain many shear bands in planes perpendicular to the rolling plane, we switched to T-specimens (whose axes were in the through-the-thickness direction) for which all the Mode I shear bands would lie in the desired planes. The first four T-specimen experiments (T-1, T-2, T-3, and T-5), using PETN explosive densities similar to those used in all previous CFC experiments,^{6,7} yielded only incipient Mode I shear banding. However, the final three experiments (T-7, T-9, and T-10), using much higher explosive densities, yielded significant quantities of both incipient and large shear bands, as well as some fragmentation. Photographs of these specimens are shown in Figures 26 and 27.

Data analysis for the RHA CFC experiments is proceeding. The analysis consists of three items: (1) determining the final wall thickness



MA-7893-74

FIGURE 21 CROSS SECTION OF RHA CONTAINED FRAGMENTING CYLINDER EXPERIMENTS



MA-5084-21

FIGURE 22 GEOMETRY AND NOMENCLATURE FOR SHEAR BANDS IN FRAGMENTING CYLINDER EXPERIMENTS

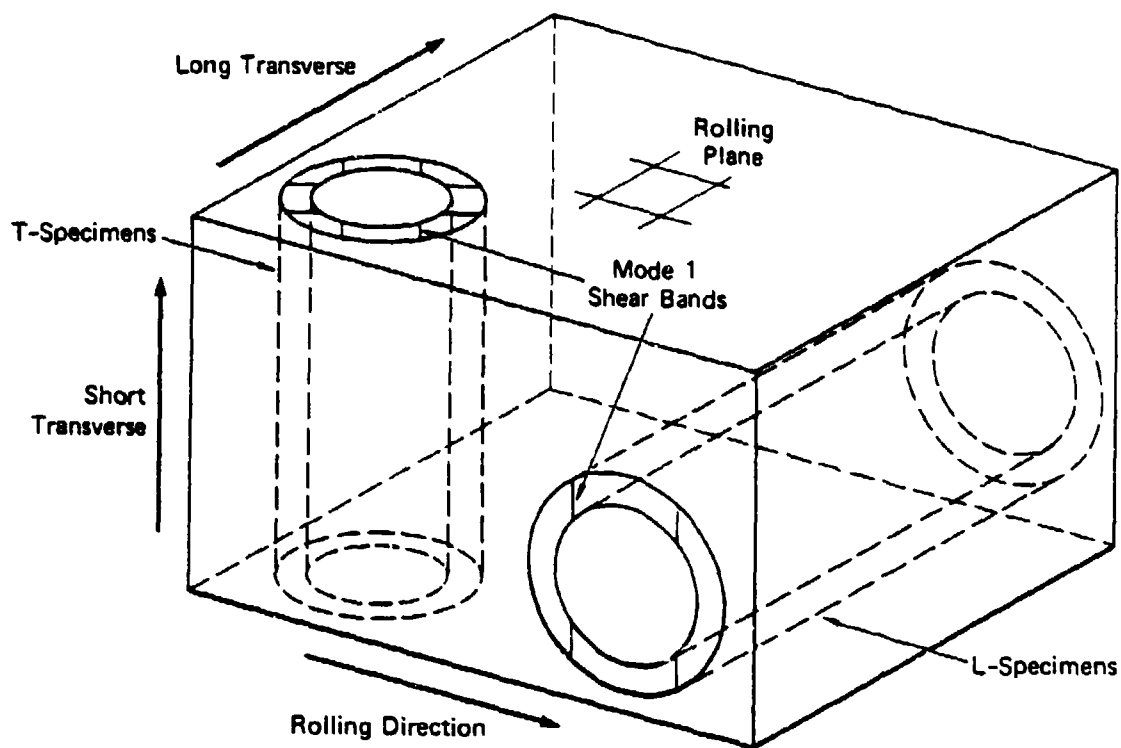
Table 1

PARAMETERS AND QUALITATIVE RESULTS FOR RHA
CONTAINED FRAGMENTING CYLINDER EXPERIMENTS

Specimen	Lucite Buffer Thickness (cm)	PETN Density (g/cm ³)	Calculated Detonation Pressure (kbar)	Qualitative Shear Banding Results
L-4 [*]	0.873	1.2	122	Substantial Mode 1 banding concentrated in rolling direction.
L-2	0.873	1.0	80	Same as L-4.
T-1 [†]	0.873	1.2	122	A few incipient Mode 1 bands (some tensile cracking on outer surface in midaxial region).
T-3	0.873	1.35	162	Incipient Mode 1 banding over most of inner surface (some tensile cracking as in T-1 above).
T-2	1.600	1.2	122	Few incipient Mode 1 bands. Moderate Mode 2 banding in midaxial region.
T-5	1.600	1.35	162	Extensive incipient Mode 1 banding. Few moderate Mode 2 bands in midaxial region.
T-7	1.600	1.47 to ≈ 1.77	202 to ≈ 324	Substantial Mode 1 banding. Substantial Mode 2 banding in narrow midaxial region.
T-9	1.27	1.54	228	Substantial Mode 1 banding. Mode 2 bands in midaxial region cuts specimen in two.
T-10	1.27	1.6	250	Same as T-9, with some fragmentation.

* L-specimens have axes parallel to long transverse direction of RHA block.

† T-specimens have axes parallel to short transverse (through the thickness) direction.



MA-7893-47

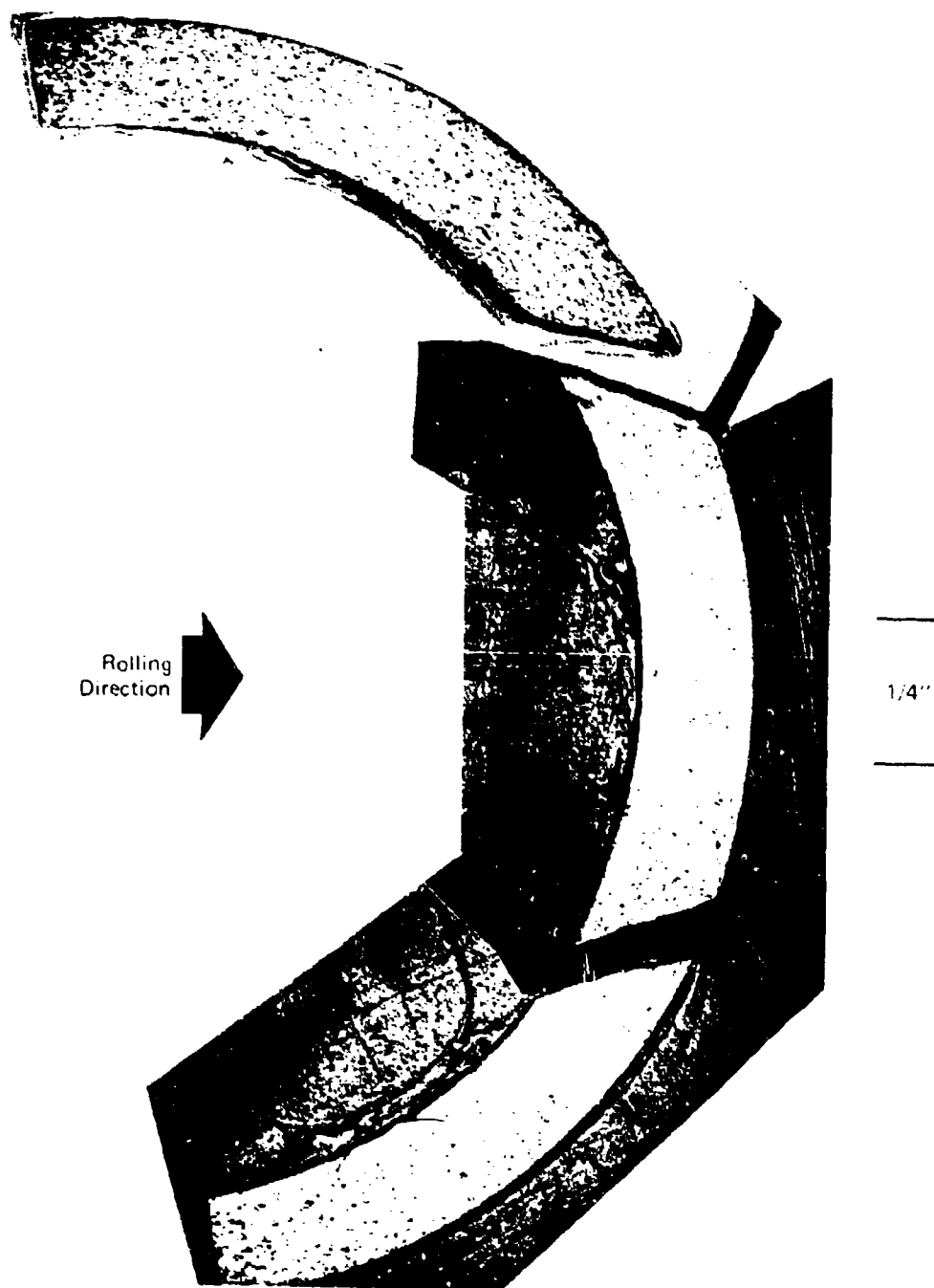
FIGURE 23 CFC SPECIMENS MACHINED FROM RHA SLAB, SHOWING MODE 1 SHEAR BANDS IN PLANES PERPENDICULAR TO ROLLING PLANE



MP-7893-43

FIGURE 24 TWO VIEWS OF HALF OF THE RHA SPECIMEN TUBE L-4 RECOVERED FROM CFC EXPERIMENTS

Detonation proceeds from top to bottom.



MP-7893-44

FIGURE 25 POLISHED AND ETCHED SECTION THROUGH RHA SPECIMEN TUBE L-4, SHOWING PREPONDERANCE OF SHEAR BANDING DAMAGE IN ROLLING DIRECTION
Plane is cut at a distance of 2-3/8 inches from bottom of specimen tube.



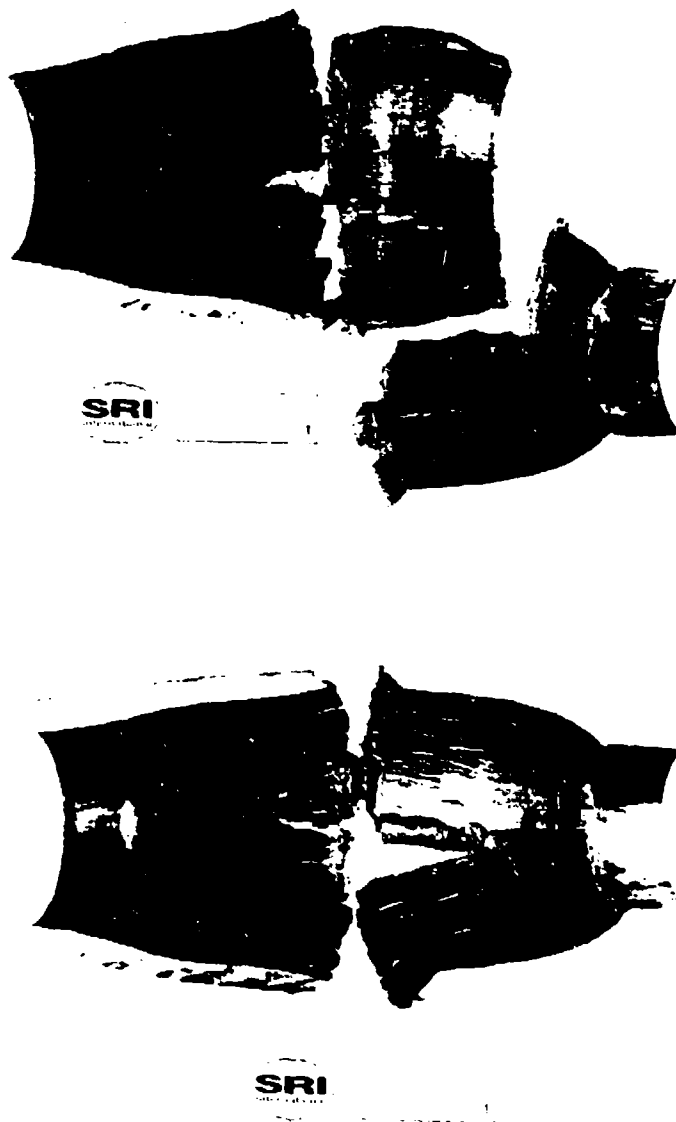
MA-7893-75

(b)

RECOVERED FROM CFC EXPERIMENT

(a)

FIGURE 26 TWO VIEWS OF HALF OF THE RHA SPECIMEN TUBE T-7
Detonation proceeds from top to bottom.



(a)

(b)

MP-7893-76

FIGURE 27 HALF OF RHA SPECIMEN (a) T-9, AND (b) T-10 RECOVERED FROM CFC EXPERIMENTS
Detonation proceeds from top to bottom.

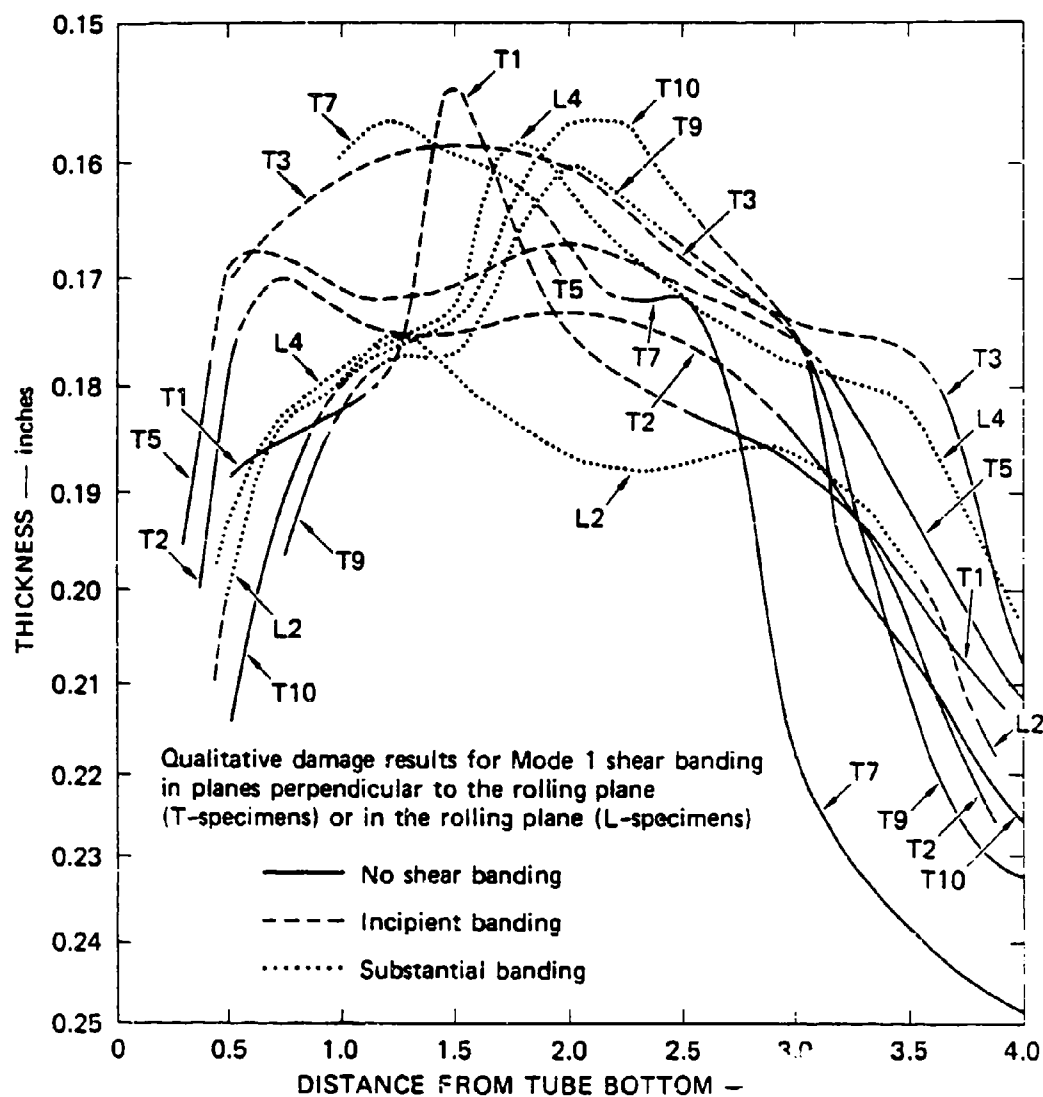
(and, for lower damage cases, the final inside radius) of the recovered specimen tube as a function of axial position, (2) determining the shear band size distribution as a function of axial position, and (3) determining the shape or outline of the shear band in its slip plane.

Final wall thickness measurements are made after slicing the specimen tube parallel to the axis. They are first used for comparison with initial no-damage computer simulations of the CFC experiments to check if the explosive parameters and bulk material properties (before shear band damage) used in the code are correct. Later the measurements are used with damage simulations to determine if further plastic strain following shear band nucleation is apportioned correctly between bulk strain and localized (shear banding) strain.

The final wall thickness plots for all nine RHA CFC experiments are shown in Figure 28, along with qualitative damage values. Note that the qualitative damage results shown in Figure 28 refer only to damage by Mode 1 banding. The presence of Mode 2 banding, which accounts for much of the equivalent plastic strain in the peak of the curve T-1, for example, is not shown.

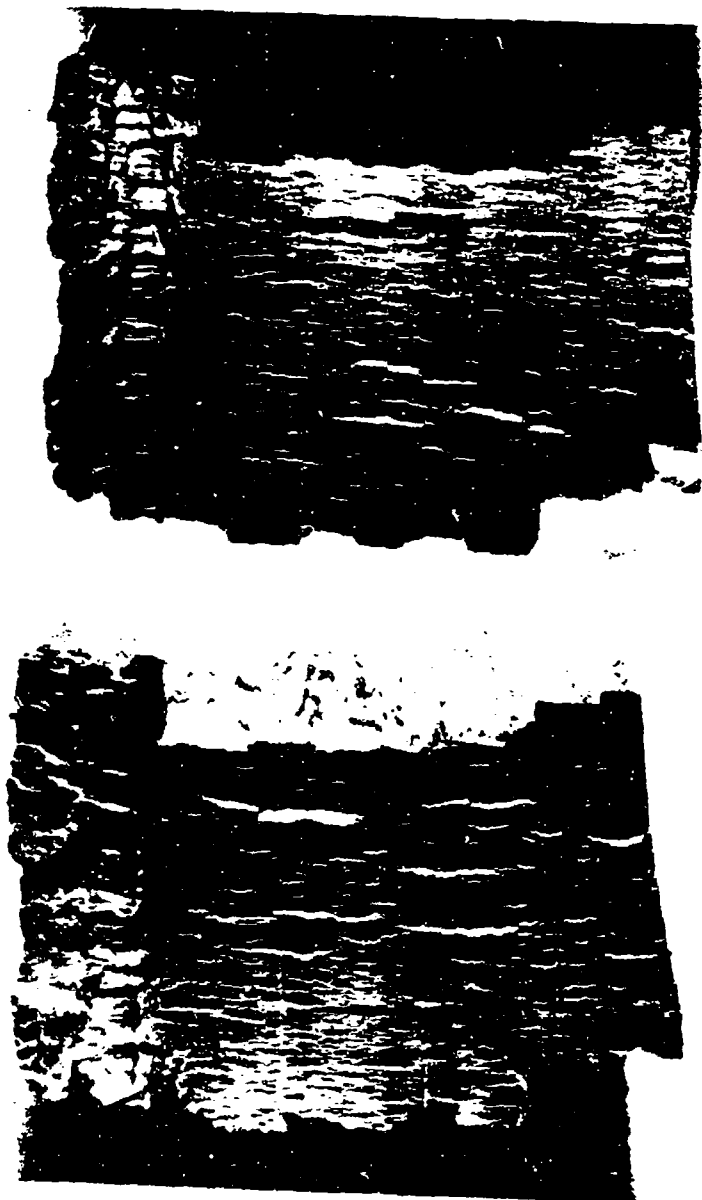
For determining the shear band size distribution as a function of axial position, the specimen is cut axially into segments no greater than about 60° of circumferential arc. (For cases of higher damage, the existence of fragments of the appropriate size makes cutting unnecessary.) Each segment is first divided into zones by scribing lines perpendicular to the axis, and then photographed. Light is provided at a grazing angle from alternate sides to highlight the Mode 1 shear bands intersecting the surface at the two different 45° angles. Figure 29 is such a photograph of a segment from specimen T-7. The zones are $\approx 1/4$ inch (6.35 mm) wide. Then for each zone, a shear band size distribution is determined, such as the one shown in Figure 30 for a 4340 steel specimen from a previous program. This type of plot will provide the data base for comparison with computer simulations performed to obtain shear band parameters for RHA.

We have been experiencing difficulty obtaining the shear band size distributions for RHA from the optical photographs because of the



MA-7893-80A

FIGURE 28 FINAL WALL THICKNESS AS A FUNCTION OF AXIAL POSITION FOR ALL OF THE RHA SPECIMEN TUBES RECOVERED FROM CFC EXPERIMENTS



(a)

(b)

MP-7893-77

FIGURE 29 PHOTOGRAPHS OF INSIDE SURFACE OF ONE PIECE OF SPECIMEN T-7

Two views highlight mode I shear bands intersecting surface at different 45° angles.

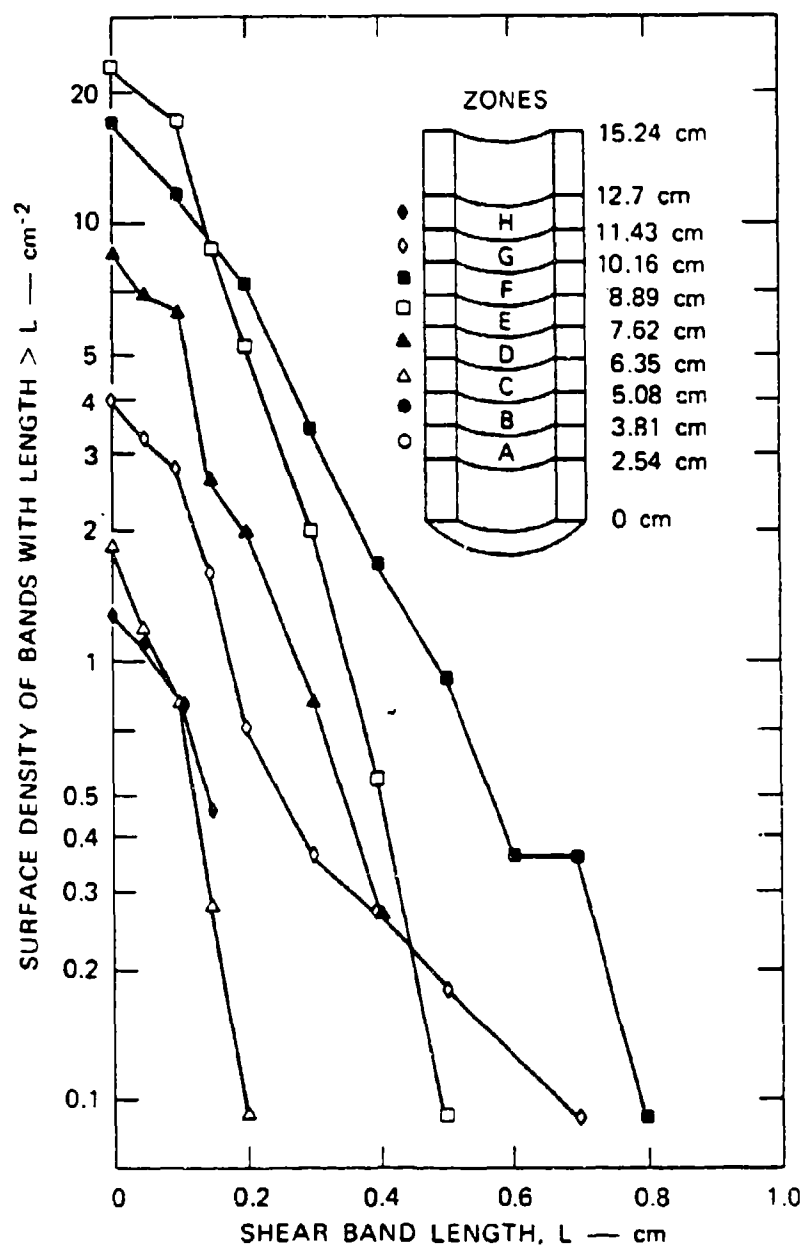
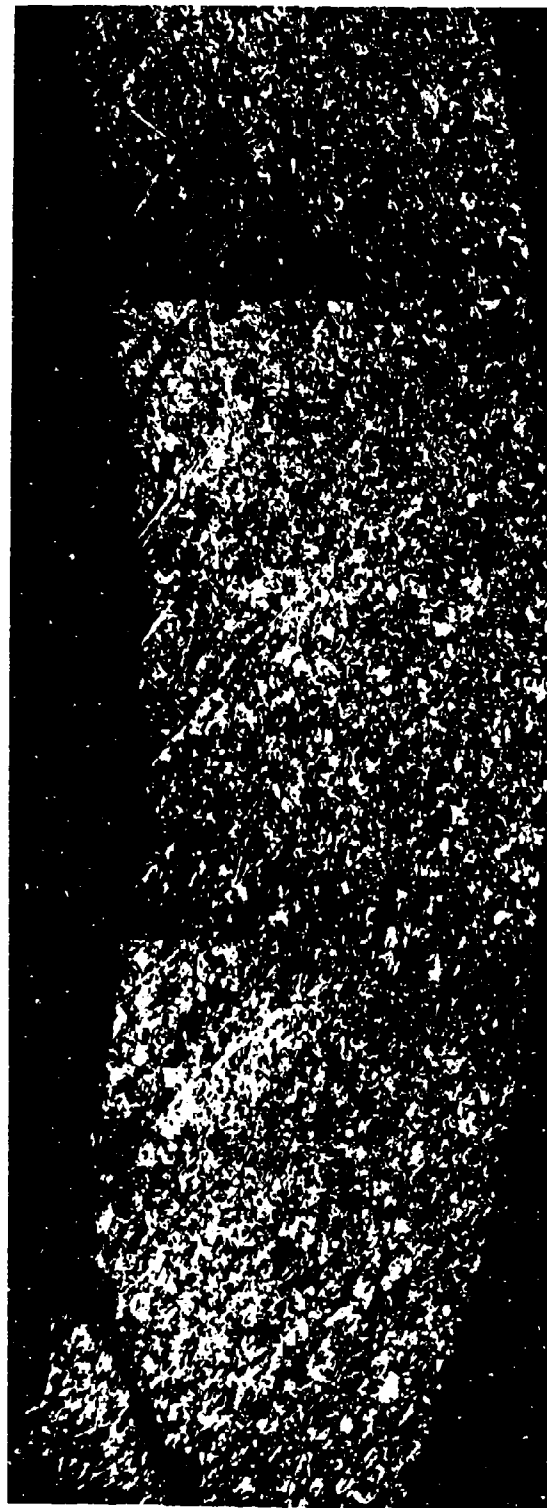


FIGURE 30 SAMPLE SHEAR BAND SIZE DISTRIBUTION FROM 4340 STEEL CFC EXPERIMENTS

myriad of smaller bands and the poor contrast with the background metallic surface. We are currently investigating scanning electron microscopy as well as other optical photographic techniques in hopes of improving the situation.

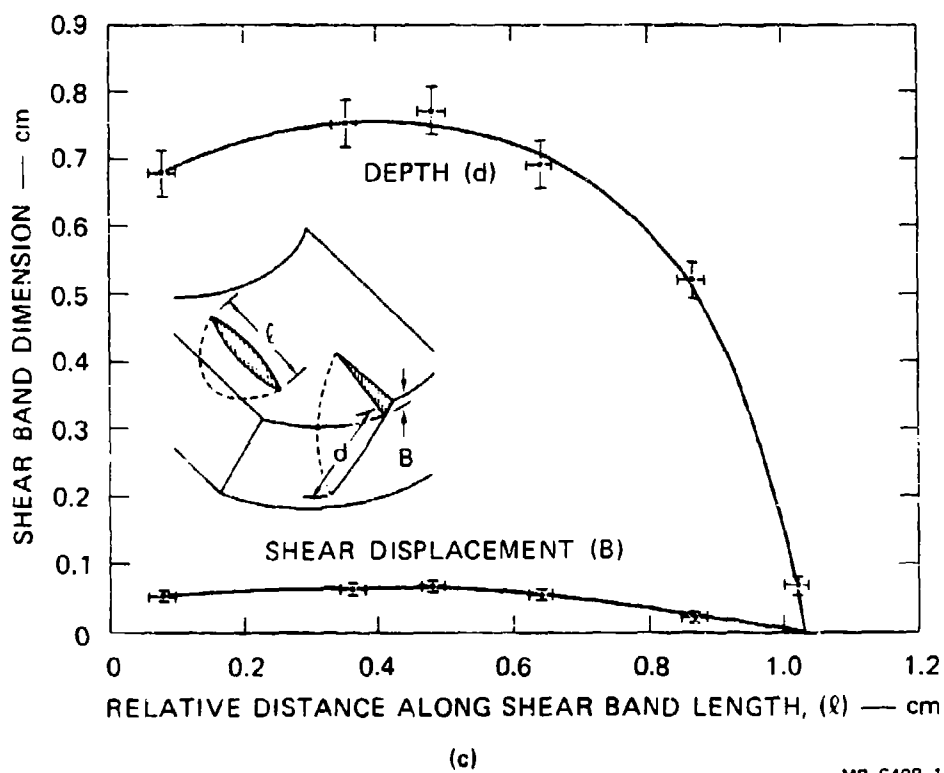
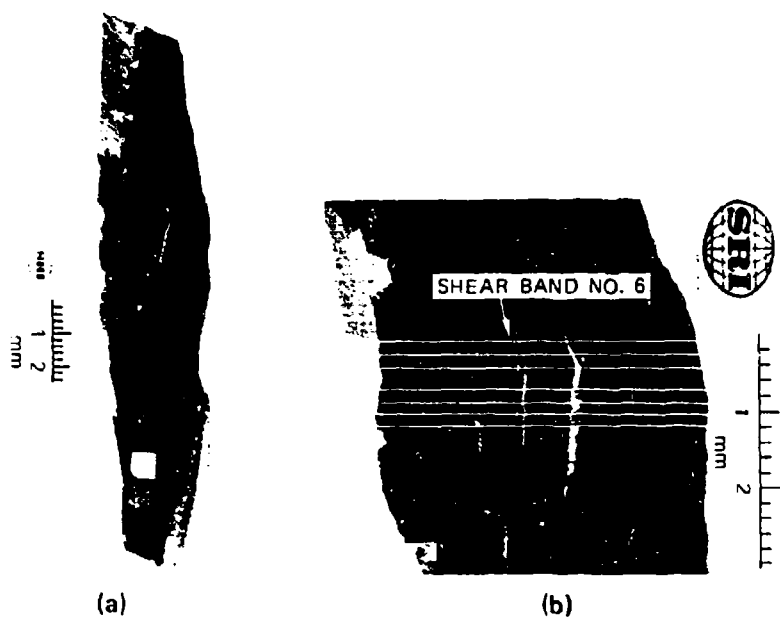
For determining the shape or outline of the shear band in its slip plane, the specimen is sliced perpendicular to the axis, polished, etched, and photomicrographed to obtain an edge-on view of the shear bands, as in Figure 31. The depth (d) and displacement (B) of each band (see Figure 22) are measured. We then slice or grind a known small amount off the specimen, repolish, etch, and measure d and B at this new position. Finally, we relate these measured values of d and B with the value of the length (l) for the same band as measured on the inside surface before slicing the specimen. Figure 32 shows results of a similar analysis of data on 4340 steel, which exhibits nearly semi-circular shear bands.

Again, we are experiencing difficulty with the measurement of d because of the high density of bands and because the poor contrast obscures the lower end of the bands (see Figure 31). One encouraging note, however, is that all the bands appear to intersect the inside surface of the specimen tube, as was the case for 4340 steel.⁷ Therefore, measuring a surface shear band size distribution will yield a complete picture of the damage. We need to make only a few slices through the tube perpendicular to the axis to determine the relationship between d , B , and l .



MP-7893-79

FIGURE 31 SECTION PERPENDICULAR TO AXIS OF RHA SPECIMEN T-7, SHOWING HIGH DENSITY OF SHEAR BANDS
AND DIFFICULTY IN DETERMINING BAND DEPTH



MP-6408-13

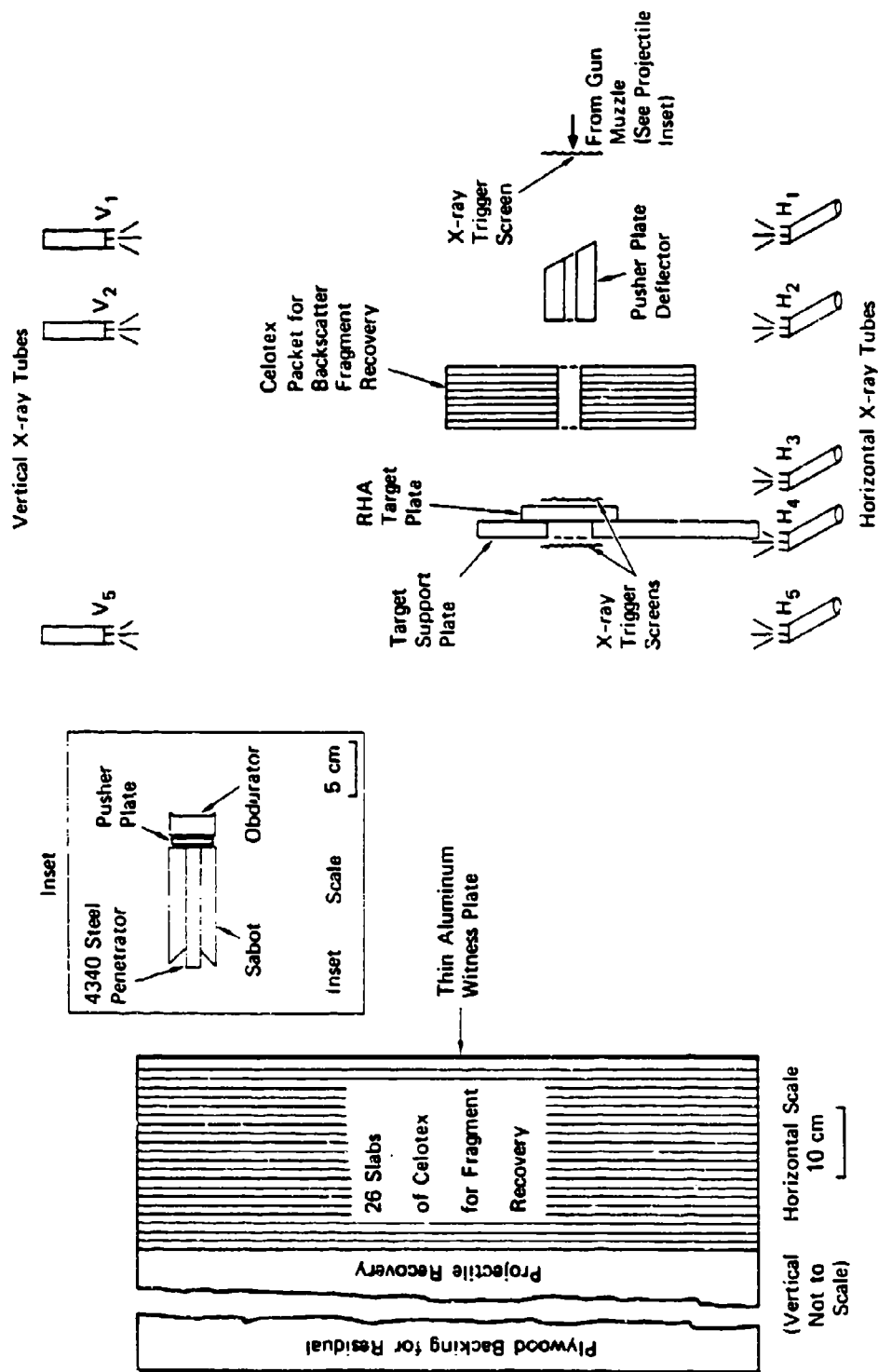
FIGURE 32 FRAGMENT (a); AND (b) USED IN SHEAR BAND PROFILE STUDY FOR 4340 STEEL AND MEASURED PROFILE (c) OF SHEAR BAND NO. 6

IV DOWNRANGE FRAGMENTATION DATA BASE ACQUISITION

J. Barb and A. J. Richiazzi of BRL have provided us with a substantial amount of fragmentation data on impact of DU into RHA at various velocities and obliquities. We expect these data to be of great value to use for comparison with our computer calculations. However, we will have shear banding model parameters for RHA and 4340 steel before we expect to have them for DU, and our code will handle a normal impact before it is expected to be able to handle an oblique impact. Therefore, to make an early comparison between downrange fragmentation data and our computational model predictions, and hence determine at an early stage the ability of our phenomenologically based model to predict fragmentation, we performed, at the quarter-scale facility at BRL, the penetration experiment described below.

A 1.02-cm-diameter by 10.16-cm-long right circular cylinder of 4340 steel (R_c 40) was launched at zero obliquity and a velocity of 1.55 km/s into a 2.54-cm-thick by 15.24-cm-diameter RHA plate (cut from a 10-cm-thick RHA slab). The experimental arrangement is shown in Figure 33. The target plate was positioned on the uprange side of a large steel holder plate having a 7.62-cm-diameter hole concentric with the impact axis. Celotex recovery packets were placed both uprange and downrange of the target to capture fragments emerging from the two sides of the target plate. Eight x-rays (three vertical and five horizontal) were triggered from appropriately placed screens to record preimpact projectile velocity and yaw as well as postimpact fragmentation.

The first two pairs of orthogonal radiographs are shown in Figure 34. Measurements from these x-rays reveal an impact velocity of 1.55 km/s and a final yaw of less than 2°. (The yaw was fortuitously improved by the impact of the penetrator with the pusher plate deflector; however, this unplanned impact prevented the deflector from accomplishing its original purpose.)



MA-7893-106

FIGURE 33 SCHEMATIC OF BRL BALLISTICS EXPERIMENT



MP-7893-107

FIGURE 34 VERTICAL (V_1 AND V_2) AND HORIZONTAL (H_1 AND H_2) RADIOGRAPHS
SHOWING PENETRATOR TRAVEL (from right to left) BEFORE IMPACT
Images shown are 100.6 μ s apart.

The three postimpact horizontal radiographs are shown in Figure 35. The image labeled H_3 , taken ≈ 30 μ s after impact, shows the projectile more than halfway into the front of the target and many fragments, most of them probably from the penetrator, backscattered from the target. (We were unable to recover any of the backscattered fragments because the uprange Celotex recovery pocket was destroyed by debris from the pusher plate deflector.)

The two images labeled H_4 and H_5 taken ≈ 145 and 285 μ s, respectively, after impact, show the fragments and residual penetrator traveling down-range at a velocity of 1.257 km/s or slightly more than 80% of the impact velocity.

The white numbers adjacent to each fragment image identify the fragment for computational analysis, and the white lines show possible fragment trajectories between the two images. Note that the large fragment with an "X" on it is a piece of the pusher plate and not a fragment of interest.

The postimpact vertical radiograph V_5 , taken at the same time as H_5 , is shown in Figure 36, along with an entirely different set of identifying numbers. The computational analysis consists of several steps. First, the positional coordinates of the endpoints of each fragment in the two orthogonal radiographs are determined. Computer-drawn pictures based on these readings are shown in Figure 37. In each radiograph, about 350 fragments are identified, and each fragment is represented by a triangle that gives an accurate length in the direction of penetration and an approximate width parameter. A computer program then matches the fragments images from the two radiographs and calculates the true length, velocity, and trajectory angles for each fragment.

The next step in the analysis is to determine the mass distribution of these fragments. The total mass available for the fragments is roughly 98 grams: the 34 grams lost from the target plus the 39-gram residual penetrator plus the ≈ 25 grams eroded from the penetrator. However, this total is reduced by the unknown mass of the fragments backscattered uprange (mostly from the penetrator). Our method was to





MP-7893-108

FIGURE 35 HORIZONTAL RADIOGRAPHS
 REVEALING BACKSCATTER FRAG-
 MENTATION (H_3 at $\approx 30 \mu s$ after
 impact) AND DOWNRANGE FRAG-
 MENTATION (H_4 and H_5 at ≈ 145
 and $285 \mu s$, respectively, after impact).
 White numbers and lines identify frag-
 ments and their paths for computa-
 tional analysis.

locate the downrange fragments captured in the recovery packet, determine the trajectory of each fragment from the position coordinate of the entrance hole on the aluminum witness plate, and measure each fragment's mass and length. By comparing trajectories, lengths, and general shapes from the witness plate data with those from the x-ray data, we might be able to make a one-to-one correlation between many of the fragments (mostly the larger ones) recovered and their images on the radiographs. In addition, a mass-versus-length curve can be obtained and used to estimate the mass for those radiographic images that could not be directly correlated with the recovered fragments.

The hole pattern on the 0.5-mm-thick aluminum witness plate is shown in Figure 38 along with a detailed photograph of the area around the axis of impact. The triangles in Figure 38(b) represent dents made by penetrator or target fragments (or perhaps in some cases other debris) with insufficient energy to either stick to or perforate the witness plate. The 300 circles represent the fragments that did stick to or perforate the plate; about 240 of these fragments were recovered, ranging in length from less than 0.6 mm to 16.7 mm and in mass from less than 0.2 mg to more than 2 g.

A relationship between the maximum dimension (ℓ) of any fragment and the fragment mass (m) was obtained by plotting the data and by fitting them to a fifth order least-squares polynomial of the form

$$\ln m = \sum_{i=0}^5 A_i \ell^i$$

where m = mass in g, ℓ = length in mm, and A_0 through A_5 = -9.62, 3.54, -0.790, 9.85×10^{-2} , -5.89×10^{-3} , and 1.32×10^{-4} , respectively. The mass versus length data and the polynomial fit are shown in Figure 39.

A preliminary calculation of the downrange fragment mass and velocity distributions was performed at BRL, using the above mass-versus-length curve, but without attempting to correlate individual fragments. The results are shown in Figure 40. These data were transformed into the cumulative mass distribution shown in Figure S2 of the Summary (and

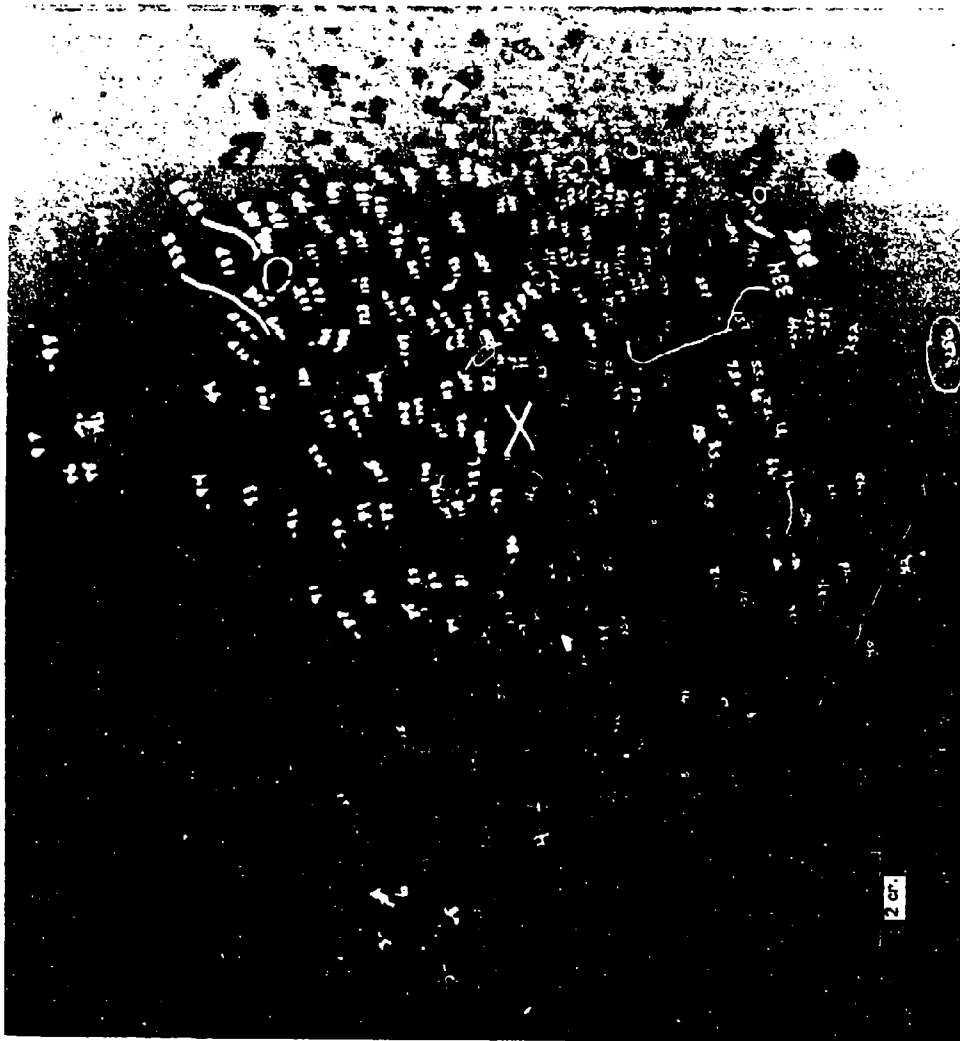
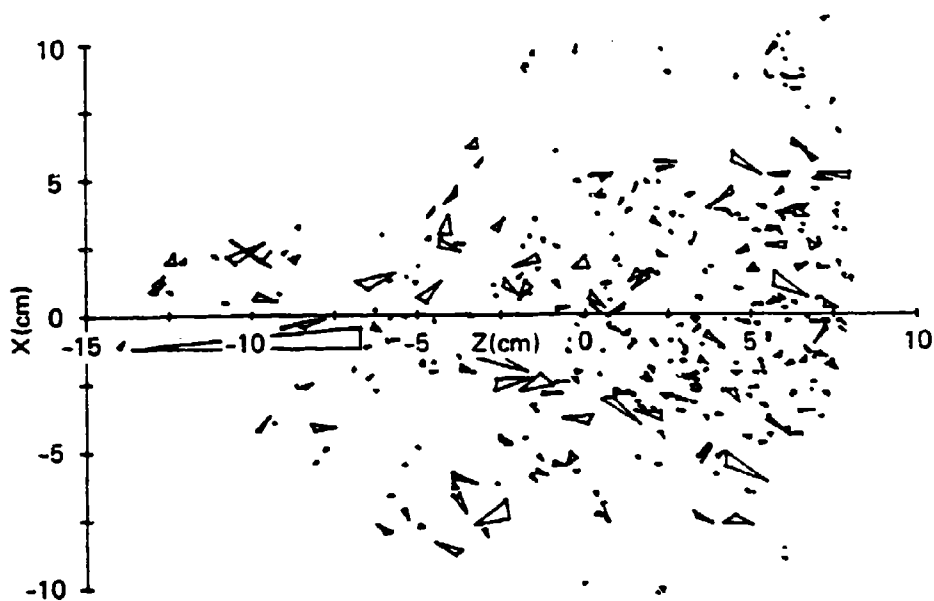
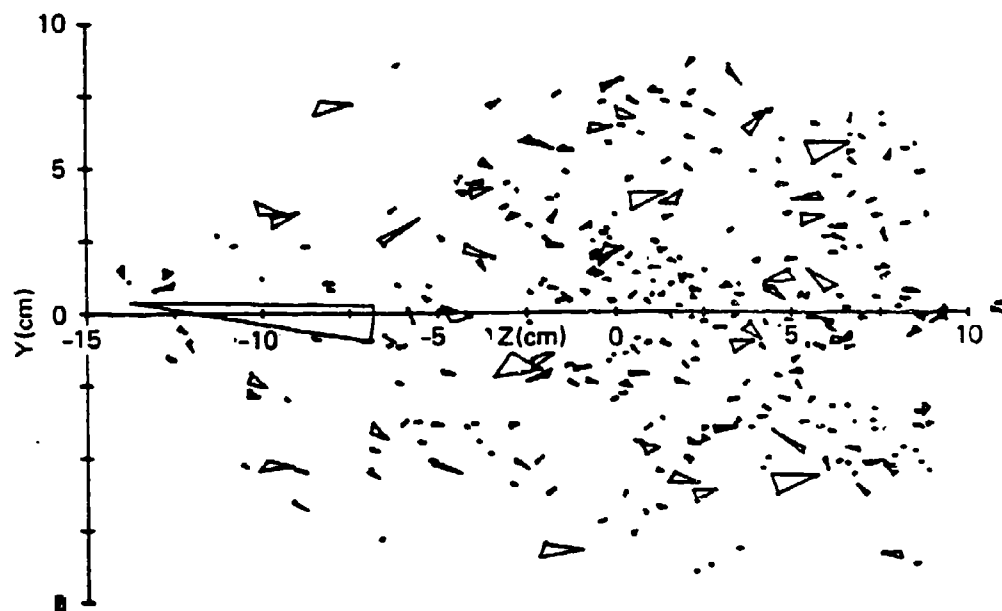


FIGURE 36 VERTICAL RADIOGRAPH V₅ REVEALING DOWNRANGE FRAGMENTATION
AT $\approx 285 \mu s$ AFTER IMPACT.
White numbers identify fragments for computational analysis.



(a) TOP VIEW



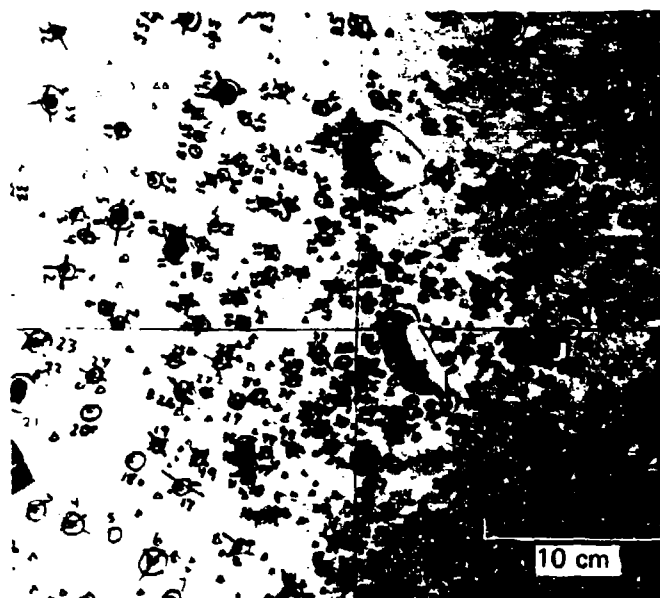
(b) SIDE VIEW

MP-7893-110

FIGURE 37 COMPUTER PLOTS OF FRAGMENTS OBSERVED ON (a) VERTICAL RADIOGRAPH V_5 AND (b) HORIZONTAL RADIOGRAPH H_5 , AS RECEIVED FROM BRL



(a)

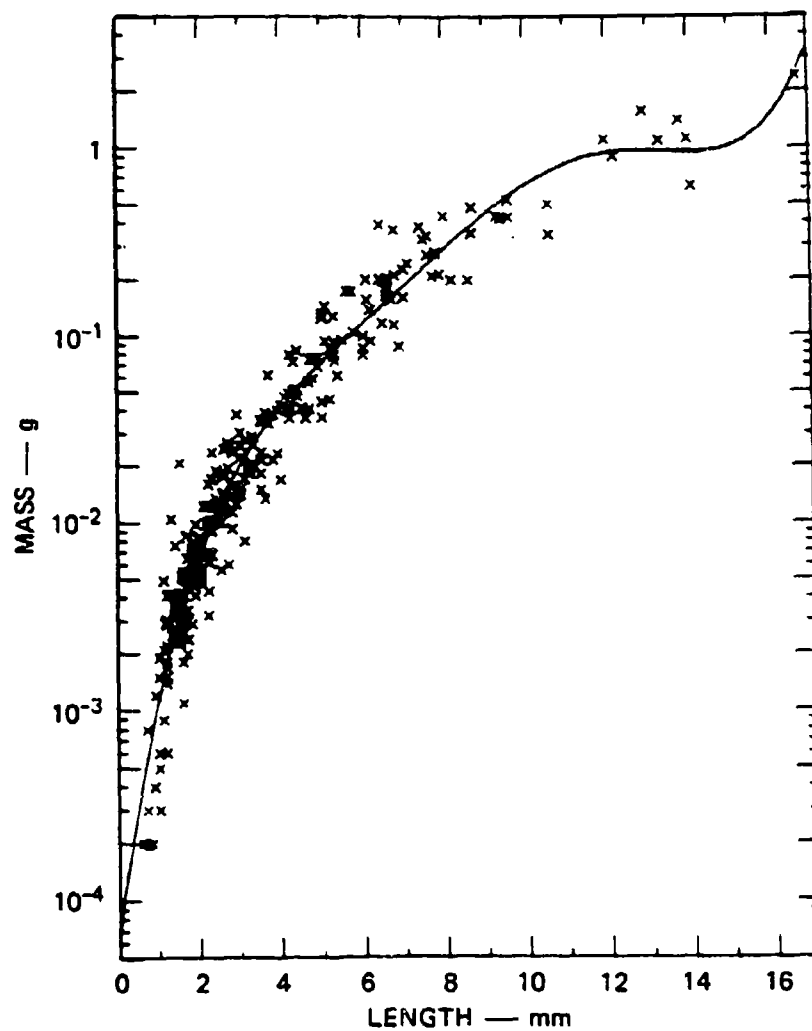


(b)

MP-7893-113

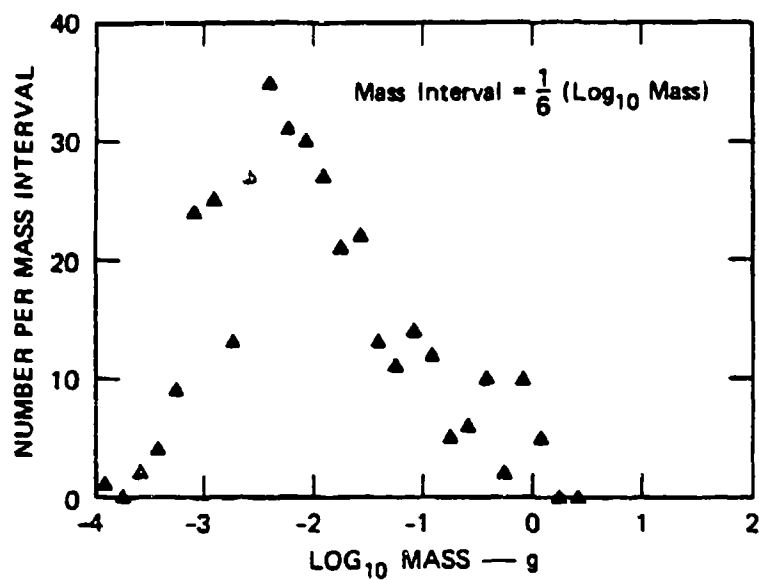
FIGURE 38 OVERALL VIEW (a) OF WITNESS PLATES WITH DETAIL (b) OF HEAVILY IMPACTED REGION WITH FRAGMENT HOLES (Circles) NUMBERED.

Triangles denote impacts that did not perforate aluminum.

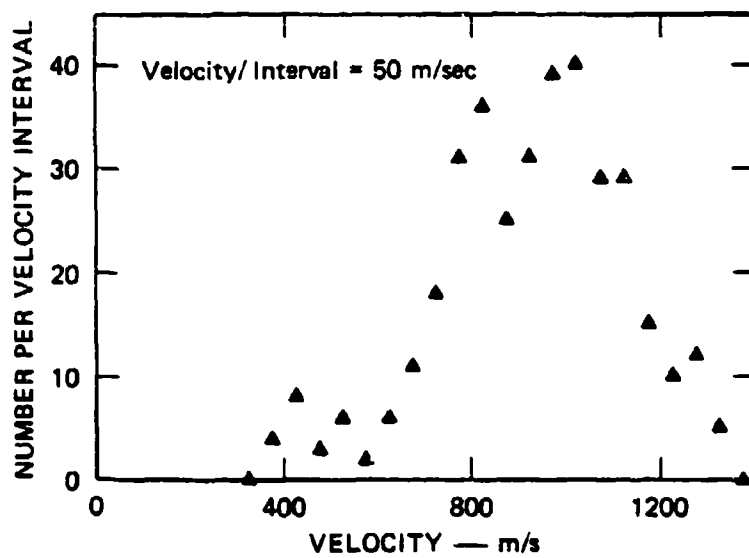


MA-7893-117

FIGURE 39 MEASURED MASS-VERSUS-LENGTH DATA FOR THE RECOVERED FRAGMENTS AND A LEAST-SQUARES FIFTH-ORDER POLYNOMIAL FIT TO THE DATA



(a)



(b)

MA-7893-118

FIGURE 40 PRELIMINARY MASS (a) AND VELOCITY (b) DISTRIBUTIONS CALCULATED FOR QUARTER-SCALE TEST, AS RECEIVED FROM BRL

discussed in Section VII) to compare with computational predictions. Continued analysis of this experiment, including a one-to-one correlation between the larger fragments and their radiographic images, is proceeding.

V SHEAR BAND MODEL DEVELOPMENT

The shear band model has been developed to represent the primary fracture process of ductile materials under compression and large shear strains. The model represents behavior in penetrator and armor during long-rod impacts and in exploding cylinders. The current model, SHEAR3, is an extension of earlier models developed for fragmenting cylinders.⁶⁻⁹ SHEAR3 is based on a careful study of a series of contained fragmenting cylinders of 4340 steel. The model has now been fitted to these data and appears to fit all aspects of the data fairly well. From this agreement, we have developed a general procedure for fitting the model to data from fragmenting cylinders. Three main topics are covered in this section: results of fitting SHEAR3 to the 4340 data, modification of SHEAR3, and the fitting procedure.

A. Shear Band Parameters for 4340 Steel, $R_c 40$

The 4340 data were obtained from eight contained-fragmenting-cylinder experiments.⁷ Shear band parameters (listed in Table 2) for the SHEAR3 model were obtained to represent these data. The nature of the shear band data and a comparison of the simulated results with these data are described here.

The shear band data were obtained by counting and measuring the shear bands observed on the surfaces of six cylinders after contained-fragmenting-round experiments. (Negligible numbers of bands were observed in the other two cylinders.)

As shown in Figure 21 in Section III, the experimental configuration consists of the test cylinder filled with explosive and surrounded by three cylinders: an acrylic buffer cylinder, a steel confining cylinder, and an outer lead cylinder. The buffer thickness and the density of the explosive were varied to provide a range of strain rates, peak strains and levels of shear banding. The explosive at either end of the cylinder is

Table 2

INPUT DATA FOR SHEAR BANDING IN 4340 STEEL, $R_c 40$

Symbol	Value	Definition
General		
ρ_o	7.85 g/cm ³	Density
K	1.59×10^{12} dyn/cm ²	Bulk modulus
G	8.19×10^{11} dyn/cm ²	Shear modulus
Γ	1.69	Grüneisen ratio
Shear band array		
BFR(M,22)	14.0	Growth coefficient, C
BFR(M,23)	35.0	Nucleation coefficient, A_n
BFR(M,24)	0.01 cm	Nucleation size parameter, R_n
BFR(M,25)	10 per cm ³	Number at first nucleation
BFR(M,26)	0.15	Threshold plastic shear strain
BFR(M,27)	0.07	Shear strain ratio, b
BFR(M,28)	0.04 cm	Maximum nucleation band radius, R_{bn}
BFR(M,29)	0.25	Volume effect coefficient, c
BFR(M,30)	0.577	Tan ϕ , friction coefficient on shear-banded planes
BFR(M,31)	2	Storage indicator. "2" means store all plastic strains
BFR(M,32)	2-	Definition of τ . "2" means $\tau = \text{TAUZ}$ (2)
BFR(M,33)	-	Work-hardening modulus, unused (see yield parameters below)
BFR(M,34)	10	Number of radii in each orientation
Yield strength array		
YS	1.03×10^{10} dyn/cm ² 1.07×10^{10} dyn/cm ² 1.37×10^{10} dyn/cm ²	Yield strength at three points on the nonlinear work-hardening curve
ES	0., 0.03, 1.0	Plastic strains at three points on the nonlinear work-hardening curve.

freer to expand than that in the center so the central portion of the test cylinder experiences a longer duration of loading and higher strains. As a consequence, the greatest damage occurs in the center of the cylinder, there is a reduction of damage with distance from the center, and no damage occurs at the ends where there was no explosive in direct contact.

Following counting of the shear bands, the cumulative numbers were plotted. Then each distribution was fitted to the exponential relation

$$n_g = n_0 \exp(-r/r_1) \quad (1)$$

where n_g is the cumulative number of bands/cm² with a radius greater than r

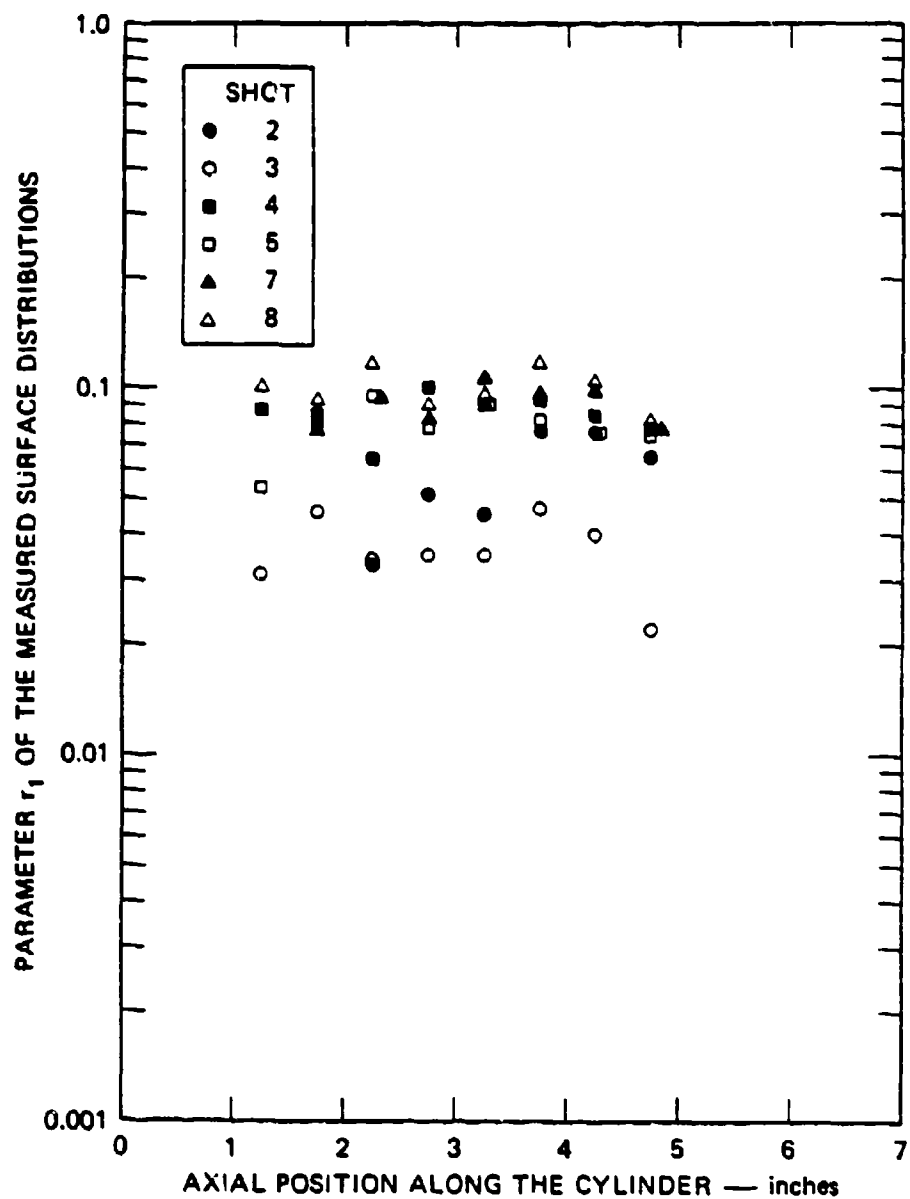
n_0 is the total number of bands/cm²

r_1 is a size parameter for the distribution.

With the distributions reduced to two characterizing parameters, n_0 and r_1 , plots were made to study the initiation, nucleation rate, and growth rate of the bands. These two characterizing parameters are exhibited in Figures 41 and 42 as functions of the axial position along the cylinder. (Detonation began at the left end.)

To match these data with a shear band model, we modified SHEAR3 slightly (as described later) and conducted simulations of the fragmenting cylinder experiments with estimated sets of the shear band parameters. The simulation results were compared with the experimental data, revised values of the parameters were estimated, and the simulations were repeated until reasonably good agreement with the experimental data was obtained. (This multiple simulation process is described later.) Most of these simulations were made for tests 2 and 8, which bracket the range of damage observed. Figures 43 and 44 compare the measured and simulated characterizing parameters n_0 and r_1 , respectively, for tests 2 and 8.

The simulated results tend to be within the range of scatter in the experimental data. Also the simulations show the flat top (on the curves) that is characteristic of the test data. The simulations show some Mode 2 and 3 bands, but there are many more Mode 1 bands; this also agrees with the data.



MA-7893-82

FIGURE 41 VARIATION OF THE DISTRIBUTION PARAMETER r_1 WITH AXIAL POSITION FOR SIX CONTAINED-FRAGMENTING-CYLINDER EXPERIMENTS IN 4340 STEEL AT $R_c = 40$

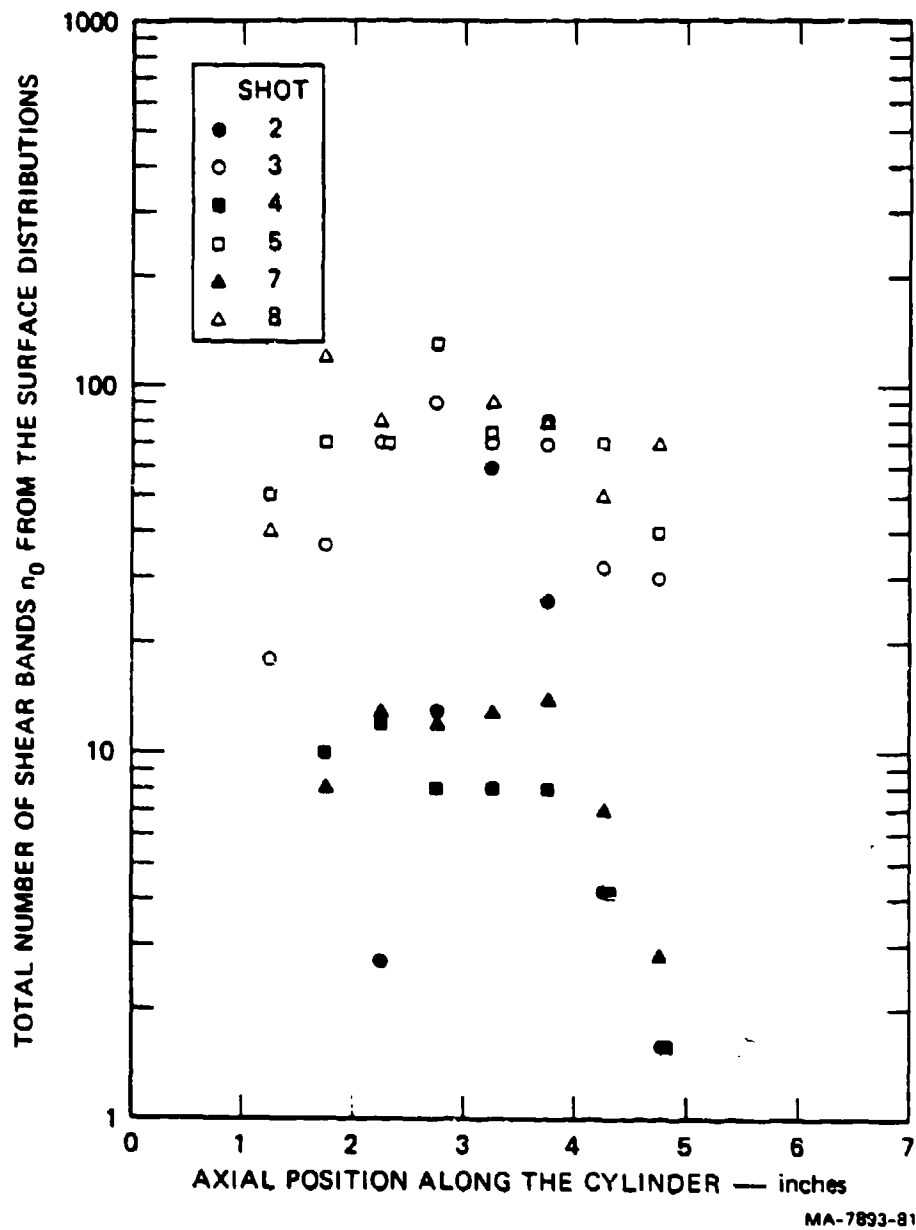
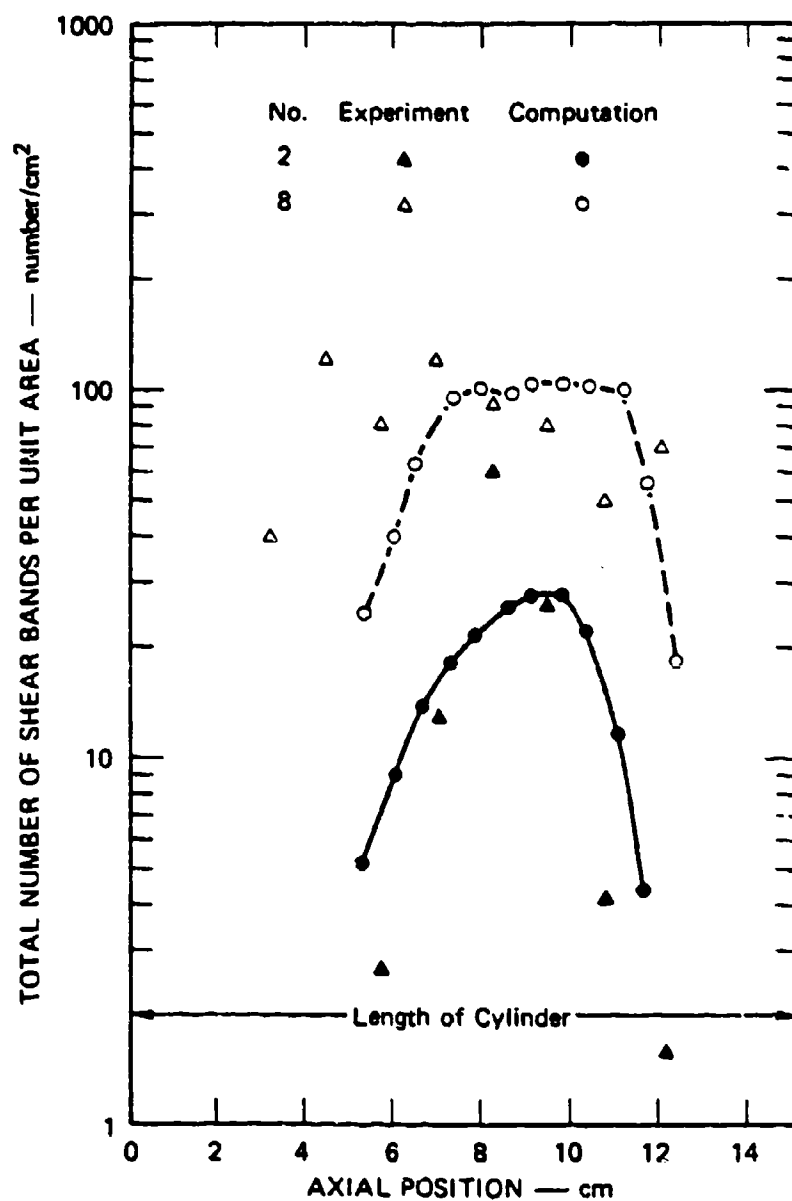
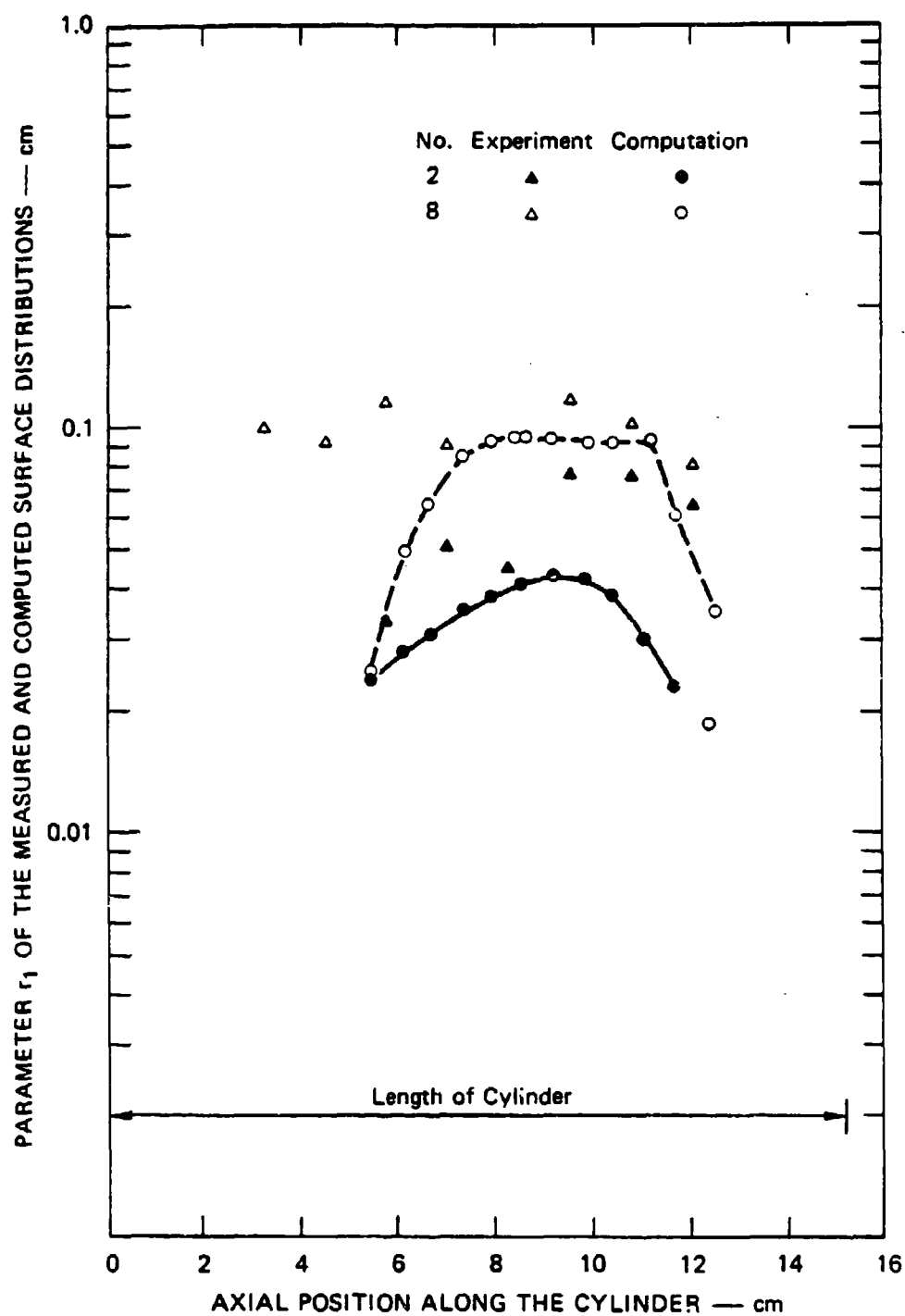


FIGURE 42 VARIATION OF THE NUMBER OF SHEAR BANDS n_0 WITH AXIAL POSITION FOR SIX CONTAINED-FRAGMENTING-CYLINDER EXPERIMENTS IN 4340 STEEL AT $R_c = 40$



MA-7893-95

FIGURE 43 COMPARISON OF THE VARIATION OF THE NUMBER OF SHEAR BANDS n_0 WITH AXIAL POSITION FOR CONTAINED-FRAGMENTING-CYLINDER EXPERIMENTS IN 4340 STEEL



MA-7893-96

FIGURE 44 COMPARISON OF THE VARIATION OF THE SIZE PARAMETER r_1 WITH AXIAL POSITION FOR CONTAINED-FRAGMENTING-CYLINDER EXPERIMENTS IN 4340 STEEL

B. Modification of the Shear Band Model SHEAR3

While fitting the shear band model to the 4340 data, we have been led to modify the nucleation and growth processes and the method for representing the shear band size distribution. Also, for listing purposes, the subroutine now transforms the shear band distribution to a surface distribution and fits the latter distribution to an exponential for ease in comparing with experimental data. A nonlinear work-hardening process has been included in SHEAR3. The interaction of the nucleation and growth processes with stress relaxation and the assignment of shear band damage to planes are both discussed.

1. Nucleation

In the current model, nucleation begins separately on each of the selected planes when the plastic shear strain on that plane exceeds a critical value ϵ_n . During nucleation, bands are initiated in a range of sizes with a distribution given by

$$N_g = \Delta N_{\phi\theta} \exp(-R/R_n) \quad (2)$$

where N_g is the number of bands/cm³ with radii greater than R
 $\Delta N_{\phi\theta}$ is the total number/cm³ nucleated on the $\phi\theta$ plane
 R_n is the nucleation size parameter, an input quantity (cm).

The number nucleated is given by the following relation

$$N_{\phi\theta} = N_{\phi\theta o} \exp(A_n \Delta \epsilon_{\phi\theta}^n) \quad (3)$$

where $N_{\phi\theta}$, $N_{\phi\theta o}$ are the current and previous numbers of bands/cm³
in the $\phi\theta$ orientation
 A_n is a nucleation coefficient
 $\Delta \epsilon_{\phi\theta}^n$ is the plastic shear strain (on the $\phi\theta$ plane)
available for nucleation.

Equation (3), which represents a change from previous versions of the model,¹ appeared to be required to correctly represent the 4340 shear band data described earlier.

Nucleation and growth both absorb plastic shear strain. For the model, it is presumed that growth requires less effort than nucleation; hence when strain is applied, growth is permitted first. If not all the strain is taken in growth, some $(\Delta\epsilon_{\phi\theta}^n)$ is available for nucleation and some new bands will be formed according to Eq. (3). If nucleation does not absorb the available strain, the remainder is taken homogeneously. Because of this interaction of nucleation and growth, and the limit on growth rate, nucleation appears to be strongly rate-dependent and non-linearly related to the amount of plastic strain in the contained fragmenting cylinder calculations, even though Eq. (3) is actually rate-independent.

2. Growth

The growth of shear bands follows the viscous growth law used in all the previous models, plus the restrictions that the growth velocity not exceed the shear velocity and that the strain taken in growth not exceed the total strain imposed. Now an additional constraint has been added: after the damage τ exceeds 1.0, the bands no longer grow. Thus, it is presumed that further straining after full damage ($\tau = 1.0$) is taken by sliding of fragments, and not by growth. (No nucleation or homogeneous plastic strain occurs either.) This change in the growth process leads to the flat tops on the n_0 versus x and r_1 versus x curves in the contained-fragmenting-cylinder simulations (Figures 43 and 44).

3. Representation of the Distribution

Shear band size distributions tend to have the approximately exponential form shown in Figure 30 in Section III, which shows the 4340 steel data from Experiment 2. In various versions of the shear band model, we have represented these distributions either by a single exponential or by a series of points. Neither was very satisfactory, so the problem of representing the distribution was reexamined. The results are a new multiple-size-group method and a single exponential method. For the multiple-size group representation, there is also a provision for transforming to an exponential for displaying the results.

The new multiple-size group version, described in Appendix A, provides for an exponential between points of the distribution. This representation provides high accuracy in defining the shape of the distribution and also in the computation of the damage, τ . (This latter feature is an improvement over the previous use of a multiple-point distribution.)

Because the multiple-point distributions require much more computer storage than the single exponential versions, we made several efforts to condense the distribution to a single exponential. In the most recent attempt, described in Appendix B, the requirements for the distribution are to conserve the damage τ and to represent a midpoint slope of the true distribution. The new condensation procedure is superior to previous ones, but it still tends to underestimate the damage. However, the procedure should be useful in many situations where high fidelity is not required.

To aid in comparing the multiple-point distribution results with experimental data, two new features were added:

- The volume distributions are transformed to surface distributions.
- The surface distributions are fitted to an exponential form.

The volume distributions (number per unit volume) of shear bands are used in all the shear band calculations. However, for printing the damage, a conversion is made to the numbers of bands that would intersect a plane passed through the material. This number per unit area is obtained by a statistical transformation described in Appendix C.

Following the transformation to a surface distribution, this distribution is fitted to an exponential, using the damage τ as a weighting factor. The least squares fit procedure is outlined in Appendix C. The fitted distribution parameters are then readily compared with the experimental data, as in Figures 43 and 44.

4. Work Hardening

A general model for work hardening was incorporated into SHEAR3 for treating homogeneous straining in the intact material around shear

bands. The work-hardening yield strength is taken to be a function of the scalar plastic strain, in the common power-law form

$$Y = A_i (\bar{\epsilon}^p)^{n_i} \quad (4)$$

where Y is the current yield strength

n_i and A_i are constants pertaining to the i^{th} interval of the work-hardening curve

$\bar{\epsilon}^p$ is the plastic strain.

The yield strength versus plastic strain function is inserted as a series of points, and it is presumed that the curve between the points has the form of Eq. (4). The model is described in detail in Appendix D.

This work-hardening model has been inserted into SHEAR3 for shear banding calculations. The yield curve parameters are read into SHEAR3 at initialization with the other special shear banding input data. The yield stress calculation is made in SHEAR3 immediately following the stress-relaxation calculation (which computes $\bar{\epsilon}^p$). Because of this order of calculations, the stress-relaxation algorithm is always using a yield strength appropriate to the beginning of a time increment instead of the end. This lack of correct centering of the yield strength should not cause significant errors, however, because the subroutine subcycles to avoid strain increments exceeding about 0.2% and very little change occurs in the yield strength for such a strain increment.

5. Damage Assignment

When shear band damage occurs, strengths and stresses in several directions are reduced. The current shear band model SHEAR3 contains a complex stress relaxation process (outlined in Appendix A of Ref. 1) for relating the damage to the stress tensor and reducing the strengths and stresses. In this section, we review the procedure for assigning the damage to the stress orientation and clarify the nomenclature somewhat.

The purpose of the damage assignment procedure is to determine the effect of a band or distribution of bands on stresses in any arbitrary orientation. The following requirements for the procedure were developed

for computational purposes and do not necessarily reflect physical requirements:

- The bands remain circular. Hence, shear strain in one direction in the plane causes uniform growth in all directions in the plane, and strength is reduced equally in all directions in the plane.
- Only the size and orientation of the band have an effect on stress, not the growth in the last time increment. Hence, only the residual strength is determined. This method should be satisfactory if the work-hardening modulus is much less than the elastic modulus.
- When damage is assigned to three orthogonal planes, the total damage on all three planes is constant and independent of the orientation of the damage. This assignment criterion tends to make the damage invariant under coordinate rotations.
- Shear strength and stress are reduced for shear bands such that S_{12} , S_{21} , S_{23} , and S_{32} in Figure 45 are reduced.

These four requirements have been met by considering three orthogonal planes, such as the 1-2 plane in Figure 45, one at a time. The damage in each shear band orientation is assigned to each of these three planes using the proposed relation

$$\tau_{ij} = \sum_p \tau_p \sin^2 \psi_{pij} \quad (5)$$

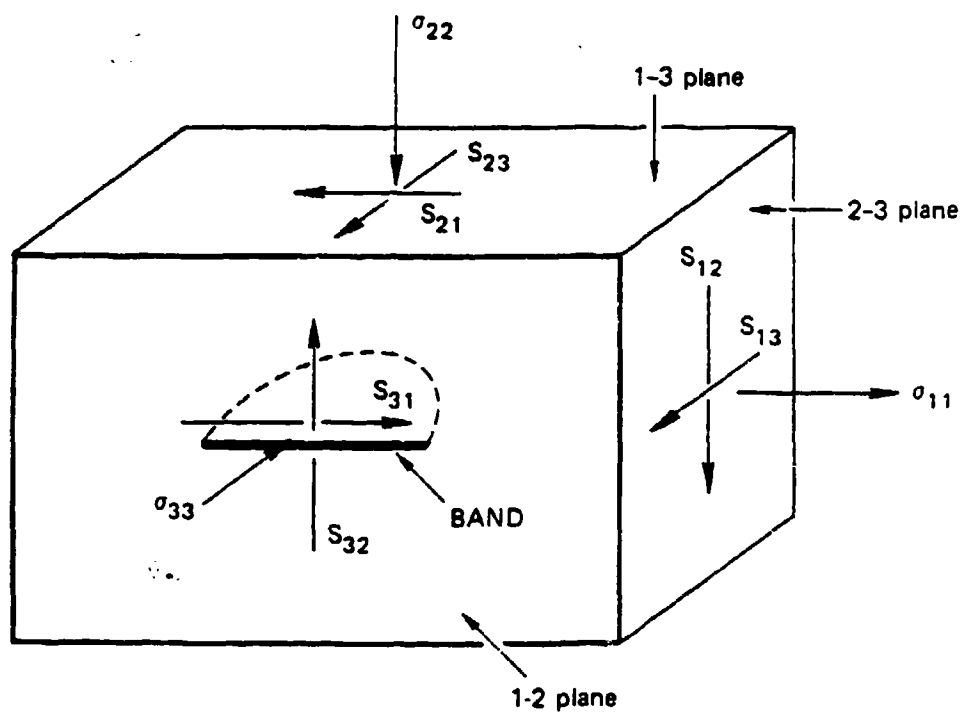
where τ_{ij} is the damage on any plane such as 1-2 in Figure 45

τ_p is the damage in the p^{th} shear band orientation

ψ_{pij} is the angle between the normal to the ij plane and the normal to the shear band orientation.

With these definitions, $\psi = 90^\circ$ for the angle between the band shown and the 1-2 plane (and also for the 2-3 plane). That is, $\tau_{12} = \tau_p$ and $\tau_{23} = \tau_p$. However, for the 1-3 plane, $\psi = 0$, and the band has not effect on the S_{13} stresses.

The sine-squared factor in Eq. (5) is not rigorously derived but proposed by similarity to the more usual cosine-squared relations



MA-7893-97

FIGURE 45 SHEAR (S) AND NORMAL (σ) STRESSES ON A BLOCK CONTAINING A SHEAR BAND

and by its ability to meet the four requirements. With the sine-squared factor, the sum of the damage is

$$\tau_{13} + \tau_{23} + \tau_{12} = 2\tau_p \quad (6)$$

This invariance can be verified by considering an arbitrary vector with cosines l , m , and n to three orthogonal axes. These axes can be the normals to our three planes of interest. Then the sum of the sines squared is

$$\Sigma \sin^2 \psi = (1 - l^2) + (1 - m^2) + (1 - n^2) = 2$$

because $l^2 + m^2 + n^2 = 1$. This invariance can also be verified by examining Table A-3 of Ref. 1 and summing rows of the weighting factor, $\sin^2 \psi$.

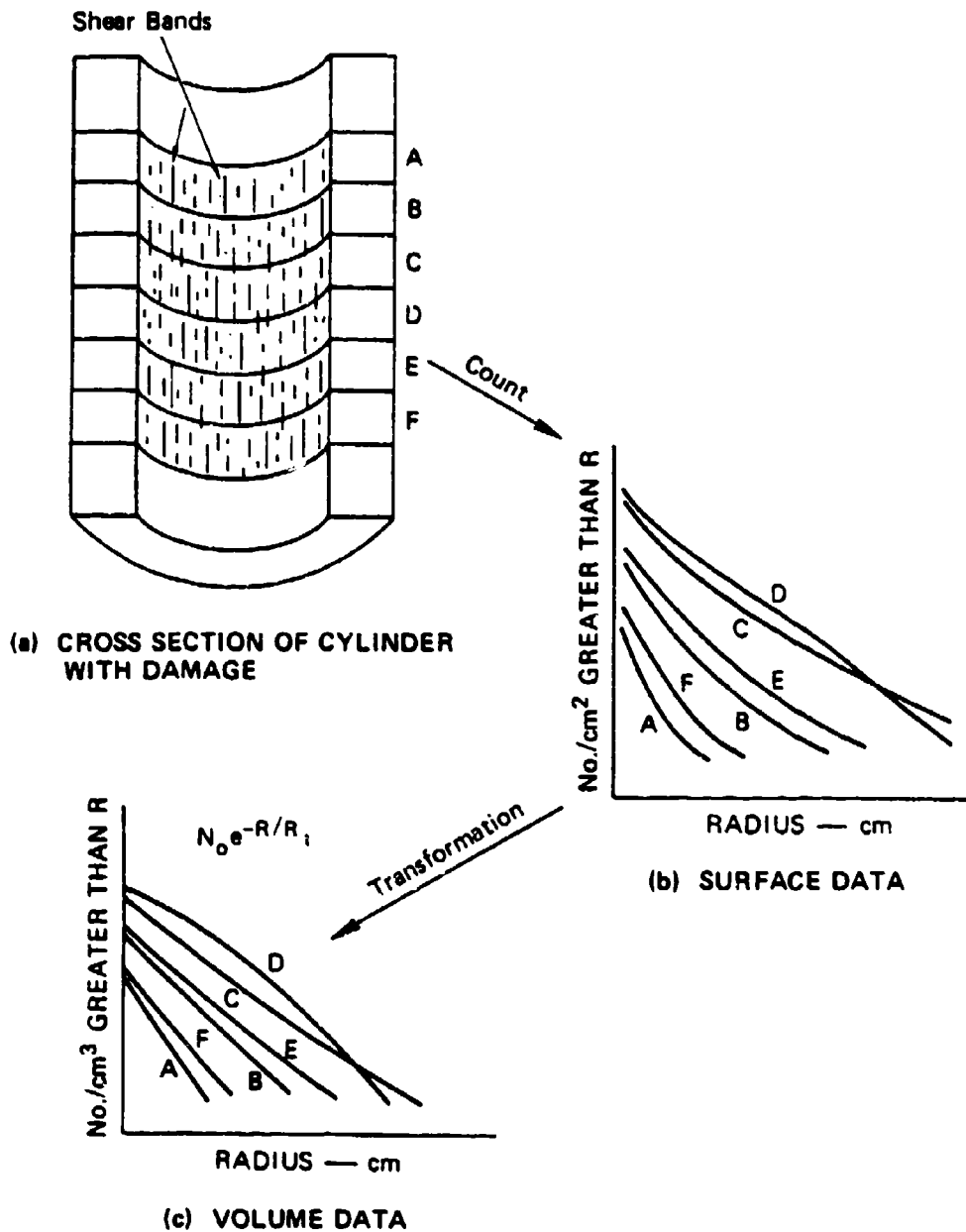
Thus, the damage assignment procedure used in SHEAR3 appears to meet qualitative physical requirements and also an invariance criterion.

C. Procedure for Fitting Shear Band Model to Data

Based on the analysis of the 4340 fragmenting cylinder data, the following tentative procedure has been developed for determining shear band model parameters from the data.

The cylinder data should represent a range of damage levels and strain rates. The cylinders are sectioned, and then shear bands are counted at several positions along the cylinders and assembled to cumulative size distributions as in Figure 46. These surface counts (Figure 46b) are then transformed to volume counts (Figure 46c) using a standard metallurgical transformation process such as that of Scheil^{10,11} or of Seaman et al.¹² or the approximate procedure described in Appendix E. The volume size distributions are each fitted to the exponential function

$$N_g = N_o \exp (-R/R_1) \quad (7)$$



MA-7893-98

FIGURE 46 STEPS IN OBTAINING CUMULATIVE SHEAR BAND DISTRIBUTIONS FROM CONTAINED FRAGMENTING CYLINDER DATA

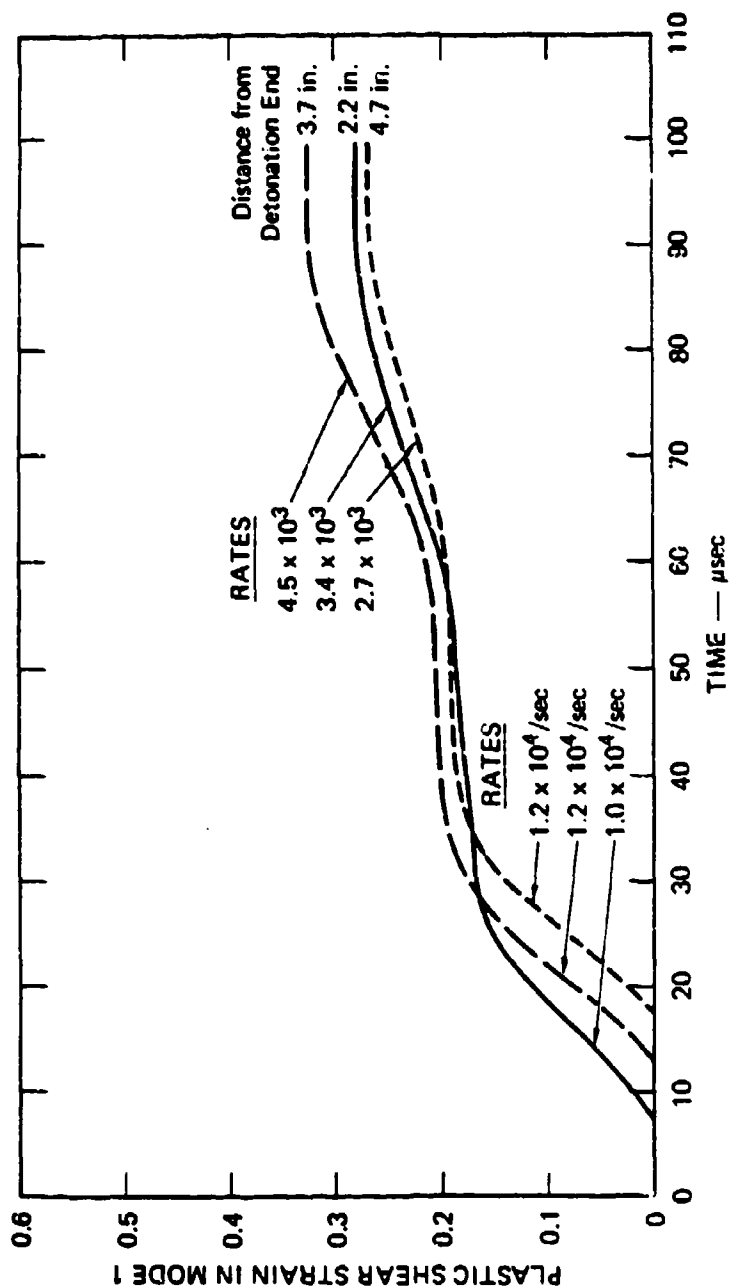
where N_g is the number/cm³ with radii greater than R , and N_0 and R_1 are parameters of the distribution. The N_0 and R_1 parameters are then plotted versus their position along the cylinder. (The plots are like those in Figures 41 and 42 for n_0 and r_1 .)

To obtain estimates of the strains in the cylinder, a computer simulation (without damage) is made of each cylinder test. The final radii and elongation of the simulated cylinder should be compared with the experimental values to verify that the explosion process and material properties are being represented correctly in the simulation. From these simulations, the values of ϵ_k^p , plastic shear strain on the k -th shear band plane, are derived for the locations along the cylinders where the counts were made. Such computer-generated strain histories are shown in Figure 47. Then the experimental parameters N_0 and R_1 are plotted versus the computed shear strains to obtain estimates of the nucleation and growth rate parameters for the shear band model, as shown in Figures 48 and 49.

With these shear band parameters, the cylinder tests are simulated again using SHEAR3 to obtain computed values of N_0 and R_1 as functions of axial location. These computed values of N_0 and R_1 are compared with the measured values at each axial location for each cylinder. This comparison may suggest revisions in the growth or nucleation parameters. If so, the parameters are changed, the simulations are repeated and the results are again compared. Alternatively, the surface distribution parameters n_0 and r_1 may be compared to determine how to modify the nucleation and growth parameters.

The foregoing procedure was used in a more expanded and less direct form for the 4340 data because the nucleation and growth functions as well as the parameters were being changed, and the shear band model was being developed at the same time.

From the nucleation and growth equations, it might appear that there would be no need for repeated simulations of the experiments to obtain the shear band parameters. However, the model is written with an interaction between nucleation, growth, and stress-relaxation that causes some



MA-7893-84

FIGURE 47 COMPUTED PLASTIC SHEAR STRAIN IN THE MODE 1 DIRECTION AT THREE AXIAL POSITIONS IN 4340 STEEL CYLINDER 2

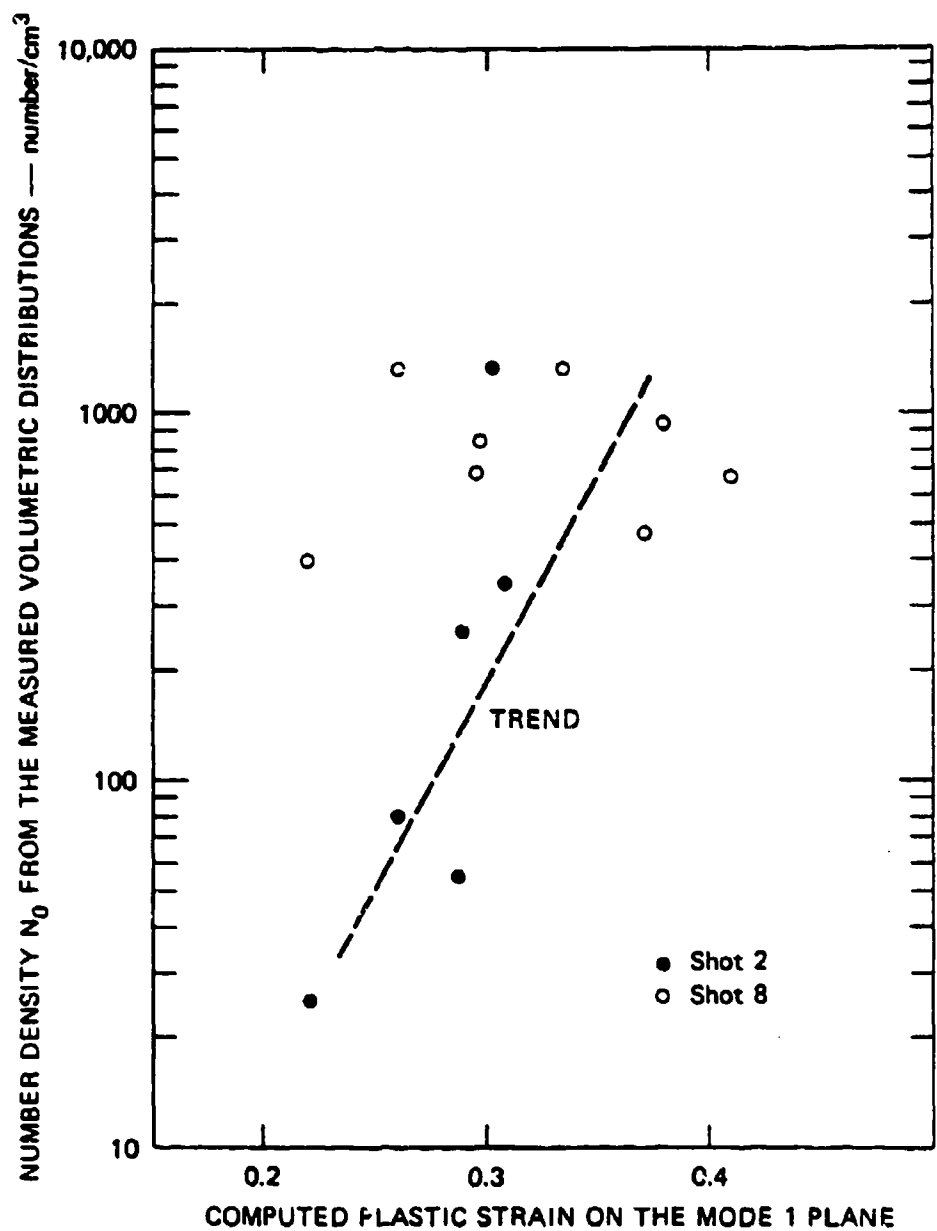


FIGURE 48 MEASURED NUMBER OF SHEAR BANDS VERSUS COMPUTED PLASTIC STRAIN FOR DETERMINING AN INITIAL ESTIMATE OF THE NUCLEATION RATE PARAMETER

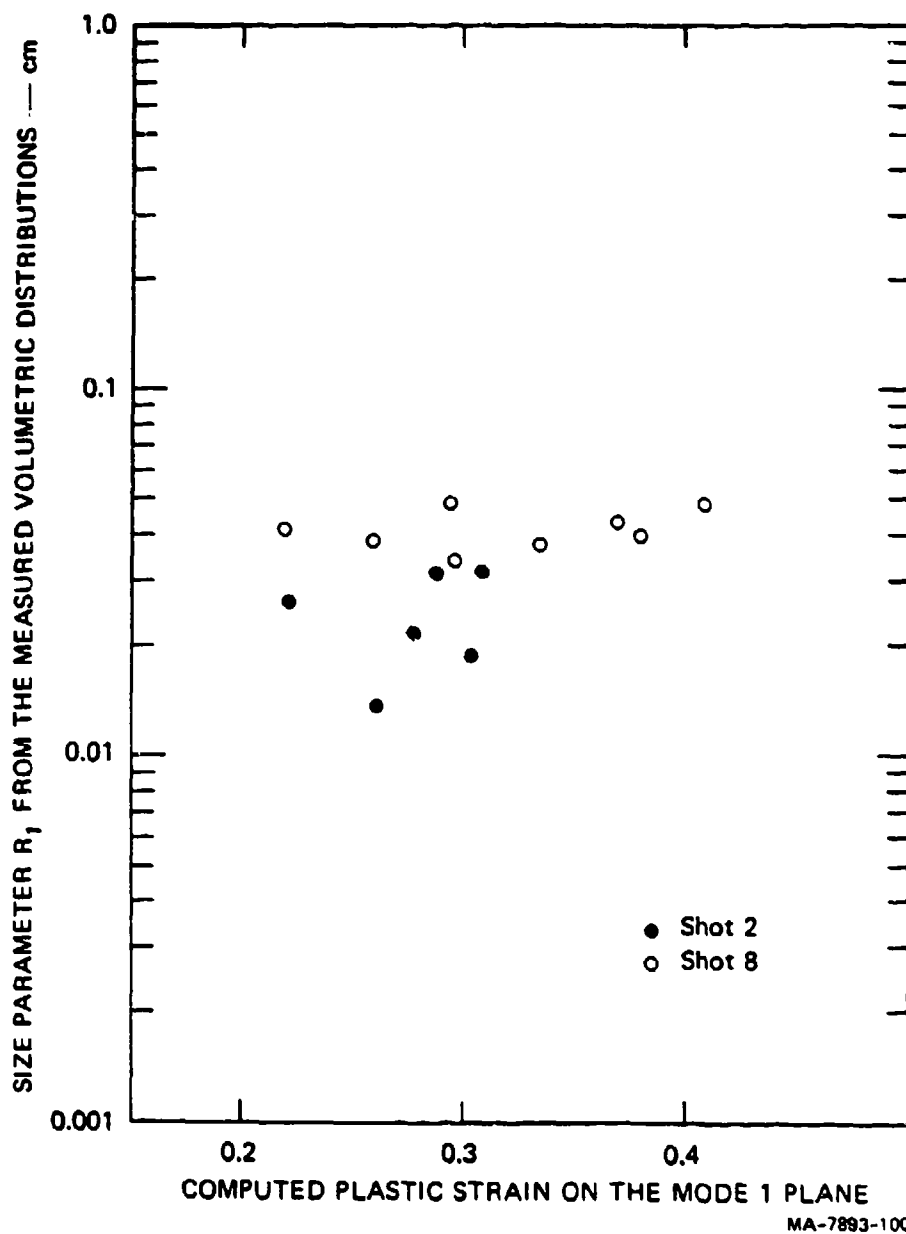


FIGURE 49 MEASURED SIZE PARAMETER FOR SHEAR BANDS VERSUS COMPUTED PLASTIC STRAIN FOR DETERMINING AN INITIAL ESTIMATE OF THE GROWTH RATE PARAMETER

nonlinearity. As mentioned in the previous section under nucleation, the plastic strain is first taken in growth. The remaining strain causes nucleation of new bands. If some strain has not been absorbed in growth and nucleation, that remainder is taken homogeneously. The developing damage causes stress relaxation that may alter adjacent damage growth. Therefore, multiple simulations of the experiments are required to obtain a reasonable match to the experimental shear band data.

D. Plans for the Shear Band Model Refinement

The observations of damage in the long-rod penetration into RHA reported in Section II and our experience in the simulations reported below in Section VII have led us to examine some areas of the shear band model that should be modified. RHA shows significant anisotropy in the production of shear bands: bands form much more readily in the plane normal to the short transverse direction than in the other planes. Also we notice that the coalescence and fragmentation processes have not been treated in sufficient detail. Here we describe these problem areas further and outline approaches toward their solution.

1. Anisotropy

The anisotropy of RHA probably plays an important role in the penetration process. Shear bands appear to form normal to the short transverse direction (in the plane of the plate) at about 20% plastic strain, but do not appear in the plugging direction until about 60% plastic strain occurs. The type of anisotropy observed might be termed *orthotropy* because only one plane differs from all others. This anisotropy affects the production of bands, but does not directly affect the elasticity relations or the yielding process in RHA. The introduction of this anisotropy into SHEAR3 will require several changes:

- Addition of damage orientations to account separately for bands in the weak plane and normal to it (these two sets of bands are treated as one set now).
- Provision for different nucleation and growth processes for each band orientation.

- A revision of the band rotation process to account for the fact that the angular inclination between bands initially is 90° , but gradually approaches smaller values during large deformation.
- A complete change of the yield and stress relaxation calculations.

The first three changes are considered minor because they add only a special treatment of one shear band orientation. The changes in the stress calculation, however, are major. We envision a complete change of the stress computation portion of the subroutine. Instead of determining the principal stress directions and using these for the yield calculations, we will use a stress orientation that has one axis lying in the weak plane. The yield calculations will be performed using three Mohr stress diagrams: one lying in the weak plane and two in planes orthogonal to that plane and to each other. These Mohr diagrams will not necessarily contain the principal stresses and therefore provide only an approximation to the yield process. To improve the accuracy of yielding calculation, we will add one or more intermediate planes and construct Mohr diagrams on these planes also. Initial tests of this approximation technique indicate that, with four Mohr planes, the stresses will be accurate within 5% of the yield strength in the worst case.

We expect the anisotropic treatment of yielding to require a somewhat smaller amount of code than the previous treatment, but one additional orientation of shear bands. Hence the next version of SHEAR3 will not be significantly larger or harder to use.

2. Coalescence and Fragmentation

The coalescence and fragmentation processes in SHEAR3 will require some additional effort to complete them in a physically realistic manner. Currently, the subroutine ends with a size distribution of shear bands. What is needed is either an added section in SHEAR3 or a post-processor (a program such as MOTT, which is run after the penetration calculation) to monitor the intersection of bands to form fragments and to produce a fragment size distribution. The first step is to borrow features from the MOTT program; however, further effort should be directed toward understanding and quantifying the intersection process leading to fragmentation.

VI SYNTHESIS OF A COMPOSITE CODE FOR PENETRATOR SIMULATIONS

To predict penetration and back-surface fragmentation in a penetrator-target encounter, it is necessary to have a computational procedure for simulating the materials and geometry of a penetration event in considerable detail. From phenomenological studies of penetrators and targets (Section II) and from preliminary simulations of projectile penetrations (to be discussed in Section VII) we have generated a set of requirements for a computational procedure. Here we list these requirements and review the capabilities of the available codes that have been used. A choice is made of a basic code (HEMP) plus elements from other codes to enhance its capabilities. Some current results with the Composite HEMP are shown to indicate the state of development.

A. Requirements

The basic problem considered is the penetration of a long-rod missile into one or a series of armor plates. The target may be defeated by formation of a plug, excessive plastic flow allowing perforation, rear-surface spall, or a combination of these effects. The rod may be defeated by excessive plastic flow, shear banding and fracture near the tip, or by fracture along its length. The initial problem we are considering is two-dimensional: either a normal impact of an axisymmetric missile onto a plate or an oblique impact of a slab onto a slab. Later, the possibility of simulating oblique impacts of symmetric missiles (a three-dimensional problem) should be investigated.

Our attempts and those of others to simulate the penetration encounter have led us to outline several basic requirements for a computer program for the simulation:

- Slide lines
- Rezoning
- Material model for fracture damage.

The slide lines permit materials to slip past each other or to impact and separate. The penetrator nose and sides must be able to slide along the upper surface of the target and on the sides of the crater as it forms. In addition, the target may be severed to form a plug: the interface between the plug and the remainder of the target requires a slide line if the relative motion is significant. The length and direction of the severing line is determined during the penetration, so the slide lines must be able to unzip gradually and to wander through the finite difference or finite element grid. The large distortions experienced by both penetrator and target during a simulation indicate a capability to rezone or reconfigure the computational grid at intervals during the calculation.

The material property model is essential for determining the ballistic limit and for predicting the fragment spray at the end of the event. Because such a model requires many variables, the penetration code must be configured to permit large data arrays for cells in which the material is undergoing damage.

Besides these basic requirements, there are a number of nominal requirements that make a computer program readily usable:

- Input in a free-field format, like the AMMRC version of HEMP
- Finite element numbering, as in EPIC
- Usable on available computers
- Documentation.

The convenience of a simple input form is important because it may greatly reduce the time required to lay out a new problem and it makes the problem definition more apparent to other users.

The finite element numbering method allows the cells to be configured in a more general way than in rows and columns. This numbering is convenient for discretizing nonrectangular or multiply connected bodies. It seems essential for providing slide lines that extend in both x and y directions, as along the nose of a projectile and then along the side. The computational logic of a self-directed slide line seems more straightforward with finite element numbering because new nodes can be readily added and the relationships between these nodes and the cells can be easily updated.

The code must be in a standard form that can be used on CDC, CRAY, Univac, Digital (VAX), and other computers. This transportability means that the code must be in standard FORTRAN (without the special and different advantages of each computer vendor), use a fairly small memory, and not depend on availability of special peripheral devices.

The code must be well documented. Documentation includes a manual with derivations and sample input and a code with ample comment statements and equations written with the same variables as the manual.

B. Review of Available Codes

A review was made of many codes that have been used for penetration calculations. The review was limited to general-purpose wave propagation codes written for large-deformation problems in solids treated by complex material models. Here only some of the special advantages or features of these codes are described.

The Eulerian codes HELP and HULL are able to treat large distortion problems, although this advantage leads to difficulties in treating sharply defined boundaries and slide lines. Also there tends to be smearing of cell properties such as the fracture quantities.

The Lagrangian finite element code EPIC has both two- and three-dimensional versions and thus is particularly suited to oblique impacts. The triangular cells resist large distortions, but falsify the stresses computed from pressure-sensitive stress-strain relations. A simple, frictionless slide-line treatment is available in the code.

STEALTH is also Lagrangian and has two- and three-dimensional versions. It features automatic rezoning and slide-line capabilities.

The Lagrangian code TOODY has been used in many penetration calculations. It has a discrete rezoner: wave propagation calculations are halted, the entire mesh is reconfigured, and then the calculation continues. The slide line treatment is particularly accurate. The cells on each side of the slide line are accounted for in detail so that, if no slip occurs, the presence of the line should be undetected. Stick or frictionless conditions and Coulomb friction properties are provided on the slide line.

The slide line is tied to the usual row-and-column scheme. The number of variables per cell can be readily increased, but all cells are assigned the same number of variables.

WAVEL is a Lagrangian code with advanced slide line and continuous or automatic rezoning. It has been developed for penetration problems and extended to a quasi-three-dimensional form for oblique impacts.

HEMP is the forerunner of many two-and three-dimensional, finite-difference Lagrangian codes used in penetration calculations. It has a discrete rezoner, as TOODY has, and a slide line capability that is tied to the row-and-column cell numbering. A recent version is HEMPDS, which has a double slide line (intersecting slide line) capability, but no rezoner. The double slide provision required a major restructuring of HEMP, so it is not a minor addition nor an element that can be readily transferred to another code. The HEMP code has many versions, each with different capabilities. The version available at AMMRC has an input provision termed a NAMELIST READ statement. This provision permits all numerical quantities to be identified by name and all data to occur in a free-field format (no fixed positions on a line). This greatly simplified input provision speeds the laying out of new problems and minimizes errors.

DYNA2D is a large finite-element code that has been used for simulating self-forging fragments and penetrations. It has a capability for a slide line that can extend both horizontally and vertically at the same time. Elements of higher order than the constant strain elements in HEMP are available for use on elastic or other small-distortion problems.

The small two-dimensional Lagrangian code TROTT, which we have used in many of our applications, has the advantage of simplicity in adding new material models with large numbers of variables. The new model is added by the insertion of one or two call statements. Extra variables for the cells treated by special material models are available, and the number of extra variables is designated in the input. The number of variables per cell varies from cell to cell so that relatively inactive cells can have a minimum number of variables, while cells in the region of fracturing, for example, can have 50 or 100 extra variables. TROTT also has automatic rezoning, like that in WAVEL and STEALTH. A simple frictionless slide line treatment is available.

The review of available codes indicated to us that there are many good candidates. Although no one code has all the desired features, all the desired features are available. Therefore, a synthesis from existing codes seemed desirable.

C. Synthesis and Testing of a Code

The HEMP code was chosen as the basic code to work with. Onto this has been added finite-element numbering, automatic rezoning, a TOODY-like slide provision, free-field input, and provision of large numbers of variables for cells requiring them. These features are outlined in this section.

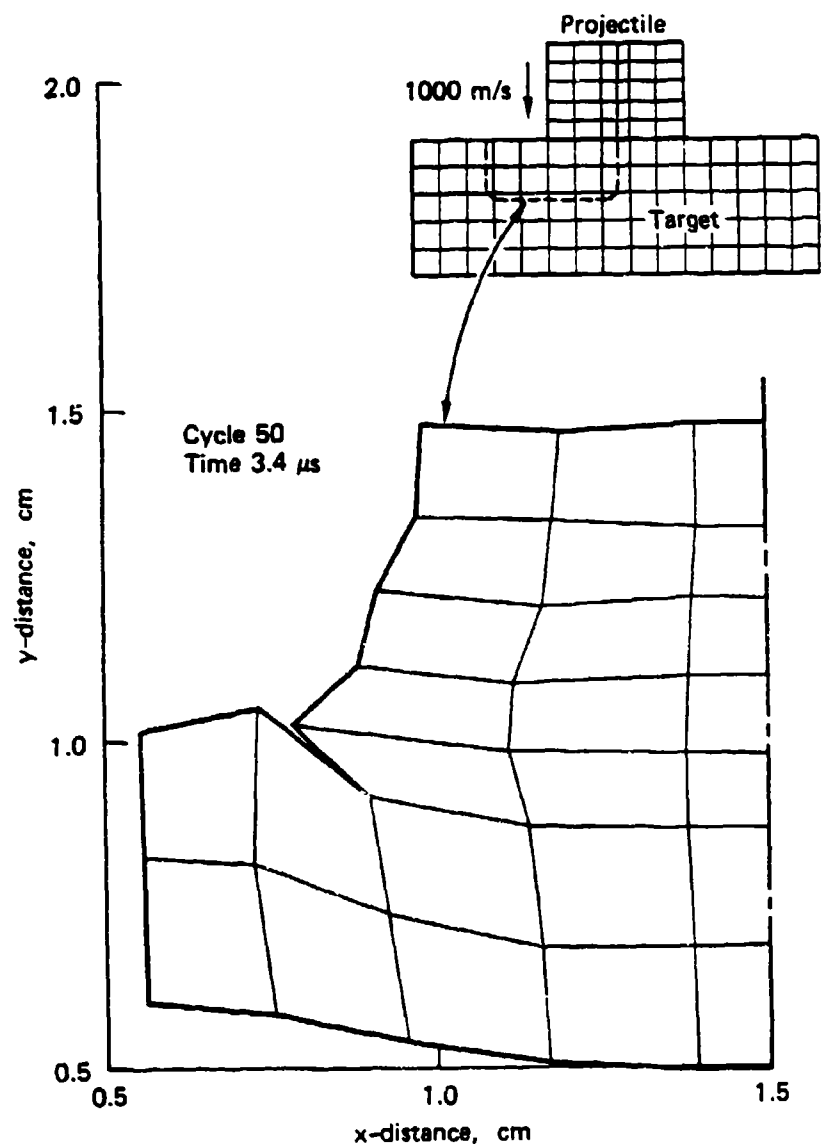
The status of each portion of the code is noted in Table 3, with the source of the portion. The subroutine containing that portion of the code is listed in parentheses. The remaining portions to be debugged are the slide and rezoning parts. The rezoner is a translation of the TROTT subroutine REZONT, which has been tested on impact problems. The slide line treatment is based largely on the HEMP logic, but with the use of some concepts from TOODY and from STEALTH.

Three test cases have been used in debugging composite HEMP. Test problem 1 was a one-dimensional impact of a steel projectile onto a steel target at 1000 m/s. The impact stress achieved was about 225 kbar, attended by the usual oscillations. These results were compared with analytic values to verify the accuracy. For test problem 2, a two-dimensional planar impact was simulated. A detail of the mesh distortion near the plane of impact is shown in Figure 50. The results were examined for correct stress levels under the impactor (like the one-dimensional case) and physically reasonable motions elsewhere. Test problem 3 represents a blunt-nosed projectile fired into a rigid circular trough as shown in Figure 51. This problem was constructed to test the boundary conditions and the time step control under severe cell distortion. A corresponding TROTT calculation showed very similar results.

Test problem 3 is being used now to test rezoning. Comparable rezoning runs have also been made with TROTT, so we have an indication of the results to expect.

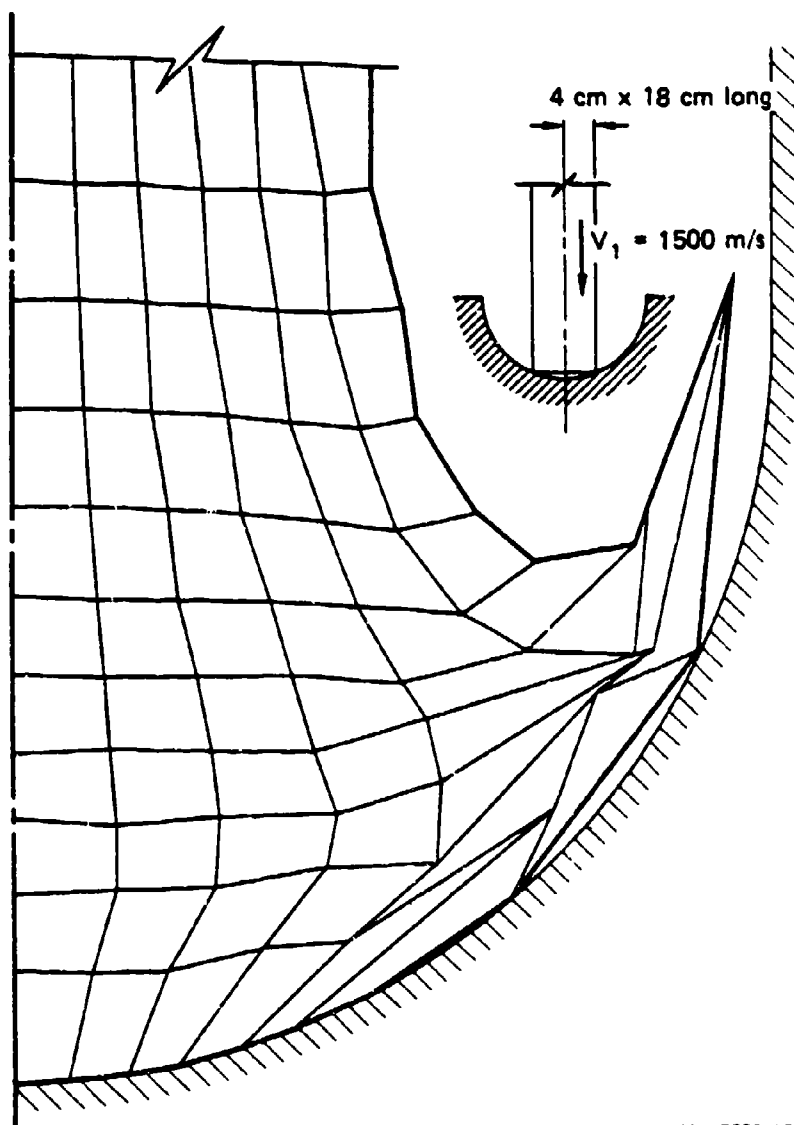
Table 3
STATUS OF COMPOSITE HEMP

<u>Portion of Code</u>	<u>Purpose</u>	<u>Source</u>	<u>Status</u>
Input (in GENR)	Read the input data	HEMP (BRL and AMMRC versions)	In use
Setup (in GENR)	Lay out and initialize arrays	HEMP, with finite element logic	In use
CYCLE	Wave propagation calculations	HEMP	In use
VQP	Call stress-strain models	HEMP, TROTT	In use
Material Models (VQP)	Compute stresses at each cycle	TROTT	All models used in TROTT are in, but not tested
Slide (CYCLE)	Permit slide lines	TOODY, HEMP	Written, not tested
Double slide	Intersecting slide lines	HEMPDS	Planning
Rezone (REZONH)	Modify mesh to minimize cell distortion	TROTT, STEALTH	Written, in debugging
Grid listing (CYCLE)	List status of all cell and node quantities	HEMP	In use
Histories (EDIT)	List histories of all cell and node variables	HEMP, TROTT	Written and tested for some variables



MA-7893-136

FIGURE 50 CONFIGURATION AND DETAIL OF RESULTS FOR TEST PROBLEM 2 USING COMPOSITE HEMP



MA-7893-137

FIGURE 51 CONFIGURATION FOR TEST PROBLEM 3 AND COMPUTED RESULTS
AT $37 \mu\text{s}$ (300 cycles), USING COMPOSITE HEMP

Following the rezoning test, we plan a slide line test with a geometry like that in test problem 2, but the projectile block will have a tangential velocity component. The next test will be a normal impact near the ballistic limit and with the material represented by the shear band model. This fifth test will initially include only a slide line between the projectile and target, but will later include rezoning.

Five special features of the composite HEMP (input, finite-element numbering, time step control, rezoning, and slide lines) are described in greater detail in Appendix F.

VII SIMULATIONS OF PROJECTILE PENETRATIONS

Preliminary projectile penetration calculations using the shear band model were made with the TROT two-dimensional wave propagation computer program, an SRI program that is similar to HEMP. These computations were conducted to study the feasibility of performing such calculations with a wave-propagation code, locate computational problem areas, and aid in planning an augmented code with the capability to readily handle the simulations. In addition we wished to assess the possibility of predicting the observed fracture and fragmentation using a shear band or other fracture model.

Two penetration calculations were made with blunt-nosed cylindrical projectiles of 4340 steel impacting normally onto rolled homogeneous armor (RHA) targets. The penetrators were 10.16 cm long and 1.016 cm in diameter and the targets were 2.54 cm thick. In both cases the 4340 was simulated with shear band parameters obtained from our fit to the fragmenting round data, as described in Section V. The RHA was also simulated with the shear band model using a set of parameters derived mainly from the 4340 set, but with some modifications to fit obvious characteristics of the RHA. The strain threshold was raised from 15% for 4340 to 20% for RHA to represent the initiation of shear banding on the weakest plane (normal to the short transverse direction). The initial yield strength for 4340 was 1.03 GPa and for RHA it was 0.55 GPa. Work-hardening functions derived from quasi-static tensile data were provided for each steel.

The penetration calculation without a slide line was stopped at 17 μ s because excessive cell distortion had led to infinitesimally small time steps in the calculational cycle. The final configuration of the target and projectile is shown in Figure 52. The figure also contains contours of equivalent plastic strain $\bar{\epsilon}^P$. Although the shear band development on a particular plane is a function of individual tensor components of strain,

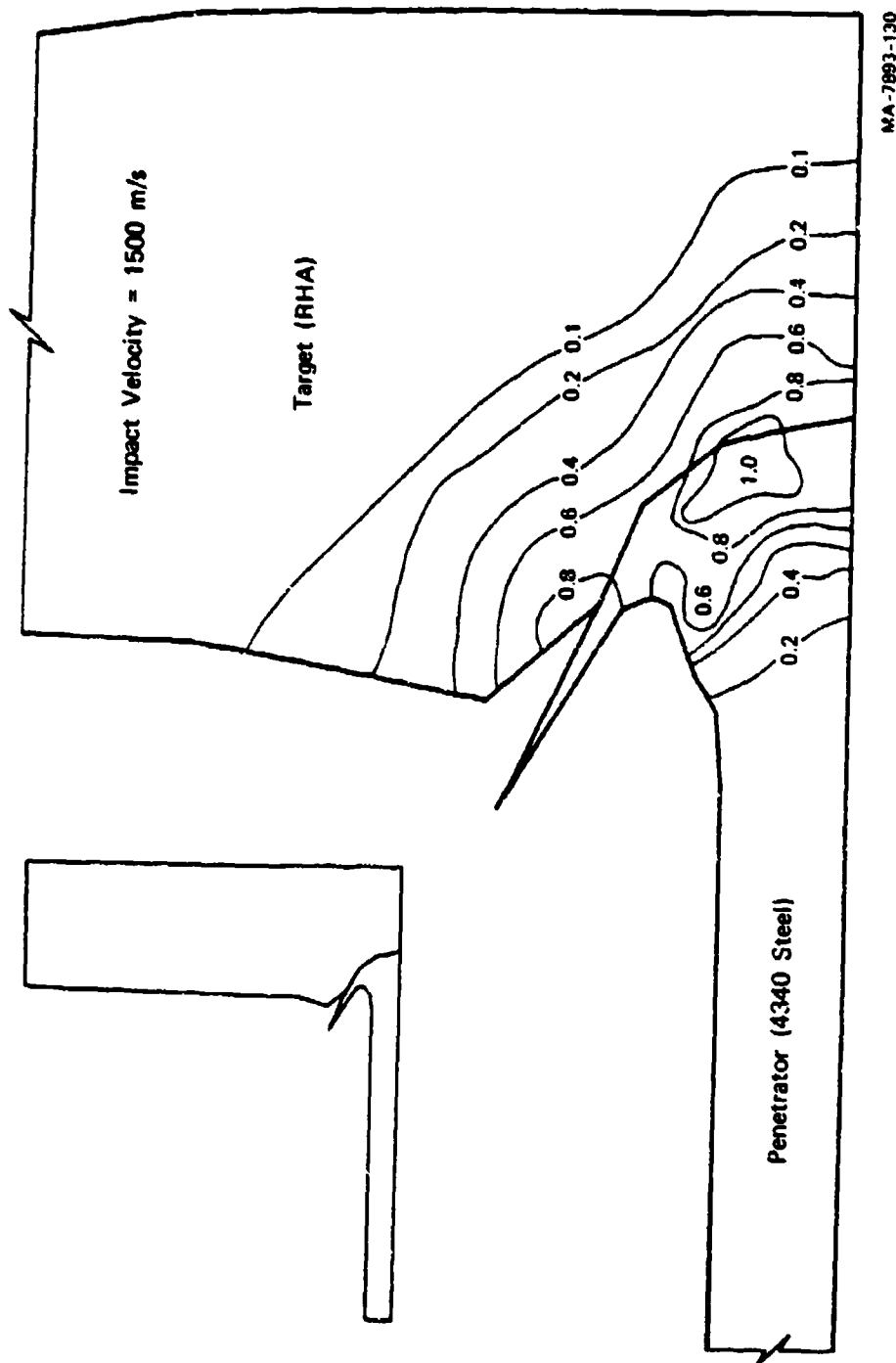
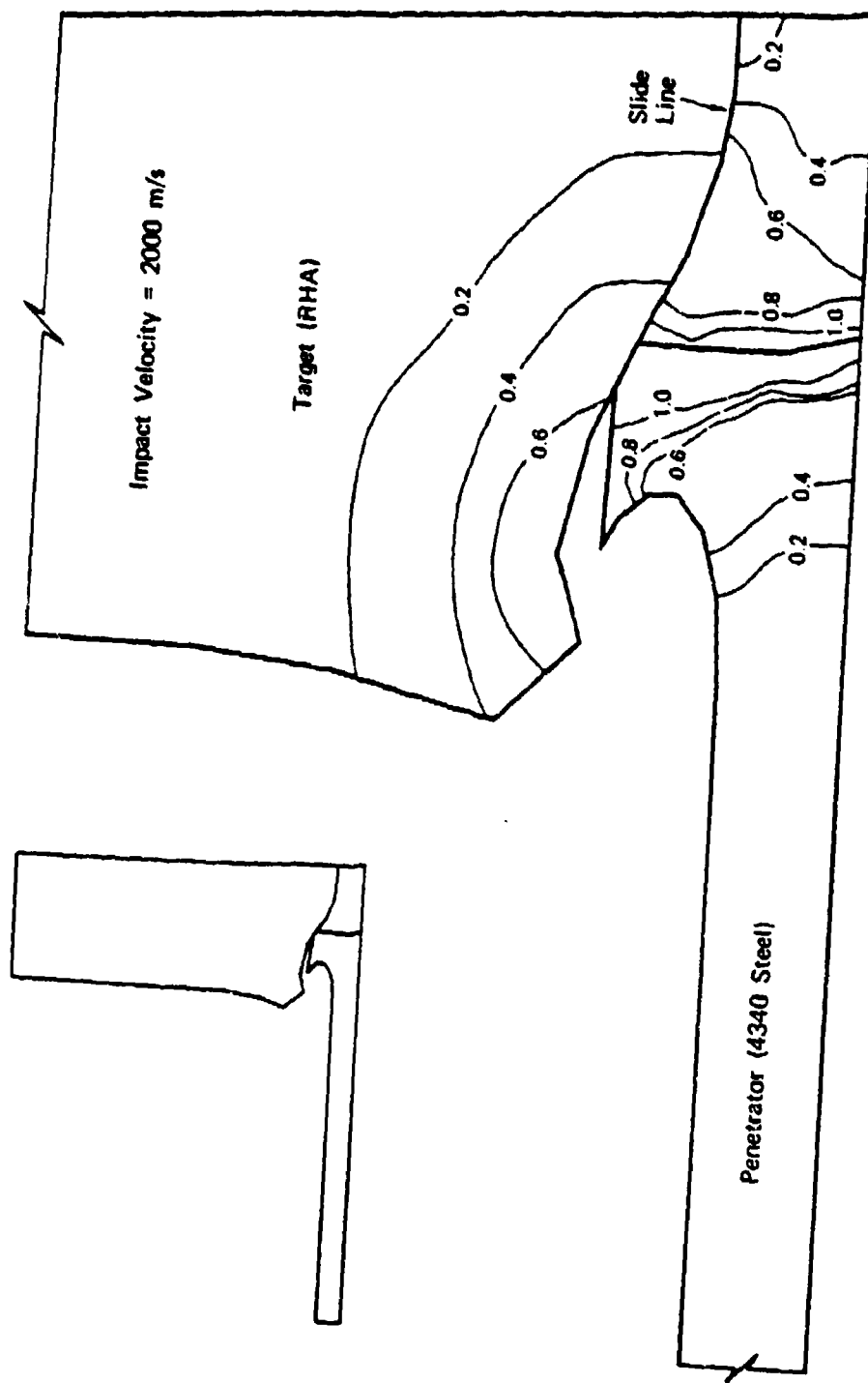


FIGURE 52 CONFIGURATION OF TARGET AND PENETRATOR AT 17 μ s IN TROTT SIMULATION WITH NO SLIDE LINE. INCLUDING CONTOURS OF EQUIVALENT PLASTIC STRAIN

the equivalent plastic strain is a good measure of the general level of shear band damage. In the penetrator there is a concentration of plastic strain near the impact plane and essentially no distortion in the rest of the rod. The target shows large amounts of plastic strain at the edge of the crater and just beneath the penetrator. In the target under the penetrator, there is little radial variation of strain until a radius equal to that of the penetrator is reached; then the contours change direction. From this calculation, we can note that the front 35% of the penetrator and considerable material in the target around the crater would be fragmented. Because the projectile still has considerable forward momentum, the final state of penetrator and target cannot yet be estimated from the calculation.

In the second penetrator calculation, a slide line was provided within the target at a radius equal to that of the penetrator. As the shear band criterion for initiation was reached in adjacent cells, the predetermined slide line was activated and sliding was permitted. In this calculation, it was necessary to increase the penetrator velocity to 2000 m/s to avoid the impact of the sides of the penetrator onto the upper surface of the target. Figures 53 and 54 show the configurations of penetrator and target at 17 μ s (to compare with Figure 52) and at 23 μ s, respectively. The calculation was halted at 23 μ s because of cell distortion. At this time the slide line had propagated from the impact point to the last node at the back of the target.

The geometry and strain levels in Figures 52 and 53 can be compared directly because the conditions and time differ only by the presence of the slide line in the second calculation. The amount of penetrator damaged in the two cases and the level of damage are nearly identical. However, with the slide line, the penetrator has gone nearly twice as deep and retained a nearly flat front. In contrast the penetrator in Figure 52 is heavily distorted and the front is very curved. For the calculation with a slide line, the target crater is much larger in radius as well as in depth. Also there is a discontinuity in strain contours along the slide line. The strain contours in the target in Figure 53 also differ from those in Figure 52 because of the greater depth of the penetrator.



MA-7893-131

FIGURE 53 CONFIGURATION OF TARGET AND PENETRATOR AT 17 μ s IN TROTT SIMULATION WITH UNZIPPING SLIDE LINE, INCLUDING CONTOURS OF EQUIVALENT PLASTIC STRAIN

At 23 μ s (Figure 54), the penetrator is 0.3 cm deeper into the target than it was at 17 μ s. The plastic strain contours have extended deeper into the target, but are essentially unchanged in the penetrator.

The major problems that arose during the calculations were

- Cell distortion, which led to very small time steps and hence effectively halted the calculation.
- Lack of an appropriate criterion for propagation of the slide line.
- No provision for contact between the target and the sides of the penetrator.

The problem of cell distortion can probably be treated by a discrete or continuous (automatic) rezoner, which will reconfigure the cells to keep them approximately square. The slide line propagation problem became apparent because there was not a strong concentration of plastic strain or shear band damage along the path the slide line was expected to take. This problem may be diminished by using smaller cells so that steeper strain gradients can be maintained. Resolution of this problem will probably require careful study of both the slide line process and the shear banding, as well as the coupling between the two.

The third problem was the tendency for the free surface of the target to rise and eventually coincide with the bulging sides of the penetrator. Hence there is a need for a slide line between the front and sides of the penetrator and the top of the target. In our two calculations, the penetrator had a flat front and so the computation began with contact between penetrator and target. No separation or sliding between the two was permitted. In the penetration calculation with a slide line in the target, the impact velocity was artificially raised to avoid impact of the projectile sides onto the target.

Thus, a complete calculation appears to require a rezoner, a slide line between the sides and front of the penetrator and the top of the target, and a propagating slide line in the target. All these features are available in some wave propagation codes, although not in the same code, so the performance of a full penetration calculation seems feasible.

To get an indication of the fragment size distribution that would be computed if the penetrator completely perforated the target, we examined the state of shear banding at 23 μ s. The MOTT program described elsewhere⁹ was used for the transformation from shear bands to fragments. For this calculation, the damage, τ_f , is described by

$$\tau_f = \beta \gamma^3 T_f \sum_m \sum_n N_{mn} R_{mn}^3 ,$$

where β is the ratio of number of fragments to number of bands, γ is the ratio of fragment radius to band radius, T_f is a constant factor related to fragment aspect ratio, N is the number of shear bands/cm³, and R is the radius of a shear band. The subscripts m and n refer to the orientations and the sizes, respectively in a shear band distribution. When the material is fully fragmented, $\tau_f = 1.0$. For partial fragmentation ($\tau_f < 1.0$), we use τ_f as the fraction of cell mass that is fragmented. When these rules were used in the MOTT program, total masses of fragments and size distributions of fragments were obtained separately for the penetrator and target.

The computed mass fraction of the penetrator that was completely fragmented at the time shown in Figure 54 is 31%, in fair agreement with the value of 40% obtained by measuring the mass of the recovered unfragmented distal portion. Furthermore, the computed mass lost from the target in the form of the plug and collaterally fragmented material is 35 grams, in good agreement with the 34 grams obtained by weighing the armor plate before and after the experiment.

Comparison of these computations with experimental observations (transformed from Figure 40(a) of Section IV) in Figure 55 shows that we compute too many small fragments and too few large ones. This discrepancy can have several causes. First, a large but unknown number of small fragments were not recovered in the experiment, as evidenced by the large number of nonperforating dents in the witness plate shown in Figure 38(b) of Section IV. Second, since the SHEAR3 parameters for RHA have not yet been derived from the CFC data, in the computations we used the measured nucleation threshold strain for RHA, but the nucleation rate function

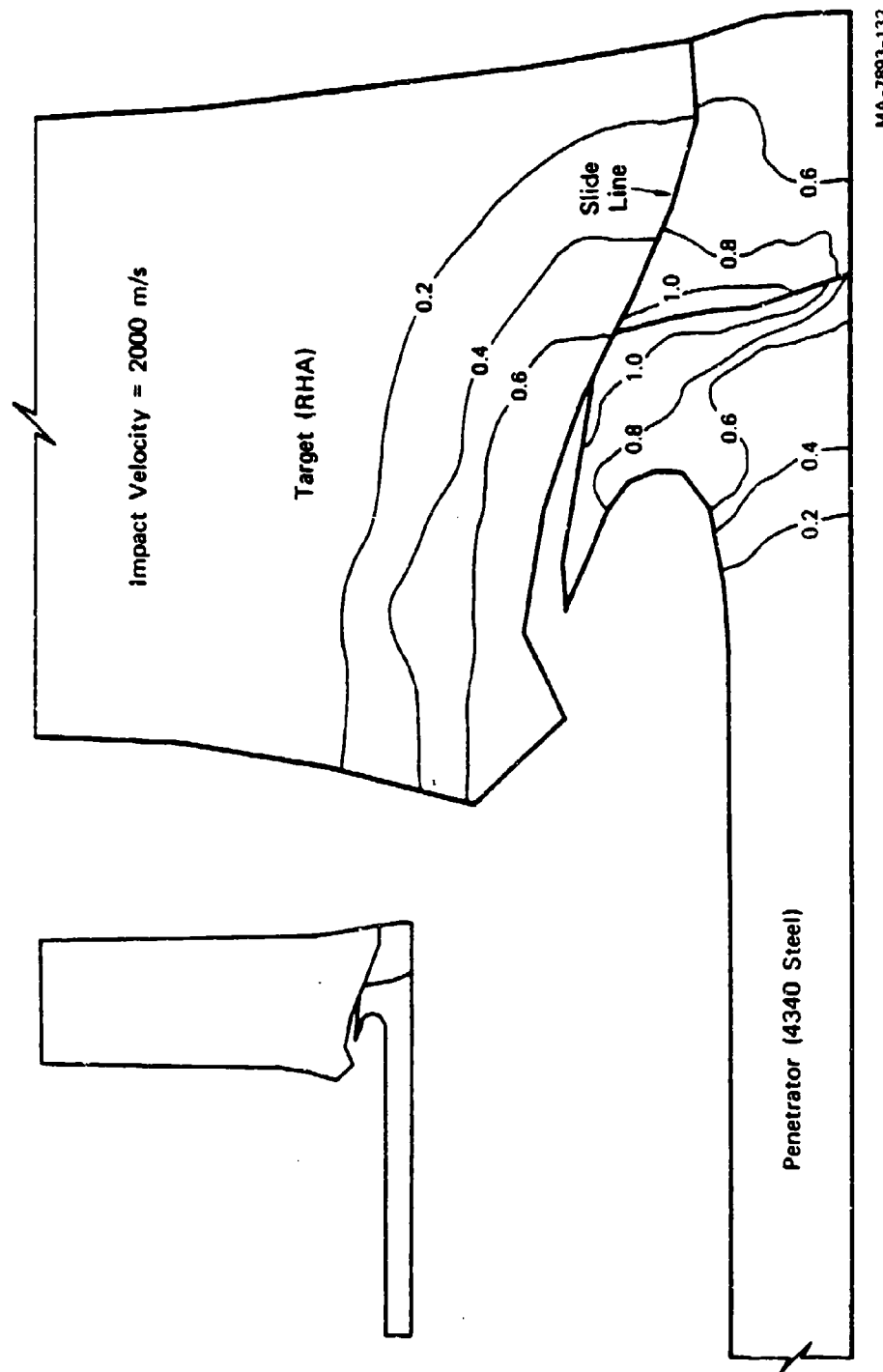
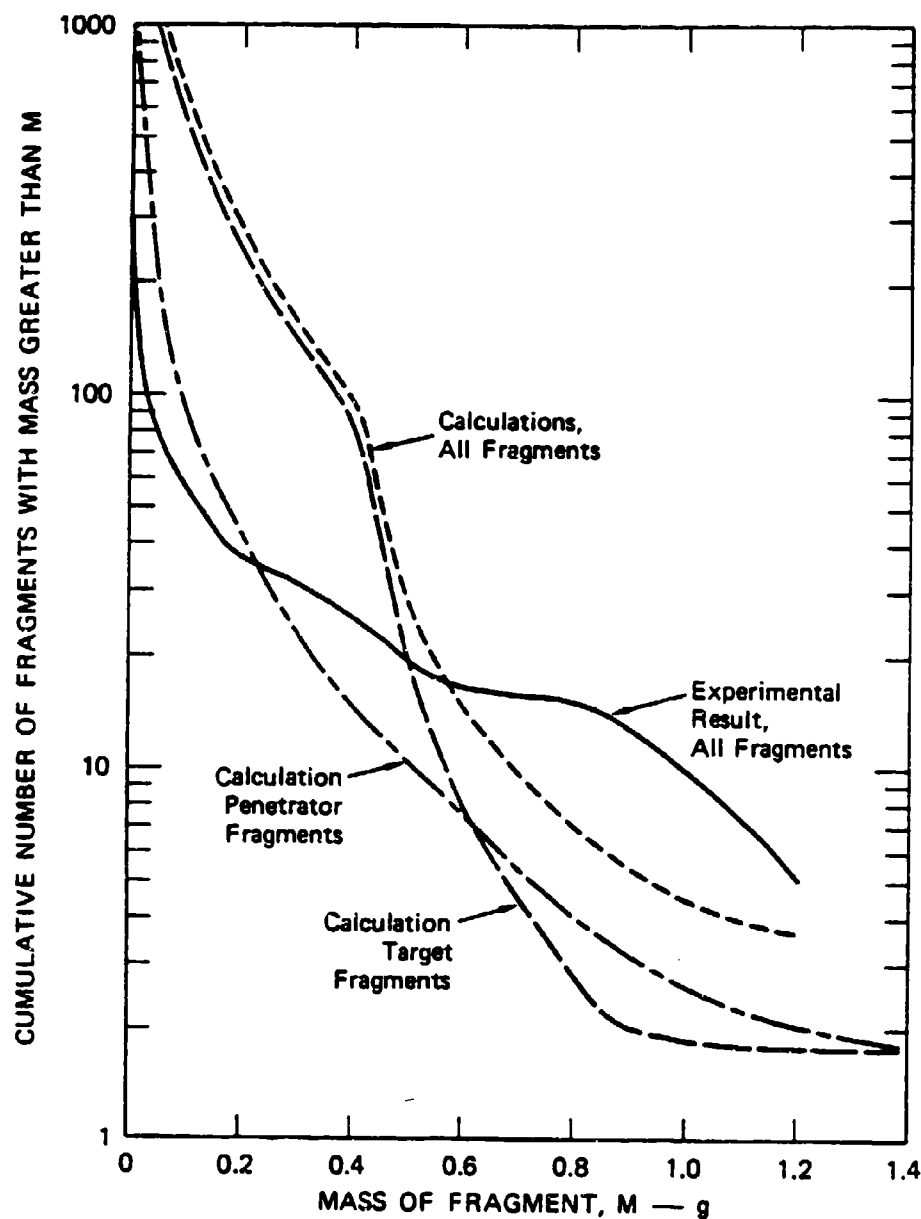


FIGURE 54 CONFIGURATION OF TARGET AND PENETRATION AT 23 μ s IN TROTT SIMULATION WITH UNZIPPING SLIDE LINE, INCLUDING CONTOURS OF EQUIVALENT PLASTIC STRAIN



MA-7893-128

FIGURE 55 COMPARISON OF MEASURED DOWNRANGE FRAGMENT SIZE DISTRIBUTION FROM EXPERIMENT SHOWN IN FIGURE S1 WITH DISTRIBUTIONS CALCULATED FROM COMPUTER SIMULATION

appropriate for the 4340 penetrator steel. On the basis of our experience with another ductile steel (Armco iron), we expect the nucleation rate to be less for the RHA than for the 4340 steel. Furthermore, the calculations of Figure 54 used a somewhat higher impact velocity than was achieved in the experiment. Accounting for all three of these factors would reduce the differences between observation and computation. An additional cause for computational error is the as-yet unmodeled effect of the significant anisotropy of the RHA.

The above uncertainties mean that these comparisons of computed and observed fragment size distributions can only be semiquantitative. Nevertheless, the computations provided the information desired. The overall approach is shown to be promising; SHEAR3 parameters obtained from laboratory CFC experiments appear to produce encouraging results in the penetration computations. At an impact velocity well above the ballistic limit, SHEAR3 will produce a spray of target and penetrator fragments with a reasonable mass or size distribution. Work is continuing to perform a similar computational simulation of the case in which a plug formed at a velocity just above the ballistic limit (Figure S6 of the Summary). Further calculations must then await the determination of the SHEAR3 parameters for RHA material.

VIII PLANS FOR THE THIRD YEAR

For the experimental phase of this program, our tentative plans for the third year are as follows:

- (1) Phenomenology experiments. No new phenomenological studies are planned. We feel that we have a substantial data base for understanding the mechanisms of penetrator nose erosion and RHA target plate penetration at the velocities and obliquities of most interest. Studies by Netherwood of BRL¹³ have shown that breakup of the distal portions of the penetrator during a multiple-plate impact do not appear to be as common as once thought. So we have cancelled plans for tests at BRL to study this problem.
- (2) Material characterization experiments. We plan to conclude the analysis of the RHA CFC experiments and to obtain shear band size distributions for use in conjunction with our computer simulations. We also plan to begin some characterization experiments on DU. In particular, we plan to perform quasi-static tensile tests and CFC tests on the DU specimens that have been machined for us. The tensile specimens include axial specimens and radial specimens with and without centerline porosity. The CFC specimens include only axial specimens; that is, their axes coincide with the axes of the cylinders from which they were machined.
- (3) Downrange fragmentation data base experiments. No new experiments are planned, but we will conclude (with the help of J. Barb of BRL) the analysis of the quarter-scale normal-impact test and obtain final fragment size, velocity, and angle distributions.

The plans for the computational portion of the program next year include completing the development of a method for predicting fracture and fragmentation during a long-rod projectile impact. This method is based on a shear band model that suitably represents the fracture and fragmentation process and on a wave propagation code that can handle the large distortions occurring during the penetration.

The shear band model will require development of an anisotropic treatment of strength and a more detailed coalescence and fragmentation process. These plans were given in detail in Section VD. In addition,

we plan to fit the model to the shear band data obtained from a series of RHA contained fragmenting cylinders.

In the development of Composite HEMP, the next step is testing the rezoning subroutine. Probably some minor adjustments to the rezoner will be required later as we gain experience with it. The slide line development will proceed as follows: test the single slide treatment, add an unzipping or propagating slide line, and add the intersecting or double-slide treatment. Continued effort will be made to minimize the user effort by introducing automatic layout features.

Simulations of normal impacts will be continued to test the development of code features, guide the insertion of new features, and test the suitability of the shear band model. Oblique impact simulations will be made later. We expect these simulations to guide in further code and shear band model developments.

REFERENCES

1. D. R. Curran et al., "Computational Model for Armor Penetration," SRI Annual Report on Contract DAAK11-78-C-0115 for U.S. Army Ballistic Research Laboratory Aberdeen, MD, and Army Materials and Mechanics Research Center, Watertown, MA (November, 1979).
2. R. F. Benck, "Quasi-Static Tensile Stress Strain Curves--II, Rolled Homogeneous Armor," BRL Memorandum Report No. 2703, USA Ballistics Research Laboratory, Aberdeen, MD (November 1976).
3. G. E. Hauver, "The Alpha-Phase Hugoniot of Rolled Homogeneous Armor," BRL Memorandum Report No. 2703, USA Ballistics Research Laboratory, Aberdeen, MD (August 1979).
4. M. Hansen, Constitution of Binary Alloys, p. 1239, McGraw-Hill, New York (1958).
5. R. E. Reed-Hill, Physical Metallurgy Principles, p. 421, Van Nostrand-Reinhold Co., New York (1964).
6. D. C. Erlich, L. Seaman, D. A. Shockey, and D. R. Curran, "Development and Application of a Computational Shear Band Model," SRI Final Report on Contract DAAD05-76-C-0762 for U.S. Army Ballistic Research Laboratory, Aberdeen, MD (May 1977).
7. D. C. Erlich, D. R. Curran, and L. Seaman, "Further Development of Computational Shear Band Model," SRI Final Report, Contract No. DAAG46-77-C-0043, for U.S. Army Materials and Mechanics Research Center, Watertown, MA (May 1979).
8. L. Seaman, D. A. Shockey, D. R. Curran, and R. E. Tokheim, "Development of a Shear Band Model for Fragmentation in Exploding Cylinders," SRI Final Report, Contract No. N001780-74-C-0450, for Naval Surface Weapons Center, Dahlgren, VA (August 1975).
9. D. C. Erlich, L. Seaman, D. R. Curran, and D. A. Shockey, A Preliminary Study of Armor Penetration by Shear Banding, Final Report, SRI International for U.S. Army Ballistic Research Laboratory, Aberdeen Proving Ground, MD (August 1978).
10. E. Scheil, Die Berechnung der Anzahl und Grossenverteilung kugelformiger Kristalle in undurchsichtigen Körpern mit Hilfe durch einen ebenen Schnitt erhaltenen Schnittkreise, Z. Anorg. Allgem. Chem., 201, 259 (1931).

11. E. Scheil, Statistische Gefügeuntersuchungen I, Z. Metallk., 27, 199 (1935).
12. L. Seaman, D. R. Curran, and R. C. Crewdson, "Transformation of Observed Crack Traces on a Section to True Crack Density for Fracture Calculations," J. Appl. Phys. 49(10), p. 5221-5229 (October 1978).
13. P. Netherwood, private communication.
14. J. von Neumann and R. D. Richtmyer, "A Method for the Numerical Calculation of Hydrodynamic Shocks," J. Appl. Phys., 21, p. 232 (1950).
15. R. D. Richtmyer and K. W. Morton, Difference Methods for Initial-Value Problems, 2d ed. (Interscience Publishers, New York, 1967).
16. W. Herrmann, P. Holzhauser, and R. J. Thompson, "WONDY, A Computer Program for Calculating Problems of Motion in One Dimension," SC-RR-66-601, Sandia Corporation, Albuquerque, New Mexico (February 1967).

APPENDIX A
REPRESENTATION OF THE SHEAR BAND DISTRIBUTION BY MULTIPLE SIZE GROUPS

The shear band size distribution may be represented by a series of exponential line segments as shown in Figure A1. The user may select the number of segments or nodes and thereby determine the precision with which the distribution is represented. This section describes the method for specifying the distribution and treatment during nucleation, growth, and the computation of damage.

At the first nucleation, a shear band distribution is created with a series of radii R_j as abscissae and N_j as ordinates at the nodes. The number of intervals in BFR(M,34), and the size of the largest $R = R_{\max}$ is BFR(M,28). The smaller radii are initialized by the formula

$$R_j = \frac{R_{j+1}}{C_{\text{RATIO}}} \quad (\text{A1})$$

where C_{RATIO} is provided in the initialization portion of SHEAR3 as 1.4. The individual N_j values are initialized from a nucleated distribution of the form

$$N = N_n e^{-R/R_n} \quad (\text{A2})$$

where N_n and R_n are the number and size parameters of the nucleated distribution. Then N_j is given by

$$N_j = N_n e^{-R_j/R_n} \quad (\text{A3})$$

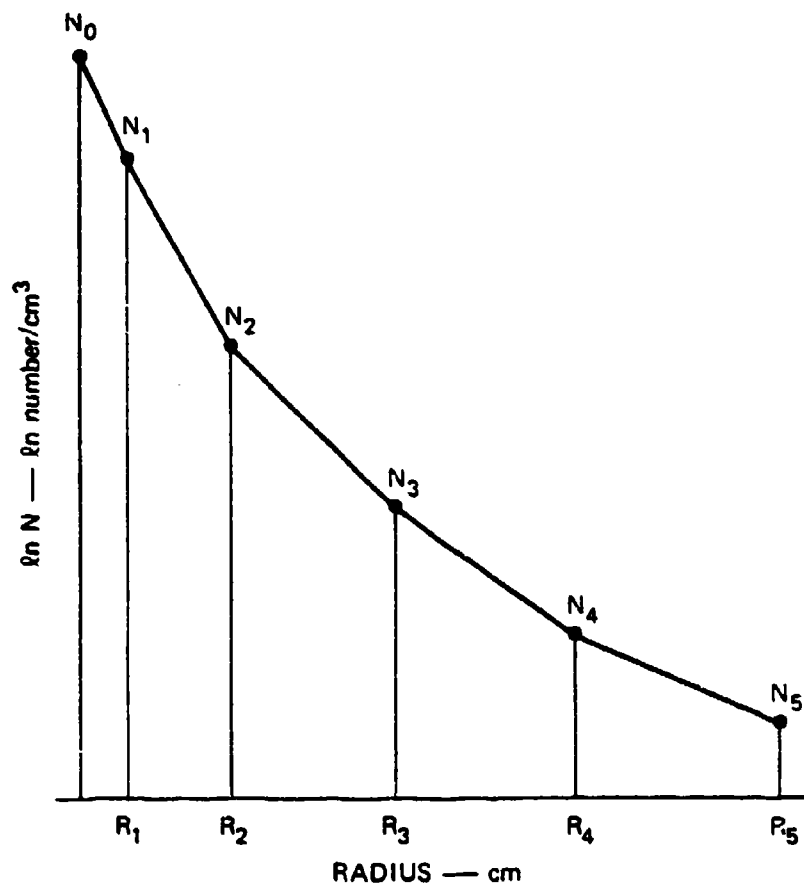
The numbers and radii are stored in the CN array in the SHEAR3 subroutine in the order

$$N_0, R_1, N_1, R_2, N_2, \dots, R_{\text{NS}}, N_{\text{NS}}$$

where $\text{NS} = \text{BFR}(\text{M},34)$, the number of intervals.

For nucleation on cycles following initialization of the distribution, the numbers at each node are merely incremented as shown in Figure A2 (a).

$$N_j = N_{j0} + N_n \exp(-R_j/R_n) \quad (\text{A4})$$



MA-7893-101

FIGURE A1 SHEAR BAND SIZE DISTRIBUTION REPRESENTED BY A SERIES OF POINTS AND EXPONENTIAL LINE SEGMENTS

where N_{j0} is the number before the time increment. Thus the nucleated distribution is added to the old distribution at the nodes of the old distribution. Between these nodes the distribution is assumed to remain a series of straight line segments. This segmented distribution is only an approximation to the actual sum because the sum of two exponentials is not in general an exponential.

Growth of the bands is represented by an increase in the R_j at all the nodes as shown in Fig. A2b. The rate of growth is given by the following viscous law.⁵

$$\frac{dR_j}{dt} = C_G R_j \frac{d\epsilon_{\phi\theta}^{PS}}{dt} \quad (A5)$$

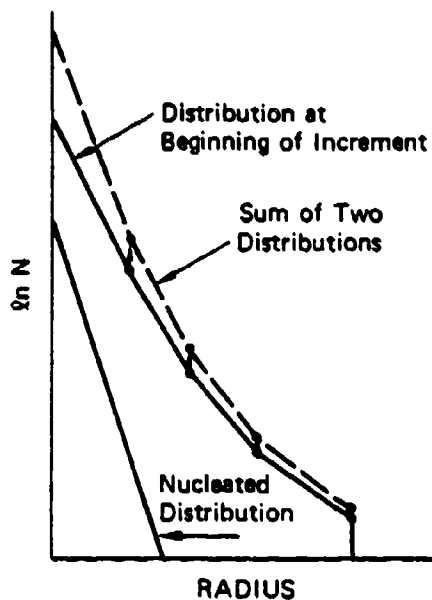
where C_G is a growth coefficient and $\epsilon_{\phi\theta}^{PS}$ is the plastic strain on the plane associated with the shear bands under consideration. Eq. (A5) is used with the constraint that the growth velocity cannot exceed the shear wave velocity. When an exponential distribution grows according to Eq. A5, it remains an exponential. Thus the straight line segments exactly represent the growth of the distribution (see Fig. A2b). However, if the limit velocity is reached over some part of the distribution, the new distribution is no longer exponential and the line segments are only a discrete approximation to the grown distribution (see Fig. A2c). Thus both nucleation and growth are readily treated with the distribution represented by multiple size groups, although approximations occur in both computations.

The computation of the damage τ is performed exactly under the assumption of an exponential curve between nodes of the distribution. Here the expression for this curve is obtained in terms of the coordinates at the adjacent nodes and then an integration is performed to obtain τ . Within each interval the distribution is given by

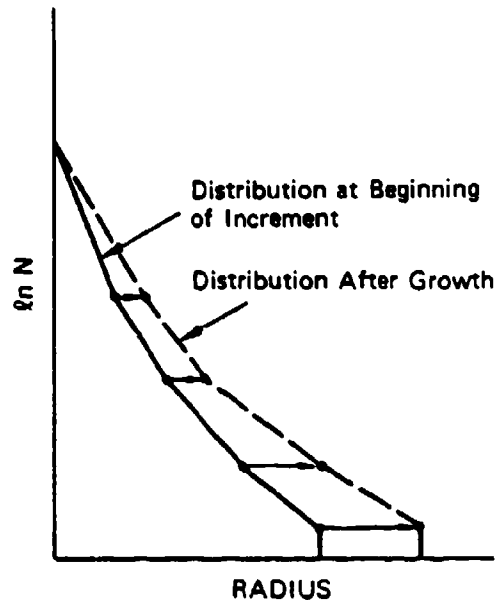
$$N = N_{mj} \exp(A_{mj} R) \quad (A6)$$

Then the number at the nodes on either end of the interval are

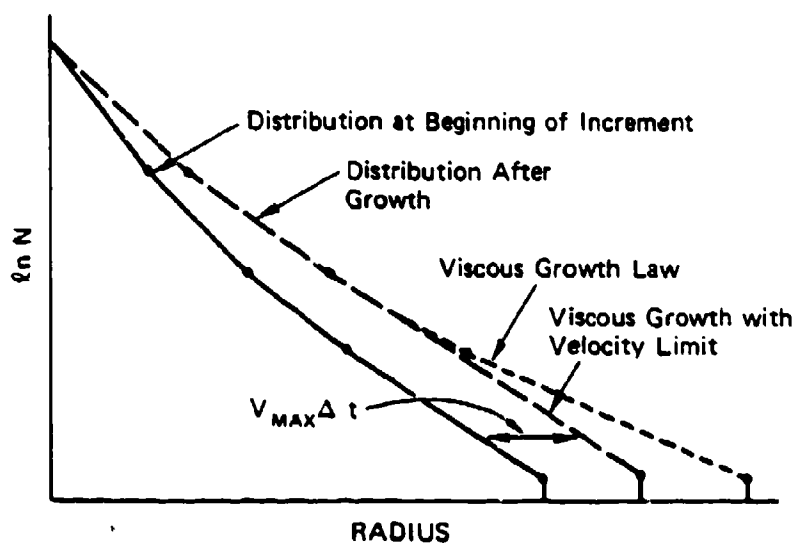
$$N_{j-1} = N_{mj} \exp(A_{mj} R_{j-1}) \quad (A7)$$



(a) SUMMATION OF A PREVIOUS DISTRIBUTION AND A NUCLEATED DISTRIBUTION



(b) GROWTH OF A MULTIPLE POINT DISTRIBUTION



(c) GROWTH OF A DISTRIBUTION NEAR THE LIMITING VELOCITY

MA-7893-102

FIGURE A2 NUCLEATION AND GROWTH PROCESSES FOR A SHEAR BAND DISTRIBUTION GIVEN BY A SERIES OF POINTS

$$N_j = N_{mj} \exp (A_{mj} R_j) \quad (A8)$$

Equations (A7) and (A8) can be used to solve for N_{mj} and A_{mj}

$$\ln N_{mj} = \frac{R_j \ln N_{j-1} - R_{j-1} \ln N_j}{R_j - R_{j-1}} \quad (A9)$$

$$A_{mj} = \frac{\ln (N_{j-1}/N_j)}{R_j - R_{j-1}} \quad (A10)$$

with the expression for the curve N versus R defined (Eq. A6 with constants from A9 and A10), the integral for τ can be evaluated.

The damage factor τ in any orientation is defined as a sum over the entire distribution

$$\tau = \sum \Delta N \cdot cR \cdot \pi R^2 \quad (A11)$$

where ΔN is the number of shear bands per unit volume with radius R , c is a proportionality factor [in the range 0.1 to 1.0; input as BFR(M,29)], and πR^2 is the area of the band. The factor cR is introduced to form a volume of material πcR^3 , which is associated with the band. For an interval from node $j-1$ to node j , the damage τ is

$$\tau_j = \pi c \int_{R_j}^{R_{j-1}} R^3 dN \quad (A12)$$

The limits on the integral are reversed to make the sum positive. To prepare the integral, dN is obtained as a function of R from Eq. (A6). Then

$$\tau_j = \pi c N_{mj} A_{mj} \int_{R_j}^{R_{j-1}} R^3 \exp (A_{mj} R) dR \quad (A13)$$

Let $\xi = A_{mj}R$. Then the integral becomes

$$\tau_j = \frac{\pi c N_{mj}}{A_{mj}^3} \int_{\xi_j}^{\xi_{j-1}} \xi^3 e^{\xi} d\xi \quad (A14)$$

This integral has the solution

$$\tau_j = \frac{\pi c N_{mj}}{A_{mj}^3} e^{\xi} \left(\xi^3 - 3\xi^2 + 6\xi - 6 \right) \Bigg|_{\xi_j}^{\xi_{j-1}} \quad (A15)$$

For convenience, a new quantity Z is defined

$$Z = -\frac{e^{\xi}}{6} (\xi^3 - 3\xi^2 + 6\xi - 6) = e^{\xi} (1 - \xi + 1/2\xi^2 - 1/6\xi^3) \quad (A16)$$

Then τ makes the form

$$\tau_j = \frac{6\pi c N_{mj}}{A_{mj}^3} (Z_j - Z_{j-1}) \quad (A17)$$

The Z quantity is approximately equal to one and ξ is always negative. The first and last intervals are treated somewhat differently. For the first interval $R_{j-1} = R_0$ is always taken as zero and is therefore not stored in the array. Then $Z_{j-1} = Z_0 = 1.0$. For the last interval the original expression for τ (Eq. A11) is reexamined. The distribution shown in Fig. A1 contains a number of bands $N_{NS} = N_5$ at $R = R_5$ and then a continuous distribution for all smaller radii. The damage quantity is therefore

$$\tau_{NS} = \pi c \left[R_{NS}^3 N_{NS} + \int_{R_{NS}}^{R_{NS-1}} R^3 dN \right] \quad (A18)$$

$$= \pi c \left[R_{NS}^3 N_{NS} + \frac{6N_{mj}}{A_{mj}^3} (Z_j - Z_{j-1}) \right]$$

With appropriate transformations, these terms on the right can be combined.

$$R_{NS}^3 N_{NS} = R_{NS}^3 N_{mj} \exp (A_{mj} R_{NS})$$

$$= \frac{\xi_{NS}}{A_{mj}^3} N_{mj} \exp (\xi_{NS})$$

with $j = NS$. Now τ_{NS} becomes

$$\begin{aligned} \tau_{NS} &= \frac{6\pi c N_{mj}}{A_{mj}^3} \left[Z_j - Z_{j-1} + 1/6 \xi_{NS}^3 \exp (\xi_{NS}) \right] \\ &= \frac{6\pi c N_{mj}}{A_{mj}^3} (Y_j - Z_{j-1}) \end{aligned} \quad (A19)$$

where the new function Y has the definition

$$Y = e^{\xi} (1 - \xi + 1/2 \xi^2) \quad (A20)$$

With the use of Eqs. (A17) and (A19), the damage τ can be computed for the multiple size distribution.

The approximations noted above in the assumption of an exponential curve in each interval of the distribution gives some indication of the number of intervals required. A single interval with three data items-- N_0 , R_1 , and N_1 --can be used but will lead to too large values of N and τ .

Three or four intervals (7 or 9 variables) are probably sufficient if the ranges in radii are selected so that they span the distribution well (RATIO may be modified to assist in the representation). In our simulations of the fragmenting round data to determine the shear band parameters, we used ten intervals.

APPENDIX B

COMBINATION PROCESS TO MAINTAIN THE DISTRIBUTION AS A SINGLE EXPONENTIAL

The experimental size distribution for shear bands has approximately the shape of a single exponential. Therefore, it should be possible to use a single exponential instead of the multiple size groups to represent the distribution in the SHEAR3 computations. The purpose of this appendix is to develop a procedure for computing the parameters of the single exponential in a way that provides reasonable fidelity both to the shape of the true N-R distribution and to the value of τ . Such a procedure has the advantage of requiring only 3 variables to represent the distribution instead of the 7 to 21 required for the multiple size group representation.

In these calculations, we first consider the distribution changes associated with growth and nucleation, and then the means for combining the growing and nucleated distributions into a single exponential. The damage τ is computed and comparisons are made between results from the single exponential and from a multiple-size-group calculation.

The distribution is represented by three parameters: N_0 (the intercept at $R = 0$), R_1 (the shape parameter), and R_b (the maximum radius).

$$N = N_0 \exp (-R/R_1) \quad R \leq R_b \quad (B1)$$

Growth of this distribution is treated by allowing both R_1 and R_b to grow according to the viscous growth law (Eq. A5), with the shear wave velocity limit on the growth rate.

The first step for nucleation is to compute a nucleated distribution with the form of Eq. (B1), but with the nucleation parameters ΔN_n and R_n .

$$N = \Delta N_n \exp (-R/R_n) \quad R \leq R_{bn} \quad (B2)$$

where ΔN_n is computed according to the nucleation process, and R_n and R_{bn} are input parameters.

The nucleated and growing distributions are then combined to form one exponential distribution that has the same damage, τ , and represents the general slope of the sum of the two distributions. This second requirement was made specific by noting that in some central portion of the N-R distribution there is a major contribution to the τ integral. Hence there is a central point where $d\tau/dR$ is maximum. The function in the vicinity of this point must be well-represented for the combined distribution to reasonably match the sum of the nucleated and growing distributions. The two requirements are then:

- The slopes $d\tau/dR$ in the combined distribution and the sum reach maxima at the same R value.
- τ of the combined distribution equals τ of the sum.

For a single exponential, $d\tau/dR$ reaches a maximum when $d^2\tau/dR^2$ equals zero.

$$\frac{d\tau}{dR} = R^3 \frac{dN}{dR} = - \frac{N_o R^3}{R_1} \exp(-R/R_1) \quad (B3)$$

$$\frac{d^2\tau}{dR^2} = \frac{N_o R^2}{R_1} \exp(-R/R_1) \left(3 - \frac{R}{R_1}\right) \quad (B4)$$

$$\text{Setting } d^2\tau/dR^2 = 0 \text{ gives } R = 3R_1 \quad (B5)$$

when $d\tau/dR$ is maximum.

The corresponding expressions for the sum are

$$\frac{d\tau}{dR} = - R^3 \left[\frac{N_{10}}{R_{10}} \exp(-R/R_{10}) + \frac{\Delta N_n}{R_n} \exp(-R/R_n) \right] \quad (B6)$$

$$\begin{aligned} \frac{d^2\tau}{dR^2} = & (-3R^2 + \frac{R^3}{R_{10}}) \frac{N_{10}}{R_{10}} \exp(-R/R_{10}) \\ & + (-3R^2 + \frac{R^3}{R_n}) \frac{\Delta N_n}{R_n} \exp(-R/R_n) \end{aligned} \quad (B7)$$

where R_{10} and N_{10} are the shape parameter and intercept number, respectively, of the growing distribution. Setting $d^2\tau/dR^2$ to zero in Eq. (B7), we can obtain a value of $R = R_c$ at the point of maximum $d\tau/dR$ (the solution procedure is outlined below). Then from Eq. (B5),

$$R_1 = R_c/3 \quad (B8)$$

Hence the combined distribution is set to have its maximum $d\tau/dR$ at the same radius as for the maximum of the sum.

The condition to conserve τ is approximated as

$$N_o R_1^3 = N_{10} R_{10}^3 + \Delta N_n R_n^3 \quad (B9)$$

in which the cutoff of the distribution at $R = R_b$ has been neglected. With R_1 known from Eq. (B8), Eq. (B9) can be used to determine N_o . Thus the two parameters N_o and R_1 of the combined distribution are determined.

The solution of Eq. (B7) for $R = R_c$ is obtained starting with a change of variable. Let

$$R_1 = \frac{R_c}{3} = (1-\eta)R_{10} \quad (B10)$$

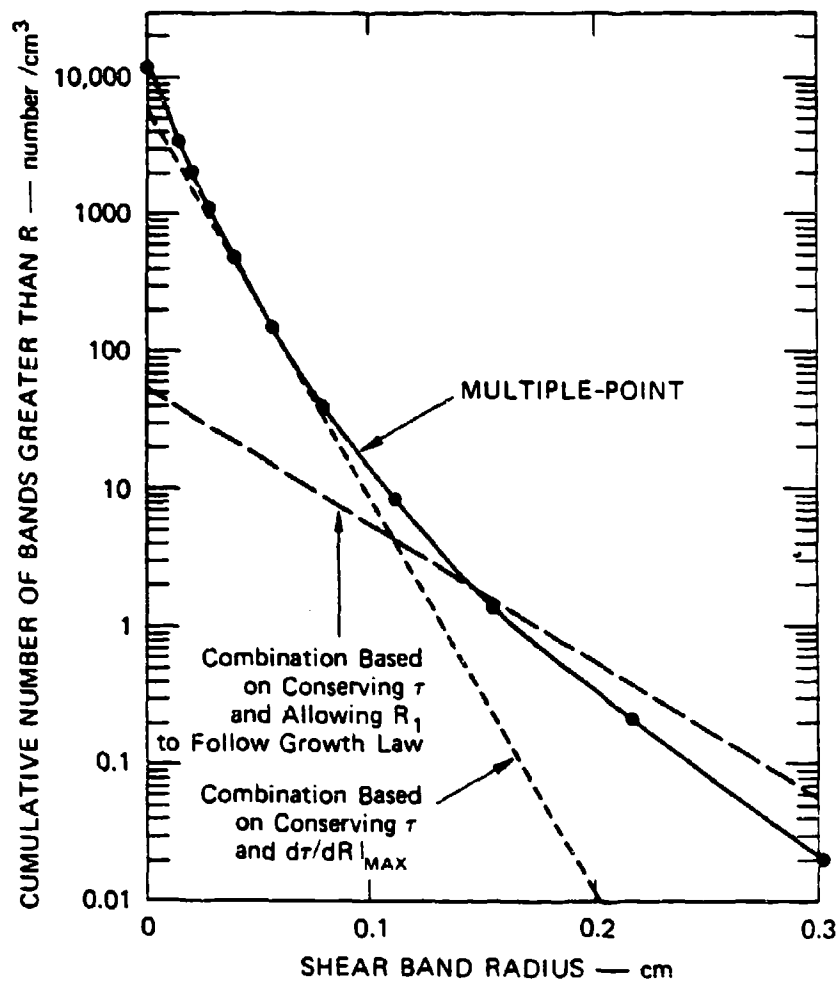
so that η , the new unknown, is a small, dimensionless quantity. Eq. (B7) then takes the form:

$$\eta = \left[(1-\eta) \frac{R_{10}}{R_n} - 1 \right] \frac{\Delta N_n R_{10}}{N_{10} R_n} \exp \left[-3(1-\eta) \left(\frac{R_{10}}{R_n} - 1 \right) \right] \quad (B11)$$

This relation is readily solved by iteration and the equation is cast in the form appropriate for the solution method used. The initial estimate of η is zero. This value is used on the right-hand side and the second estimate is obtained as the value on the left-hand side. This process is repeated until successive values of η differ by less than 10^{-4} . Usually only one to four iterations are required because η is small.

Three test calculations were made to compare results of the current combination procedure with those from a multiple-point size distribution and from a previous combination procedure. A shear strain of 43% was imposed in 37 equal steps to reach the size distribution shown in Figure B1. The variation of τ values during the calculations are shown in Figure B2. The multiple-point results are probably the most accurate. The current combination procedure gives a distribution (Fig. B1) that is tangent to the multiple-point curve in the vicinity of the maximum $d\tau/dR$, but provides a smaller τ (Fig. B2). The previous combination procedure gives a very poor indication of both the shape of the distribution and the value of τ .

Comparisons of the combination and multiple-point procedures have also been made for complete fragmenting-cylinder simulations. The combination procedure gave significantly lower amounts of damage. These comparisons of results with the current combination procedure and with the multiple-point procedure suggest that the combination procedure should be used only for rough approximations. Probably the shear band parameters should be determined with the multiple-size version.



MA-7893-103

FIGURE B1 SHEAR BAND SIZE DISTRIBUTIONS COMPUTED BY SHEAR3 AT 43% PLASTIC STRAIN USING DIFFERENT PROCEDURES FOR REPRESENTING THE BAND SIZE DISTRIBUTION

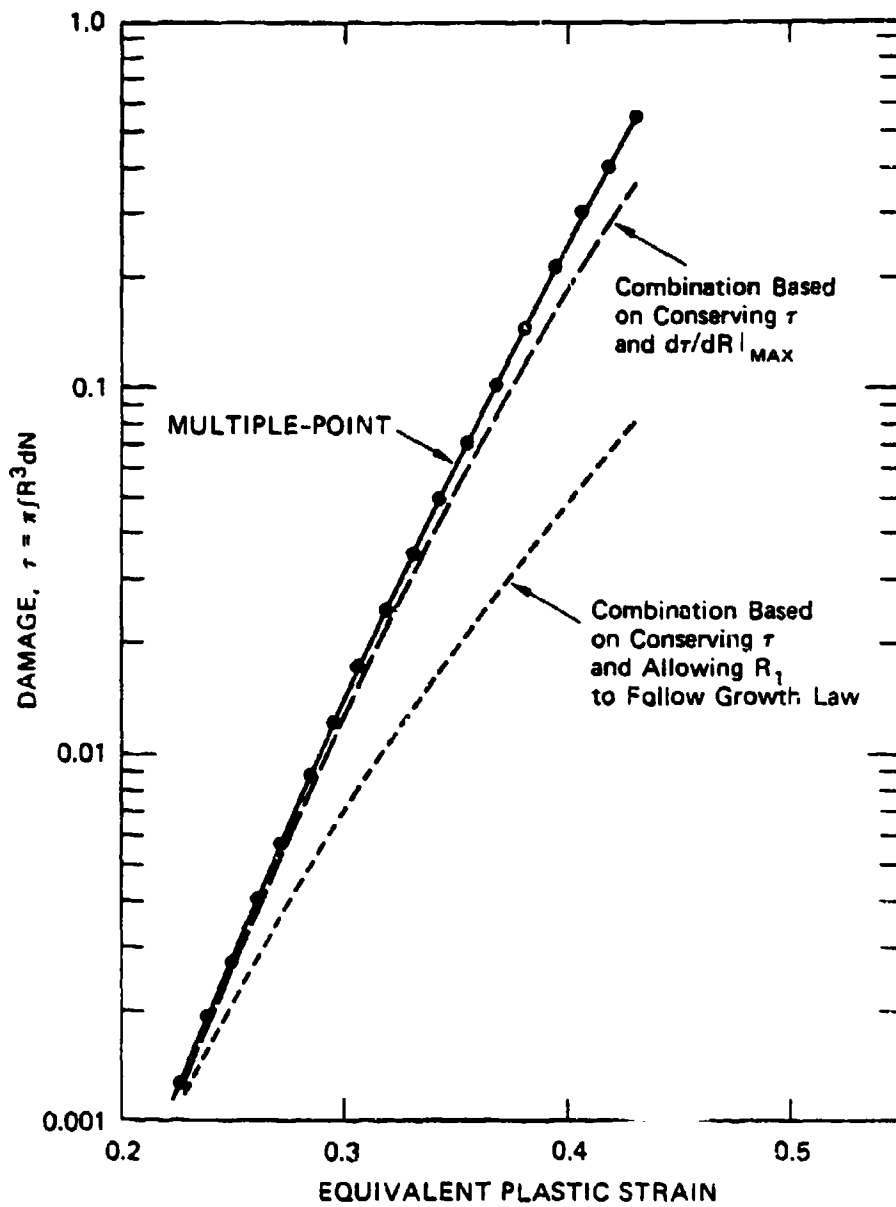


FIGURE B2 RESULTS OF THREE PURE SHEAR TESTS WITH SHEAR3 USING DIFFERENT PROCEDURES FOR REPRESENTING THE BAND SIZE DISTRIBUTION

APPENDIX C
VOLUME-TO-SURFACE TRANSFORMATION FOR SHEAR BANDS

In our model calculations of shear bands, the bands occur as number densities or number per unit volume. However, the shear bands are observed experimentally as a number that intersects a surface and are therefore counted as a number per unit area. To make a comparison between the computed and measured values, a transformation must be made. In our study it is convenient to transform the volume quantities to surface quantities as part of the operation of the SHEAR3 shear band subroutine.

The following analysis includes a derivation of the equations and the solution procedure used. The method differs from Scheil's¹⁰ in that the radius intervals are of variable size in the present analysis. Following the transformation, the surface distribution is fitted to an exponential for ease in comparing with experimental data.

The desired transformation relates the areal counts N_a to the volume counts N_v . For the transformation both functions are discretized into counts that pertain to a radius interval. The relation between the counts is then

$$N_a(i) = \sum_{j=1}^J \alpha_{ij} N_v(j) \quad (C1)$$

where $N_a(i)$ is the number of circles per unit area with radii between r_i and r_{i+1} , $N_v(j)$ is the number of bands per unit volume with radii between R_j and R_{j+1} , α_{ij} is the transformation matrix to be derived, and J is the number assigned to the upper limit of observed radii.

In addition to the discrete distribution quantities N_a and N_v , we assume the existence of continuous distribution functions $\xi(r)$ and $\rho(R)$, the areal and volume densities, respectively. These are defined such that

$$N_a(i) = \int_{r_i}^{r_{i+1}} \xi(r) dr \quad (C2)$$

$$N_v(i) = \int_{R_i}^{R_{i+1}} \rho(R) dR \quad (C3)$$

For the derivation we define $\xi'(r,R)dR$ as the number of bands of radius R per unit area that intersect the plane of polish with a circle of radius r , and $\xi''(R)dR$ as the total number of bands of radius R to intersect the plane of polish. The densities $\xi'(r,R)$ and $\xi''(R)$ are related by a probability function P :

$$\xi'(r,R) = P(r,R) \xi''(R) \quad (C4)$$

where P is the probability of r , given R . This probability can be readily derived from Figure C1. The differential probability for a slice with a thickness dh is

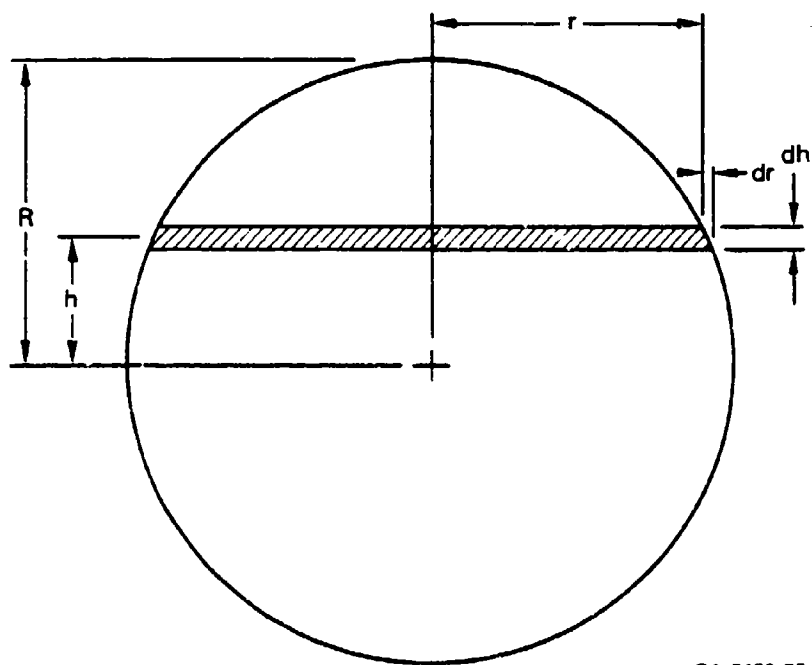
$$dP = P(h)dh = P(r,R)dr = \frac{dh}{R} = \frac{1}{R \sqrt{R^2 - r^2}}$$

$$P(r,R) = \frac{r}{R \sqrt{R^2 - r^2}} \quad \text{for } r < R$$

$$= 0 \quad \text{for } r \geq R \quad (C5)$$

The areal density $\xi(r)$ is related to the volume density of bands $\rho(R)$ by noting that the plane of polish intersects all circles of radius R whose centers lie within R of the plane, that is, in the volume $2R \cdot A$ (A = area). For a unit area

$$\xi''(R) = 2R \rho(R) \quad (C6)$$



GA-7456-75

FIGURE C1 SLICE OF THICKNESS dh THROUGH A CIRCLE OF RADIUS R

Combine this with Eqs. (C4) and (C5) to get

$$\xi(r) = \int_0^{\infty} \xi'(r,R) dR = \int_0^{\infty} P(r,R) \xi''(R) dR = \int_0^{\infty} P(r,R) 2R \rho(R) dR \quad (C7)$$

The areal counts are numbers between two radii; that is, from Eq. (C7),

$$N_a(i) = \int_{r_i}^{r_{i+1}} \xi(r) dr = 2 \int_{r_i}^{r_{i+1}} \int_0^{\infty} P(r,R) R \rho(R) dR dr \quad (C8)$$

The order of integration is reversed and the integral is separated into four components as follows:

$$\int_{r_i}^{r_{i+1}} \int_0^{\infty} + \int_0^{r_i} \int_{r_i}^{r_{i+1}} + \int_{r_i}^{r_{i+1}} \int_{r_i}^R + \int_{r_i}^{r_{i+1}} \int_R^{r_{i+1}} + \int_{r_{i+1}}^{\infty} \int_{r_i}^{r_{i+1}}$$

(r) (R) (R) (r) (R) (r) (R) (r) (R) (r)

The first and third of the integrals on the right are zero according to the second part of Eq. (C5). The resultant equation is

$$\begin{aligned} N_a(i) &= 2 \int_{r_i}^{r_{i+1}} \int_{r_i}^R \frac{r}{\sqrt{R^2 - r^2}} \rho(R) dr dR \quad (R < r_{i+1}) \\ &+ 2 \int_{r_{i+1}}^{\infty} \int_{r_i}^{r_{i+1}} \frac{r}{\sqrt{R^2 - r^2}} \rho(R) dr dR \quad (R > r_{i+1}) \\ &= 2 \int_{r_i}^{r_{i+1}} \sqrt{R^2 - r_i^2} \rho(R) dR + 2 \int_{r_{i+1}}^{\infty} (\sqrt{R^2 - r_i^2} - \sqrt{R^2 - r_{i+1}^2}) \rho(R) dR \quad (C9) \end{aligned}$$

The procedure for computing the $N_a(i)$ is essentially the same as Scheil's: Rewrite Eq. (C9) in the form of Eq. (C1), using Eq. (C9) to define the α 's. Then using Eq. C3 to define $N_v(i)$, we obtain

$$\alpha_{ii} = \frac{2 \int_{r_i}^{r_{i+1}} \rho(R) \sqrt{R^2 - r_i^2} dR}{\int_{r_i}^{r_{i+1}} \rho(R) dR} \quad (C10)$$

and

$$\alpha_{ij} = \frac{2 \int_{r_j}^{r_{j+1}} \rho(R) (\sqrt{R^2 - r_i^2} - \sqrt{R^2 - r_{i+1}^2}) dR}{\int_{r_j}^{r_{j+1}} \rho(R) dR} \quad (C11)$$

To make the computation of the α 's tractable, we use the approximation of Scheil and let $\rho(R)$ be constant in each radius interval. Then the α 's become

$$\alpha_{ii} = 2 \int_{r_i}^{r_{i+1}} \frac{\sqrt{R^2 - r_i^2} dR}{r_{i+1} - r_i} \quad (C12)$$

and

$$\alpha_{ij} = 2 \int_{r_j}^{r_{j+1}} \left(\frac{\sqrt{R^2 - r_i^2} - \sqrt{R^2 - r_{i+1}^2}}{r_{j+1} - r_j} \right) dR \quad (C13)$$

These integrals can be evaluated to obtain

$$\alpha_{ij} = \left[\begin{array}{l} r_{j+1} S_{j+1,i} - r_i^2 T_{j+1,i} - r_j S_{j,i} + r_i^2 T_{j,i} - r_{j+1} S_{j+1,i+1} \\ r_{i+1}^2 T_{j+1,i+1} + r_j S_{j,i+1} - r_{i+1}^2 T_{j,i+1} \end{array} \right] (r_{j+1} - r_j) \quad (C14)$$

where

$$S_{j,i} = \sqrt{r_j^2 - r_i^2}$$

$$T_{j,i} = \ln(r_j + \sqrt{r_j^2 - r_i^2})$$

The corresponding expression for α_{ii} is

$$\alpha_{ii} = r_{i+1} S_{i+1,i} - r_i^2 \ln r_i \quad (C15)$$

The system of equations specified by Eq. (C1) has the form

$$N_a(J) = \alpha_{J,J} N_v(J)$$

$$N_a(J-1) = \alpha_{J-1,J-1} N_v(J-1) + \alpha_{J-1,J} N_v(J) \quad (C16)$$

$$N_a(1) = \alpha_{1,1} N_v(1) + \alpha_{1,2} N_v(2) \dots \alpha_{1,J} N_v(J)$$

where J is the number of radius intervals. When the coefficients α are computed and the volume quantities N_v are known, the N_a values are easily evaluated from Eq. C16. From the N_a values, the cumulative numbers C larger than the given radius are determined.

$$C(r_i) = \sum_{j=1}^J N_a(j) \quad (C17)$$

The $C(r_i)$ values then form the surface distribution, which may be compared to experimental data.

Because the surface data in the form of $C(r)$ versus r tend to be approximately exponential, it is convenient to fit the points to an exponential of the form

$$C(r) = n_0 \exp(-r/r_1) \quad (C18)$$

where n_0 and r_1 are the parameters of the exponential. The fitting uses the standard least squares procedure with a weighting factor. Let $\ln n(r)$ be approximated by the series

$$y(r) = \sum_{k=0}^k a_k r^k \quad (C19)$$

The coefficients a_k are obtained by minimizing the square of the difference

$$\epsilon_i = \ln C(r_i) - y(r_i)$$

at the nodes r_i of the distribution. That is, minimize

$$\sum_{i=1}^J w_i \epsilon_i^2 = \sum_{i=1}^J w_i \left[\ln n(r_i) - \sum a_k r_i^k \right]^2 \quad (C20)$$

Differentiation of this expression with respect to a_0 and a_1 and setting the derivatives to zero leads to

$$a_0 = \frac{\sum w_i \ln C(r_i) \sum w_i r_i^2 - \sum w_i r_i \ln C(r_i) \sum w_i r_i}{\sum w_i \sum w_i r_i^2 - (\sum w_i r_i)^2} \quad (C21)$$

$$a_1 = \frac{\sum w_i \sum w_i r_i \ln C(r_i) - \sum w_i r_i \sum w_i \ln C(r_i)}{\sum w_i \sum w_i r_i^2 - (\sum w_i r_i)^2}$$

Taking the logarithm of Eq. (C18) and comparing the result with Eq. (C19), we can identify a_0 and a_1 as

$$a_0 = \ln n_0 \quad \text{or} \quad n_0 = \exp(a_0)$$

$$a_1 = -1/r_1 \quad \text{or} \quad r_1 = -1/a_1 \quad (C22)$$

To emphasize the portion of the distribution that contributes most to damage in computing the fit, the weighting factor was chosen as

$$w_i = C(r_i)r_i^2 \quad (C23)$$

Thus the weighting factor is effectively r_i .

The preceding transformation and least squares fit procedures were inserted into the printing section at the end of SHEAR3. The printing is requested as part of edit listings on some computational cycles. Then the volume density quantities are listed as usual, plus the surface densities, and n_o and r_i .

APPENDIX D
WORK-HARDENING MODEL

A general model for elastic-plastic work-hardening is derived here for use in the intact material in the shear banding model SHEAR3. Yield strength is taken as a function of the scalar plastic strain $\bar{\epsilon}^P$ only. For the model, the yield versus $\bar{\epsilon}^P$ curve is divided into a series of strain intervals. Within each interval (except the first), the yield strength varies with the power law

$$y \propto (\bar{\epsilon}^P)^n$$

In the first interval the $y - \bar{\epsilon}^P$ relation is linear.

The model derivations are made considering the elastic loading and unloading paths and the yield function shown in Figure D1. The ordinate $\bar{\sigma}$ is the equivalent stress, a scalar measure of the distortional stresses.

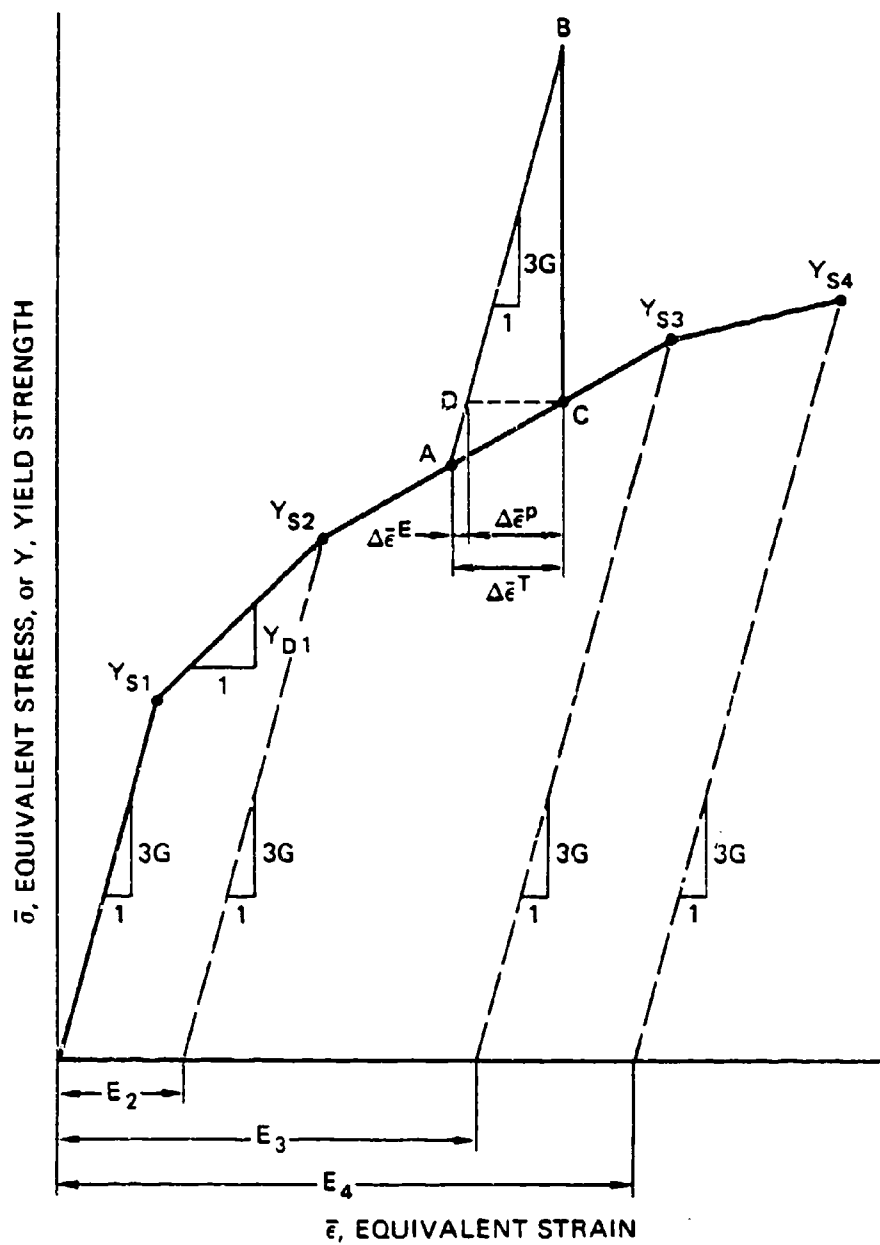
$$\bar{\sigma} = \sqrt{\frac{3}{2} \left(\sigma_{11}^2 + \sigma_{22}^2 + \sigma_{33}^2 \right) + 3\sigma_{12}^2} \quad (D1)$$

where σ'_{ij} are deviator stresses. The abscissa is an equivalent strain $\bar{\epsilon}$, a scalar measure of the distortional strains.

$$\bar{\epsilon} = \int d\bar{\epsilon} \quad (D2)$$

$$d\bar{\epsilon} = \sqrt{\frac{2}{3} \left(d\epsilon_{11}^2 + d\epsilon_{22}^2 + d\epsilon_{33}^2 \right) + \frac{4}{3} d\epsilon_{12}^2} \quad (D3)$$

The definitions of $\bar{\sigma}$ and $d\bar{\epsilon}$ are written so that $\bar{\sigma}$ is the axial stress and $\bar{\epsilon}$ is the axial plastic strain for a uniaxial test.



MA-6110-90A

FIGURE D1 DEFINITION OF QUANTITIES FOR MULTISEGMENTED WORK-HARDENING CURVE

The data for the model are inserted as a series of yield strain points (Y_i, ϵ_i). In the first interval the yield curve has the linear form

$$Y = Y_1 + A_1 \epsilon \quad (D4)$$

In all subsequent intervals the power law form is used

$$Y = A_i (\epsilon_i)^{n_i} \quad (D5)$$

For convenience in using the program, only the yield curve points are input data: the parameters A_i and n_i are initialized in the subroutine.

During initialization the points in the yield curve are read in and then A_i and n_i are computed. For the first interval, $n_i = 1.0$, and

$$A_1 = \frac{Y_2 - Y_1}{\epsilon_2} \quad (D6)$$

and ϵ_1 is required to be zero. In subsequent strain intervals, n_i and A_i are initialized by comparing the yield strengths at each end of the strain interval.

$$\begin{aligned} Y_{i-1} &= A_i (\epsilon_{i-1})^{n_i} \\ Y_i &= A_i (\epsilon_i)^{n_i} \end{aligned} \quad (D7)$$

Hence

$$n_i = \frac{\ln Y_i / Y_{i-1}}{\ln \epsilon_i / \epsilon_{i-1}} \quad (D8)$$

and

$$A_i = Y_i / \left(\epsilon_i \right)^{n_i} \quad (D9)$$

With these preparatory calculations, the computations for each cell are made very quickly using Eqs. (D4) or (D5).

APPENDIX E

AN ANALYTICAL TRANSFORMATION OF SURFACE COUNTS
TO A VOLUME SIZE DISTRIBUTION

Surface counts of voids or cracks in a single plane often lead to cumulative size distributions with an exponential form. For this case an approximate analytical transformation can be made to a volume size distribution that is also exponential. This analytical transformation is outlined here.

The surface crack or void size distribution is assumed to be in the form

$$n(r) = n_0 e^{-r/r_1} \quad (E1)$$

where

$n(r)$ is the cumulative number per unit area with observed radii greater than r

n_0 is the total number per unit area in the distribution

r_1 is the shape parameter of the distribution.

Hence, it is assumed that the count data have been fitted to Eq. (E1) to obtain the parameters n_0 and r_1 .

The desired volume size distribution has the form

$$N(R) = N_0 e^{-R/R_1} \quad (E2)$$

where

$N(R)$ is the number per unit volume with true radii greater than R

N_0 is the number per unit volume

R_1 is the shape parameter of the distribution.

The transformation of Eq. (E1) was performed numerically with BABS1, a computer program based on the transformation analysis of Scheil^{10,11}. Then the resulting $N(R)$ values were nondimensionalized and plotted. These distributions were then fitted to the exponential function in Eq. (E2) to determine N_0 and R_1 .

The transformed volumetric distributions were nondimensionalized and plotted as $r_1 N(R)/n_0$ versus R/r_1 . The results are shown in Fig. E1 for $r_1 = 2$ and $r_1 = 4$; The two sets of points were indistinguishable except at large R/r_1 . The differences at large R/r_1 are probably caused by inaccuracies in the BABS1 transformation.

Having the computed points of a volumetric size distribution, we next fit these points to the exponential form in Eq. (E2). Because of the nonlinearity of the volumetric distribution, subsets of the distribution were selected. For a fit over one decade in N , the parameters are

$$N_0 = 0.94 n_0 / r_1$$

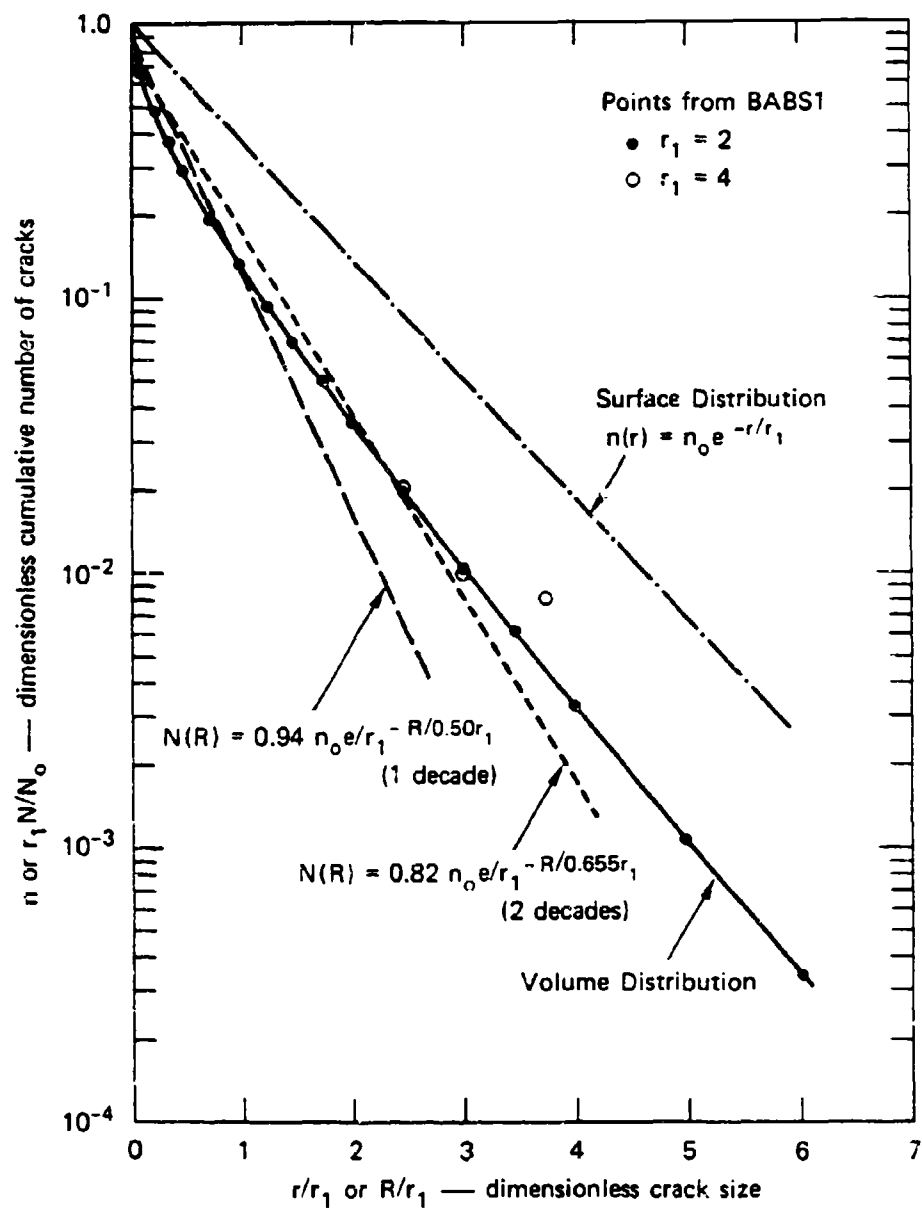
$$R_1 = 0.50 r_1,$$

and for two decades in N , the parameters are

$$N_0 = 0.82 n_0 / r_1$$

$$R_1 = 0.655 r_1$$

With these fitted results, an approximate transformation to a volumetric size distribution can be made very quickly.



MA-7893-105

FIGURE E1 VOLUME COUNTS N, R COMPUTED FROM THE AREA COUNT $n = n_0 e^{-r/r_1}$

APPENDIX F
FEATURES OF COMPOSITE HEMP

Progress has been made toward developing a two-dimensional wave propagation code for penetration calculations by combining the best features of several codes. The basic structure is that of the HEMP code, but a free-form data input technique like that available with a few versions of HEMP has been incorporated. Other additions include automatic rezoning, an advanced slide line treatment, a new time step control, and finite-element numbering. These five features are outlined in this appendix. The code is still under development, so it is anticipated that some of these features will be modified later. As a background for these features, the physical and numerical basis for wave propagation calculations is given first.

Wave Propagation Calculations

The HEMP programs are all based on the solution of the Lagrangian equations governing motion of a continuous medium. The solution technique is called the method of artificial viscosity because of the introduction of viscous forces to permit a continuous-flow computation in regions of high stress gradients. Such regions are interpreted as locations of shock fronts, although no discontinuities occur in the computed flow field. With this artificial viscosity method, the equations of continuous flow can be used everywhere and no special equations are required at shock fronts. HEMP uses the leapfrog method of von Neumann and Richtmyer¹⁴ to integrate the flow equations. This method provides second-order precision in time and space without the use of second differences.

In the following paragraphs we first introduce the Lagrangian set of partial differential equations governing one-dimensional planar flow. These are then changed to integral and numerical form, and those requiring it are extended to multidimensional form. Then the solution procedure is outlined.

The Lagrangian partial differential equations to be solved for one-dimensional planar flow are

$$\left(\frac{\partial X}{\partial t}\right)_h = U \quad (\text{velocity}) \quad (\text{F-1})$$

$$\left(\frac{\partial U}{\partial t}\right)_h = -\frac{1}{\rho_0} \left(\frac{\partial T}{\partial h}\right)_t \quad (\text{momentum}) \quad (\text{F-2})$$

$$\left(\frac{\partial E}{\partial t}\right)_h = -T \left(\frac{\partial V}{\partial t}\right)_h \quad (\text{energy}) \quad (\text{F-3})$$

$$\left(\frac{\partial X}{\partial h}\right)_t = \frac{\rho_0}{\rho} \quad (\text{mass}) \quad (\text{F-4})$$

$$\begin{aligned} T &= P + \sigma' + Q & (\text{constitutive relations}) & (\text{F-5}) \\ &= f(E, \rho, \dots) \end{aligned}$$

where X = Eulerian or current position

t = time

h = Lagrangian or initial position

U = particle velocity

ρ, ρ_0 = current and original density

T, σ' = total mechanical stress and deviator stress in the direction of propagation

V = $1/\rho$, specific volume

P, Q = pressure and artificial viscous stress

E = internal energy.

These equations relate velocity to coordinate motion; provide for conservation of momentum, energy, and mass; and give the stress-strain or constitutive relations.

Now each of these five equations is examined, extended to two or three dimensions, and put into numerical form. The velocity relation, Eq. (F-1), is expanded to a vector form

$$\left(\frac{\partial x_i}{\partial t} \right)_h = U_i \quad (F-6)$$

where i runs over the three coordinate directions and h refers to all three directions. In numerical form the integral of Eq. (F-6) is simply

$$x_{ij}^{n+1} = x_{ij}^n + U_{ij}^{n+1/2} \Delta t^{n+1/2} \quad (F-7)$$

Here n and $n+1$ refer to times t^n and t^{n+1} and j refers to the node number. Velocity U and time increment Δt are labeled to indicate that they are centered midway between t^n and t^{n+1} .

The momentum equation (F-2) takes the following three-dimensional form:

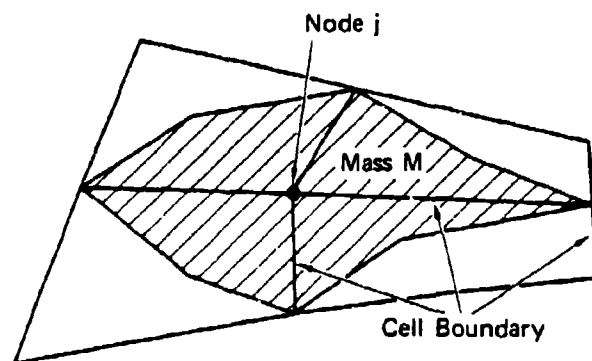
$$\left(\frac{\partial U_i}{\partial t} \right)_h = - \frac{1}{\rho_o} \left(\frac{\partial T_{ix}}{\partial h_x} + \frac{\partial T_{iy}}{\partial h_y} + \frac{\partial T_{iz}}{\partial h_z} \right) \quad (F-8)$$

Here i again takes the values x , y , and z , and h_x , h_y , h_z are Lagrangian coordinates. Several strategies such as those in HEMP, TOODY, and STEALTH are available in the literature for putting Eq. (F-8) into suitable numerical form. Instead of using any of these, we return to a simple integral form of (F-8):

$$\left(\frac{\partial U_i}{\partial t} \right)_h = \frac{\Sigma F_i}{M} \quad (F-9)$$

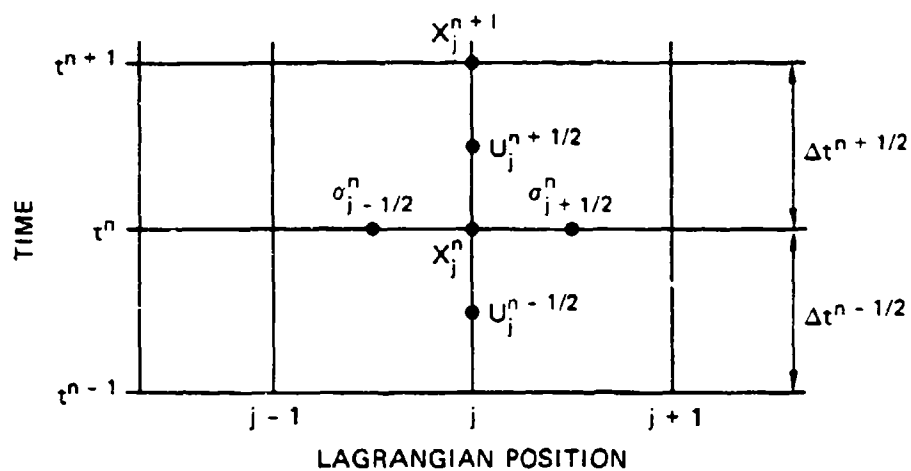
which is clearly $F = Ma$. The mass M is one-half of the sum of the masses of the cells surrounding the node j as indicated in Figure F1. The summation over F is constructed from the i -th components of the products of the stresses in each cell times the area (of the mass M) on which they act. These i -th components of the forces can be written as a stress times a projected area

$$F_i = T_{ik} \Delta A_k \quad (F-10)$$



MA-7893-133

FIGURE F1 CONFIGURATION OF FOUR CELLS SURROUNDING
NODE j AND ITS ASSOCIATED MASS M



MA-7893-134

FIGURE F2 GRID FOR LEAPFROG CALCULATIONS SHOWING INCREMENTS
IN SPACE AND TIME

Hence we have effectively found a discretization for the derivatives in Eq. (F-8)

$$-\frac{1}{\rho_0} \frac{\partial T_{ik}}{\partial h_k} \longrightarrow \frac{T_{ik} \Delta A_k}{M} \quad (F-11)$$

Hence in the indicial notation of Eq. (F-7), Eq. (F-8) becomes

$$U_{ij}^{n+1/2} = U_{ij}^{n-1/2} + \frac{\Delta t^n}{M_j} \sum_{\ell, k} T_{ik\ell} \Delta A_{\ell k} \quad (F-12)$$

Here the subscript ℓ refers to the four cells (in two dimensions) surrounding the j -th node. In planar two-dimensional flow, the sum will contain eight terms for each direction i . The time increment Δt^n is

$$\Delta t^n = t^{n+1/2} - t^{n-1/2} = \frac{\Delta t^{n+1/2} + \Delta t^{n-1/2}}{2} \quad (F-13)$$

Although (F-12) is obtained from a finite element viewpoint, it agrees exactly with the results of finite-difference derivations for planar two-dimensional flow. Differences arise only in axisymmetric flow.

The energy equation (F-3) is rewritten in tensor form as

$$\frac{\partial E}{\partial t} = v \sum_{i,k} T_{ik} \frac{\partial \epsilon_{ik}}{\partial t} \quad (F-14)$$

where ϵ_{ik} is the strain tensor. For each cell this expression takes the numerical form

$$E^n = E^{n-1} + \bar{v}^n \sum_{i,k} \bar{T}_{ik}^n \Delta \epsilon_{ik}^{n-1/2} \quad (F-15)$$

Here the barred quantities are averages

$$\bar{v}^n = \frac{v^n + v^{n-1}}{2} \quad \text{and} \quad \bar{T}^n = \frac{T^n + T^{n-1}}{2}$$

The sum in Eq. (F-15) runs over four terms in two dimensions.

The expression for the conservation of mass (F-4) takes the simple form

$$\rho^n = \rho_0 \frac{\Delta V_0}{\Delta V^n} = \frac{M}{\Delta V^n} \quad (F-16)$$

where ΔV^n is the cell volume at time t^n .

The constitutive relation (F-5) is expanded to

$$T_{ik} = P + \sigma'_{ik} + Q \quad (F-17)$$

where P and Q remain scalar pressures.

In the leapfrog scheme of von Neumann and Richtmyer¹⁴, the five fundamental equations are not solved simultaneously, but in a prescribed order. This order is suggested in the diagram in Figure F2. First there are the cell calculations at the time t^n and mid-node positions $j - 1/2$ and $j + 1/2$:

$$\rho^n, \Delta \epsilon^n, E^n, T^n.$$

These are followed by the node point calculations:

$$u_j^{n+1/2}, x_j^{n+1}$$

These steps are undertaken for each cell and node. Then the time is incremented and the process is repeated. In composite HEMP, these calculations are performed in two separate loops: one over all cells and one over all nodes. This separation of the loops was dictated by the finite element numbering procedure. In the section on time-step control, this separation of cell and node loops will be seen to have a significant advantage over the usual combined loop.

Data Input

The data are provided to composite HEMP in a free-field form like that required for the HEMP version at AMMRC and the version sent to BRL from SRI in 1979. In this form each number is provided with an alphanumeric label. The data items can be inserted in a nearly arbitrary order. Position of the labels and numbers on a line are also fairly arbitrary. Some sample input decks are presented and described below, the rules for

constructing the input are given, and the method used in the code for interpreting this input is outlined.

Sample Input

The data input is grouped under several type labels: TITLE, GENERAL, MATERIAL, BLOCK, BOUNDARY, HISTORY, AND REZONE. Specific input parameters and labels are provided under each of these type labels as shown in Table F-1. An example of this input is shown in Figure F3. The first line is the TITLE line and need not contain the word TITLE. All other data must be preceded on each line by one of the type labels. For example, on the line beginning with GENERAL in Figure F3, AMAT is the label for the material name, RHO is the label for the density, 7.85. The next lines begin with \$, the continuation symbol. Some labels, such as ABC under BOUNDARY, can precede a series of numbers.

The problem described by the data in Figure F3 is also illustrated by a sketch there. A steel plate is impacting a circular trough from the left. The BLOCK data provide the configuration as one quadrilateral contained within four points given in counterclockwise order. BLOCK also specifies the initial velocities, number of cells in each direction, and the material. The BOUNDARY specifications provide the line of symmetry ($Y = 0$) and the configuration of the trough (given by 10 points). Histories of several quantities are requested at a number of points in the plate. The data include a request for a complete rezoning every five cycles, leaving the points on the line of symmetry and the rear of the projectile untouched.

Data Input Rules

The following general rules have been developed to govern all input.

- Each line is in the form: "typelabel label number label number" or "typelabel label number number number"
- Labels and numbers must be separated by one or more of the three characters: blank, equal sign, and comma.
- Numbers may be provided in integer, decimal, or exponent form and may be positive or negative. Repeated numbers

Table F1

INPUT PARAMETERS AND DEFINITIONS

<u>Parameter</u>	<u>Block (Type Label)</u>	<u>Definitions</u>
A	HISTORY	Area, cm^2
AM	HISTORY	Mass assigned to a nodal point, g or g/cm
AMAT	MATERIAL	Name of material (alphanumeric)
BC,BCN	HISTORY	Boundary condition indicators
CLIN	GENERAL	Coefficient of linear artificial viscosity, nominally 0.05
COMC	HISTORY	Array for cell variables
CQSQ	GENERAL	Coefficient of quadratic artificial viscosity, nominally 4.0
D	HISTORY	Density, g/cm^3
DEXX, DEYY,DEZZ	HISTORY	Strain increments in the X, Y, or Z directions
DEXY	HISTORY	Tensor shear strain increment in the X-Y plane
E	HISTORY	Internal energy, erg/g
EQSTC	MATERIAL	Bulk modulus, dyn/cm^2
EQSTD	MATERIAL	Second coefficient in series for bulk modulus, dyn/cm^2
EQSTE	MATERIAL	Sublimation energy, erg/g
EQSTG	MATERIAL	Grüneisen ratio
EQSTH	MATERIAL	Gas Grüneisen ratio
EQSTN	MATERIAL	Exponent in expansion equation of state

Table F1 (continued)

<u>Parameter</u>	<u>Block (Type Label)</u>	<u>Definitions</u>
EQSTS	MATERIAL	Third coefficient in series for bulk modulus, dyn/cm ²
ESC	MATERIAL	Material property array
EXX, EYY,EZZ	HISTORY	Strain in the X, Y, or Z direction
EXY	HISTORY	Tensor shear strain in the X, Y plane
FX,FY	HISTORY	Forces in the X, Y directions assigned to a nodal point, dyn or dyn/cm
G2	MATERIAL	Twice the shear modulus, dyn/cm ²
IDIR	BOUNDARY	Direction of definition for a wall or slide line: positive for master material or wall on left when facing in direction of increasing node point numbers
IPRINT	GENERAL	Cell and node listings are provided at time steps that are multiples of IPRINT, nominally 10
MAT	BLOCK	Number of the material in the quadrilateral
MU	MATERIAL	Shear modulus, dyn/cm ²
NBCPI	BOUNDARY	Number of points in the XBC, YBC array for a wall condition
NBCTYP	BOUNDARY	Boundary condition type: 1 - simple control on X or Y 3 - slide on wall 4 - slide on wall, can leave wall and impact 5 - sticks to wall 6 - sticks to wall, can leave wall and impact

Table F1 (continued)

<u>Parameter</u>	<u>Block (Type Label)</u>	<u>Definitions</u>
NC12, NC23	BLOCK	Number of cells between 1st and 2nd and between 2nd and 3rd points in the quadrilateral
NFREQ	REZON	The rezoning pattern on four consecutive cycles begins at time steps that are multiples of NFREQ
NGEOM	GENERAL	Problem geometry: 1 for planar, 2 for axisymmetric
NMAX	GENERAL	Maximum number of time steps in the calculation
P	HISTORY	Pressure, dyn/cm^2 , positive in compression
PMIN	MATERIAL	Minimum (tensile) pressure permitted, a spall cutoff, dyn/cm^2
REZMIN	REZON	Minimum amount of node motion that is considered in rezoning, nominally 0.02
REZWT	REZON	Fraction determining the amount of computed rezone motion to apply to a node, nominally 0.5
RHO	MATERIAL	Initial density (distinguished from RHOS for a porous material), g/cm^3
RHOS	MATERIAL	Initial density of a solid, g/cm^3
SBAR	HISTORY	Equivalent stress, $\bar{\sigma}$, dyn/cm^2
SPRIN1, SPRIN2, SPRIN3	HISTORY	Principal stresses in first, second, and third directions, dyn/cm^2 , positive in tension
SP2	HISTORY	Sound speed squared, cm^2/sec^2

Table F1 (continued)

<u>Parameter</u>	<u>Block (Type Label)</u>	<u>Definitions</u>
STOPT	GENERAL	Maximum problem time in the calculation, sec
SXX, SYY,SZZ	HISTORY	Thermodynamic stress in the X, Y, or Z directions, dyn/cm ²
TH	HISTORY	Rotation, radians, positive counter-clockwise
TRIQ	GENERAL	Coefficient of triangular artificial viscosity, nominally 0.02
TXX, TTY,TZZ	HISTORY	Total stresses in the X, Y, or Z directions, dyn/cm ² , positive in tension
TXY	HISTORY	Shear stress on X or Y planes, dyn/cm ² , tensile positive sign conversion
WBFR	MATERIAL	Array of special fracture properties
WCMP	MATERIAL	Indicator for a composite material model
WDS	MATERIAL	Indicator for a deviator stress model
WEQS	MATERIAL	Number of material property parameters used, usually at least 30
WFR	MATERIAL	Indicator for a fracture model
WH	HISTORY	Condition indicator
WMAT	HISTORY	Material number
WPOR	MATERIAL	Indicator for a porous material model
WTSR	MATERIAL	Array of special material properties

Table F1 (continued)

<u>Parameter</u>	<u>Block (Type Label)</u>	<u>Definitions</u>
WVAR	MATERIAL	Number of extra variables requested for each cell
X, Y	HISTORY	Nodal positions, cm
XA,YA	BLOCK	Four coordinates of a quadrilateral listed in counterclockwise order, cm
XAFECT, YAFECT	REZON	Nonzero values indicate that the X or Y value should not be rezoned
XAFECT	BOUNDARY	Type of boundary condition control used with NBCTYP = 1: 1 X greater than or equal to XBC 2 X less than or equal to XBC 3 X equal to XBC 4 or 0 X free
XBC, YBC	BOUNDARY	Point or points defining a boundary condition, cm
XCONST, YCONST	BOUNDARY	X and Y values used in defining boundary points to be affected by a particular boundary condition, cm
XCONST, YCONST	REZON	X and Y values used in defining points to be affected by a rezoning restriction, cm
XD, YD	HISTORY	Nodal velocities, cm/s
XDNOT, YDNOT	BLOCK	Initial velocities of a quadrilateral, cm/s
XO, YO	HISTORY	Initial nodal positions, cm
YAD	MATERIAL	Work hardening modulus, dyn/cm ²

Table F1 (concluded)

<u>Parameters</u>	<u>Block (Type Label)</u>	<u>Definitions</u>
YAFECT	BOUNDARY	Type of boundary condition control used with NBCTYP = 1: 0 or 1 Y greater than or equal to YBC 2 Y less than or equal to YBC 3 Y equal to YBC 4 Y free
YC	MATERIAL	Initial yield strength, dyn/cm ²
YY	HISTORY	Yield stress, dyn/cm ²
Z	HISTORY	Mass, g or g/cm

C. HEMP TEST NO. 3 PROJECTILE IMPACT AT 1500 M/SEC INTO A CIRCULAR TROUGH

```

GENERAL IPRINT=10      NMAX=20      STOPT=1.0
$      CLIN=0.05      CUSQ=0.0      TRIQ=0.02

MATERIAL AMAT=STEEL      NEG3=50.0      NYAM=1.0      RHO=7.85
$      E3TC=1.59E+12      E3TD=5.17E+12      E3TS=5.17E+13      E3TG=1.69
$      YC=1.03E+10      MU=0.19E+11

BLOCK YDNOT=0.0      XDNOT=1.5E+5
$      XA=-4.93774      13.06226      13.06226      -4.93774
$      YA      0.0      0.0      4.0      4.0
$      NC12=15      NC23=5      MAT=1

BOUNDARY NBCTYP=1
$      YCONST=0.0      XAFECT=0.0      YAFECT=3.0

BOUNDARY NBCTYP=4      IDIR=1      NBCTP=10
$      XBC 5.0 5.0 9.0782 9.5 10.7851 11.8944 13.06226 13.4572
$      XBC 13.8633 14.0
$      YBC 10.0 9.0 9.4572 7.7942 6.8944 5.7851 4.0 3.0782
$      YBC 1.5628 0.0
$      XCONST=13.06226      XAFECT=0.0      YAFECT=0.0

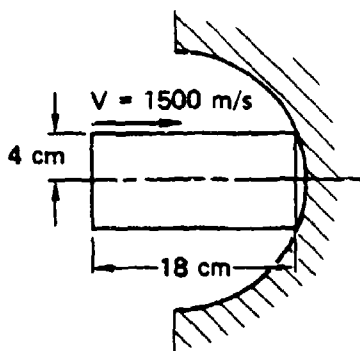
BOUNDARY NBCTYP=4      IDIR=1      NBCTP=10
$      XBC 5.0 5.0 8.0782 9.5 10.7851 11.8944 13.06226 13.4572
$      XBC 13.8633 14.0
$      YBC 10.0 9.0 8.4572 7.7942 6.8944 5.7851 4.0 3.0782
$      YBC 1.5628 0.0
$      YCONST=4.0      XAFECT=0.0      YAFECT=0.0

BOUNDARY NBCTYP=1      XBC 14.0
$      XCONST=13.06226      YCONST=0.0      XAFECT=2.0      YAFECT=3.0

HISTORY ITX D P 13.0 0 13.0 4.0 EXX COM2 12.0 1.0 CUMN16 XD YO
$      10.0 3.5 10.0 1.5

REZONE NFREQ=5      REZMIN=0.01      REZMT=0.5
$      YCONST=0.0      YAFECT=2.
$      XCONST=-4.93774      XAFECT=1.      YAFECT=2.

```



MA-7893-122

FIGURE F3 DATA INPUT AND GEOMETRY FOR A STEEL PROJECTILE IMPACTING A RIGID CIRCULAR TROUGH

may be inserted with a star as the repeat symbol. Thus 3*2.6 means three values of 2.6.

- A dollar sign can be used to replace a repeated typelabel.
- Abbreviated labels and typelabels may be used if they are unique: M may be used for MATERIAL but BL instead of B is the shortest abbreviation for BLOCK because BOUNDARY also starts with B.
- Expanded labels such as BLOCKTARGETRHA may also be used if they contain no separators.

In addition to these general rules, there are special interpretations used for input under each typelabel.

The BLOCK input is read by the subroutine BLOCK, which also initializes the X, Y arrays for cells and nodes. This layout occurs whenever all the data for a block have been read. BLOCK determines that a block is complete when another typelabel BLOCK is encountered (not merely a repeat symbol) or when additional values of any of the quantities XA, YA, XDNOT, YDNOT, MAT, NC12, or NC23 is encountered. The input "SLIDE 1 TO 3" permits a disconnection between the nodes from the first to third corners of a quadrilateral block. Thus a slide line is provided between this block and a previously described block.

Two kinds of data are provided under the typelabel BOUNDARY: those governing the nature of the boundary condition and those describing the nodal points affected. Boundary types are designated by NBCTYP with the meanings given in Table F1. NBCTYP must precede all other BOUNDARY data for each type. The labels XAFECT and YAFECT are used with NBCTYP 1 to specify the control desired for X and/or Y quantities. XBC and YBC are arrays containing coordinates of a boundary line. The individual nodes or lines of nodes affected by the boundary conditions are provided by X, Y values labeled XCONST and YCONST. The boundary condition indicators at all nodes are updated following the reading of a line containing XCONST and/or YCONST. Hence the other boundary data such as XBC, YBC, and IDIR should precede XCONST and YCONST. Also only one XCONST and/or YCONST set should be inserted on a line. Because of the immediate effect on the layout, the BLOCK data must precede BOUNDARY data.

The HISTORY data permit a request for histories of cell or node quantities at a series of X, Y locations. Following reading of this input, the subroutine HISTORY selects the cell center or node point nearest the designated X and Y point for each history. Note that the requested quantities need not be array variables. The requested quantities are stored in arrays during the cell and node loops in subroutine CYCLE and then printed as histories by EDIT at the end of a calculation.

For the MATERIAL input, AMAT must be the first label encountered for each new material: AMAT triggers the counter that keeps track of the material number and storage locations allotted for the material, and it initializes some indicators. In Figure F4 the input deck contains some special labels: SHEAR and EXPLODE. These labels call for the material model subroutines by the same names. These subroutines read the data preceded by these labels.

In the MATERIAL arrays, the two indicators WEQS and WVAR designate the space to be allocated for the material data. WEQS indicates the number of equation of state constants (such as density, moduli, sound speed) and indicators required to describe the material. These quantities are stored sequentially in the COM2 array. WVAR gives the number of additional variables required for each cell. Usually there are 19 variables per cell in the COM1 array: these include a yield strength, cell rotation, and a condition indicator, as well as mass, stress, density, and other quantities. If more variables are required to describe quantities such as porosity, fracture processes, or dislocations, these are provided by setting WVAR to the number needed.

Two types of data are provided to govern rezoning: those governing the nature of the rezoning and those designating the nodes to be rezoned. The REZONE input must follow the block data because WREZ, a nodal quantity, is set following reading of each line containing the XCONST and/or YCONST values. Several lines of XCONST and YCONST values can be inserted to control rezoning at nodes or lines of nodes. The labels XAFECT and YAFECT mean that X and Y, respectively, are not to be changed

C. HEMP FRAGMENTING ROUND OF 4340 STEEL, SHOT 8

```

GENERAL IPRINT=100      NMAX=700      STOPT=1.E-4
$ CLIN=0.1              COSQ=4.0      TRIO=0.02
$ NGEOM=2

MATERIAL AMAT=PETH      NEQS=12      RHO=0.539
$ NPAR=1                NVAR=2        EQSTG=0.93
$ EXPLODE NTYPE=12      QEXPL=3.E10  XDET=5.0      DIST=0.5

MATERIAL AMAT=4340STEEL NEQS=30      RHO=7.85
$ NPAR=3                NVAR=93
$ EQSTC=1.59E12          EQSTD=5.17E12 EQSTS=5.15E13
$ EQSTE=7.36E10          EQSTG=1.69   EQSTM=0.25
$ SHEAR BFR=21=0., 10., 35., 0.01, 10., 0.15, 0.07, 0.04
$ SHEAR BFR2=0.25, .577, 2., 2., 0., 10.
$ SHEAR FNUC=1., 1., 1., 1.
$ SHEAR NTYPE=2          NRRANGE=3
$ SHEAR YS=1.03E10, 1.07E10, 1.37E10
$ SHEAR ES=0., 0.03, 1.0
$ SHEAR YC=1.03E10      MU=0.19E11

MATERIAL AMAT=PMMA(KOHN) NEQS=30      RHO=1.18
$ NPAR=2                NVAR=93
$ EQSTC=8.94E10          EQSTD=4.57E10 EQSTS=4.36E11
$ EQSTE=1.E10            EQSTG=1.      YC=1.E6      MU=1.45E10

MATERIAL AMAT=4140STEEL NEQS=30      RHO=7.85
$ NPAR=2                NVAR=93
$ EQSTC=1.59E12          EQSTD=5.17E12 EQSTS=5.17E13
$ EQSTE=7.36E10          EQSTG=1.69   MU=0.19E11
$ YC=6.E9

MATERIAL AMAT=LEAD(KOHN) NEQS=30      RHO=11.4
$ EQSTC=5.01E11          EQSTD=4.99E11 EQSTS=2.02E12
$ EQSTE=9.16E9           EQSTG=2.2

BLOCKEXP XA=0.035      13.335      13.335      0.035      MAT=1
$ YA=0.                0.          2.28       2.28
$ NC12=40              NC23=6

BLOCK4340 XA=0.        15.24       15.24       0.          MAT=2
$ YA=2.28              2.28       3.42       3.42
$ NC12=25              NC23=1
$ SLIDE 1 TO 2

BLOCKPMMA XA=0.        15.24       15.24       0.          MAT=3
$ YA=3.42              3.42       4.37       4.37
$ NC12=25              NC23=1

BLOCKSTEEL XA=0.       15.24       15.24       0.          MAT=4
$ YA=4.37              4.37       10.16      10.16
$ NC12=25              NC23=2

BLOCKLEAD XA=0.        15.24       15.24       0.          MAT=5
$ YA=10.16             10.16      12.7       12.7
$ NC12=25              NC23=2

BOUNDARY NBCTYP=1      YCONST=0.      YAFECT=3

BOUNDARY NBCTYP=11     MASTER=2

HISTORY COMC22,         COMC24,         COMC25,         COMC40,
$ COMC41,              COMC48,         COMC49          5., 3.
$ 9., 3., 12., 3.

```

MA-7893-123

FIGURE F4 DATA INPUT FOR A RUNNING DETONATION IN A CONTAINED FRAGMENTING CYLINDER

by rezoning. The numerical values provided for XAFECT and YAFECT have no significance here.

Two more sample input decks are shown in Figures F5 and F6. These are for the first two test cases run with Composite HEMP.

Subroutines to Handle Input

The free field input form is handled by four subroutines (POP, FIND, BESTMATCH, and UNPACK) plus special data-insertion statements in the initialization subroutines. POP reads the data lines one character at a time, examines these characters, and assembles them into arrays of labels (LABEL) and numbers (RLABEL). FIND is called to compare labels in the data line with the standard labels of each subroutine to determine which variable is being initialized. If no exact match is found, FIND calls BESTMATCH to examine parts of the labels. BESTMATCH first calls UNPACK to separate the input and standard labels into separate characters. Then BESTMATCH counts how many matches there are between characters in the input label and each of the standard labels. The initialization routine GENR controls reading and calls appropriate routines such as BLOCK to accept the input data. BLOCK examines the LABEL values with the aid of FIND and assigns the numbers in RLABEL to the correct constants or arrays.

Discussion

The free field input form sketched above has several advantages over the traditional fixed location format used with most wave propagation codes. This format is especially convenient to use on a video screen where column positions are not provided. Only the required data are inserted; standard data are provided by default and unneeded variables are omitted. Because all data are labeled, the input tends to be easily understood and confusion is minimized. The use of abbreviations and extended names provides added convenience to the programmer. When new variables are needed, they can be readily added by appending new

C. HEMP FIRST 1-D RUN IMPACT STEEL ON STEEL

GENERAL IPRINT=1 NMAX=50 STOPT=1.0
\$ CLIN=0.05 COSQ=4.0 TRIQ=0.02
\$ NGEOM=1

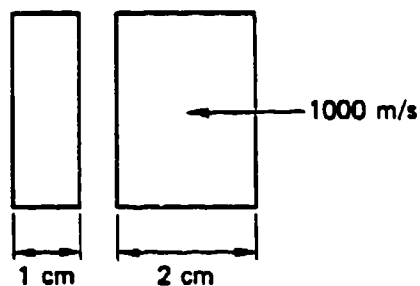
MATERIAL AMAT=STEEL RHO=7.85 WEQS=30
\$ EQSTC=1.59E12 EQSTD=5.17E12 EQSTS=5.17E13
\$ EQSTG=1.69 YC=1.03E10 MU=8.19E11

BLOCK XA=0. 0.2 0.2 0. MAT=1
\$ YA=0. 0. 1.0 1.0
\$ NC12=1 NC23=5

BLOCK XA=0. 0.2 0.2 0. MAT=1
\$ YA=1.0 1.0 3.0 3.0
\$ NC12=1 NC23=10 YDNOT=-1.E5

BOUNDARY NBCTYP=1 XCONST=0. XAFECT=3

BOUNDARY NBCTYP=1 XCONST=0.2 XAFECT=3



MA-7893-124

FIGURE F5 DATA INPUT AND GEOMETRY FOR A ONE-DIMENSIONAL IMPACT OF TWO STEEL PLATES

C. HEMP FIRST 2-D RUN IMPACT STEEL ON STEEL

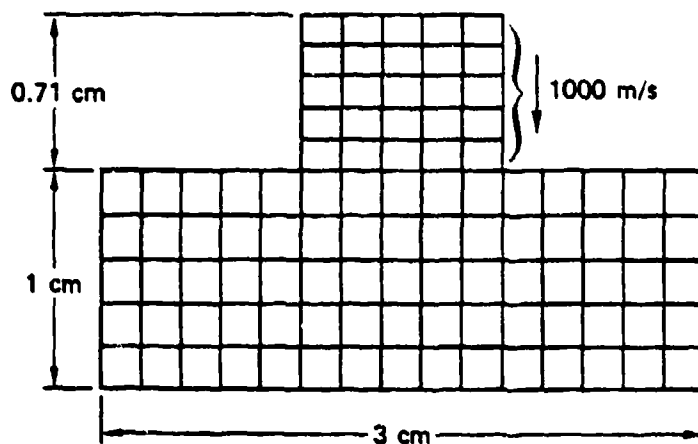
GENERAL IPRINT=5 NMAX=50 SIOPT=1.0
 \$ CLIN=0.05 CQSQ=4.0 THIQ=0.02
 \$ NGEOM=1

MATERIAL AMAT=STEEL RHO=7.85 WEQS=30
 \$ EQSTC=1.59E12 FQSTO=5.17E12 EQSTS=5.17E13
 \$ EQSTG=1.69 YC=1.03E10 MU=8.19E11
 \$ WVAR=2

BLOCKTARGET XA=0. 3.0 3.0 0. MAT=1
 \$ YA=0. 0. 1.0 1.0
 \$ NC12=15 NC23=5

BLUCKPROJ XA=1.0 2.0 2.0 1.0 MAT=1
 \$ YA=1.0 1.0 1.71 1.71
 \$ NC12=5 NC23=5 YUNOT=-1.E5

HISTORY TXX, EXX, P, 1.1 0.9, 1.3 0.9



MA-7893-125

FIGURE F8 DATA INPUT AND GEOMETRY FOR A TWO-DIMENSIONAL
 PLANE-STRAIN IMPACT OF TWO STEEL PLATES

labels to the lists available and adding replacement statements [such as `VARIABLE = RLABEL (LM3)`] in the appropriate initialization subroutine.

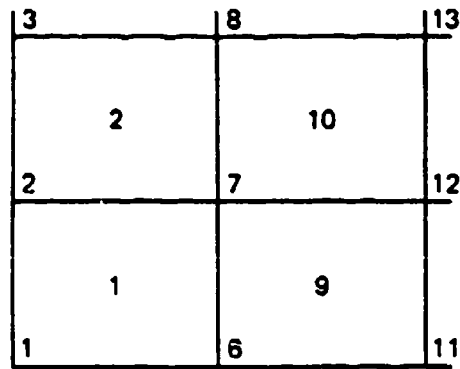
Finite-Element Numbering

With finite-element numbering, each cell and node is numbered independently of its position in the grid. This contrasts with the *i,j*-numbering common to most finite difference codes in which a fixed numbering relationship exists between each node or cell and its neighbors. This finite-element numbering allows a somewhat more flexible layout of cells in problems with complex shapes. It is essential for problems in which new cells or nodes are created as by wandering slide lines or by general rezoning (grid reconfiguration). The disadvantage is that the nodes around each cell and cells around each node must be individually designated because there is no automatic node-cell relationship as in the *i,j*-numbering system. Here we describe the indicator arrays required to show these relationships and then exhibit some cell layouts that are possible with the finite-element numbering.

Adjacency Arrays

During layout, the nodes and cells are numbered in the order in which they are constructed. A partial node and cell numbering for a quadrilateral is shown in Figure F7. During layout three special arrays are constructed to provide the needed adjacency relationships. The `WNOD` array of four integers designates the nodes surrounding each cell. For cell 10 in Figure F7, the `WNOD` array is 12, 13, 8, and 7. The nodes are provided in counterclockwise order.

The nodes and the cells around each node must be available to the rezoner: these integers are in the `WCELL` and `WNDND` arrays. For node 7, the surrounding cells are `WCELL` = 1, 9, 10, 2, and the nodes are `WNDND` = 2, 6, 12, 8. These sets of cell and node numbers are both in counterclockwise order. Also `WNDND(i)` and `WNDND(i+1)` are on either side of `WCELL(i)`. For node 6 only two cells are adjacent so these two arrays are



MA-7893-126

FIGURE F7 A PORTION OF A GRID SHOWING INDEPENDENT
NUMBERING OF NODES AND CELLS

WCELL = 9, 1

WNDND = 11, 7, 1.

In BLOCK these two arrays are filled with cell and node numbers in ascending order. Then ORDER is called by GENR to rearrange the elements of each array to produce the special relationships referred to above.

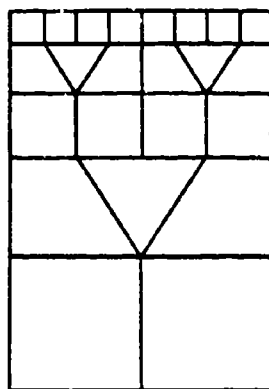
Grids Using Finite-Element Numbering

The finite element numbering provides some added flexibility in laying out the grid or in changing it during a calculation. Here we describe three situations: a problem where a varying grid size is required, a computation with a nonrectangular object, and a calculation with a moving slide line.

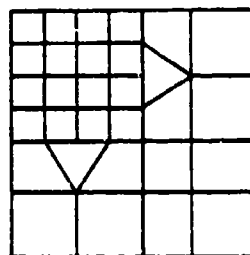
Often it is of interest to provide small cells in one region of a problem and large cells elsewhere. For accuracy, the cells should vary gradually from small to large and should remain nearly square. In general, these requirements cannot be met with an i,j-numbering procedure without introducing slide-line discontinuities in the grid. Even then the slide line is restricted to one direction (i or j, not both) so the cell size can be varied in only one direction. Figure F8 shows four cell configurations that permit gradual changes in cell sizes in one or two directions in a finite-element numbering scheme. Because of the irregular adjacency relations, these schemes cannot be used with i,j-numbering procedures. They all show regions in which the cell size varies 10% to 50%: this variation may be too rapid for wave propagation problems, but is satisfactory for intermediate rate problems such as projectile penetrations.

Odd-shaped objects such as projectiles and spheres are difficult to construct with nearly square cells with an i,j-numbering technique. Figure F9 shows a sphere (modeling a human head) with a finite-element numbering technique. Note that all cells are approximately equal in area and have aspect ratios near one.

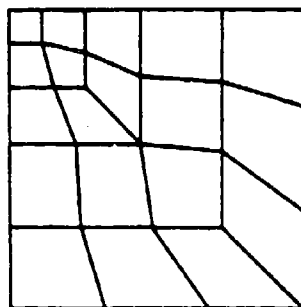
A third feature of codes that shows the need for finite-element numbering is the slide line, especially a slide line that propagates



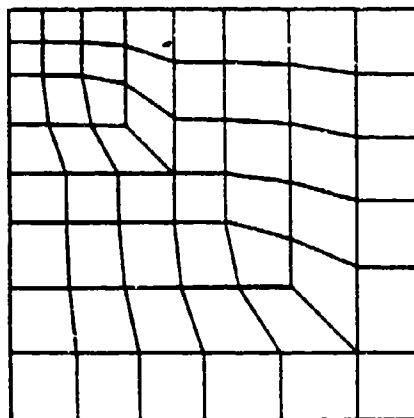
(a) A One-Directional Cell Size Variation



(b) One Possible Two-Directional Cell Size Variation Derived From the One-Directional Variation



(c) Pattern for a 25% Cell Size Increase Per Cell in Two Directions



(d) Pattern for a 10% Cell Size Increase Per Cell in Two Directions

MA-7893-127

FIGURE F8 CELL SIZE VARIATION PATTERNS THAT MAY BE USED WITH A FINITE-ELEMENT NUMBERING TECHNIQUE

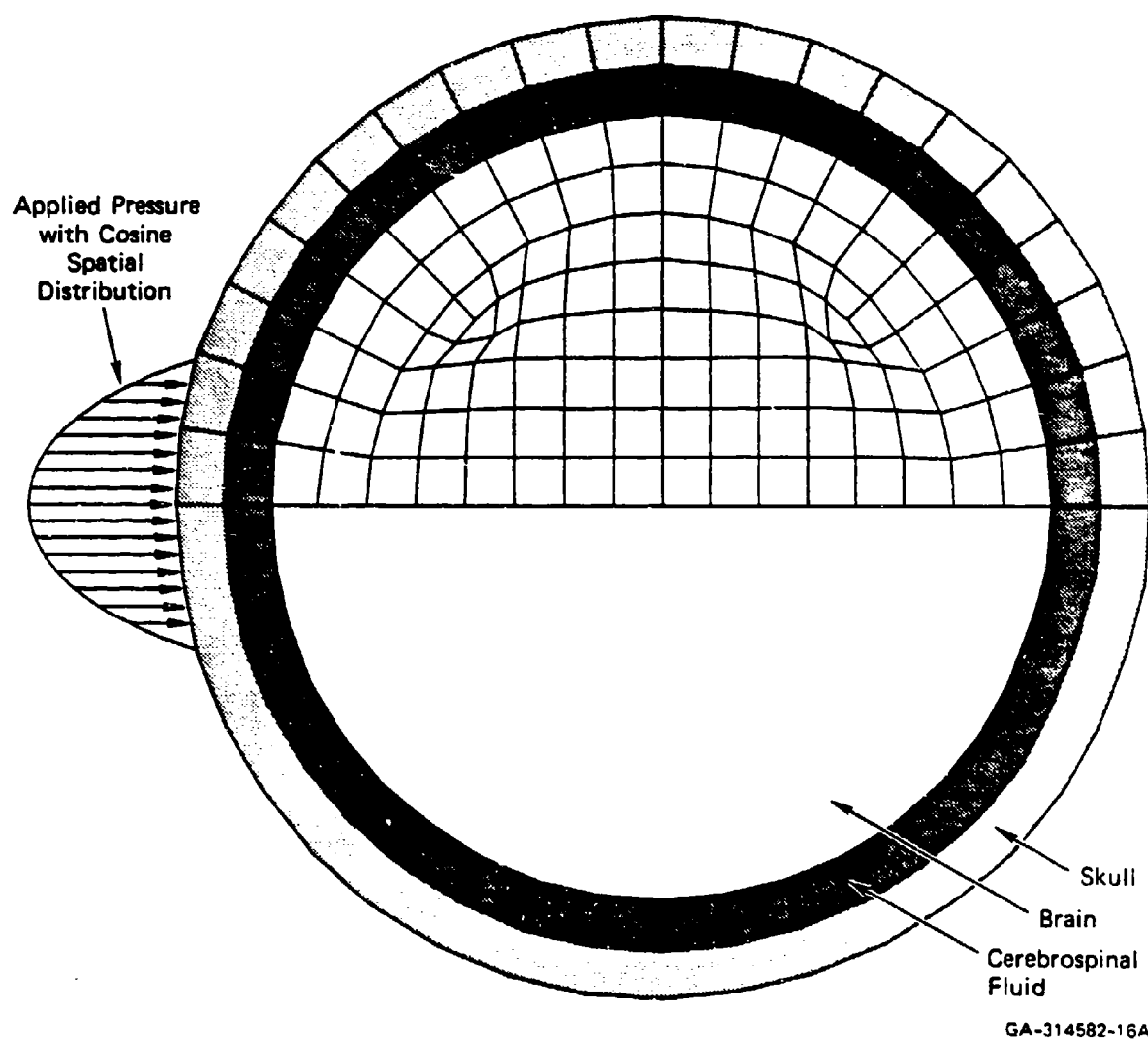


FIGURE F9 GEOMETRY OF HUMAN HEAD FOR STUDY OF IMPACT AND CONCUSSION
SHOWING FINITE-ELEMENT LAYOUT FOR CIRCULAR OBJECT

during the calculation along an irregular and unpredetermined direction. Such a general slide line is illustrated in Figure 10. As the slide line moves through the grid, we presume that it may move to any adjacent node along its general direction of travel. In some moves it merely separates cells. Then one node such as A must be divided into two to permit separate motions of the adjacent cells. However, if the slide line divides a quadrilateral as along BC into two triangles, additional nodes are required at B, C, D, and E. The nodes at D and E are needed to turn the new triangles back into quadrilaterals. Following the construction of new nodes, the WNODE, WCELL, and WNDND arrays of adjacent nodes and cells are revised to account for the new node. The new node (or cell) is merely added to the node (or cell) list and provided with the usual properties. None of these steps is trivial, but they can be accomplished without modifying the basic computational algorithm: the only changes are those required at the time of cell and node creation.

Time Step Control

A new time step control procedure was derived to prevent the excessive distortion that results in quadrilateral cells with negative area. The procedure is based on the Courant condition as usual, but includes several beneficial new features.

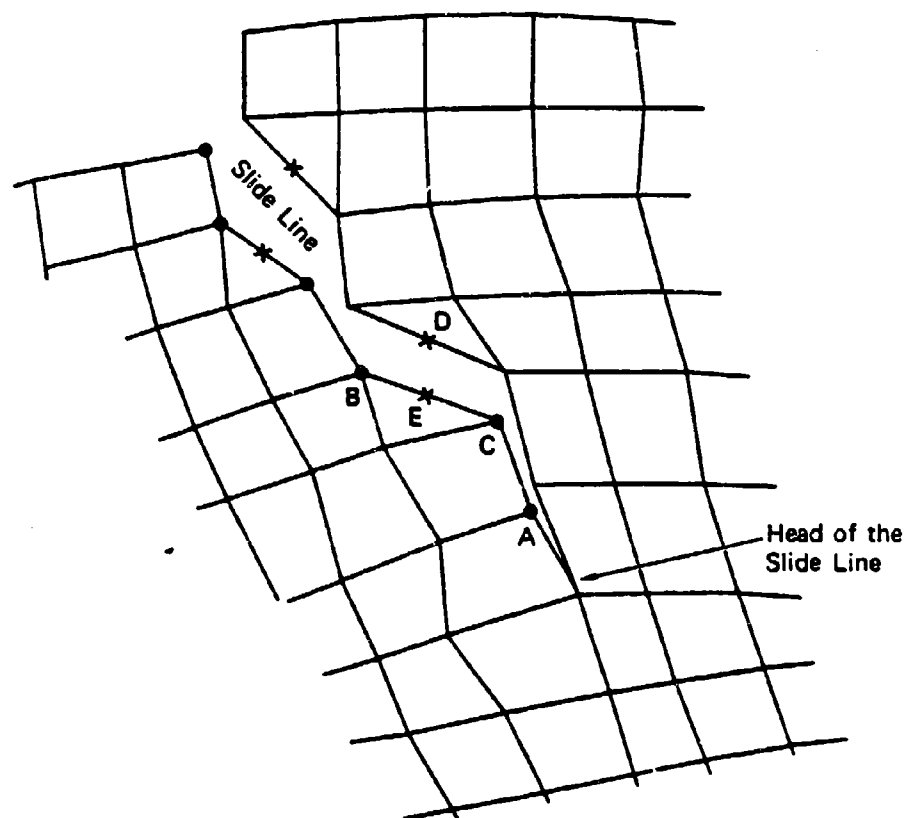
The Courant condition requires that the computational time step not exceed the time for stress waves to cross a cell. Thus the time step is

$$\Delta t \leq \frac{\Delta X}{C} \quad (F-18)$$

where ΔX is the cell dimension and C is the sound speed. This condition is required for stability of wave propagation calculations in which an explicit solution method is used, as in HEMP.

The time step control procedure is derived below, including

- Expansion of the Courant stability condition to allow treatment of general, time-dependent, stress-strain relations and the artificial viscous stress.



- Nodes added to permit separation of cells at nodes
- X Nodes added to maintain quadrilateral cells

MA-7893-128

FIGURE F10 POSSIBLE CONFIGURATION OF CELLS AND NODES ALONG A WANDERING SLIDE LINE REPRESENTING A GROWING CRACK OR SHEAR BAND

- Addition of a convective term, which is especially important in regions of large distortion and wherever particle velocity is comparable to sound speed.
- Extension of the Courant condition and convective correction from the usual one-dimensional form to a two-dimensional form.
- Placement of the time step calculation at a optimum location in the flow of the hydrodynamic computations to make the time step sensitive to the current cell configuration.

One computational result with the new time step control is given below to illustrate its effectiveness.

Courant Stability Condition

For one-dimensional hydrodynamic calculations, a fairly full investigation of the Courant condition has been undertaken by Richtmyer and Morton¹⁵ and by Herrmann et al.¹⁶ However, a further development is required for a situation in which more general, time-dependent, stress-strain relations are included in one- or two-dimensional calculations.

Here a new concept for stability is developed based on the hypothesis that all forms of stability depend simply on an effective sound speed. The addition of artificial viscosity or other types of viscosity tend to require shorter time steps in the calculations because they increase the effective sound speed. This effective sound speed is related to an effective modulus for the material as follows:

$$M_e = \frac{\Delta P + 2Q}{-\frac{\Delta V}{V}} + \frac{\frac{2}{3} \Delta \sigma_1}{\epsilon_1 - \frac{\Delta V}{3V}} \quad (F-19)$$

where

ΔP = the change in pressure at a given cell during the current time increment

Q = the artificial viscous stress

$\frac{\Delta V}{V}$ = the relative change in volume

$\Delta\sigma'_i$ = the change in deviator stress

ϵ_i = the strain in the i^{th} direction.

First a calculation is made for the one-dimensional problem to compare the results from the hypothesis above with that of the more usual approach followed by Herrmann et al.¹⁶. The linear and quadratic forms for the artificial viscosity are

$$Q = C_L \Delta X C \frac{\partial \rho}{\partial t} + \rho C_Q^2 \left(\frac{1}{\rho} \frac{\partial \rho}{\partial t} \right)^2 \Delta X^2 \quad (\text{F-20})$$

where

C_L, C_Q = coefficients of the linear and quadratic terms for artificial viscosity

ΔX = cell thickness

C = sound speed for elastic waves

ρ = density

t = time

This expression is used only if Q is positive, that is, for compression; Q is set to 0 for rarefaction waves. Equation (F-20) is transformed by using the identities relating density and specific volume, and the following equation describing mass conservation

$$\frac{1}{\rho} \frac{\partial \rho}{\partial t} = - \frac{\partial u}{\partial x} \quad (\text{F-21})$$

Equation (F-20) then takes the following form in which the absolute value sign is used with the change in particle velocity so that Q will be positive in compression.

$$Q = - \frac{\Delta V}{V} \rho \frac{\Delta X}{\Delta t} [C_Q^2 |\Delta u| + C_L C] \quad (\text{F-22})$$

where

V = the specific volume

Δt = the time increment used in the computations.

From Eq. (F-22), a modulus can be defined as in Eq. (F-19), that is,

$$M_Q = \frac{Q}{-\frac{\Delta V}{2V}} = 2\rho \frac{\Delta X}{\Delta t} [C_Q^2 |\Delta u| + C_1 C] \quad (F-23)$$

The factor 2 is inserted because the Q is computed at $\Delta t/2$, providing twice the stiffness that would occur if M_Q were averaged over the interval. Then the effective sound speed which will govern stability of the calculations, is from Eqs. (F-19) and (F-23)

$$\bar{c}^2 = \frac{M_e}{\rho} = \frac{\Delta P}{-\rho \frac{\Delta V}{V}} + \frac{2Q}{-\rho \frac{\Delta V}{V}} + \frac{\frac{2}{3} \Delta \sigma_1}{\rho \left(\epsilon_1 - \frac{\Delta V}{3V} \right)} \quad (F-24a)$$

$$= \frac{K}{\rho} + \frac{M_Q}{\rho} + \frac{\frac{4}{3} \mu}{\rho} \quad (F-24b)$$

$$= c^2 + 2(C_Q^2 |\Delta u| + C_1 C) \frac{\Delta X}{\Delta t} \quad (F-24c)$$

where

K = bulk modulus

μ = shear modulus

C = the usual sound speed based on these moduli.

For stable calculations, the Courant-Friedrichs-Lewy condition as follows is used to determine the time increment permitted

$$\Delta t \leq \frac{\Delta X}{\bar{c}} \quad (F-25)$$

where C^* is usually interpreted to be the local sound speed, but here it will be taken as the effective sound speed \bar{C} given by Eq. (F-24). Insertion of Eq. (F-24) into relation (F-25) gives

$$\Delta t^2 \leq \frac{\Delta X^2}{\bar{C}^2} = \frac{\Delta X^2}{C^2 + (C_Q^2 |\Delta u| + C_1 C) \frac{\Delta X}{\Delta t}} \quad (F-26)$$

When this quadratic is solved for the maximum time increment, the criterion is found to be

$$\Delta t \leq \frac{\Delta X}{\bar{C}} \left[- \left(C_Q^2 \left| \frac{\Delta u}{C} \right| + C_1 \right) + \sqrt{\left(C_Q^2 \left| \frac{\Delta u}{C} \right| + C_1 \right)^2 + 1} \right] \quad (F-27)$$

This expression is identical to that found on page 73 of reference 16. Hence the new concept does appear to give the correct stability criterion for one-dimensional flow.

For multidimensional problems, the last term in Eq. (F-24a) is taken as the maximum of the values in the three principal directions. An alternate, and simpler, course is to use the last term from Eq. (F-24b) with μ equal to the largest shear modulus. Then the effective sound speed is

$$\bar{C}^2 = \frac{\Delta P + 2Q}{-\rho \frac{\Delta V}{V}} + \frac{4\mu_{\max}}{3\rho} \quad (F-28)$$

This criterion is sufficiently general for stress relaxation and other time-dependent stress-strain relations.

Particle Velocity (Convective) Effect in One Dimension

In the time step algorithm used here, we introduce a convective term to account for the fact that ΔX changes size during the time step. In small-distortion problems, this correction is unnecessarily meticulous, but it is vital in preventing the cell tangling that occurs in large-distortion problems. Cell tangling occurs when any node of a quadrilateral

moves through an opposite side. Such motion can have no physical meaning in a continuum, so the physical relevance of the calculation ceases at that time.

The convection calculation begins with the Courant condition (Eq. F-18). Here ΔX is rewritten as the average cell dimension during the time step. That is,

$$\Delta t = \frac{\Delta X}{C} = \frac{x_2^{n+1} + x_2^n - x_1^{n+1} - x_1^n}{2C} \quad (F-29)$$

The cell extends from x_1 to x_2 . The superscripts n and $n+1$ refer to time increments such that $t^{n+1} - t^n = \Delta t$. The locations at the $n+1$ time are replaced by using the velocity relation:

$$x^{n+1} = x^n + U^{n + \frac{1}{2}} \Delta t \quad (F-30)$$

where $U^{n + \frac{1}{2}}$ is the particle velocity at $t^n + \Delta t/2$. Then Eq. (F-29) becomes

$$\Delta t = \frac{x_2^n - x_1^n + \frac{1}{2} (U_2^{n + \frac{1}{2}} - U_1^{n + \frac{1}{2}}) \Delta t}{C}$$

Combining the Δt terms, we obtain

$$\Delta t = \frac{x_2^n - x_1^n}{C \left(1 - \frac{U_2^{n + \frac{1}{2}} - U_1^{n + \frac{1}{2}}}{2C} \right)} \quad (F-31)$$

In the denominator this expression for Δt contains the convective correction $\Delta U/C$, which characterizes the cell compression during the time interval.

Crossing Time and Convective Effect in Two Dimensions

A two-dimensional geometry is examined here to determine the effective cell dimension ΔX for Eqs. (F-18) or (F-31) and the convective correction $\Delta U/C$. For a quadrilateral cell, the minimum distances for waves

to travel are from a node to an opposite side. The eight possible minimum paths for a general quadrilateral are shown in Figure F11. Some perpendiculars from the nodes to the sides, such as a and b, lie outside the cell; in this case the minimum path is the side 1-2. If the interior angle at a node such as 1 is greater than 90° , then perpendiculars from adjacent nodes (2 and 4) to sides intersecting at 1 will lie outside the cell (perpendiculars b and h). The paths are therefore computed by calculating the interior angle for each node and then the two paths pertaining to that node. After the paths are determined, the relative velocity along each path is found. Then the time step is computed from Eq. (F-31).

The computation of the minimum crossing distance ΔX and the convective correction $\Delta U/C$ requires calculation of the following quantities:

- The lengths of the sides of the quadrilateral.
- The angles between the sides of the quadrilateral at each joint.
- The relative velocity in the direction of a side.
- The perpendicular distance from a node to a line.
- The relative velocity along the perpendicular distance between a node and a line.

The derivations, which are not included here, are all readily performed by treating the quadrilateral sides and other lines as vectors and using dot or cross products.

Placement of the Time Step Calculation

The location of the time step calculation in the flow of the wave propagation calculations is critical for obtaining a time increment that is a good estimate for the next computational cycle. Here, an optimum location is found, and a test showing the importance of this location is described.

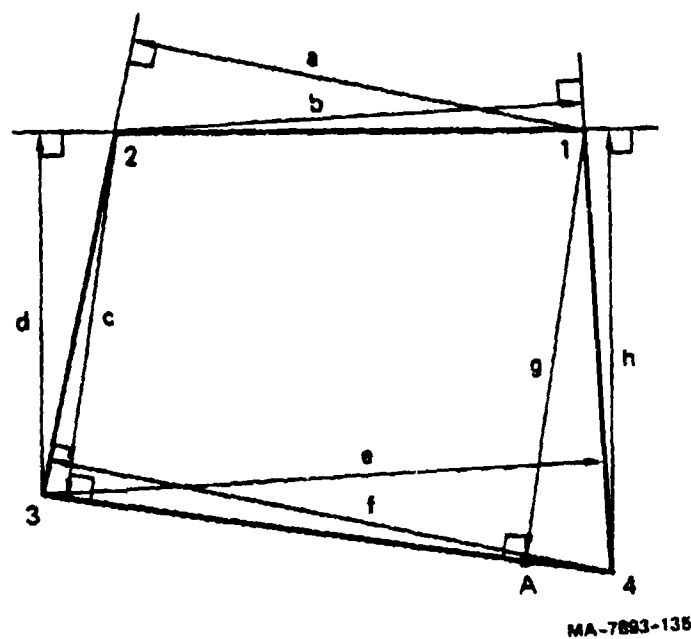


FIGURE F11 MINIMUM WAVE PATHS FOR A QUADRILATERAL CELL

The six basic steps in the wave propagation calculations are assembled here for determining where to put the time step calculation.

(cell loop)

$$1. \rho^n = M/\Delta V^n \quad (F-16)$$

$$2. \Delta \epsilon^{n-1/2} = f(X^n, X^{n-1}, U^{n-1/2}) \Delta t^{n-1/2} \quad (F-32)$$

$$3. E^n = E^{n-1} + \bar{V}^n \sum_{i,k} \bar{T}_{ik}^n \Delta \epsilon_{ik}^{n-1/2} \quad (F-15)$$

$$4. T_{ik}^n = P^n(\rho^n) + \sigma_{ik}^n(\epsilon_{ik}^{n-1}, \Delta \epsilon_{ik}^{n-1/2}) + Q^n \quad (F-17)$$

(node loop)

$$5. U_{ij}^{n+1/2} = U_{ij}^{n-1/2} + \frac{\Delta t^n}{M_j} \sum_{l,k} T_{ikl} \Delta A_{lk} \quad (F-12)$$

$$6. X_{ij}^{n+1} = X_{ij}^n + U_{ij}^{n+1/2} \Delta t^{n+1/2} \quad (F-7)$$

The desired time step is $\Delta t^{n+1/2}$ from Eq. (F-31), or

$$\Delta t^{n+1/2} = g(X^n, U^{n+1/2}) \quad (F-31a)$$

Now we note that $\Delta t^{n+1/2}$ is required for the velocity calculation in step 5, because Δt^n is an average of $\Delta t^{n+1/2}$ and $\Delta t^{n-1/2}$. However, the $U^{n+1/2}$ required for the time step is available only after step 5.

To resolve the conflict in priority over calculations of $\Delta t^{n+1/2}$ and $U^{n+1/2}$, we separated step 5 into parts. First, the right-hand side of (F-12) is evaluated and an estimate of $U_{ij}^{n+1/2}$ is made based on $\Delta t^{n-1/2}$

$$U_{ij}^{est} = U_{ij}^{n-1/2} + \frac{\Delta t^{n-1/2}}{M_j} \sum_{l,k} T_{ikl} \Delta A_{kl} \quad (F-33)$$

This velocity estimate is used in Eq. (F-31) to obtain the time step. Finally $U^{n+1/2}$ is computed from Eq. (F-12). In the code these calculations of U_{ij}^{est} and $\Delta t^{n+1/2}$ are made in an additional loop over all cells: this loop occurs between the main cell and node loops.

This estimation procedure for obtaining $U_{ij}^{n+1/2}$ is satisfactory because we need only correct limits on the velocity to obtain safety from the time step calculation. If U_{ij}^{est} represent an expansion, the velocity terms in the calculation of $\Delta t^{n+1/2}$ are neglected. If U_{ij}^{est} represents a change toward compression, $\Delta t^{n+1/2}$ will be less than $\Delta t^{n-1/2}$, and the change is overestimated. Hence in the worst case, the calculation of $\Delta t^{n+1/2}$ will give a slight underestimate.

To test the advantages of the placement of the time step calculation, a projectile impact simulation was made that had also been made with TROTT. In the TROTT run, the time step calculation with the convective correction was made following step 4 and was therefore based on $U_{ij}^{n-1/2}$. The TROTT calculations halted at about 16 μs because of cell tangling. The corresponding Composite HEMP calculation was halted at 37 μs with the cell pattern shown in Figure 53 of Section VII. The cells are very distorted, but tangling or formation of negative areas has not occurred. An examination of the time steps for the two calculations showed no significant differences. So the new procedure does not require excessively small time steps to produce the added stability. Hence the placement of the time step calculation in Composite HEMP appears to be a clear improvement.

Rezoning

A subroutine REZONH has been developed for rezoning. The rezoner operates on a rectangular grid of cells such as that used in finite-difference wave propagation computer programs. As the cells are distorted by material motion, the rezoner modifies the cell coordinate positions to produce an approximately rectangular grid. REZONH is a continuous rezoner; it makes small changes in some of the coordinate locations at regular intervals, rather than moving all coordinate locations at a few discrete times during a wave propagation problem. From our review of rezoners used with STEALTH, TOODY, and HEMP, the continuous rezoner was selected as being more reliable, requiring less programmer intervention in running a problem, and being easier to write. (The disadvantage of the continuous rezoner is that it tends to smear properties more than a discrete rezoner does.)

The rezoner operates on the entire grid, selecting alternate nodes for possible motion. For each selected node, the distances to adjacent nodes are tested. If the distances are not approximately equal, the node is moved to make the distances more nearly equal. In the current rezoning, the moved node may be in the center of four cells or on a boundary and adjacent to one or two cells. Rezoning cannot yet occur on boundaries between materials unless that boundary is also a slide line.

A rezoning pattern requires four standard computational cycles. Following the first cycle, all odd-numbered nodes are rezoned. After the second cycle, even-numbered nodes are rezoned. After the third and fourth cycles, odd-and even-numbered nodes, respectively, are rezoned starting with the last node and proceeding towards the first.

Described below are the input controls, the coordinate moving algorithm, the procedure for allocating stresses and other properties to the newly configured cells, and the system for computing velocities so that momentum is conserved. Because each of these procedures differs from those used in other codes, the subroutine represents a new approach.

The REZONH subroutine requires input of controls for the frequency and degree of rezoning and to indicate any nodes for which rezoning is not permitted. The input parameters are NFREQ, REZMIN, and REZWT. NFREQ is the rezoning frequency. For NFREQ equal to 10, the standard rezoning pattern occurs following the first four computational cycles, there is no rezoning for six cycles, and then the sequence is repeated. REZMIN is the minimum amount of relative motion that the rezoner will consider; for lesser rezoning motions, the node is skipped and not rezoned. REZWT is the weighting factor determining how rapidly the nodes are moved toward the equal-distance position chosen by the rezoner.

For each node, two rezoning steps occur. First, the nodal motion is computed and then the cell masses and other properties are calculated for the new cell configuration. The equal nodal distance criteria result in indicated motion ΔX and ΔY . Next ΔX and ΔY are compared with REZMIN to determine whether the rezoning should occur. If the criterion is exceeded, the node is moved $REZWT \cdot \Delta X$ and $REZWT \cdot \Delta Y$ in the X and Y directions.

Moving the coordinate points necessitates the redefinition of the size and other properties of all the contiguous cells. First, the masses Z_n of the new cells are computed by an exact sectioning of the volumes of the old cells based on the new and old coordinate lines.

$$Z_n(i) = Z_o(i) + \sum_{j \neq i} C_{ij} \quad (F-34)$$

and

$$C_{ij} = \rho_k V_{ij} \quad (F-35)$$

where $Z_o(i)$ is the mass of the i^{th} old cell

ρ_k is the density of the k^{th} old cell

V_{ij} is the overlap of the i^{th} new cell and the j^{th} old cell.

The cell index k is determined by the nature of the overlap. If the new i cell overlaps the old j cell, then V_{ij} is positive and $\rho_k = \rho_j$. If the overlap is reversed, so that the old i cell overlaps the new j cell, then V_{ij} is negative and $\rho_k = \rho_i$.

New cell densities are computed as the ratio of mass to cell volume, whereas cell area is computed directly. By a mass-weighting calculation, all other cell-centered quantities (e.g., stresses, internal energy, yield strength, fracture state quantities) are computed for the new cells.

For example, the pressure is computed from

$$P_n(i) = \sum_j C_{ij}^+ P_o(j) / \sum_j C_{ij}^+ \quad (F-36)$$

where P_n and P_o are new and old cell pressures, and

$$\begin{aligned} C_{ij}^+ &= \rho_j V_{ij} \text{ as above if mass is added to the } i^{\text{th}} \text{ cell from the } j^{\text{th}} \text{ cell} \\ &= 0 \text{ if mass is removed from the cell} \\ &= Z_n(i) - \sum_{k \neq i} C_{ik}^+ \text{ for } i = j. \end{aligned}$$

With the special definition of the weighting factor C_{ij}^+ , the cell quantities are unaltered if portions of the cell are lost in rezoning, but an averaging occurs if mass is added to the cell. Note that

$$z_n(i) = \sum_j C_{ij}^+ \quad (F-37)$$

The velocity of the new coordinate point is computed by requiring an exact conservation of linear momentum. For this calculation, each of the four (or two for a coordinate point along an edge) adjacent cells are partitioned into four submasses z_k , as they would be for a normal momentum calculation. Each of the submasses is assigned to its nearest coordinate point. Then the momentum balance equation is

$$\sum_k u_k z_{ok} = \sum_{k \neq c} u_k z_{nk} + u_c \sum_{on\ c} z_{nk} \quad (F-38)$$

where

u_k, u_c are the velocities at all the old coordinate points, and
the velocity (to be computed) at this new coordinate point
 z_{ok}, z_{nk} are old and new submasses.

The first summation runs over all 16 submasses, but the second skips the four submasses around the central (new) coordinate. The last summation is for the four central masses. With this equation, the velocity u_c can be computed.

The rezoner has been written and combined with Composite HEMP and a calculation of a projectile impact has been attempted. The impact is one in which large shear distortions occur so that rezoning is needed. REZONH will require some debugging before this calculation can be completed.

Slide Lines

The slide line is constructed to permit relative motion between adjacent materials. A slide line is usually required to represent the interface between a penetrator and target: the slide allows gradual contact of the penetrator and target surfaces and permits the penetrator

to slip along the target. The slide line also represents the formation and relative motion of a distinct slip surface within the target.

A single* slide line treatment has been derived and written into the CYCLE subroutine of Composite HEMP. The coding permits a variety of slip conditions: free sliding with no shear stress, stick conditions, a shear stress with a Coulomb friction limit, and a viscous shear stress. The latter two may be combined so that Coulomb friction determines the shear stress above which sliding can occur. For sliding, the shear stress is given by a viscous expression. In any case, separation and impact can occur on the slide line.

The slide line strategy generally follows that in TOODY. Of the two surfaces making up the slide line, one is designated the master and the other the slave. As in TOODY, the treatment of the two surfaces is nearly identical so it is not important which is designated the master. The TOODY technique also provides a satisfactory transfer of shear stress across the slide.

The slide calculations occur at two locations in CYCLE: during the momentum computation and during the boundary condition treatment. For the momentum calculation, the forces applied by the slave nodes on the master nodes and the forces of the masters on the slaves are computed. Then during the boundary calculations, the slave nodes are forced to lie on the master surface. Also in this last step, if any momentum is lost or gained, it is stored for use during the next momentum calculation. To avoid the "chatter" of impact and separation that often occurs on slide lines, impact is permitted only on the boundary portion of the cycle and separation only on the momentum portion. For separation, a tensile stress criterion must be met.

The slide line logic has been constructed with continuous rezoning in mind. With rezoning, nodes may be shifted by arbitrary amounts, may

*Single means nonintersecting. Several such single slide lines can occur in a problem.

penetrate the slide line, or separate from it. Therefore, the first step in each slide calculation is to locate the point with respect to the nodes on the mating surface. This location process is the most difficult of the several slide operations.

Approaches have been formulated for treating intersecting slide lines and wandering slide lines, but these ideas have not been completely developed or coded. The intersecting slide lines require an overseer section in CYCLE to assess the intersection conditions and keep track of which portions of the bounding surfaces are master, which are slave, and which have other conditions. This overseer can be added later without major changes to the existing coding.

The wandering or unzipping slide lines will permit a plug to be formed in a target. In our plan, the direction and speed with which the slide line is formed will depend on shear band damage in adjacent cells. The slide may proceed either along cell boundaries or diagonally across cells as illustrated in Figure F10. The computations associated with construction of the slide line and generation of new nodes and cells is greatly facilitated by the finite-element numbering technique. Following the renumbering associated with unzipping the slide, the new cells and nodes can be treated by the standard algorithms used for all other cells and nodes.

Currently, only the single slide treatment has been written, and it has been tested only for impact of a projectile onto a cylindrical wall. (The case is illustrated in Figure 53 of Section VII.) Both the wall and the projectile surface are represented by a series of node points. Thus, the test verifies the methods used to locate adjacent nodes on the mating surface, to detect penetration of the master line by slave nodes, and to slide nodes along the master line.

Further tests are planned for the single slide treatment, and then the intersecting and wandering slide development will begin.

DISTRIBUTION LIST

<u>No. of Copies</u>	<u>Organization</u>	<u>No. of Copies</u>	<u>Organization</u>
12	Administrator Defense Technical Info Center ATTN: DTIC-DDA Cameron Station Alexandria, VA 22304-6145	1	Director US Army Air Mobility Research and Development Laboratory Ames Research Center Moffett Field, CA 94035
1	HQDA (DAMA-ART-M) Washington, DC 20310	1	Commander US Army Communications - Electronics Command ATTN: AMSEL-ED Fort Monmouth, NJ 07703
1	Commander US Army Materiel Command ATTN: AMCDRA-ST 5001 Eisenhower Avenue Alexandria, VA 22333-0001	1	Commander ERADCOM Technical Library ATTN: DELSD-L (Reports Section) Fort Monmouth, NJ 07703-5301
1	Commander Armament R&D Center US Army AMCCOM ATTN: SMCAR-TSS Dover, NJ 07801	1	Commander US Army Missile Command Research, Development and Engineering Center ATTN: AMSMI-RD Redstone Arsenal, AL 35898
1	Commander Armament R&D Center US Army AMCCOM ATTN: SMCAR-TDC Dover, NJ 07801	1	Director US Army Missile & Space Intelligence Center ATTN: AIAMS-YDL Redstone Arsenal, AL 35898-5500
1	Commander US Army Material Technology Laboratory ATTN: John Mescall Watertown, MA 02172	1	Commander US Army Tank-Automotive Command ATTN: AMSTA-TSL Warren, MI 48397-5000
1	Director Benet Weapons Laboratory Armament R&D Center US Army AMCCOM ATTN: SMCAR-LCB-TL Watervliet, NY 12189	3	Director US Army TRADOC Systems Analysis Activity ATTN: ATAA-SL White Sands Missile Range, NM 8002
1	Commander US Army Armament, Munitions and Chemical Command ATTN: SMCAR-ESP-L Rock Island, IL 61299	1	Commandant US Army Infantry School ATTN: ATSH-CD-CSO-OR Fort Benning, GA 31905
1	Commander US Army Aviation Research and Development Command ATTN: AMSAV-E 4300 Goodfellow Blvd St. Louis, MO 63120		

DISTRIBUTION LIST

<u>No. of Copies</u>	<u>Organization</u>	<u>No. of Copies</u>	<u>Organization</u>
1	Commander US Army Development & and Employment Agency ATTN: MODE-TED-SAB Fort Lewis, WA 98433	10	Central Intelligence Agency Office of Central Reference Dissemination Branch Room GE-47 HQS Washington, DC 20502
1	AFWL/SUL Kirtland AFB, FL 87117		<u>Aberdeen Proving Ground</u>
1	AFATL/DLODL Eglin AFB, FL 32542-5000		Dir, USAMSAA ATTN: AMXSY-D AMXSY-MP (H. Cohen)
1	AFATL (Joe Foster) Eglin AFB, FL 32452-5000		Cdr, USATECOM ATTN: AMSTE-TO-F
2	US Army Research Office ATTN: George Mayer Robert Singleton P. O. Box 12211 Research Triangle Park, NC 27709		Cdr, CRDC, AMCCOM ATTN: SMCCR-RSP-A SMCCR-MU SMCCR-SPS-IL
2	Naval Surface Weapons Center ATTN: William H. Holt Willis Mock, Jr. Dahlgren, VA 22448		
1	Naval Research Laboratory ATTN: Rick Mako Washington, DC 20375		

USER EVALUATION SHEET/CHANGE OF ADDRESS

This Laboratory undertakes a continuing effort to improve the quality of the reports it publishes. Your comments/answers to the items/questions below will aid us in our efforts.

1. BRL Report Number _____ Date of Report _____
2. Date Report Received _____
3. Does this report satisfy a need? (Comment on purpose, related project, or other area of interest for which the report will be used.) _____

4. How specifically, is the report being used? (Information source, design data, procedure, source of ideas, etc.) _____

5. Has the information in this report led to any quantitative savings as far as man-hours or dollars saved, operating costs avoided or efficiencies achieved, etc? If so, please elaborate. _____

6. General Comments. What do you think should be changed to improve future reports? (Indicate changes to organization, technical content, format, etc.) _____

CURRENT ADDRESS

Name _____

Organization _____

Address _____

City, State, Zip _____

7. If indicating a Change of Address or Address Correction, please provide the New or Correct Address in Block 6 above and the Old or Incorrect address below.

OLD ADDRESS

Name _____

Organization _____

Address _____

City, State, Zip _____

(Remove this sheet, fold as indicated, staple or tape closed, and mail.)

----- FOLD HERE -----

Director
US Army Ballistic Research Laboratory
ATTN: DRXBR-OD-ST
Aberdeen Proving Ground, MD 21005-5066



NO POSTAGE
NECESSARY
IF MAILED
IN THE
UNITED STATES

OFFICIAL BUSINESS
PENALTY FOR PRIVATE USE, \$300

BUSINESS REPLY MAIL
FIRST CLASS PERMIT NO 12062 WASHINGTON, DC
POSTAGE WILL BE PAID BY DEPARTMENT OF THE ARMY

Director
US Army Ballistic Research Laboratory
ATTN: DRYBR-OD-ST
Aberdeen Proving Ground, MD 21005-9989



----- FOLD HERE -----